

# Measurements of Top Quark Production with the CMS Detector at the LHC

Jeson Jacob

September 2015



A dissertation submitted to the University of Bristol in accordance with the requirements for  
award of the degree of Doctor of Philosophy in the Faculty of Science, School of Physics,  
September 2015.

Word Count: XX,XXX words

## **Abstract**



# Acknowledgements

The author would like to thank...



# **Declaration**

I declare that the work in this dissertation was carried out in accordance with the requirements of the University's Regulations and Code of Practice for Research Degree Programmes and that it has not been submitted for any other academic award. Except where indicated by specific reference in the text, the work is the candidate's own work. Work done in collaboration with, or with the assistance of, others, is indicated as such. Any views expressed in the dissertation are those of the author.

Signed:.....

Date:.....



# Contents

<b>1</b>	<b>Introduction</b>	<b>1</b>
<b>2</b>	<b>The CMS Detector at the LHC</b>	<b>5</b>
2.1	Introduction to the LHC . . . . .	5
2.2	Overview of CMS . . . . .	7
2.3	Sub-Detectors . . . . .	9
2.3.1	Tracker . . . . .	9
2.3.2	Electromagnetic Calorimeter . . . . .	12
2.3.3	Hadronic Calorimeter . . . . .	14
2.3.4	Superconducting Magnet . . . . .	15
2.3.5	Muon Chambers . . . . .	16
2.3.6	Trigger and Data Acquisition . . . . .	18
2.4	Upgrades . . . . .	21
<b>3</b>	<b>CMS Computing and Offline</b>	<b>23</b>
3.1	CMS Computing . . . . .	23
3.2	Event Data Model . . . . .	24
3.3	Object Reconstruction and Identification . . . . .	25
3.3.1	Track Reconstruction . . . . .	25
3.3.2	Pileup Subtraction . . . . .	26
3.3.3	Electron Reconstruction . . . . .	27
3.3.4	Muon Reconstruction . . . . .	29
3.3.5	Jet Reconstruction . . . . .	30
<b>4</b>	<b>The Standard Model</b>	<b>33</b>
4.1	Introduction . . . . .	33
4.1.1	Gauge Principle . . . . .	35
4.1.2	Quantum Electrodynamics . . . . .	36
4.1.3	Electroweak Theory . . . . .	39
4.1.4	Quantum Chromodynamics . . . . .	41
4.1.5	Spontaneous Symmetry Breaking . . . . .	43
4.2	Incompleteness of, and physics beyond, the SM . . . . .	44
<b>5</b>	<b>Top Physics at the LHC</b>	<b>49</b>
5.1	Introduction . . . . .	49
5.1.1	Top Quark Production and Decay . . . . .	49
5.1.2	Single Top background . . . . .	52
5.1.3	W/Z+jets background . . . . .	53
5.1.4	QCD background . . . . .	54
5.2	Monte Carlo Simulation . . . . .	55
5.2.1	MadGraph . . . . .	56
5.2.2	MCatNLO . . . . .	56
5.2.3	PYTHIA . . . . .	57

5.2.4	POWHEG . . . . .	57
5.3	Theoretical Systematics . . . . .	57
5.3.1	Factorisation & Matching Threshold . . . . .	57
5.3.2	Detector Simulation (GEANT) . . . . .	58
<b>6</b>	<b>b-tagging Study</b>	<b>59</b>
6.1	Observables used in b-tagging algorithms . . . . .	60
6.2	b-tagging algorithm descriptions . . . . .	62
6.3	Performance Comparison . . . . .	64
6.4	Efficiency . . . . .	64
6.5	Algorithm Comparison . . . . .	65
<b>7</b>	<b>7 TeV and 8 TeV Differential Cross Section Measurement: Data, Simulation and Selection</b>	<b>69</b>
7.1	Outline . . . . .	69
7.2	Data and Simulated Samples . . . . .	71
7.2.1	Data . . . . .	71
7.2.2	Simulated Samples . . . . .	72
7.3	Selection . . . . .	73
7.3.1	Preselection . . . . .	73
7.3.2	Electron selection . . . . .	74
7.3.3	Muon selection . . . . .	74
7.3.4	Jets selection . . . . .	75
7.3.5	Multi-jet background selection . . . . .	75
7.4	Data-MC scale factors . . . . .	79
7.4.1	Pileup . . . . .	79
7.4.2	b-tagging . . . . .	80
7.4.3	Jet Energy Scale . . . . .	81
7.4.4	Missing Transverse Energy Corrections . . . . .	81
7.4.5	Trigger, Lepton ID and Isolation Efficiencies and Corrections . . . . .	83
<b>8</b>	<b>7 TeV and 8 TeV Differential Cross Section Measurement: Fitting, Unfolding and Measurement</b>	<b>91</b>
8.1	Data-MC Comparison . . . . .	91
8.2	Binning Choice . . . . .	93
8.3	Maximum Likelihood Fit . . . . .	101
8.3.1	Choice of templates . . . . .	102
8.3.2	Fit Results . . . . .	108
8.4	Fit cross-checks . . . . .	113
8.5	Background Subtraction . . . . .	113
8.6	Unfolding . . . . .	113
8.6.1	Measurement . . . . .	119
<b>9</b>	<b>7 TeV and 8 TeV Differential Cross Section Measurement: Systematic Uncertainties and Results</b>	<b>121</b>
9.1	Systematic uncertainties . . . . .	121
9.1.1	Experimental Uncertainties . . . . .	122
9.1.2	Theoretical Uncertainties . . . . .	124

9.1.3	Systematic Uncertainty Tables	127
9.2	Results	127
<b>10</b>	<b>Summary</b>	<b>135</b>
<b>A</b>	<b>b-tagging Study Plots</b>	<b>137</b>
<b>B</b>	<b><math>t\bar{t}</math> different cross section analysis</b>	<b>139</b>
B.1	Datasets in differential cross section analysis	139
B.2	Data - Monte Carlo corrections	139
B.3	Binning in the muon+jets channel	143
B.4	Binning choice tables	146
B.5	Fitting Variable Distributions	151
B.6	Fitting variable QCD background template comparisons	153
B.7	Fitting variable V+jets background template comparisons	158
B.8	Fit Results Tables	163
B.9	Fit correlations	174
B.10	Systematic Uncertainties	176
B.11	Results	187
B.11.1	7 TeV	187
B.11.2	8 TeV	190
<b>C</b>	<b>CMS Binary Chip</b>	<b>193</b>
C.1	Introduction and previous studies	193
C.2	Measuring signal noise using a capacitor	195
C.3	Gain	196
C.4	Investigating change in Preamp Input Branch Bias Current	197
C.5	Summary	197
<b>References</b>		<b>199</b>



# List of Figures

<b>1</b>	<b>Introduction</b>	
1.1	Map of LHC location. . . . .	2
<b>2</b>	<b>The CMS Detector at the LHC</b>	
2.1	Schematic of LHC and experiments. . . . .	5
2.2	Cumulative luminosity delivered to CMS during 2010, 2011 and 2012. . . . .	7
2.3	Diagrammatic sectional view of the CMS detector. . . . .	8
2.4	Cross-sectional diagram of the CMS strip tracker. . . . .	11
2.5	Diagram of the ECAL showing barrel supermodules, endcaps and preshower detectors. . . . .	14
2.6	A longitudinal schematic of the CMS HCAL. . . . .	15
2.7	Bore of the CMS solenoid magnet in vertical position in the CMS assembly hall, SX5. . . . .	16
2.8	Schematic representation of a quarter of the CMS muon system. . . . .	17
2.9	Single muon HLT rates at low and high luminosities. . . . .	20
<b>3</b>	<b>CMS Computing and Offline</b>	
3.1	Muon transverse momentum resolution using muon system and the tracking system. . . . .	29
<b>4</b>	<b>The Standard Model</b>	
4.1	Elementary electromagnetic processes. . . . .	37
4.2	The Higgs field potential. . . . .	44
4.3	Invariant mass in $H \rightarrow \gamma\gamma$ (left) and $H \rightarrow ZZ$ (right) channels. . . . .	45
4.4	The composition of the universe showing the amounts of dark matter, dark energy and ordinary matter. . . . .	47
<b>5</b>	<b>Top Physics at the LHC</b>	
5.1	Feynman diagrams of leading order $t\bar{t}$ production processes. . . . .	50
5.2	Proton parton distribution functions at $Q^2 = 10 \text{ GeV}^2$ . . . . .	50
5.3	$t\bar{t}$ production cross sections at $1.96 \text{ TeV}$ at CDF and DØ at the TeVatron and at $7 \text{ TeV}$ and $8 \text{ TeV}$ at CMS and ATLAS at the LHC. . . . .	51
5.4	Feynman diagram of the electron+jets semi-leptonic $t\bar{t}$ decay channel. . . . .	52
5.5	Relative branching ratios of the $t\bar{t}$ system . . . . .	53
<b>6</b>	<b>b-tagging Study</b>	
6.1	Graphical representation of a secondary vertex. . . . .	60
6.2	Graphical representation of a track impact parameter. . . . .	61
6.3	Discriminator values produced by the Combined Secondary Vertex algorithm after normalisation. . . . .	65
6.4	Non b-jet efficiencies as a function of b-jet efficiency for the CSV algorithm. . . . .	66
6.5	udsjet efficiencies as a function of b-jet efficiencies for all algorithms. . . . .	66
<b>7</b>	<b>7 TeV and 8 TeV Differential Cross Section Measurement:</b>	Data, Simulation

7.1	PF relative isolation distributions in the muon+jets channel at $\sqrt{s} = 7 \text{ TeV}$ and $\sqrt{s} = 8 \text{ TeV}$ . . . . .	77
7.2	Comparison of QCD selections in the electron+jets channel at $\sqrt{s} = 7 \text{ TeV}$ and at $\sqrt{s} = 8 \text{ TeV}$ . . . . .	78
7.3	Distributions of the number of reconstructed vertices in an event in the electron+jets channel before and after implementing pileup reweighting at $\sqrt{s} = 7 \text{ TeV}$ and $\sqrt{s} = 8 \text{ TeV}$ . . . . .	80
7.4	Distributions of the number of b-tags in an event in the electron+jets channel before and after applying b-tag scale factors at $\sqrt{s} = 7 \text{ TeV}$ and $\sqrt{s} = 8 \text{ TeV}$ . . . . .	82
7.5	Fits of the invariant mass distribution of all tag-and-probe pairs and tag-and-probe pairs in which the probe satisfies the identification and isolation criteria. . . . .	84
7.6	Identification and isolation efficiencies as a function of $\eta$ and $p_T$ in data and $t\bar{t}$ Monte Carlo simulation. . . . .	85
<b>8</b>	<b>7 TeV and 8 TeV Differential Cross Section Measurement: Fitting, Unfolding and</b>	
8.1	Comparison of Monte Carlo simulation to data in the electron+jets channel after final selection at $\sqrt{s} = 7 \text{ TeV}$ . . . . .	94
8.2	Comparison of Monte Carlo simulation to data in the muon+jets channel after final selection at $\sqrt{s} = 7 \text{ TeV}$ . . . . .	95
8.3	Comparison of Monte Carlo simulation to data in the electron+jets channel after final selection at $\sqrt{s} = 8 \text{ TeV}$ . . . . .	96
8.4	Comparison of Monte Carlo simulation to data in the muon+jets channel after final selection at $\sqrt{s} = 8 \text{ TeV}$ . . . . .	97
8.5	Graphical representation of bin purity and stability. . . . .	98
8.6	Generated versus reconstructed distributions of the primary variable at $\sqrt{s} = 7 \text{ TeV}$ . . . . .	99
8.7	Generated versus reconstructed distributions of the primary variables at $\sqrt{s} = 8 \text{ TeV}$ . . . . .	100
8.8	Normalised distributions of the templates for the three fit variables, inclusive across all primary variable bins at $\sqrt{s} = 7 \text{ TeV}$ . . . . .	104
8.9	Normalised distributions of the QCD templates for the three fit variables in $E_T^{\text{miss}}$ bins at $\sqrt{s} = 8 \text{ TeV}$ . . . . .	106
8.10	Normalised distributions of the V+jets templates for the three fit variables in $E_T^{\text{miss}}$ bins. . . . .	107
8.11	Comparison of Monte Carlo simulation to data in the electron+jets channel after fitting at $\sqrt{s} = 7 \text{ TeV}$ . . . . .	109
8.12	Comparison of Monte Carlo simulation to data in the muon+jets channel after fitting at $\sqrt{s} = 7 \text{ TeV}$ . . . . .	110
8.13	Comparison of Monte Carlo simulation to data in the electron+jets channel after fitting at $\sqrt{s} = 8 \text{ TeV}$ . . . . .	111
8.14	Comparison of Monte Carlo simulation to data in the muon+jets channel after fitting at $\sqrt{s} = 8 \text{ TeV}$ . . . . .	112
8.15	Correlation between fit processes for the $E_T^{\text{miss}}$ variable in the electron+jets channel at $\sqrt{s} = 8 \text{ TeV}$ . . . . .	114
8.16	$\log d_i $ plots at $\sqrt{s} = 8 \text{ TeV}$ . . . . .	117
8.17	Unfolding closure tests for the $E_T^{\text{miss}}$ variable at $\sqrt{s} = 8 \text{ TeV}$ . . . . .	119

8.18	Pull distribution using toy Monte Carlo datasets for the $E_T^{\text{miss}}$ variable using a $k$ value of 3 for the $E_T^{\text{miss}}$ variable at $\sqrt{s} = 8 \text{ TeV}$	120
<b>9</b>	<b>7 TeV and 8 TeV Differential Cross Section Measurement:</b>	<b>Systematic Uncert</b>
9.1	Diagrams of semi-leptonic and dileptonic $\tau$ events.	123
9.2	Comparison of the signal and fake distributions in the $E_T^{\text{miss}}$ variable from semi-leptonic $t\bar{t}$ events in the electron+jets channel at $\sqrt{s} = 8 \text{ TeV}$ .	124
9.3	Comparison of the $E_T^{\text{miss}}$ distributions in the nominal measurement and in the tau energy down variation in data and in simulation.	125
9.4	$E_T^{\text{miss}}$ and electron $ \eta $ shape comparison of W+jets templates in $\sqrt{s} = 7 \text{ TeV}$ and $\sqrt{s} = 8 \text{ TeV}$ in the electron+jets channel.	126
9.5	Comparison of the measured normalised differential cross section with respect to $E_T^{\text{miss}}$ , $H_T$ and $S_T$ to different Monte Carlo generators and predictions at $\sqrt{s} = 7 \text{ TeV}$ .	130
9.6	Comparison of the measured normalised differential cross section with respect to $p_T^W$ and $M_T^W$ to different Monte Carlo generators and predictions at $\sqrt{s} = 7 \text{ TeV}$ .	131
9.7	Comparison of the measured normalised differential cross section with respect to $E_T^{\text{miss}}$ , $H_T$ and $S_T$ to different Monte Carlo generators and predictions at $\sqrt{s} = 8 \text{ TeV}$ .	132
9.8	Comparison of the measured normalised differential cross section with respect to $p_T^W$ and $M_T^W$ to different Monte Carlo generators and predictions at $\sqrt{s} = 8 \text{ TeV}$ .	133
<b>A</b>	<b>b-tagging Study Plots</b>	
A.1	Discriminator distributions produced by CMS b-tagging algorithms.	137
A.2	c-jet, g-jet and uds-jet efficiencies as a function of b-jet efficiency for CMS b-tagging algorithms.	138
<b>B</b>	<b><math>t\bar{t}</math> different cross section analysis</b>	
B.1	Distributions of the number of reconstructed vertices in an event in the muon+jets channel before and after implementing pileup reweighting at $\sqrt{s} = 7 \text{ TeV}$ and $\sqrt{s} = 8 \text{ TeV}$ .	140
B.2	Distributions of the number of b-tags in an event in the muon+jets channel before and after applying b-tag scale factors at $\sqrt{s} = 7 \text{ TeV}$ and $\sqrt{s} = 8 \text{ TeV}$ .	141
B.3	Fits of the invariant mass distribution of tag-and-probe electron pairs.	142
B.4	Trigger efficiencies as a function of $\eta$ and $p_T$ in data and $t\bar{t}$ Monte Carlo simulation.	142
B.5	Generated versus reconstructed distributions of the primary variables at $\sqrt{s} = 7 \text{ TeV}$ in the muon+jets channel.	144
B.6	Generated versus reconstructed distributions of the primary variables at $\sqrt{s} = 8 \text{ TeV}$ in the muon+jets channel.	145
B.7	Normalised distributions of the templates for the three fit variables inclusive across all primary variable bins at $\sqrt{s} = 8 \text{ TeV}$ .	152
B.8	Normalised distributions of the QCD templates for the three fit variables in $H_T$ bins at $\sqrt{s} = 8 \text{ TeV}$ .	154
B.9	Normalised distributions of the QCD templates for the three fit variables in $S_T$ bins at $\sqrt{s} = 8 \text{ TeV}$ .	155
B.10	Normalised distributions of the QCD templates for the three fit variables in $M_T^W$ bins at $\sqrt{s} = 8 \text{ TeV}$ .	156

B.11 Normalised distributions of the QCD templates for the three fit variables in $p_T^W$ bins at $\sqrt{s} = 8 \text{ TeV}$ . . . . .	157
B.12 Normalised distributions of the V+jets templates for the three fit variables in $H_T$ bins at $\sqrt{s} = 8 \text{ TeV}$ . . . . .	159
B.13 Normalised distributions of the V+jets templates for the three fit variables in $S_T$ bins at $\sqrt{s} = 8 \text{ TeV}$ . . . . .	160
B.14 Normalised distributions of the V+jets templates for the three fit variables in $M_T^W$ bins at $\sqrt{s} = 8 \text{ TeV}$ . . . . .	161
B.15 Normalised distributions of the V+jets templates for the three fit variables in $p_T^W$ bins at $\sqrt{s} = 8 \text{ TeV}$ . . . . .	162
B.16 Correlation between fit processes for the $E_T^{\text{miss}}$ variable in the electron+jets channel at $\sqrt{s} = 7 \text{ TeV}$ . . . . .	175
B.17 Comparison of the measured normalised differential cross section, with background subtraction results, with respect to $E_T^{\text{miss}}$ , $H_T$ , $S_T$ , $p_T^W$ and $M_T^W$ to different Monte Carlo generators and predictions at $\sqrt{s} = 7 \text{ TeV}$ . . . . .	189
B.18 Comparison of the measured normalised differential cross section, with background subtraction results, with respect to $E_T^{\text{miss}}$ , $H_T$ , $S_T$ , $p_T^W$ and $M_T^W$ to different Monte Carlo generators and predictions at $\sqrt{s} = 8 \text{ TeV}$ . . . . .	192
<b>C CMS Binary Chip</b>	
C.1 Schedule of LHC upgrades over the next decade. . . . .	194
C.2 Noise as a function of added capacitance for channel 65 in 'electrons' mode (left) and 'holes' mode (right). . . . .	195
C.3 Noise for all channels with injection cable connected to channel 60 but with no pulse injected, in 'electrons' mode (left) and 'holes' mode (right). . . . .	196
C.4 S-curve mid-point (a) as a function of pulse generator delay and (b) as a function of injected charge in 'holes' mode at 20 °C. . . . .	197
C.5 Variation in s-curve mid-point over range of Ipre1 register values for temperatures from -40 °C to 40 °C. . . . .	198

# List of Tables

<b>4 The Standard Model</b>		
4.1 Fundamental fermions, split into their three generations, and bosons of the Standard Model. Particle properties taken from [81]. . . . .	34	
<b>5 Top Physics at the LHC</b>		
5.1 Threshold transverse energy for matching systematic uncertainty . . . . .	58	
<b>7 7 TeV and 8 TeV Differential Cross Section Measurement:</b>		<b>Data, Simulation</b>
7.1 7 TeV data sets by run period with the corresponding integrated luminosities ( $L_{int}$ ) and run numbers. . . . .	72	
7.2 8 TeV data sets by run period with the corresponding integrated luminosities ( $L_{int}$ ) and run numbers. . . . .	72	
7.3 7 TeV Monte Carlo signal datasets used for this analysis. . . . .	73	
7.4 7 TeV Monte Carlo background datasets used for this analysis. All samples are generated inclusively if not marked otherwise (* generator cut on in-flight-decays of b- and c-hadrons, $\ominus$ enriched in conversion electrons; $l$ means all leptonic decays: $l = e, \mu, \tau$ ; • generator cut on $m_{Z/\gamma} > 50$ GeV). . . . .	87	
7.5 7 TeV Monte Carlo systematic datasets used for this analysis. All samples are produced with the MADGRAPH generator. W + jets and Z + jets samples were not available and so have been scaled from available 8 TeV samples. . .	88	
7.6 8 TeV Monte Carlo signal datasets used for this analysis. . . . .	88	
7.7 8 TeV Monte Carlo background datasets used for this analysis. All samples are generated inclusively if not marked otherwise (* generator cut on in-flight-decays of b- and c-hadrons, $\ominus$ enriched in conversion electrons; $l$ means all leptonic decays: $l = e, \mu, \tau$ ; • generator cut on $m_{Z/\gamma} > 50$ GeV). . . . .	89	
7.8 8 TeV Monte Carlo systematic datasets used for this analysis. All samples are produced with the MADGRAPH generator. . . . .	90	
<b>8 7 TeV and 8 TeV Differential Cross Section Measurement:</b>		<b>Fitting, Unfolding</b>
8.1 Expected and observed event yields at several stages of the electron+jets selection (upper) and the muon+jets channel selection(lower) at $\sqrt{s}=7$ TeV. . .	92	
8.2 Expected and observed event yields at several stages of the electron+jets selection (upper) and the muon+jets selection (lower) at $\sqrt{s}=8$ TeV. . . . .	92	
8.3 Optimal $k$ -values for all primary variables at both 7 and 8 TeV. . . . .	118	
<b>9 7 TeV and 8 TeV Differential Cross Section Measurement:</b>		<b>Systematic Uncertainties</b>
9.1 Typical systematic uncertainties in percent (median values) for the normalised $t\bar{t}$ differential cross section measurement at $\sqrt{s} = 7$ TeV (combination of electron and muon channels). Typical values of the total systematic uncertainty are also shown. . . . .	128	
9.2 Typical systematic uncertainties in percent (median values) for the normalised $t\bar{t}$ differential cross section measurement at $\sqrt{s} = 8$ TeV (combination of electron and muon channels). Typical values of the total systematic uncertainty are also shown. . . . .	129	

## B $t\bar{t}$ different cross section analysis

B.1	HLT Triggers used in 2011 and 2012 data in the electron and muon channels.	139
B.2	JSON files used for the 2011 and 2012 data taking periods. . . . .	139
B.3	The selected bins for the measurement in the electron channel at a centre-of-mass energy of 7 TeV. In addition to the bin ranges the purity, stability and number of expected $t\bar{t}$ events are shown. . . . .	147
B.4	The selected bins for the measurement in the muon channel at a centre-of-mass energy of 7 TeV. In addition to the bin ranges the purity, stability and number of expected $t\bar{t}$ events are shown. . . . .	148
B.5	The selected bins for the measurement in the electron channel at a centre-of-mass energy of 8 TeV. In addition to the bin ranges the purity, stability and number of expected $t\bar{t}$ events are shown. . . . .	149
B.6	The selected bins for the measurement in the muon channel at a centre-of-mass energy of 8 TeV. In addition to the bin ranges the purity, stability and number of expected $t\bar{t}$ events are shown. . . . .	150
B.7	Fit results for the $E_T^{\text{miss}}$ variable at a centre-of-mass energy of 7 TeV (electron channel). . . . .	163
B.8	Fit results for the $E_T^{\text{miss}}$ variable at a centre-of-mass energy of 7 TeV (muon channel). . . . .	163
B.9	Fit results for the $H_T$ variable at a centre-of-mass energy of 7 TeV (electron channel). . . . .	164
B.10	Fit results for the $H_T$ variable at a centre-of-mass energy of 7 TeV (muon channel). . . . .	164
B.11	Fit results for the $S_T$ variable at a centre-of-mass energy of 7 TeV (electron channel). . . . .	165
B.12	Fit results for the $S_T$ variable at a centre-of-mass energy of 7 TeV (muon channel). . . . .	165
B.13	Fit results for the $p_T^W$ variable at a centre-of-mass energy of 7 TeV (electron channel). . . . .	166
B.14	Fit results for the $p_T^W$ variable at a centre-of-mass energy of 7 TeV (muon channel). . . . .	167
B.15	Fit results for the $M_T^W$ variable at a centre-of-mass energy of 7 TeV (electron channel). . . . .	168
B.16	Fit results for the $M_T^W$ variable at a centre-of-mass energy of 7 TeV (muon channel). . . . .	168
B.17	Fit results for the $E_T^{\text{miss}}$ variable at a centre-of-mass energy of 8 TeV (electron channel). . . . .	169
B.18	Fit results for the $E_T^{\text{miss}}$ variable at a centre-of-mass energy of 8 TeV (muon channel). . . . .	169
B.19	Fit results for the $H_T$ variable at a centre-of-mass energy of 8 TeV (electron channel). . . . .	170
B.20	Fit results for the $H_T$ variable at a centre-of-mass energy of 8 TeV (muon channel). . . . .	170
B.21	Fit results for the $S_T$ variable at a centre-of-mass energy of 8 TeV (electron channel). . . . .	171
B.22	Fit results for the $S_T$ variable at a centre-of-mass energy of 8 TeV (muon channel). . . . .	171

B.23 Fit results for the $p_T^W$ variable at a centre-of-mass energy of 8 TeV (electron channel). . . . .	172
B.24 Fit results for the $p_T^W$ variable at a centre-of-mass energy of 8 TeV (muon channel). . . . .	172
B.25 Fit results for the $M_T^W$ variable at a centre-of-mass energy of 8 TeV (electron channel). . . . .	173
B.26 Fit results for the $M_T^W$ variable at a centre-of-mass energy of 8 TeV (muon channel). . . . .	173
B.27 Systematic uncertainties for the normalised $t\bar{t}$ cross section measurement with respect to $E_T^{\text{miss}}$ variable at a centre-of-mass energy of 7 TeV (combination of electron and muon channels). . . . .	177
B.28 Systematic uncertainties for the normalised $t\bar{t}$ cross section measurement with respect to $H_T$ variable at a centre-of-mass energy of 7 TeV (combination of electron and muon channels). . . . .	178
B.29 Systematic uncertainties for the normalised $t\bar{t}$ cross section measurement with respect to $S_T$ variable at a centre-of-mass energy of 7 TeV (combination of electron and muon channels). . . . .	179
B.30 Systematic uncertainties for the normalised $t\bar{t}$ cross section measurement with respect to $p_T^W$ variable at a centre-of-mass energy of 7 TeV (combination of electron and muon channels). . . . .	180
B.31 Systematic uncertainties for the normalised $t\bar{t}$ cross section measurement with respect to $M_T^W$ variable at a centre-of-mass energy of 7 TeV (combination of electron and muon channels). . . . .	181
B.32 Systematic uncertainties for the normalised $t\bar{t}$ cross section measurement with respect to $E_T^{\text{miss}}$ variable at a centre-of-mass energy of 8 TeV (combination of electron and muon channels). . . . .	182
B.33 Systematic uncertainties for the normalised $t\bar{t}$ cross section measurement with respect to $H_T$ variable at a centre-of-mass energy of 8 TeV (combination of electron and muon channels). . . . .	183
B.34 Systematic uncertainties for the normalised $t\bar{t}$ cross section measurement with respect to $S_T$ variable at a centre-of-mass energy of 8 TeV (combination of electron and muon channels). . . . .	184
B.35 Systematic uncertainties for the normalised $t\bar{t}$ cross section measurement with respect to $p_T^W$ variable at a centre-of-mass energy of 8 TeV (combination of electron and muon channels). . . . .	185
B.36 Systematic uncertainties for the normalised $t\bar{t}$ cross section measurement with respect to $M_T^W$ variable at a centre-of-mass energy of 8 TeV (combination of electron and muon channels). . . . .	186
B.37 Normalised $t\bar{t}$ cross section measurement with respect to $E_T^{\text{miss}}$ variable at a centre-of-mass energy of 7 TeV (combination of electron and muon channels). The errors shown are combined statistical, fit and unfolding errors ( $\dagger$ ) and systematic uncertainty (*). . . . .	187
B.38 Normalised $t\bar{t}$ cross section measurement with respect to $H_T$ variable at a centre-of-mass energy of 7 TeV (combination of electron and muon channels). The errors shown are combined statistical, fit and unfolding errors ( $\dagger$ ) and systematic uncertainty (*). . . . .	187

B.39 Normalised $t\bar{t}$ cross section measurement with respect to $S_T$ variable at a centre-of-mass energy of 7 TeV (combination of electron and muon channels). The errors shown are combined statistical, fit and unfolding errors ( $\dagger$ ) and systematic uncertainty (*).	188
B.40 Normalised $t\bar{t}$ cross section measurement with respect to $M_T^W$ variable at a centre-of-mass energy of 7 TeV (combination of electron and muon channels). The errors shown are combined statistical, fit and unfolding errors ( $\dagger$ ) and systematic uncertainty (*).	188
B.41 Normalised $t\bar{t}$ cross section measurement with respect to $p_T^W$ variable at a centre-of-mass energy of 7 TeV (combination of electron and muon channels). The errors shown are combined statistical, fit and unfolding errors ( $\dagger$ ) and systematic uncertainty (*).	188
B.42 Normalised $t\bar{t}$ cross section measurement with respect to $E_T^{\text{miss}}$ variable at a centre-of-mass energy of 8 TeV (combination of electron and muon channels). The errors shown are combined statistical, fit and unfolding errors ( $\dagger$ ) and systematic uncertainty (*).	190
B.43 Normalised $t\bar{t}$ cross section measurement with respect to $H_T$ variable at a centre-of-mass energy of 8 TeV (combination of electron and muon channels). The errors shown are combined statistical, fit and unfolding errors ( $\dagger$ ) and systematic uncertainty (*).	190
B.44 Normalised $t\bar{t}$ cross section measurement with respect to $S_T$ variable at a centre-of-mass energy of 8 TeV (combination of electron and muon channels). The errors shown are combined statistical, fit and unfolding errors ( $\dagger$ ) and systematic uncertainty (*).	191
B.45 Normalised $t\bar{t}$ cross section measurement with respect to $M_T^W$ variable at a centre-of-mass energy of 8 TeV (combination of electron and muon channels). The errors shown are combined statistical, fit and unfolding errors ( $\dagger$ ) and systematic uncertainty (*).	191
B.46 Normalised $t\bar{t}$ cross section measurement with respect to $p_T^W$ variable at a centre-of-mass energy of 8 TeV (combination of electron and muon channels). The errors shown are combined statistical, fit and unfolding errors ( $\dagger$ ) and systematic uncertainty (*).	191

# 1 | Introduction

Particle physics research over the last century or so has provided us with our current basic understanding of the fundamental particles that have made up the universe since its origin, and their interactions with each other. This is summarised by the Standard Model (SM) of particle physics, which has been developed incrementally in recent decades and has stood up well to scientific scrutiny. The Large Hadron Collider (LHC) at the Organisation Européenne pour la Recherche Nucléaire (CERN) near the Swiss city of Geneva (Figure 1.1) was constructed with the aim of investigating the SM. Areas of current interest such as electroweak symmetry breaking, the Higgs mechanism and physics beyond the SM (BSM) such as supersymmetry (explained in further detail in Section 4), require the acceleration of particles to high energies (of the order of several TeV). The start of data-taking from proton-proton collisions at the LHC in 2009 ushered in a new era in terms of energies at particle colliders, taking over as the highest energy particle collider from the TeVatron at Fermilab. In 2010 and 2011 the LHC collected data at a centre of mass energy of 7 TeV ( $5.1 \text{ fb}^{-1}$ ), followed by 8 TeV ( $21.8 \text{ fb}^{-1}$ ) in 2012 and currently in 2015 after the first long shutdown at 13 TeV.

The Compact Muon Solenoid (CMS) general-purpose detector is one of four detectors located around the LHC (the others being ATLAS, LHCb and ALICE), approximately 100 m below ground level. The geographical site and location of the various experiments are shown in Figure 1.1.

This thesis presents an analysis based on the full proton-proton collision data from the CMS experiment in 2011 and 2012. The analysis investigates the top-antitop ( $t\bar{t}$ ) differential cross section with respect to global level event variables, specifically in semileptonic  $t\bar{t}$  decays in the electron+jets and muon+jets channels. This investigation is motivated primarily

## Carte de situation

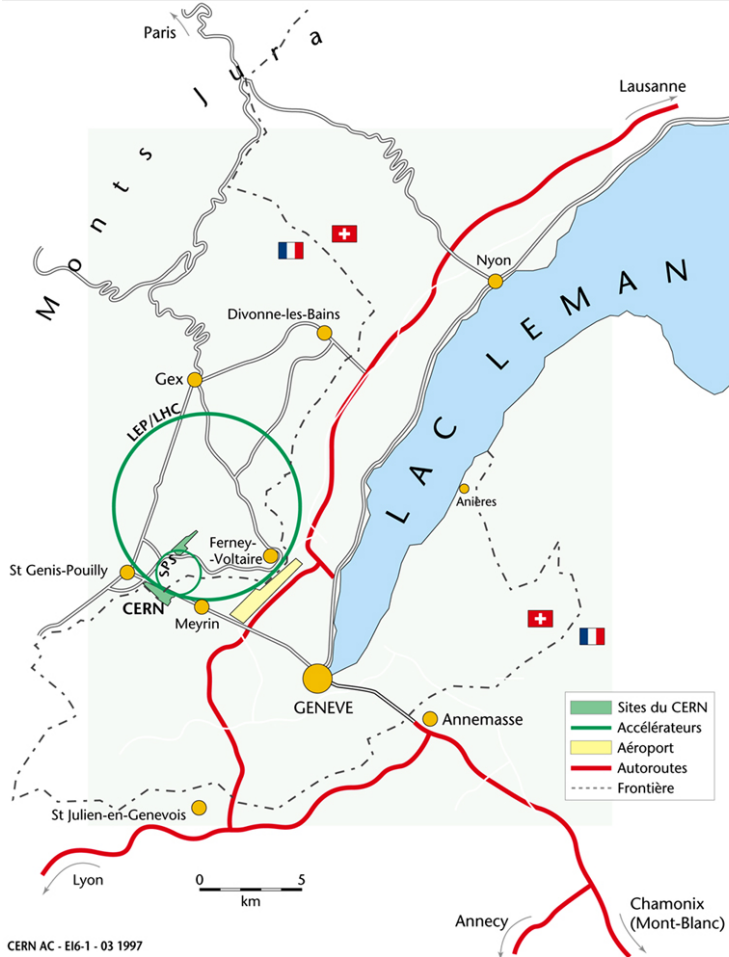


Figure 1.1: Map of LHC location.

by the importance of understanding  $t\bar{t}$  events since they are a significant background in many new physics analyses. It is also helpful in understanding QCD and event generators. Rare Standard Model processes such as  $t\bar{t} + W \rightarrow l\nu$  or  $t\bar{t} + Z \rightarrow \nu\bar{\nu}$  would appear in  $E_T^{\text{miss}}$  distribution tail, and  $t\bar{t} + X$  where  $X$  is massive would appear in the  $H_T$  and  $S_T$  distributions. There are also possible new physics scenarios such as stop pair production,  $\tilde{t}\tilde{t} \rightarrow t\tilde{\chi}_0\bar{t}\tilde{\chi}_0$  which could show hints of dark matter.

The work presented here was carried out in collaboration with Emyr Clement, Lukasz Kreczko, Sergey Senkin, Philip Symonds under the supervision of Professors Joel Goldstein and Greg Heath. The main contribution of the author to these studies lay in development of the C++ and Python software frameworks and scripts used in the analyses. Related to this, maintaining up-to-date particle object definitions, corrections, efficiencies and prescription

recommendations from working groups within CMS was a large component of the author’s work. In terms of the technical workflow employed, the author was heavily involved in producing n-tuples from the analysis-ready AOD data format, running the software to perform the prescribed analysis methods, and running final scripts on the output ROOT data to perform the final calculation and to produce results plots and tables. Particular areas of focus regarding physics included synchronisation of the event selection and comparison of distribution shapes between 7 TeV and 8 TeV data, implementing aspects of the analyses such as selection criteria, b-tagging and jet energy resolution. Also included in this thesis is a description of the author’s service work contribution to the CMS experiment, a requirement of all members of the CMS collaboration.

Chapter 2 describes the LHC and the CMS detector, including information about the object reconstruction process based on detector readout, to represent particles produced in collisions. Chapter 4 provides an overview of the Standard Model theory and some of its shortcomings, followed by a review of physics of the top quark at the LHC in Chapter 5. A small study investigating the b-tagging algorithms used in CMS is described in Chapter 6, and the main  $t\bar{t}$  differential cross section analysis is then covered in Chapters 7,8 and 9. To conclude, Chapter 10 contains a summary and outlook to the future. Additional data, tables and plots from the presented analyses are given in the Appendices A to B.11. Finally, the author’s service work is outlined in Appendix ??.

From the outset, natural units are used throughout this thesis, unless otherwise specified, so that

$$\hbar = c = 1, \quad (1.1)$$

meaning that mass, momentum and energy all have the same units of electronVolts (eV).



## 2 | The CMS Detector at the LHC

### 2.1 Introduction to the LHC

The CMS general-purpose detector is one of four detectors located around the LHC, approximately 100 m below ground level. The CERN accelerator complex and the locations of the various experiments around the LHC are shown in Figure 2.1.

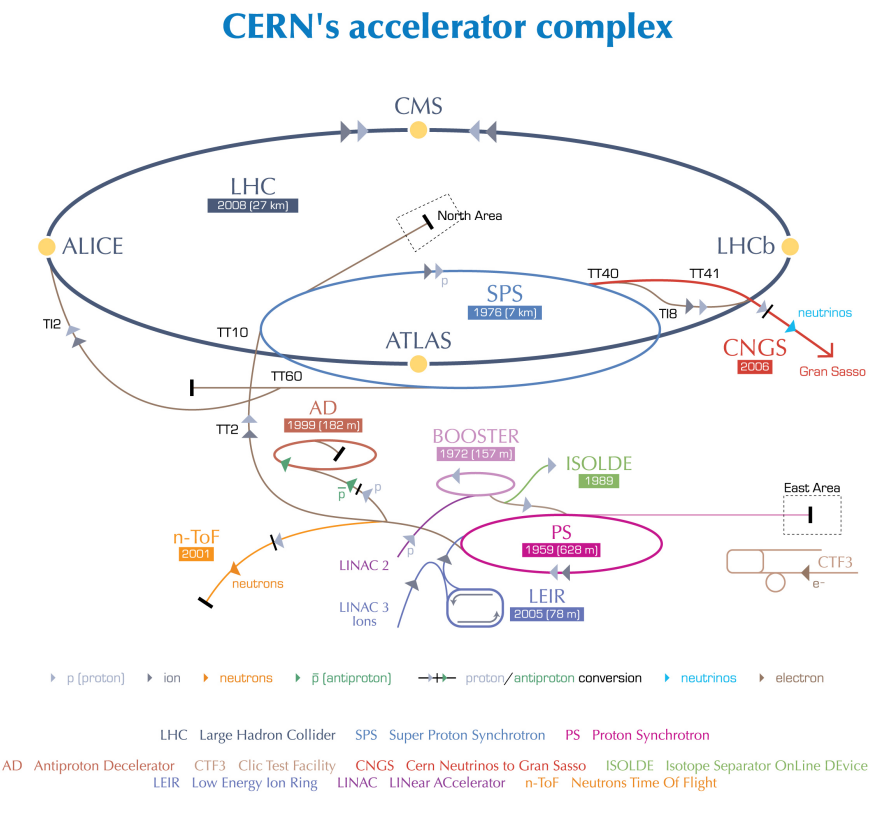


Figure 2.1: Schematic of CERN accelerator complex including the LHC and experiments. CMS is located at Point 5 on the LHC ring.

The 27 km circumference LHC can collide two proton beams, each composed of 2808 bunches, at a design energy of 7 TeV per beam (meaning a 14 TeV centre of mass energy,  $\sqrt{s}$ , in collisions) with a luminosity of  $10^{34} \text{ cm}^{-2}\text{s}^{-1}$  at a collision rate of 25 ns (40 MHz). Each

event that is recorded in the CMS detector is one crossing of the bunches of protons of which the beams are comprised. During the first part of Run 1 in 2011 the machine ran at a centre of mass energy of 7 TeV at a bunch spacing of 50 ns (leading to 8 proton-proton interactions per bunch crossing) and CMS recorded a peak instantaneous luminosity of  $3.7 \times 10^{33} \text{ cm}^{-2}\text{s}^{-1}$ . In 2012 the centre of mass energy was increased to 8 TeV (21 proton-proton interactions per bunch crossing) and CMS recorded a peak instantaneous luminosity of  $7.7 \times 10^{33} \text{ cm}^{-2}\text{s}^{-1}$ . Since Run 2 began in May 2015 after Long Shutdown 1, the LHC has been operating at a collision energy of 13 TeV and CMS recorded a peak instantaneous luminosity of  $4.7 \times 10^{33} \text{ cm}^{-2}\text{s}^{-1}$  at a collision rate of 25 ns initially, before switching to 50 ns. The design collision energy and luminosity are scheduled to be attained later in Run 2 and after Long Shutdown 2 (in 2019) respectively.  $6.1 \text{ fb}^{-1}$  and  $23.3 \text{ fb}^{-1}$  of data was delivered to CMS during the 2011 and 2012 data taking periods respectively; Figure 2.2 shows the increase in integrated luminosities delivered to CMS over time during 2010--2012.

The acceleration process begins with a tank of hydrogen (see Figure 2.1). After stripping electrons off the hydrogen atoms using an electric field, the remaining protons are inserted into the LINAC2 which accelerates them up to 50 MeV. From here, the proton beam is injected into the Proton Synchrotron Booster (PSB) which increases the energy to 1.4 GeV, followed by the Proton Synchrotron (PS) which accelerates the beam to 25 GeV and the Super Proton Synchrotron (SPS) where the beam energy reaches 450 GeV. Finally, the protons are injected into the LHC where two beampipes carry the beams in a clockwise and an anti-clockwise direction while accelerating them up to the required collision energy. Filling the LHC rings takes approximately 4 minutes, followed by approximately 20 minutes until the beams reach energies of 4 TeV (during 2012 data taking). The beams are accelerated by radio frequency cavities, and superconducting dipole magnets bend the beams to maintain their trajectory around the LHC beampipe. Once the collision energy has been attained, the beams are “squeezed” to focus them into a cross-sectional area of approximately 16  $\mu\text{m}$  using superconducting quadrupole magnets. Collimators act to scrape away protons, thereby maintaining beam losses to the superconducting magnets below the level that would cause

quenching. The counter-circulating beams are brought to collide at the four main LHC experiments CMS, ATLAS, LHCb and ALICE. ATLAS, like CMS, is a general purpose detector, ALICE is specifically designed to investigate heavy ion collisions (as opposed to protons), while LHCb investigates b-meson physics.

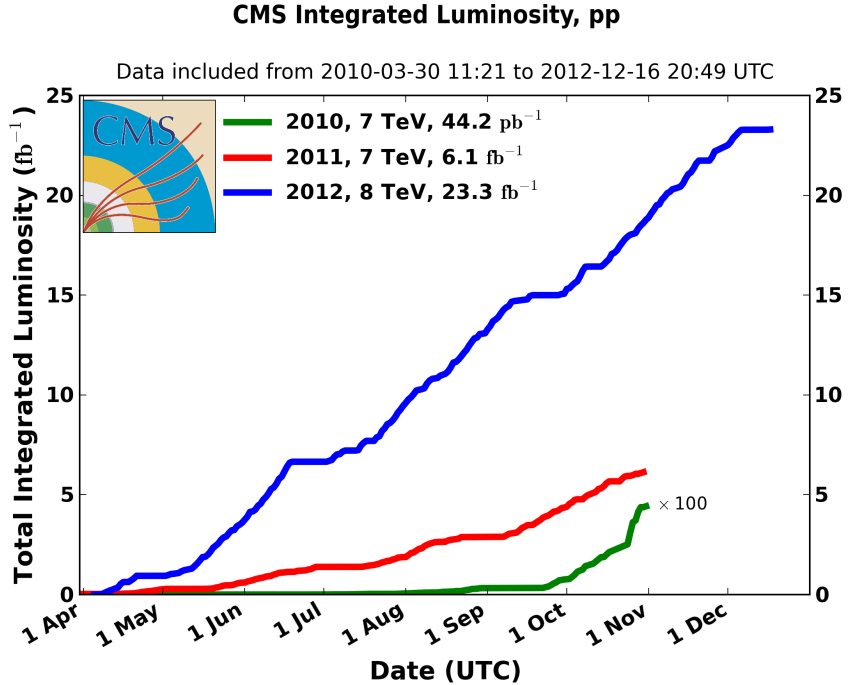


Figure 2.2: Cumulative luminosity delivered to CMS over time during 2010, 2011 and 2012 proton-proton data taking periods.

## 2.2 Overview of CMS

Compact Muon Solenoid is both the name of the detector at the LHC, and of the collaboration of people worldwide who work to build, operate, maintain and upgrade it, and to analyse the data it records.

CMS is a general-purpose detector, designed to be efficient at detecting new physics with a wide range of signals. The detector measures 14.6 m in diameter and 21.6 m in length, and weighs 12500 tonnes [28]. The different sub-detectors of CMS are arranged in concentric layers around the point of the beam pipe at which the two beams of proton bunches collide, known as the interaction point (see Figure 2.3). As the products of any collisions that

occur in the bunch crossing travel outwards from the interaction point, they pass through the sub-detectors depositing energy, resulting in signals being produced. A subset of the information from some sub-detectors (the calorimeters and muon chambers, described in Section 2.3) is then processed by a trigger while information from other sub-detectors is buffered on the detector.

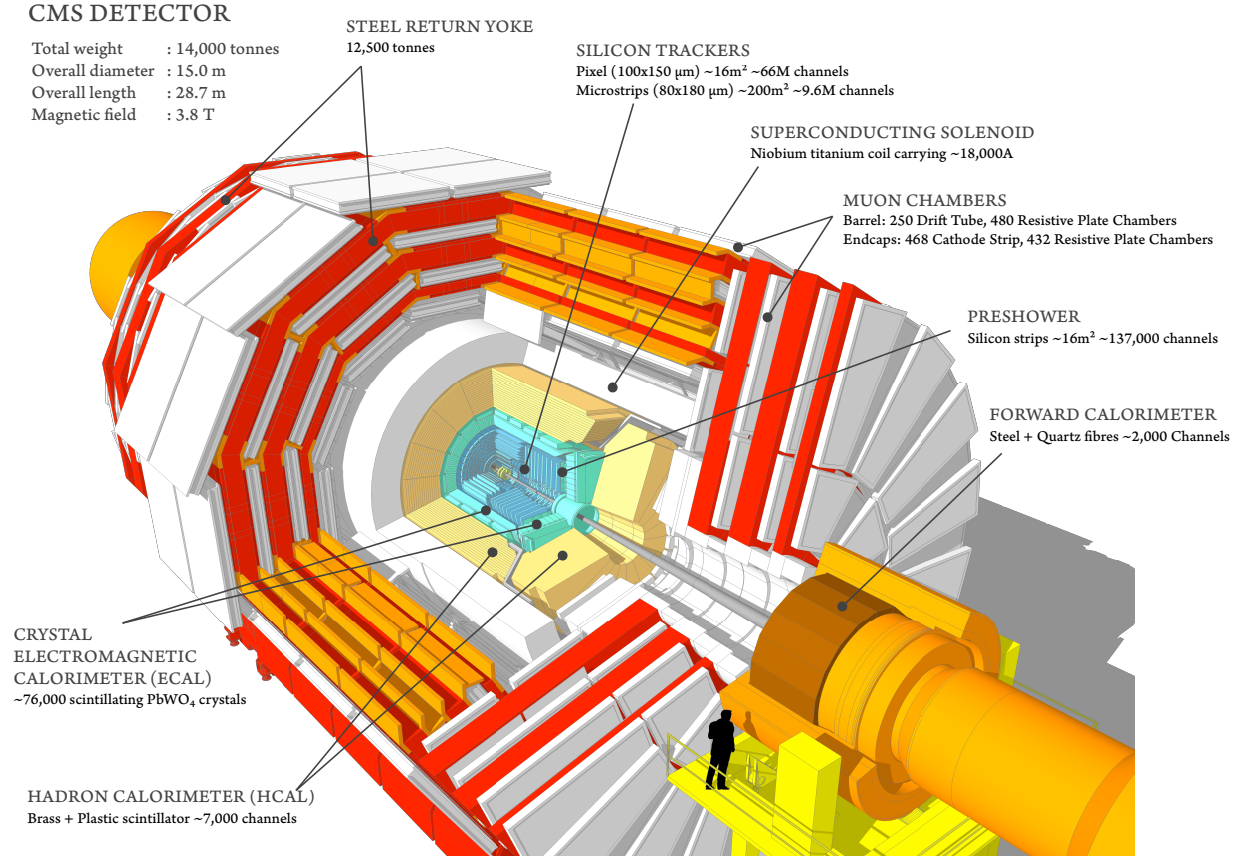


Figure 2.3: Diagrammatic sectional view of the CMS detector [86].

The design of CMS is based firstly around a superconducting solenoid magnet. Around and inside the magnet are the sub-detectors: the pixel and strip tracker, the electromagnetic calorimeter, the hadronic calorimeter, the return yoke for the magnet and the muon detectors. The coordinate system of the detector is designated with the origin as the intersection point of the two beams in the beam pipe, the x-axis positive towards the centre of the LHC ring, the y-axis positive vertically upwards and the z-axis pointing along the beampipe in an anticlockwise direction. The azimuthal angle,  $\phi$ , is defined as the angle in the x-y plane, transverse to the beampipe starting from the x-axis. The polar angle,  $\theta$ , is defined as the

angle in the z-y plane starting from the z-axis (the beampipe). The angle  $\theta$  is related to the pseudorapidity,  $\eta$ , by the formula  $\eta = -\ln(\tan(\theta/2))$ , so that  $\eta$  ranges from 0 at  $\theta = 90^\circ$  to  $\infty$  at  $\theta = 0^\circ$  [90]. The two ends of the detector, at high  $|\eta|$  values, are called the endcap regions while the central area at lower  $|\eta|$  values is called the barrel region. The detector volume is often denoted in terms of  $\Delta R$ , with the separation between two particles 1 and 2 being defined as

$$\Delta R = \sqrt{(\eta_1 - \eta_2)^2 + (\phi_1 - \phi_2)^2} \quad (2.1)$$

## 2.3 Sub-Detectors

### 2.3.1 Tracker

Any charged particles produced as a result of the proton-proton collisions in these bunch crossings need to be recorded for later use in reconstruction of particle information such as trajectories and charges. This is achieved using the tracker section of CMS which consists of silicon sensors in two forms: pixels and strips. As the charged particles travel through these silicon sensors, electron-hole pairs are produced that induce a current in the sensors and are processed by readout chips. This readout is carried out by the Analogue Pipeline Voltage (APV) chip. A new chip called the CMS Binary Chip (CBC) is intended to replace the APV in the HL-LHC after Long Shutdown 3, currently scheduled for 2023-2024. The CBC is described in more detail in Appendix ??.

The purpose of the tracker within the CMS detector is to track the trajectory of charged particles as they travel out from the interaction point. An important requirement of the tracker is that it must allow the above whilst not affecting the energy of the particle being tracked. The silicon in the tracker sensors also does not stop particles, thereby allowing them to pass through this innermost layer of the detector and interact with outer layers. The

tracker readout chips must also be able to distinguish from which bunch crossing a particle was produced (bunch-crossing identification) in order for the trigger to remove particles from previous bunch crossings (termed out-of-time pileup) and fully reconstruct events.

The tracker is split into two parts, with an inner silicon pixel detector and an outer silicon strip detector. A diagrammatic view of the tracker, including both pixels and strips, is shown in Figure 2.4. The inner pixel detector consists of three layers in the barrel region at distances of 4.4 cm, 7.3 cm and 10.2 cm from the beam line with two endcap discs at each end. Each pixel measures 100  $\mu\text{m}$  by 150  $\mu\text{m}$ . The entire pixel detector covers an area of only approximately 1  $\text{m}^2$  but contains 66 million pixels in total.

The strip tracker is comprised of ten layers in the barrel region at distances ranging from 20 cm to 1.1 m from the beam pipe. The four inner layers (at distances of 26 cm, 34 cm, 42 cm and 50 cm from the beampipe) are collectively named the Tracker Inner Barrel (TIB), while the outer six layers (at distances of 61 cm, 70 cm, 78 cm, 87 cm, 97 cm and 108 cm from the beampipe) are known as the Tracker Outer Barrel (TOB). The endcaps consist of twelve discs, three of which correspond to the Tracker Inner Discs (TID) at z-distances from 75 cm to 100 cm, and nine to the Tracker End Caps (TEC) at z-distances between 120 cm and 280 cm [83]. The largest silicon detector ever constructed, the strip tracker contains about ten million channels and covers an area of approximately 200  $\text{m}^2$  [28, 90]. The operating temperature of the tracker during 2011 and 2012 has been 0  $^\circ\text{C}$  for the pixels and +4  $^\circ\text{C}$  for the strips but will be lowered for both after Long Shutdown 1 [26].

As a charged particle passes through the various layers of silicon in these detectors, electrical signals are created which are then read by readout electronics. Offline algorithms then use the data relating to which strips and sensors received ‘hits’ to reconstruct the tracks of charged particles and this information is later used for particle reconstruction and identification [28, 77].

The curving of particle tracks within a magnetic field allows the calculation of the particle momentum and charge,  $mv = RqB$ , where  $mv$  is the momentum of the particle,  $R$  is the

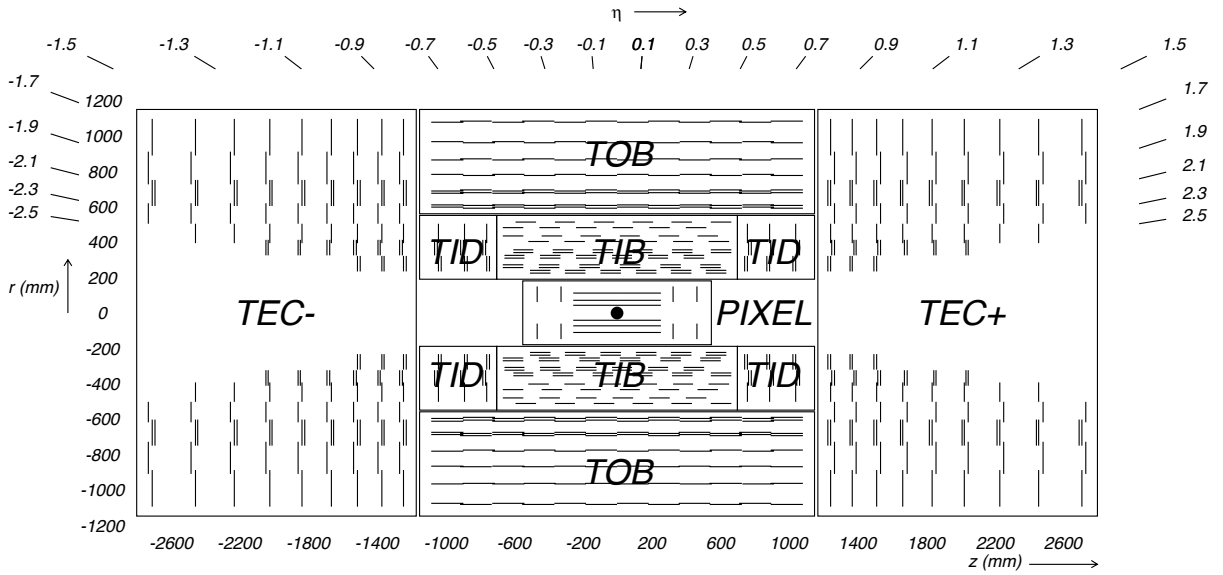


Figure 2.4: Cross-sectional diagram of the CMS strip tracker; each line represents a detector module [90]

radius of curvature,  $q$  is the electric charge, and  $B$  is the magnetic field strength.

The required tracker characteristics of high granularity and resolution, fast response to process the high data rate without losing potentially valuable information, radiation hardness and keeping detector material to a minimum to minimise interactions of the particles with detector matter, resulted in silicon being chosen to construct the tracker.

One of the advantages of using silicon over gaseous detectors is that silicon produces more charge carriers per unit of length travelled by a particle. This therefore means the silicon thickness can be reduced, typically around  $300\text{ }\mu\text{m}$  per layer. The silicon sensors that make up the strip tracker in the CMS detector vary in thickness depending on their location. Sensors of  $320\text{ }\mu\text{m}$  thickness are utilised in the TIB and TID,  $500\text{ }\mu\text{m}$  in the TOB, and a mixture of both thicknesses is used in the TEC. Thicker sensors are used in the outer sections of the strip tracker in order to maintain a high signal to noise ratio, since the increased strip lengths in this region lead to increased electronics noise due to higher capacitance [28].

Silicon also allows fast signal transfer, of the order of about 10 ns, as the charge carriers travel quickly through silicon. Furthermore, the spacing between strips in a silicon sensor,

known as the strip pitch, can be manufactured to be extremely small, down to around 50  $\mu\text{m}$ . The strip pitches and their lengths vary such that there are fifteen distinct types of sensor geometries in the strip tracker [29].

A further tracker requirement is low occupancy (the fraction of channels with a hit in an event was desired to be 1 % or lower at the nominal LHC luminosity) so that pattern recognition can be carried out efficiently and so the amount of simultaneous data to be read out is manageable. In order to maintain such a low occupancy, the strip tracker has a high granularity, with strip lengths less than 20 cm and strip pitches less than 205  $\mu\text{m}$  [83]. While high granularity is beneficial for high precision tracking, it also results in a high number of channels, which in turn requires a large amount of electronics for readout and leads to a high heat load.

On a global scale, the tracker data is read out using a combination of interoperating systems. The data from the Analogue Pipeline Voltage (APV25) tracker readout chips is taken via optical fibres to 440 off-detector Front End Drivers (FEDs) (Tracker FEDs make up 63 % of the total number of FEDs in CMS). The FEDs then forward the data to the online Data Acquisition System (DAQ). In addition, off-detector Front End Controllers (FECs) control the front-end electronics by means of approximately 350 control rings, including triggers, clock and monitoring [28, 48].

### 2.3.2 Electromagnetic Calorimeter

The electromagnetic calorimeter (ECAL), is a hermetic, homogeneous sub-detector constructed of scintillating crystals of lead tungstate ( $\text{PbWO}_4$ ), and is the next layer outside the tracker. Any electromagnetic particles such as electrons or photons are absorbed by the ECAL crystals which then scintillate emitting a blue-green coloured light. These signals are then collected and converted to electrical signals by connected photodetectors, and processed by readout electronics.

The signals in the crystals are collected by avalanche photodiodes in the barrel region and

vacuum phototriodes in the endcaps. The numbers of photoelectrons produced is dependent on temperature, with increasing temperature resulting in a decrease in the number of electrons at a rate of  $-3.8 \pm 0.4\%/\text{ }^{\circ}\text{C}$ . A cooling system is thus employed which maintains a stable operating temperature of the ECAL system to within  $\pm 0.05\text{ }^{\circ}\text{C}$ , with a nominal operating temperature of  $18\text{ }^{\circ}\text{C}$  [28]. The energy resolution of the ECAL has been shown to follow  $\sigma_E/E = 2.8\%/\sqrt{E} \oplus 12\%/E \oplus 0.3\%$  where the three constant terms come from stochastic fluctuations such as photostatistics, electronics noise and temperature stability and calibration uncertainties [35].

The barrel region of the ECAL consists of 61,200 crystals and extends up to a pseudorapidity  $\eta \pm 1.479$ . Each individual barrel crystal is  $25.8X_0$  thick, where  $X_0$  is the radiation length (the mean distance over which a high energy electron loses all but  $1/e$  of its energy through bremsstrahlung radiation [81]), and has cross-sectional dimensions of  $22 \times 22 \text{ mm}^2$ , which equates to  $0.0174 \times 0.0174$  in  $\eta - \phi$  plane. These crystals are divided into 36 supermodules, with each supermodule consisting of 4 modules. The endcaps are comprised of 7,324 crystals, cover the range  $1.479 \leq \eta \leq 3.0$  and are split into two halves known as “Dees”, each divided into operating segments of  $40\text{ }^{\circ}\text{C}$  each. The endcap crystals have slightly larger dimensions, having a thickness of  $24.7X_0$  and cross-sectional dimensions of  $28.62 \times 28.62 \text{ mm}^2$  [28, 21]. Figure 2.5 shows the layout of the ECAL.

The high density crystals used ( $8.28 \text{ g/cm}^3$ ), short radiation length of  $X_0 = 0.89 \text{ cm}$ , and small Molière radius (a measure of the transverse dimensions of electromagnetic showers in a material [81]) of  $2.2 \text{ cm}$  lead to a compact calorimeter with fast response time (80% of the light is emitted within 25ns), high granularity and of course capable of withstanding the radiation levels within CMS.

An ECAL preshower, comprised of two lead plates each followed by a layer of orthogonal silicon strip sensors (thickness 350 mm, strip pitch 2 mm) is located between the tracker and ECAL endcaps to provide a higher spatial resolution than the ECAL. This helps to identify, for instance, closely spaced photon pairs originating from pion decays which may

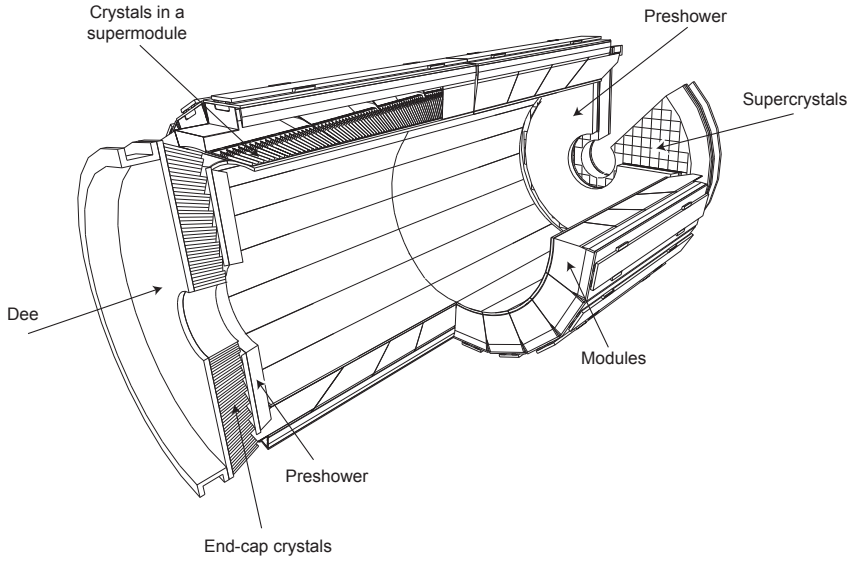


Figure 2.5: Diagram of the ECAL showing barrel supermodules, endcaps and preshower detectors [35].

otherwise be identified as a single high-energy photon based on ECAL energy deposits. As photons pass through the lead, a shower of electromagnetic particles ( $e^+e^-$  pairs) is produced that are detected by the silicon layers to give a measure of the energy of the photon, while the orthogonal strips allow a position measurement. The measured energy can then be combined with the energy measured by the ECAL.

### 2.3.3 Hadronic Calorimeter

The next sub-detector outside the ECAL is the hadronic calorimeter (HCAL) which works in a similar way to the ECAL, in this case by absorbing hadron jets. The HCAL is located at a distance of 1.77 m to 2.95 m from the beamline, with an additional outer hadronic calorimeter also installed outside the magnet due to radial restrictions imposed by the magnet coil. The HCAL barrel (HB), outer (HO) and endcaps (HE) cover the  $\eta$  range up to 3.0, with the forward HCAL (HF) placed at  $|\eta|$  up to 5.2 increasing the coverage. Figure 2.6 shows a quarter of the HCAL endcap.

The HCAL is a sampling calorimeter, meaning it is composed of alternating absorber layers (made of brass) and scintillator layers (made of plastic). A hadronic particle produces a

shower of secondary particles when it strikes an absorber layer. This process is repeated as these secondary particles themselves pass through successive absorber layers. The scintillator layers in between absorb the energy of these particles, emitting light as they do which is fed to readout electronics via optical fibres to measure the particle energies.

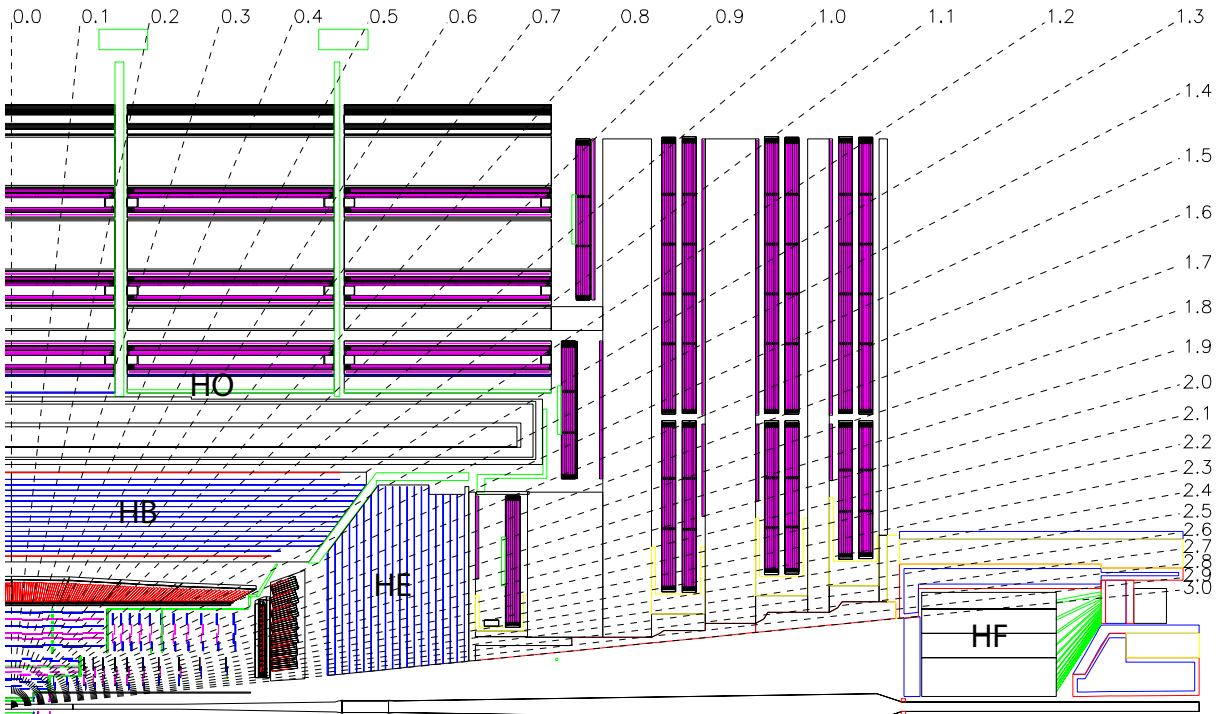


Figure 2.6: A longitudinal schematic of the CMS HCAL showing the location of the hadron barrel (HB), endcap (HE), outer (HO) and forward (HF) calorimeters [28].

### 2.3.4 Superconducting Magnet

The magnet of the CMS detector is the largest and highest field strength superconducting solenoid constructed for a physics experiment in terms of bending power for physics and total stored energy [28]. It can produce a magnetic field up to 4 T (a field strength of 3.8 T is used in normal operation) with a stored energy of 2.7 GJ [90]. The cold bore, cooled to 4.5 K using liquid helium, has dimensions of 12.5 m length and 6 m diameter, and weighs 220 tonnes [49]. Due to design constraints and structural requirements, the magnet itself provides some of the structural strength both to support itself and to withstand its own magnetic bursting force on the coil [28].



Figure 2.7: Bore of the CMS solenoid magnet in vertical position in the CMS assembly hall, SX5, prior to installation [28]

The cold bore, pictured in Figure 2.7 in the CMS assembly hall, is enclosed in a steel return yoke weighing 10,000 tonnes with the aim of containing and returning the magnetic field. The yoke is interspersed with the muon chambers and is made up of 5 barrel segments and 6 endcap discs. The magnet was designed in a manner such as to facilitate assembly at ground level prior to lowering into the CMS experimental cavern, UX5. Despite the challenges involved in constructing such a powerful magnet, the high bending-power created by the high magnetic field was desirable in order to provide good momentum resolution of the tracking components.

### 2.3.5 Muon Chambers

Muons pass through all the previous inner sub-detectors, losing very little energy as they traverse them (around 1 MeV/mm on average), leading to the muon chambers being located outermost in the detector. There are, in fact, three types of muon detectors in use in CMS. The endcaps contain Cathode Strip Chambers (CSCs), the central barrel regions contain

Drift Tubes (DTs), and both regions are equipped with Resistive Plate Chambers (RPCs). These systems, in combination with the silicon tracker, are used to determine the momentum of muons by taking advantage of their curved tracks due to the magnetic field. The different technologies are used due to the different numbers of particles expected in different areas of the detector and because of technological considerations regarding the physical areas to be covered [90]. Figure 2.8 shows a diagrammatic representation of one quarter of the CMS muon detectors. The CSCs are used in the endcaps to cover  $|\eta|$  values between 1.2 and 2.4 that experience high muon rates and where the magnetic field of the solenoid is high [90]. They take the form of four disc layers each made of 2 (inner layer) or 3 (outer 3 layers) concentric rings. They consist of volumes of gas in which positive wires placed at right angles to negative copper strips. To relate these to the name given to these detectors, the positive wires are the anodes and the negative strips are the cathodes. As a charged particle passes through the gas it ionises gas atoms and the electrons that are knocked out travel towards the anode wires. At the same time the resulting positively charged ions in the gas travel towards the cathode strips. Since the wires and strips are at right angles to each other, the CSCs provide two position co-ordinates for the passing muon. The CSC detection mechanism is a fast process so their signals are used for muon triggering [28].

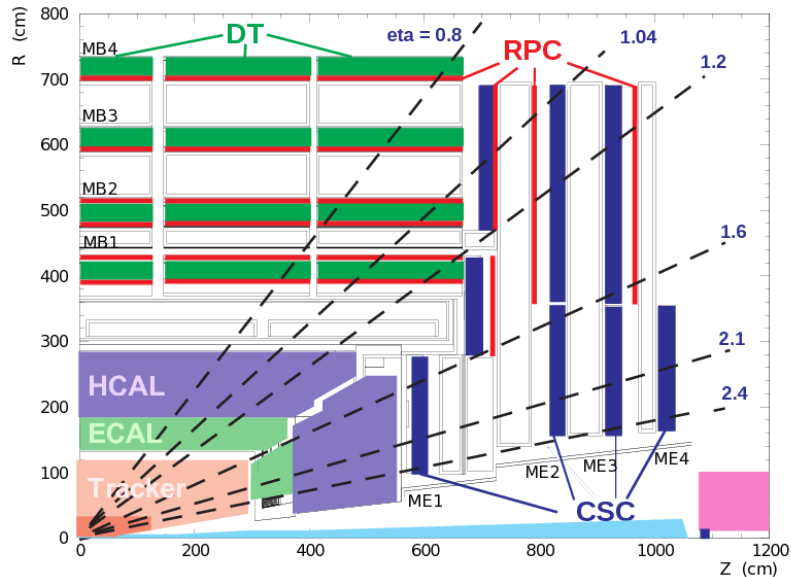


Figure 2.8: Schematic representation of a quarter of the CMS muon system [72]

The barrel region DTs cover  $|\eta|$  values of less than 1.2, that encounter low rates of low

transverse momentum muons [90]. The drift tube chambers are arranged in four cylindrical layers, or stations, among the layers of the magnet’s iron return yoke and RPC layers. The stations are slightly staggered to ensure that even a muon of high transverse momentum will be detected by at least three of the four layers. The drift tubes contain a mixture of argon (85%) and carbon dioxide (15%), and a positively charged stretched wire. As a particle with a charge traverses the volume of gas, atoms in the gas are ionised and the resulting free electrons travel along electric field lines towards the positive wire. By using the position of the electron along the wire and the time taken for the wire to detect the electron, two coordinates of the muon position can be deduced. In comparison to the DTs and CSCs, the RPCs that complement them provide a better resolution in terms of time (1 ns) but a worse resolution in terms of position, and so provide additional trigger information. As their name suggests, they are constructed of plates, one negatively charged (cathode) and one positively charged (anode) and made of a plastic with high resistance. In a similar process to the other muon detectors, a gas that makes up the volume in between the plates is ionised by a passing charged muon. The resulting electrons create an avalanche of electrons by, in turn, ionising other gas atoms; this avalanche of electrons moves towards the anode and metal readout strips outside the plastic anode detect the signal for readout. The hit strips pattern allows a calculation of the muon momentum which is then fed to trigger algorithms.

### 2.3.6 Trigger and Data Acquisition

At the design bunch crossing frequency of 40 MHz and at the design luminosity of  $10^{34} \text{ cm}^{-2}\text{s}^{-1}$ , the expected number of proton-proton collisions per second is approximately  $10^9$ , translating to 21 proton-proton collisions per bunch crossing on average. Each bunch crossing produces approximately 1 MB of data, leading to 40,000 GB/s of data. This extremely large amount of data, which is impractical to record, means that a trigger system is required to filter the events in order to record only data that are of interest for physics analyses.

There are two levels to the CMS trigger, named Level 1 Trigger (L1) and High Level Trigger (HLT). These work with the electronics and readout systems in place in the detector to filter

the events to a practically manageable amount for processing. In combination, these triggers reduce the data rate by at least a factor of  $10^6$  [28].

The L1 Trigger is a pipelined deadtimeless system comprised of calorimeter triggers, muon triggers and a global trigger that works on a combination of data from the former two. The decisions made by the L1 Trigger are carried out by custom-designed hardware processors, consisting mostly of programmable electronics such as Field Programmable Gate Arrays (FPGAs) [59]. The data from a bunch crossing are held in pipeline buffers in the electronics on the detector (at the front) end whilst the information for the triggers is processed in the CMS service cavern (USC) and the decisions transmitted back to the front end. The maximum time allowed for this process for each event is  $3.2\mu\text{s}$ , which is the time taken for the signals to be transmitted via optical fibres from the detector to the processors, processing time, and transmitted back again. This time is known as the latency [90]. The L1 Trigger outputs events to the HLT at a rate of 100 kHz [28].

As mentioned, the trigger uses calorimeter and muon chamber data to reach a decision on an event within the required timeframe. Tracker data are not currently used since track reconstruction exceeds the amount of time allowed for the L1 trigger decision. Good trigger performance is related to the quality of the calorimeters and muon systems. Factors such as good momentum resolution of high momentum muons, good charge determination of muons, good ECAL energy resolution and good missing transverse energy resolution are required for the trigger to select interesting events. The trigger was designed as described in order to allow the CMS experiment to meet the goals of the LHC physics programme [28].

Unlike the Level 1 Trigger, the High Level Trigger (HLT) is software-based and runs offline in HLT processor farms of about a thousand commercial processors [90]. If the Level 1 produces an accept decision, the data which was stored in buffers in the front end electronics is read into readout buffers from where the DAQ system accesses it. The L1 output rate of 100 kHz corresponds to a data rate of approximately 100 GB/s. The HLT software processes these events in a computer farm that carries out fast processing of offline algorithms such

as selections and object reconstructions to reduce the rate down to approximately 100 Hz. This accepted data are then stored on tape. The HLT algorithms are designed based on the principle of minimising the number of objects that need to be reconstructed in order to come to a decision, and events are discarded as early as possible, leading to the HLT consisting of many virtual levels that progressively use more information from, first, the muon chambers and calorimeters, followed by pixel tracker data, and finally full tracker information [90].

Figure 2.9 shows the variation in trigger rates at a luminosities of  $2 \times 10^{33} \text{ cm}^{-2}\text{s}^{-1}$  and  $10^{34} \text{ cm}^{-2}\text{s}^{-1}$  with increasing muon transverse momentum. The rates for different trigger levels are shown. The L1 trigger rate begins to flatten out as the  $p_T$  threshold increases because the lack of tracker information at L1 means that low momentum muons mis-measured as having high momentum are not removed. Thus, increasing the threshold would have no discernible effect on reducing the trigger rates while reducing physics performance by rejecting desirable events. In comparison, the L3 trigger rate, which includes tracker information, continues to decrease at high muon momenta, and is able to maintain the rate at the desired level.

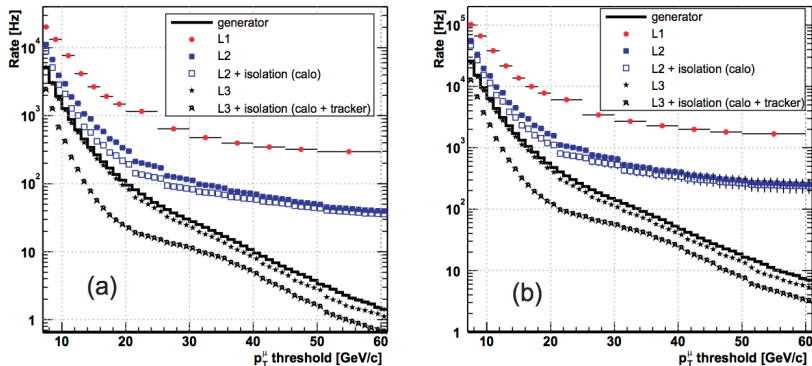


Figure 2.9: Single muon high level trigger rates at (a)  $\mathcal{L} = 2 \times 10^{33} \text{ cm}^{-2}\text{s}^{-1}$  and (b)  $\mathcal{L} = 10^{34} \text{ cm}^{-2}\text{s}^{-1}$  [40].

A more detailed description of the data acquisition (DAQ) system can be found in [28] and [90].

## 2.4 Upgrades

The CMS experiment, along with the LHC and the other detectors are in a long term programme of upgrades and maintenance. By 2023 the luminosity provided by the LHC is expected to be  $2 \times 10^{34} \text{ cm}^{-2}\text{s}^{-1}$  [42]. The various runs and shutdowns until 2023 are collectively referred to as Phase 1. In phase 2, or after 2023, long shutdown 3 is also planned to bring further improvements and upgrades to the performance of the LHC, after which the luminosity of the LHC is expected to reach  $5 \times 10^{34} \text{ cm}^{-2}\text{s}^{-1}$ . The machine in this state will be known as the high luminosity LHC, HL-LHC (also sometimes referred to as Super LHC, SLHC).

Naturally, the above dates and schedules are the latest best estimates and are liable to change over time, particularly those further in the future, as work progresses.



# 3 | CMS Computing and Offline

## 3.1 CMS Computing

The CMS offline computing takes on the workload of transferring accepted data from the triggers to both permanent and temporary storage, and the processing of this data for subsequent analysis, in addition to the production of simulated CMS data. The resources needed to process the high volumes of data involved require a distributed computing system: the Worldwide LHC Computing Grid (WLCG) infrastructure, an international collaboration of LHC experiments and computing centres, is employed to carried out these tasks.

The CMS computing resources are primarily divided into three tiers. Tier 0 (T0) consists of only one site, at CERN itself. The T0 centre has as its main aims to take accepted data from the detector and transfer it to permanent storage on tape. Tier 0 computing is also responsible for reconstructing the initial RAW data into smaller formats, by passing events through modules to produce physics objects (like electrons and jets) using algorithms to reconstruct tracks in the silicon tracker, clusters of deposits in the calorimeters, primary and secondary vertices, determine particle identification and to correct for detector characteristics such as non-functioning components (see Section 3.2 onwards for more details on data formats). From the T0 centre, copies of the data in RECO and RAW format are transferred to T1 centres around the world. Owing to its important role in ensuring the reliable transfer of RAW and RECO data, the T0 resources are not available for analysis by CMS users. There are seven Tier 1 centres located in various countries within the CMS collaboration. In the UK, the T1 centre is located at the Rutherford Appleton Laboratory in Harwell, near Oxford. T1 centres provide reliable computing resources for data storage and processing. RAW data is spread between them, providing a second copy of the RAW data stored at CERN. The

second reconstruction step, termed REREKO, is also carried out at T1 centres, in addition to the production of simulated data. These can then be provided to any of the Tier 2 centres at CMS institutes (typically universities) where they may be temporarily stored. T2 centres are also generally used to run users' final analyses and produce simulations [28, 90].

## 3.2 Event Data Model

Reconstructed data from CMS uses a data model based around an event, called the Event Data Model (EDM), where one event is one crossing of proton bunches at the centre of CMS which passes the triggers. This model is created and manipulated within a CMS software framework [41] written in C++, with the event and related objects in the object oriented data analysis framework ROOT [25].

The iterations of data from the initial recorded information to subsequent, more compact formats, are produced by passing events through a sequence of modules. The arrangement of these data takes the form of layers, with the first of these being RAW. This level contains the full information from the event in CMS and occupies approximately 1.5-2 MB/event. More information than is necessary for user analyses is included at this level, and so the majority of CMS users will not use this data format. Reconstructed level data (RECO) is slightly smaller in size (approximately 0.5 MB/event) and is essentially a compressed subset of the RAW data after modules performing reconstruction have been run.

The third level, Analysis Object Data (AOD), is the smallest of the data formats, requiring approximately 100 kB/event, which is small enough to allow the entire AOD data to be stored at computing centres worldwide. AOD format is a subset of the RECO data, and is produced by further reducing RECO leaving only high level physics objects (e.g. electrons, jets) which is adequate for most physics analyses.

In the differential cross section analysis presented in this thesis, this AOD data is processed using the Bristol Top Group's NTupleProduction code [76] to produce private ntuples which

are yet again smaller in size, at approximately 3 kB/event. These ntuples are then converted to simple ROOT histogram files after applying the required selections and corrections in the BristolAnalysisTools [74]. Scripts written in Python in DailyPythonScripts [75] are then used to produce final plots and tables.

### 3.3 Object Reconstruction and Identification

The process of producing a physics object such as an electron, photon or jet, from the data recorded by CMS is known as reconstruction and is carried out by “modules” known as EDProducers within CMSSW. The three step process of reconstructing high level objects consists of local reconstruction within a sub detector, global reconstruction using data from the whole CMS detector, and a final stage combining reconstructed objects from both of these. The reconstruction technique used in the majority of CMS analyses is called Particle Flow (PF) [3]. PF uses information from all of the sub-detectors of CMS to identify and reconstruct particles produced from a proton-proton collision.

#### 3.3.1 Track Reconstruction

Algorithms performing local track reconstruction execute a scan to identify tracker modules that receive a higher than threshold signal. Clusters are then constructed by adding adjacent strips or pixels to the originally identified seed strip or pixel. In order to reconstruct complete tracks to obtain the position and momentum of the charged particle, algorithms based on specific requirements such as high or low transverse momentum tracks are used. These algorithms in CMS are collectively known as the Combinatorial Track Finder (CTF).

Multiple passes of the CTF reconstruction software are carried out to reconstruct tracks, in a process called iterative tracking. The earliest iterations identify tracks that are easy to find such as high  $p_T$  tracks originating near the interaction point. As these tracks are reconstructed, the corresponding hits are removed from consideration in subsequent iterations, making it simpler for later iterations to identify tracks that are more difficult to find such as

those of displaced particles or with low  $p_T$ .

Six iterations are carried out in total, and each iteration can be split into four steps. Seeds are created using 2 or 3 hits to produce initial track candidates. The seed gives an estimate of the trajectories of the potential track candidates. A Kalman Filter [56, 89] based track finding algorithm then looks for further hits along an extrapolated path of the seed trajectory. A track fitter is then run using information from the previous steps to produce final values for trajectory parameters. The fourth and final step then rejects tracks which fail specified quality checks [38].

### 3.3.2 Pileup Subtraction

When reconstructing an event in CMS, all vertices (points from which multiple tracks originate) in the event must be reconstructed. By ordering the vertices in by the sum of the transverse momenta of their tracks, it is possible to identify the vertex of interest for physics analyses, known as the primary vertex (PV), as the vertex with the largest transverse momentum. The particle flow algorithm reconstructs objects, starting with those coming from the primary vertex, followed by other vertices (known as pileup). The reconstructed objects from the PV can be affected by the number of other vertices present in the event. For example, the jet momentum and lepton isolation could both increase with high pileup. This can, in turn, lead to signal events not passing selection requirements because a truly isolated lepton from the PV may appear not to be isolated. In addition, a larger number of events from background processes may pass selection requirements due to low energy jets appearing to have a higher energy. Hence, pileup subtraction, the removal of charged particles coming from vertices other than the PV is implemented to reduce these effects.

Neutral particles, however, pose a more difficult problem since they leave no tracker information for the reconstruction algorithms to easily identify their origin. One method of removing such particles from an event known as the  $\Delta\beta$  correction, uses the fact that the estimated average energy in an event from neutral particles is half that from charged particles. Thus, it

can be estimated that 0.5 times the charged particle energy comes from neutral particles. The second method, known as  $\rho$  correction, subtracts an average transverse momentum coming from pileup per unit area. While the two methods produce similar results, the  $\rho$  correction is used to correct the electron isolation and the  $\Delta\beta$  correction is used to correct the muon isolation in the differential cross sections analysis presented in this thesis, as recommended by the CMS TOP physics analysis group.

### 3.3.3 Electron Reconstruction

ECAL local reconstruction algorithms calculate the time of arrival, position and the energy of deposits. After grouping together deposits in neighbouring crystals to form clusters, deposits are then matched to deposits in the HCAL, forming a Calo Tower. Electrons are, typically, completely stopped in the ECAL and deposit their energy in a narrow cluster of crystals.

However, electrons can interact with the material between the interaction point and the ECAL, emitting a photon via bremsstrahlung radiation. Similarly, photons can convert to  $e^+e^-$ . Both of these processes result in ECAL deposits with a larger spread in  $\phi$  because of the strong magnetic field in the inner section of CMS with the tracker. In the case of photons, several clusters are grouped together to form superclusters, which are then corrected for their energies to obtain the energies of the original photon [71].

Electron reconstruction in the ECAL is carried out by two methods. The first matches superclusters with a trajectory compatible with two or three pixel detector hits and the interaction point. The second matches the supercluster to tracker tracks to identify electrons (and in the case of electrons emitting bremsstrahlung radiation, tracks with a low number of hits) [4]. Combining the seeds from the two methods, a Gaussian-Sum Filter, a generalisation of the Kalman Filter algorithm, is used to reconstruct electron paths [13].

Since other objects can leave similar signatures in the detector to electrons, such as jets or electrons from photon conversions, candidates are required to satisfy additional requirements of identification and isolation. Several electron identification methods exists and are used

in CMS analyses. The main top cross sections analysis in this thesis uses the multivariate identification (MVA ID). As the name suggests, this approach uses a multivariate analysis, with track, track quality, and supercluster variables as input, to produce a discriminator value, with higher values indicating a higher likelihood for a candidate to be a real electron. The MVA ID algorithm is optimised for identifying electrons from W and Z boson decays, and separately for triggering and non-triggering electrons [4].

The isolation of an electron is defined as the activity within a cone surrounding the electron. Isolation is used as an additional criterion to select electrons, in particular to distinguish electrons promptly produced in a proton-proton collision. Such isolated electrons would have less activity in its vicinity than electrons from within a jet, which could originate from leptonically decaying b hadrons, and jets faking electrons. Two methods exist in CMS of calculating the isolation of a particle: detector based isolation and particle based isolation. The detector based method is defined in each sub detector as the sum of the momenta or energies in a cone of  $\Delta R = 0.3$  around the electron. The particle based method uses the total transverse energy of PF reconstructed particles within a cone of  $\Delta R = 0.3$  and can remove activity coming from collisions other than the hard proton-proton interaction of interest. By normalising this isolation to the momentum or energy of the electron, a relative isolation is obtained, relating the cone activity to the electron. Termed PFRelIso, it is this relative isolation that is used in the top cross sections analysis to select electrons.

In order to avoid the selection of electrons originating from a photon conversion, a veto can be placed on a second electron in the event. However, since the two electrons in a photon conversion may not necessarily have equal transverse momentum, i.e. one may have a very low  $p_T$ , such a veto may be insufficient, and so further techniques to identify conversion events are used. Firstly, since an electron from a conversion would be produced at some distance from the interaction point and in the detector material, eliminating candidates with missing hits in the pixel tracker helps to distinguish such electrons from promptly produced electrons. In events in which the conversion occurs in the beam pipe or if the electron is matched to unassociated pixel hits, this method can also be insufficient, so an additional

track matching step is used. Tracks are matched in pairs and following geometrical cuts, can be removed if they appear to originate from a conversion [4].

### 3.3.4 Muon Reconstruction

Local reconstruction in the muon chambers provides hit position and time of arrival of a muon. This information from the DTs and CSCs is then amalgamated to create muon track hits and segments, which are then used by the muon global reconstruction algorithms to reconstruct “standalone” muons. An inner detector segment is used as a seed for a Kalman Filter [56, 89] and possible trajectories are generated. By removing hits which are not likely to have come from the track in question, the likely trajectory is constructed layer-by-layer. A final fit is carried out, including an extrapolation to the interaction point for greater momentum resolution.

Muons are also independently reconstructed in the tracker. These tracker tracks can therefore be combined with the aforementioned muon chamber information, where the magnetic field is only 2 T, to improve the  $p_T$  resolution of muons, as seen in Figure 3.1.

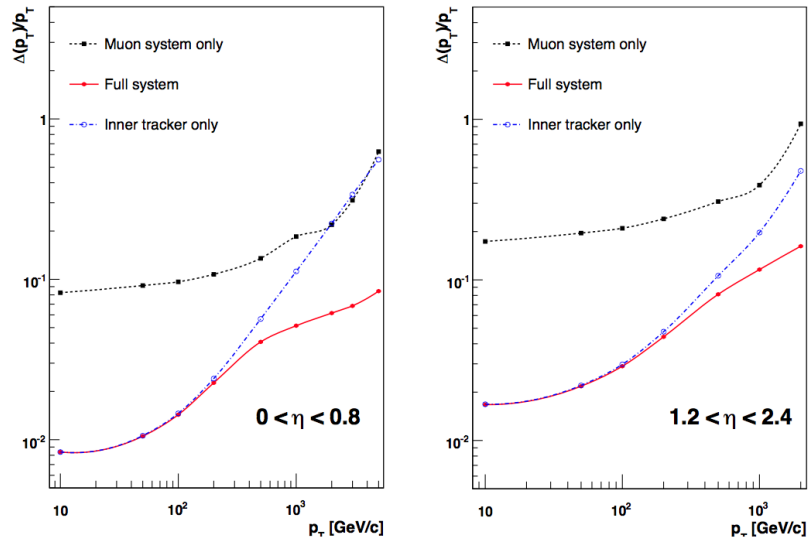


Figure 3.1: Muon transverse momentum resolution as a function of muon transverse momentum using the muon system only, using inner tracking only, and using both [33].

Two methods are employed to combine the information from the two sub-detectors. *Global muon reconstruction* matches a tracker track to a standalone muon track and carries out a fit

of the resulting *global muon* track. The second method, *tracker muon reconstruction*, tracker tracks are extrapolated outwards to the muon chambers and accepted as a muon candidate if a DT or CSC matching track is found and the muon  $p_T$  is greater than 0.5 GeV [34].

For triggering, the  $p_T$  of a muon is first estimated using the information available at Level 1 from all three types of muon detectors. At HLT level, the muon candidates from Level 1 are further refined using track finding and fitting, but still using only information from muon chambers, leading to Level 2 muons. As mentioned in Section 2.3.6, due to the time constraints required of the L1 trigger, full tracker data are not currently used. However, tracks of Level 2 muons are extrapolated into the tracker systems and a localised track finding algorithm is run to identify only nearby tracker hits. A track matching that of a Level 2 muon leads to a Level 3 muon.

### 3.3.5 Jet Reconstruction

As quarks produced in proton-proton interactions (except the top quark) hadronise [61], jets of particles are formed in the direction of travel of the quark. The time of arrival, position and the energy deposited by hadronic objects are locally reconstructed in the HCAL. If the deposit matches an ECAL deposit, a Calo Tower is formed for later use in jet reconstruction algorithms.

The particle flow (PF) algorithm performs the reconstruction of particles in the jet, and the anti- $k_t$  algorithm is used to perform the clustering of these particles into jets. The anti- $k_t$  algorithm, explained in detail in [27], is one of several jet algorithms that exist in CMS to combine reconstructed particles into jets. It defines a distance  $d_{ik}$  between reconstructed particles as

$$d_{ij} = \min \left( \frac{1}{p_{T,i}^2}, \frac{1}{p_{T,j}^2} \right) \frac{(\eta_i - \eta_j) + (\phi_i - \phi_j)^2}{R^2} \quad (3.1)$$

$p_{T,i}$  and  $p_{T,j}$  are the transverse momenta of the two particles  $i$  and  $j$ ,  $\eta_i$  and  $\eta_j$  are the

rapidities and  $\phi_i$  and  $\phi_j$  are the azimuth angles and  $R$  is the radius of the jet cone. anti- $k_t$  iteratively clusters together particles with the smallest  $d_{i,j}$  between them until all jets are reconstructed and there are no particles remaining. Events will usually consist of a small number of high- $p_T$  (hard) particles and a large number of low- $p_T$  particles. The distance between hard particles is typically small, and the distance between softer particles is larger. Soft (low- $p_T$ ) particles tending to cluster around hard (high- $p_T$ ) particles, before clustering with other soft particles.

While the PF anti- $k_t$  jets show high jet matching efficiency on Monte Carlo simulation samples, corrections are applied based on the jet  $p_T$  and  $\eta$  to correct for mismeasurements in the detector and thereby improve the agreement between generated and reconstructed particle flow jets. The factored approach to CMS jet energy corrections is comprised of three parts:

1. L1 Pile Up: corrects for additional energy from charged particles from pile-up in the event 3.3.2.
2. L2 Relative Jet Correction: corrects the reconstructed energy to match the generated jet with respect to  $\eta$ .
3. L3 Absolute Jet Correction: corrects the reconstructed energy to match the generated jet with respect to  $p_T$ .
4. L2L3Residuals: reduces any residual differences between the reconstructed and generated jet due to simulation not being perfectly tuned to data. This correction is applied to data only.

In order to identify jets in the differential cross sections analysis, further identification criteria are used to reduce electronic noise, to reduce the number of electrons mis-identified as jets and, in so doing, to ensure the selection of high quality jets. The requirements, which are known as the loose PF Jet ID, are:

- at least one constituent particle
- the neutral hadron energy fraction (NHF) must be  $< 0.99$
- for jets with  $|\eta| < 2.4$ , the charged hadron energy fraction (CHF) must be  $> 0$
- the neutral electromagnetic energy fraction (NEF) must be  $< 0.99$
- for jets with  $|\eta| < 2.4$ , the charged electromagnetic energy fraction (CEF) must be  $< 0.99$
- for jets with  $|\eta| < 2.4$ , the number of charged hadronic constituents (NCH) must be  $> 0$

## B Jets

The process of identifying jets coming from b-quarks is known as b-tagging and is very important in top quark physics due to the decay of the top to a W boson and a b-quark. b-tagging can therefore help to appreciably reduce background processes in signal. A description of b-tagging, the several algorithms available in CMS, relevant event variables used in the algorithms, and a performance comparison, is given in Chapter 6.

# 4 | The Standard Model

## 4.1 Introduction

The Standard Model (SM) is the name given to the theory developed during the course of the 20th century that describes the elementary particles that make up all known, observable matter and the three fundamental forces by which they interact (electromagnetic, weak and strong). The SM does not, however, describe the gravitational force as it is not known how to model mathematically at a quantum scale. The SM puts forward twelve fermions, with a spin quantum number of  $1/2$ , as the matter particles. These are split into two groups of six quarks and six leptons, all of which are split into three generations. The six quarks are classified according to their charge and flavour: up, down, charm, strange, top and beauty quarks. The leptons are in turn classified according to their charge and flavour: electron, muon or tau leptons, together with their corresponding neutrinos. Neutrinos, although originally thought to be massless, are now believed to carry mass due to the observation of the oscillation of neutrinos between different flavours. Table 4.1 shows these particles of the Standard Model in their respective generations in tabular form. All of these particles have a respective antiparticle which has identical quantum numbers except opposite electric charge.

All known, observable matter in the universe is composed of the aforementioned twelve fermions or their antiparticles. The only particles which are stable are the proton, which is made of two up quarks and a down quark; the neutron, which is made of one up quark and two down quarks; and the electron. All other particles are unstable and decay; they are produced only in particle colliders such as the LHC, or in cosmic radiation. Quarks also carry the charge of the strong force, termed ‘colour’, of red, green or blue. The only quark which does not ‘hadronise’ (form bound colourless states) is the top quark which has a very

Generation	Flavour	Charge / $e$	Spin	Mass / MeV
<b>Leptons</b>				
I	electron (e)	-1	$\frac{1}{2}$	0.511
	electron neutrino ( $\nu_e$ )	0	$\frac{1}{2}$	0
II	muon ( $\mu$ )	-1	$\frac{1}{2}$	105.66
	muon neutrino ( $\nu_\mu$ )	0	$\frac{1}{2}$	0
III	tau ( $\tau$ )	-1	$\frac{1}{2}$	105.66
	tau neutrino ( $\nu_\tau$ )	0	$\frac{1}{2}$	0
<b>Quarks</b>				
I	up (u)	$+\frac{2}{3}$	$\frac{1}{2}$	$2.3^{+0.7}_{-0.5}$
	down (d)	$-\frac{1}{3}$	$\frac{1}{2}$	$4.8^{+0.5}_{-0.3}$
II	charm (c)	$+\frac{2}{3}$	$\frac{1}{2}$	$(1.275^{+0.025}_{-0.025}) \times 10^3$
	strange (s)	$-\frac{1}{3}$	$\frac{1}{2}$	$95^{+5}_{-5}$
III	top/truth (t)	$+\frac{2}{3}$	$\frac{1}{2}$	$(173.21 \pm 0.51 \pm 0.71) \times 10^3$
	bottom/beauty (b)	$-\frac{1}{3}$	$\frac{1}{2}$	$(4.18^{+0.03}_{-0.03}) \times 10^3$
<b>Bosons</b>				
Force	Gauge Boson(s)	Charge / $e$	Spin	Mass / GeV
Weak	$W^+/W^-$	+1/-1	1	$80.385 \pm 0.015$
Weak	$Z^0$	0	1	$91.188 \pm 0.002$
Electromagnetic	photon ( $\gamma$ )	0	1	0
Strong	gluon (g)	0	1	0
Gravitation	graviton	0	1	0
-	Higgs (H)	0	0	$125.7 \pm 0.4$

Table 4.1: Fundamental fermions, split into their three generations, and bosons of the Standard Model. Particle properties taken from [81].

short lifetime of  $\approx 5 \times 10^{-25}$ s [81] due to its large mass.

These fermions interact via the integer spin (spin 1) gauge bosons of the three fundamental forces. Electron, muon and tau leptons interact via the electromagnetic and weak forces; their neutrinos, since they carry no electric charge, interact only via the weak force; and the quarks interact via the electromagnetic, weak and strong forces. Each of the forces are mediated by gauge bosons that are the ‘force carriers’, and lead to the formation of hadrons and atoms. The mediator of the strong force is known as the gluon, that of the electromagnetic force is the photon and those of the weak force are the  $W^+$ ,  $W^-$  and  $Z$  bosons. Table 4.1 shows the gauge bosons and their properties.

The strength of the fundamental forces is quantified by their coupling strength, denoted  $\alpha$ . Taking the strength of the strong force as the baseline, the relative strength of the electromagnetic force is  $10^{-2}$ , that of the weak force is  $10^{-13}$  and the strength of the gravitational force is  $10^{-42}$  [61]. The electromagnetic coupling strength, also known as the fine-structure constant, is defined as  $\alpha_{em} = \frac{e^2}{4\pi}$ , which at low energies is  $\approx \frac{1}{137}$ , the fine structure constant. Although the strong force is the strongest force, it has a limited range of only an estimated  $10^{-15}$  m, and the weak force has an estimated range of  $10^{-18}$  m, while the electromagnetic and gravitational forces have infinite range.

The Higgs boson, the discovery of which was announced in July 2012 by the CMS and ATLAS experiments at the LHC, is the latest component of the Standard Model to be discovered [33, 7]. The mechanism of electroweak symmetry breaking through which other particles acquire mass is due to this Higgs field, and is described in Section 4.1.5.

### 4.1.1 Gauge Principle

The underlying mathematical model of the Standard Model is a Quantum Field Theory (QFT) combining special relativity and quantum mechanics. All interactions in the the SM must conserve the kinematic quantities energy, momentum and charge. In addition, the electromagnetic and strong forces conserve the dynamical quantities colour, baryon number, lepton number and quark flavour. The weak force, if mediated by a charged propagator ( $W^\pm$ ), can allow the violation of quark flavour, meaning a quark can decay into another flavour quark.

The laws of conservation occur as a result of underlying symmetries in the theories; for instance, energy conservation stems from time symmetry and angular momentum conservation is a result of rotational symmetry. In addition to these classical symmetries, a quantum field theory can also possess gauge symmetries. The principle of gauge invariance refers to field theories in which the Lagrangian, which summarises the dynamics of the system, is invariant under local transformations (transformations that are a function of, and therefore different at

all space-time points in, a field). Note that the converse of local transformations are global transformations, in which the transformation takes place instantaneously at all space-time points. The collection of all such transformations, called gauge transformations, are called the Lie group. If the Lie group is commutative, i.e. any order of application of the symmetry transformations produces the same result, the theory is termed Abelian. Conversely, if the group is non-commutative, the theory is non-Abelian. Each Lie group has an associated generator, and each generator has a corresponding vector field, or gauge field, whose purpose is ensuring invariance under local transformations. The quanta of these fields are the gauge bosons of the Standard Model.

Group transformations can be represented as groups of  $n \times n$  matrices which possess properties such as unitarity ( $U$ ) and orthogonality ( $O$ ). A group of matrices with determinant 1 is called ‘special’ ( $S$ ), leading to further groups  $SU(N)$  and  $SO(N)$ . The Standard Model is comprised of electroweak theory (combining electromagnetism and weak theory) a gauge group of  $SU(2) \times U(1)$  and the theory of strong interactions that has a gauge symmetry of  $SU(3)$ . The Standard Model is therefore a gauge theory based on the gauge group  $SU(3) \times SU(2) \times U(1)$ .

### 4.1.2 Quantum Electrodynamics

Quantum electrodynamics (QED) is a component theory of the Standard Model that governs the interactions of electrically charged particles. The simplest electromagnetic process is shown in Figure 4.1a, and all real processes are made of some number of these processes combined together, such as electron-positron annihilation shown in Figure 4.1b.

The sum of all possible orders of Feynmann diagrams for a possible interaction is the representation of the real process. In practice, since at low energies, each vertex contributes a factor of  $\alpha$ , higher-order Feynmann diagrams with more than a few vertices contribute negligibly to the process and are often ignored.

The coupling strength of a force can be further explained in terms of vacuum polarisation.

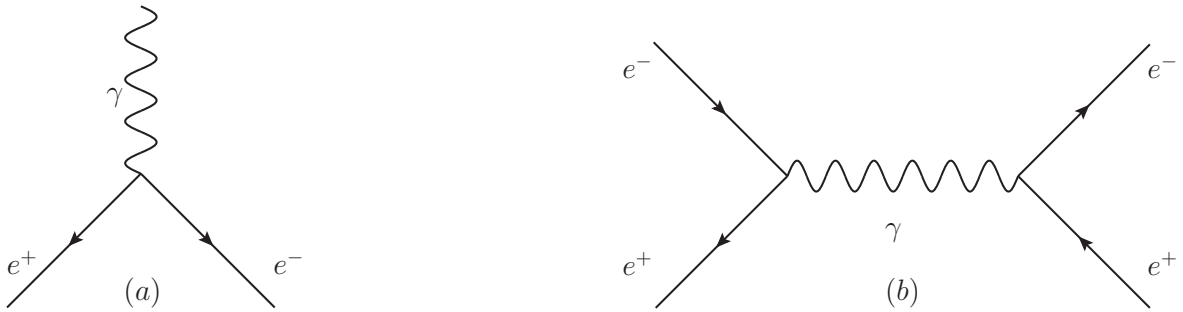


Figure 4.1: (a) the elementary electromagnetic process of an electron emitting a photon and (b) electron-positron annihilation.

This refers to the phenomenon of electron-positron pairs and photons being spontaneously created and absorbed by an electron. These virtual particles, which would be represented in Feynmann diagrams as closed loops, shield the original electron leading to the electron charge being measured at a lower value than its true charge. This measured value is called the effective, or 'screened', charge. As a result, the coupling strength of the electromagnetic force decreases as a function of distance, termed a 'running' coupling constant.

The mathematical formulation of QED stems from the Dirac equation, which describes the Lagrangian for a spin-half (Fermionic) field  $\psi$ .

$$\mathcal{L} = i(\hbar c)\bar{\psi}\gamma^{mu}\partial_{\mu}\psi - (mc^2)\bar{\psi}\psi \quad (4.1)$$

Here,  $\hbar$  is the reduced Planck's constant,  $\mu$  are the Lorentz indices and  $\gamma^{mu}$  are the gamma (or Dirac) matrices. Under a global transformation of a phase  $i\alpha$ ,

$$\psi(x) \rightarrow \psi'(x) = e^{i\alpha}\psi(x), \bar{\psi} \rightarrow \bar{\psi}'(x) = e^{-i\alpha}\bar{\psi}(x) \quad (4.2)$$

this Lagrangian is invariant (i.e. under a global transformation of the  $U(1)$  group, since this is equivalent to multiplication of the field  $\psi$  by a  $1 \times 1$  unitary matrix). However, under a local gauge transformation by a phase of  $i\alpha(x)$ , the symmetry is no longer true since the

partial derivative

$$\partial_\mu(e^{i\alpha(x)}\psi) = i(\partial_\mu\alpha(x))e^{i\alpha(x)}\psi + e^{i\alpha(x)})\partial_\mu\psi, \quad (4.3)$$

meaning the Lagrangian is not invariant:

$$\mathcal{L} \rightarrow \mathcal{L} - \bar{\psi}(x)\gamma^\mu\psi(x)[\partial_\mu\alpha(x)]. \quad (4.4)$$

Local symmetry can be maintained in this case if a new gauge field,  $A_\mu$ , is introduced to the Lagrangian by means of a covariant derivative  $D_\mu$ :

$$D_\mu = \partial_\mu + ieA_\mu. \quad (4.5)$$

Under the local transformation,  $A_{mu}$  transforms as

$$A_\mu \rightarrow A'_\mu = A_\mu - \frac{1}{e}\partial_\mu\alpha(x). \quad (4.6)$$

If the partial derivatives in the Dirac equation are now replaced with the covariant derivatives, the invariant Lagrangian is obtained:

$$\mathcal{L} = i(\hbar c)\bar{\psi}\gamma^{mu}\partial_\mu\psi - e\bar{\psi}\gamma^\mu\psi A_\mu - (mc^2)\bar{\psi}\psi - \frac{1}{4}F^{\mu\nu}F_{\mu\nu}. \quad (4.7)$$

In this way, the principle of local gauge invariance under the  $U(1)$  group is used to obtain the final Lagrangian, that of quantum electrodynamics. The physical interpretation of the gauge field  $A_\mu$  is the photon, which couples to charged particles (electrons and positrons) with a coupling strength proportional to the charge. The term  $\frac{1}{4}F^{\mu\nu}F_{\mu\nu}$  is an additional term

to account for the kinetic energy of the free particle of the new gauge field, i.e. the photon; and there is no term giving the photon mass.

In this way, the principle of local gauge invariance under the  $U(1)$  group is used to introduce additional fields to a Lagrangian in order to make it invariant under local transformations.

### 4.1.3 Electroweak Theory

The unification of the electromagnetic and weak forces in the 1960s provided a more complete theory of fundamental particles. This unification takes the form of an  $SU(2) \times U(1)$  gauge group correlating the electromagnetic and weak forces, and can be constructed in a similar way to the QED formalism in Section 4.1.4.

First, it is necessary to define isospin,  $I$ , an abstract fundamental property of fundamental particles that is conserved in weak interactions. Similarly, weak hypercharge,  $Y$ , is also a quantum property, defined as  $Y_W = 2(Q - I_3)$ , where  $Q$  represents the charge of the particle and  $I_3$  is the third component of isospin.  $I_3$  takes a value of  $1/2$  for up, charm and top quarks and for neutrinos; and  $-1/2$  for down, strange and bottom quarks and other leptons other than neutrinos.

It has been shown empirically that the weak interaction exhibits violation of parity ( $P$ ) and interacts only with left-handed particles via the charged gauge bosons ( $W^\pm$ ). Hence, the fields representing fermions are split into left handed and right handed components by defining a left handed doublet containing the left handed electron and left handed neutrino, and a right handed singlet containing the right handed electron:

$$\chi_L = \begin{pmatrix} \nu_e \\ e \end{pmatrix}_L, e_R \quad (4.8)$$

Here, the left handed doublet has  $I = \frac{1}{2}$ , and the right handed lepton has  $I = 0$ . Similar

doublets can be constructed for the other generations of leptons ( $\mu$  and  $\tau$ ) and quarks in their pairs of three generations ( $ud$ ,  $cs$  and  $tb$ ). Right handed neutrinos, which would have  $I = 0$  and  $Y = 0$ , do not exist in the Standard Model.

Four additional massless fields and their associated currents are introduced in order to impose gauge-invariance:  $W_\mu^1$ ,  $W_\mu^2$ ,  $W_\mu^3$  and  $B_\mu$ . The  $W_\mu$  fields are introduced for gauge invariance of the  $SU(2)$  group, and undergoes interactions with the third isospin component  $I_3$ . The  $B_\mu$  field similarly transforms by the unitary group  $U(1)$ , and interacts with the weak hypercharge  $Y$ . These additional fields lead to the construction of three weak isospin currents and a weak hypercharge current.

Requiring local gauge invariance under a the  $SU(2) \times U(1)$  group, the covariant derivative is

$$D_\mu = \partial_\mu + \frac{i}{2}g_W \vec{\tau} \cdot \vec{W}_\mu + ig' \frac{Y}{2} B_\mu. \quad (4.9)$$

The vectors  $W_\mu^1$ ,  $W_\mu^2$ ,  $W_\mu^3$  have coupling strengths of  $g_W$  to the three isospin currents and  $B_\mu$  couples to the hypercharge current with a strength of  $g'$ . These four bosons relate to the quanta of the new fields. A linear superposition of the  $W_\mu^1$  and  $W_\mu^2$  states gives the  $W^\pm$  bosons, while the neutral states  $W_\mu^3$  and  $B_\mu$  undergo a mixing related by the weak mixing angle,  $\theta_W$ , to give the neutral  $Z^0$  and  $\gamma$  bosons. (The weak mixing angle relates the coupling constants of the electromagnetic and weak forces by  $\tan \theta_W = \frac{g'}{g_W}$ ).

It has been experimentally observed that both W bosons and the Z boson have mass. Indeed, the strength of the electromagnetic force is of the same order as the weak force, but as a result of the weak gauge bosons having mass, the weak force appears weaker and has a shorter range. However, the local gauge invariance would be broken if terms are now included to give the bosons mass. The theory of spontaneous breaking of the symmetry underlying the  $SU(2) \times U(1)$  group addresses this problem, as explained in Section 4.1.5.

The weak force has been shown to change the flavour of quarks in an interaction, meaning flavour conservation is broken. As stated, the quarks, like leptons, come in the form of left

handed doublets within each generation,

$$\begin{pmatrix} u_L \\ d'_L \end{pmatrix}, \begin{pmatrix} c_L \\ s'_L \end{pmatrix}, \begin{pmatrix} t_L \\ b'_L \end{pmatrix} \quad (4.10)$$

with isospin  $\frac{1}{2}$ . Note that the lower quarks of the doublets are denoted with primes as they indicate a rotated state of the quark, called Cabibbo-rotated states, which are superpositions of the physical quarks. This means that in, for example, the decay of a down quark to an up quark via emittance of a  $W^-$ , the down quark to which the  $W^-$  couples is actually a superposition of ‘down type’ quarks, i.e. down, charm and beauty quarks. The Cabibbo-Kobayashi-Maskawa matrix (CKM), relates the weak interaction mixed states to the physical quark states. This is the degree of quark mixing between the different generations, and results in the measured values below of  $|V_{12}|$  for the probability of a transition from quark 1 to quark 2 in a weak interaction [81]. In reference to top physics, the  $|V_{tb}|$  value of almost 1 means that the top quark almost always decays to a  $W$  boson and a b-quark.

$$\begin{pmatrix} V_{ud} & V_{us} & V_{ub} \\ V_{cd} & V_{cs} & V_{cb} \\ V_{td} & V_{ts} & V_{tb} \end{pmatrix} = \begin{pmatrix} 0.974 & 0.225 & 0.004 \\ 0.225 & 0.973 & 0.041 \\ 0.009 & 0.041 & 0.999 \end{pmatrix} \quad (4.11)$$

#### 4.1.4 Quantum Chromodynamics

In the theory of quantum chromodynamics (QCD), the charge of the strong force is colour, and the force is independent of other particle properties such as charge and flavour. Empirical data has led to the conclusion that there are three colour charges: red, green and blue [61]. Colour conservation is a requirement of strong processes (just as charge conservation in QED), although the colour of an individual quark can be changed in a strong interaction. The mediators of the strong force, gluons, carry a positive and a negative colour charge

themselves, and so can interact directly with other gluons. The coupling constant of the strong force is a running coupling constant. At small distances of the order of the size of the proton ( $\sim 0.1$  fm),  $\alpha_S$  is small and becomes smaller as distance decreases, leading to quarks and gluons being essentially free particles and interacting weakly with each other when confined within a hadron, a phenomenon termed asymptotic freedom.

The previously mentioned colourless bound quark states are called hadrons. The process in which free gluons and quarks form bound colourless states is called hadronisation, and at high momenta manifests as a cone of particles, termed jets. Hadrons are divided into two types: mesons are composed of a quark and an antiquark with the quark carrying a colour charge and the antiquark carrying the respective anticolour; baryons are composed of three quarks or three antiquarks. Recently, the LHCb experiment at CERN published first results of the observation of a pentaquark state [9].

The proton, a baryon, consists of two u-quarks, one d-quark and gluons binding the quarks together. However, the structure of the proton becomes more complicated, consisting of more particles, as the momentum of the probing particle increases. The aforementioned three-quark-structure of the proton is evident at low momenta, while at higher momenta, virtual pairs of quarks, antiquarks and gluons are visible. These virtual quarks and gluons are termed sea-quarks and can make up most of the mass of the proton at high energy scales. In any proton, its constituent particles each carry some fraction,  $x$ , of the overall proton momentum.

The quantum field theory of QCD is determined to have the underlying symmetry of the group  $SU(3)$ , based on the fact that there are three colour charges. Imposing local gauge invariance, the Lagrangian contains eight generators of the  $SU(3)$  group. These generators lead to eight gauge fields, whose physical interpretation are the eight massless gluons that mediate the strong force. Therefore, although in principle there could be nine gluons, since there are three colours and gluons carry a colour and an anticolour charge, the  $SU(3)$  symmetry leads to a colour octet and a colour singlet [61].

Any particle that occurs in nature must be a colour singlet, and so the gluons in the colour octet are never seen in nature. However, although the final gluon is a colour singlet, it has not been observed and is thought not to exist. If it did exist, it would result in a long range strong force, but it is known that the strong force has a short range of action.

#### 4.1.5 Spontaneous Symmetry Breaking

The theory of spontaneous breaking of the electroweak  $SU(2)$  symmetry, mentioned in Section 4.1.3, also known as the Higgs mechanism, was put forward in the 1960s [63]. This theory was postulated as a mechanism by which the  $W^\pm$  and  $Z$  gauge bosons could acquire mass, since the Lagrangian of the electroweak interaction contains no mass term for these particles, and their inclusion would violate local gauge invariance.

The method by which this symmetry is spontaneously broken begins with the inclusion of two new complex scalar ‘Higgs’ fields (so in total there are four components to these two complex fields). The introduction of these fields results in an additional scalar potential energy term in the Lagrangian,  $V(\Phi)$ , where  $\Phi$  represents the newly introduced complex scalar fields. The potential  $V(\Phi)$  is chosen to be

$$V(\Phi) = -\mu^2 \Phi^\dagger \Phi + \lambda^2 (\Phi^\dagger \Phi)^2 \quad (4.12)$$

Imposing the requirement of  $\mu^2$  and  $\lambda$  both being greater than 0, gives a potential of the geometry shown in Figure 4.2. The minimum of this potential is clearly not at  $\Phi = 0$ , rather, the minimum has a circular form given by the formula  $\Phi^\dagger \Phi = \frac{\mu^2}{2\lambda} = \frac{v^2}{2}$ , where  $v = \frac{|\mu|}{\sqrt{\lambda}}$ , the ‘vacuum expectation value’ of the Higgs field. Since the minimum, i.e. the vacuum, is at a location other than  $\Phi = 0$ , the new field is said to have a non-zero vacuum expectation value, and the  $SU(2) \times U(1)$  symmetry is spontaneously broken. The observed Higgs boson is created as a result of perturbations in the potential about this minimum. In addition to this new particle, introducing the new fields also results in the fields associated with the  $W^\pm$  and  $Z^0$  bosons in the Lagrangian acquiring mass.

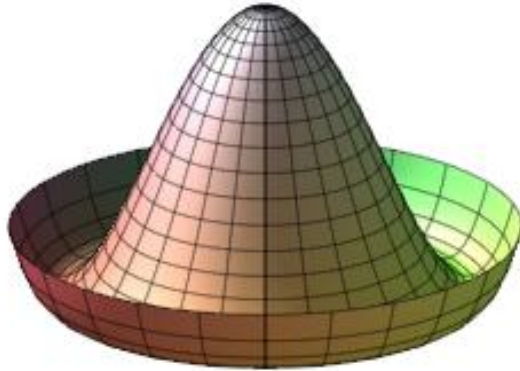


Figure 4.2: The Higgs field potential  $V(\Phi)$  [79].

Terms known as Yukawa coupling terms can be introduced to specify the interactions of  $\Phi$  with the fermion fields. It is this coupling of the Higgs field to any massive particle that gives them a proportional mass. The top quark, being the heaviest known particle at  $\sim 173$  GeV, has a Yukawa coupling to the Higgs field close to 1.

Results published at the discovery of the Higgs boson are shown in Figure 4.3 in the  $\text{Higgs} \rightarrow \gamma\gamma$  and  $\text{Higgs} \rightarrow ZZ$  channels. These plots of the invariant masses of the  $\gamma\gamma$  and  $ZZ$  combinations show a clear excess of events around 125 GeV. The latest results from CMS and ATLAS state a Higgs mass of  $125.09 \pm 0.21 \pm 0.11$  GeV [8], where the first uncertainty is statistical and the second is systematic. Since the announcement of the discovery of the Higgs boson in 2012, studies have continued to determine its quantum properties. Thus far, results show it to be in agreement with predictions from the Standard Model.

## 4.2 Incompleteness of, and physics beyond, the SM

The Standard Model has proven to be an extremely successful theory thus far. However, its inability to describe many phenomena in the universe lead to it being considered currently incomplete. Indeed, a ‘Grand Unified Theory’ combining the electromagnetic, weak and strong interactions is considered to be the next step towards a ‘Theory of Everything’ including gravity, with all of these forces being different physical manifestations of one single force.

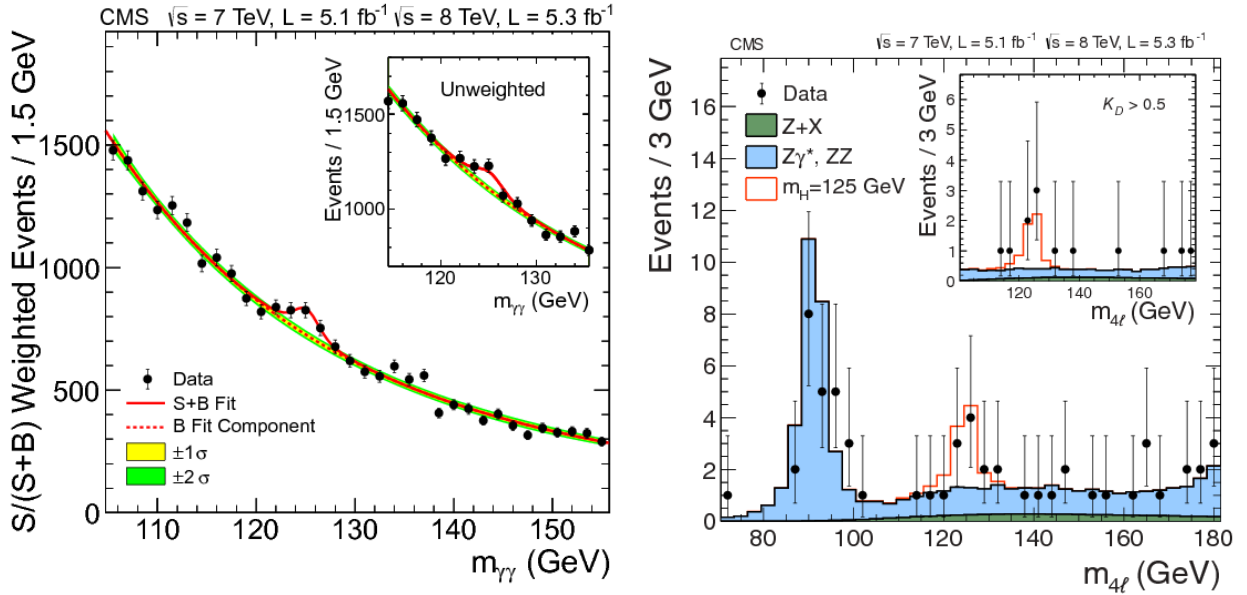


Figure 4.3: Invariant mass in  $H \rightarrow \gamma\gamma$  (left) and  $H \rightarrow ZZ$  (right) channels [33].

There are many free parameters in the Standard Model and the very reason why it takes the form it has, with four fundamental forces, six quarks and six leptons, each divided into three generations, is not explained. The gravitational force is also conspicuous by its absence from the SM. The imbalance between matter and anti-matter in the universe, despite the generally accepted view that both were created in equal quantities in the Big Bang, is also not fully explained by the SM. Although the evident matter-antimatter asymmetry in the universe could be partially explained by the observed charge-parity (CP) symmetry violation in weak interactions [39], this is not sufficient to account for the observed excess.

Furthermore, the SM does not provide a theoretical explanation for neutrino mass. Originally thought to be massless, neutrinos are now thought to have mass, albeit extremely small, based on observations of neutrino oscillations between different flavours [69, 57].

The hierarchy problem, in terms of the Higgs boson, is the term given to the fact that the Higgs mass is so much smaller than the expected value of the order of the Planck scale ( $1.22 \times 10^{19}$  GeV). The observed mass is the sum of the bare particle mass and any corrections from high order processes. This disagreement suggests that there occurs some ‘fine tuning’ of the bare Higgs mass to lead to the measured mass of approximately 125 GeV.

Supersymmetry (SUSY) is one potential solution to hierarchy problem. This theory proposes a symmetry between fermions (spin  $\frac{1}{2}$ ) and bosons (spin 1). Each particle has an associated ‘superpartner’ with identical quantum properties with the exception of spin, which differs by  $\frac{1}{2}$ , so that all Standard Model fermions have a boson superpartner, and all Standard Model bosons have a fermion superpartner. These super particles, or sparticles, are thought to have higher masses than their Standard Model counterparts since they have not been discovered yet. If this is the case, supersymmetry would be a broken symmetry. In many supersymmetry theories, the lightest SUSY particle (LSP) is stable and is a potential candidate to be a dark matter particle.

The theory of topcolor is an example of a composite model theory, that suggests the existence of a top-quark-condensate (a composite field of the top and antitop quarks) [23, 64] that acts effectively like the SM Higgs field. Such a theory gives rise to a new fundamental interaction between top quarks at high energies resulting in the large top mass. Theories of extra dimensions also exist, in which additional space-time dimensions are postulated in which only gravity propagates [22]. This could provide an explanation for the fact that the Planck scale is far larger than the electroweak force by solving the hierarchy problem.

Dark matter and dark energy are thought to constitute about 27 % dark matter, 68 % dark energy and 5 % ordinary matter (Figure 4.4) [14]. The origins and nature of the dark energy and dark matter are currently unknown and they are as yet unobserved, but their existence has been inferred from their gravitational effects on galactic masses composed of stars, gases and dust. The relatively large amounts of dark matter and dark energy hypothesised suggests that they are made up of weakly interacting massive particles.

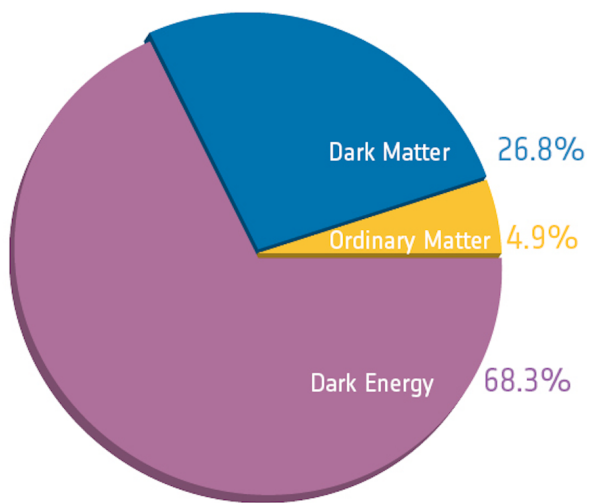


Figure 4.4: The composition of the universe showing the amounts of dark matter, dark energy and ordinary matter based on latest results from Planck/ESA [14]



# 5 | Top Physics at the LHC

## 5.1 Introduction

The top quark was discovered by the CDF and DØ collaborations at the Tevatron at Fermilab in 1995 [12, 10] and is still one of the less well studied fundamental particles in the Standard Model. The top quark is the heaviest fermion with its mass currently placed at  $173.29 \pm 0.23(\text{stat.}) \pm 0.92(\text{syst.}) \text{ GeV}/c^2$  [47]. Since the lifetime of the top quark is very short, approximately  $5 \times 10^{-25} \text{ s}$  [81], it is the only one of the quarks to decay before it hadronises, meaning that the bare quark properties can be investigated. These unique properties of the top quark within the Standard Model mean it is an interesting focus of study.

### 5.1.1 Top Quark Production and Decay

Top quarks can be produced either in top-antitop ( $t\bar{t}$ ) production through the strong interaction or single top (t-quark) production through the electroweak mechanism. During Run 1 of data taking at the LHC produced millions of top quark pair events with gluon-gluon fusion or quark-antiquark annihilation being the primary production mechanisms, as shown in Figure 5.1. Gluon-gluon fusion dominates at the LHC since protons are collided with protons, meaning antiquarks are only available from sea quarks in the proton. At low momentum fractions,  $x$ , the gluon density in the proton is large compared to the sea quarks, and increases at a higher rate than that of the sea quarks. Figure 5.2 shows the proton parton distribution functions (PDFs) at a momentum transfer,  $Q^2 = 10 \text{ GeV}^2$ , of the order required for  $\tilde{W}/Z$  production. At low  $x$ , it can be seen that the sea quarks and gluons dominate, while the valence quarks increase in number at high  $x$ .

At  $\sqrt{s} = 7 \text{ TeV}$ , gluon-gluon fusion accounts for approximately 80 % of the total t-quark

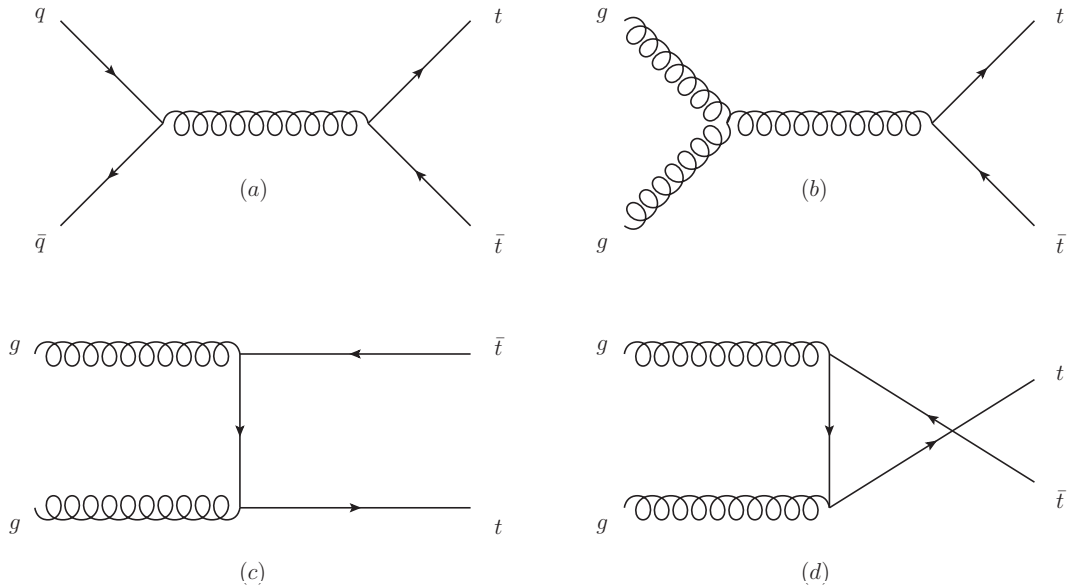


Figure 5.1: Feynman diagrams of leading order  $t\bar{t}$  production processes. (a) depicts quark-antiquark annihilation, and (b), (c) and (d) depict gluon-gluon fusion in the s, t and u channels respectively.)

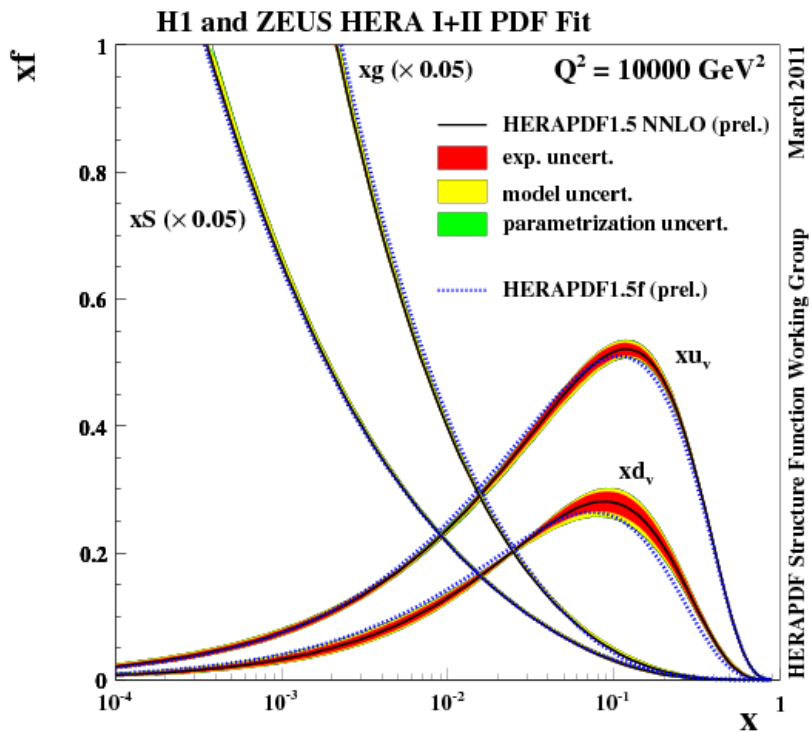


Figure 5.2: Parton Distribution Functions (PDFs) from HERA as a function of proton momentum fraction for  $Q^2 = 10 \text{ GeV}^2$  [84]

production cross section, increasing to approximately 90 % at  $\sqrt{s} = 14$  TeV [81].

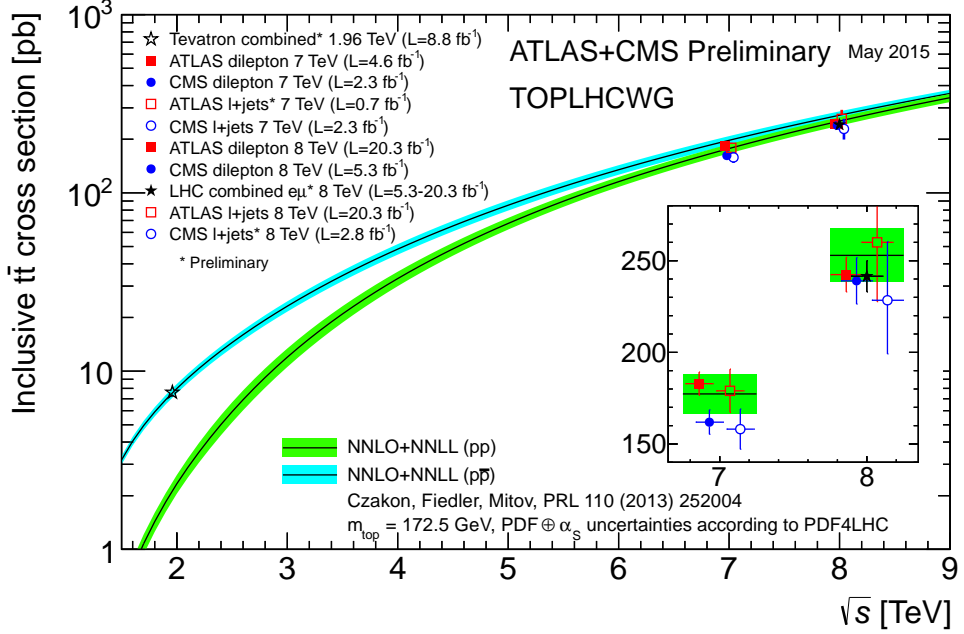


Figure 5.3:  $t\bar{t}$  production cross sections at 1.96 TeV at CDF and D $\emptyset$  at the TeVatron and at 7 TeV and 8 TeV at CMS and ATLAS at the LHC [62]

Top quarks decay almost 100 % of the time to a W boson and a b flavour jet. The W boson then decays either hadronically (into two jets) or leptonically (lepton + neutrino). Top pair events are characterised by the decay of the W bosons:

- Leptonic:  $t\bar{t} \rightarrow W^+ b W^- \bar{b} \rightarrow l\nu_l b l' \bar{\nu}_{l'} \bar{b}$ . Both W bosons decay to a lepton and a neutrino. The event would consist of 2 jets, 2 leptons and 2 neutrinos (which would show up as missing transverse energy ( $E_T^{\text{miss}}$ ) in the event). (10.5 %)
- Hadronic:  $t\bar{t} \rightarrow W^+ b W^- \bar{b} \rightarrow q\bar{q} b q\bar{q} \bar{b}$ . Both W bosons decay to two jets. The event would consist of 6 jets. (45.7 %)
- Semi-Leptonic:  $t\bar{t} \rightarrow W^+ b W^- \bar{b} \rightarrow q\bar{q} b l \nu_l \bar{b}$ . One W boson decays to a lepton and a neutrino, the other decays to two jets. The event would consist of 4 jets, 1 lepton and 1 neutrino. This decay is shown in Figure 5.4. (43.8 %)

The branching ratios for each decay mode are quoted in brackets [81], and are represented graphically in Figure 5.5. The numbers of jets in the final state of each channel could be

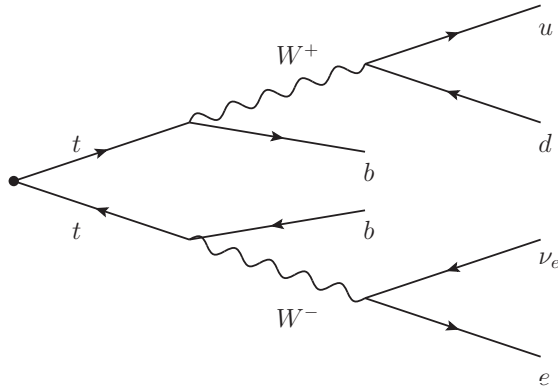


Figure 5.4: Feynman diagram of the electron+jets semi-leptonic  $t\bar{t}$  decay channel.

higher than the numbers quoted above as a result of higher order processes such as initial state radiation (radiation from the gluons before the  $t\bar{t}$  production) or final state radiation. The hadronic decay channel, with multiple jets and no leptons in the final state, is difficult to distinguish from the QCD multijet,  $W+$ jets and  $Z+$ jets backgrounds. Conversely, the leptonic channel has a very clean signature with two leptons, however the low branching ratio would limit the available statistics. The semi-leptonic channel, with one lepton and four jets provides a good balance between statistics and event identification. The lepton can be any of an electron, muon or  $\tau$ , but  $\tau$ s are not included in semi-leptonic t-quark analyses in general as they are more difficult to identify (see Section 9.1.1).

The signal channel for this analysis is semi-leptonic  $t\bar{t}$  decay, also referred to as the lepton+jets channel, where the lepton is either an electron or a muon. These channels have a branching ratio of approximately 14.2 % and 14.4 % respectively [81].

### 5.1.2 Single Top background

Single top production is one of the backgrounds considered in this analysis, and can occur via the electroweak interaction in one of three channels: s-channel or t-channel which involve the exchange of a virtual  $W$  boson, or t $W$ -channel which involves the associated production of a  $W$  boson and a top quark. Although semi-leptonic  $t\bar{t}$  decays have more jets in the final state than these single top production modes, initial state radiation and final state

## Top Pair Decay Channels

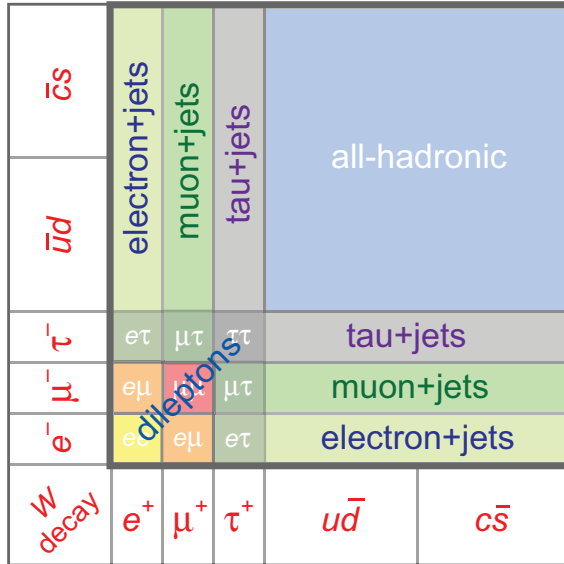


Figure 5.5: Relative branching ratios of the  $t\bar{t}$  system

radiation, where low energy gluons and quarks are produced before and after the interaction that produces the single quark, can increase the numbers of jets in single top events. This can lead to such events having a similar signature to  $t\bar{t}$  events, and providing a non-negligible background.

### 5.1.3 W/Z+jets background

$W + \text{jets}$  events present a significant background to semi-leptonic  $t\bar{t}$  analyses. This background consists of events in which a real  $W$  boson is produced together with additional jets. Events in which these  $W$  bosons decay leptonically, can provide a similar event signature after reconstruction to that of a semi-leptonic  $t\bar{t}$  decay. In general, these processes can be removed from the signal selection because the final decay products in  $W + \text{jets}$  events typically have lower energies than those from semi-leptonic  $t\bar{t}$  decays, since the top quark has a high mass. Another characteristic of  $W + \text{jets}$  events is that the jets are more likely to be light quark jets and therefore less likely to be b-jets than in  $t\bar{t}$  events. Thus,  $W + \text{jets}$  events can be separated from the  $t\bar{t}$  signal by using jet multiplicity, jet  $p_T$  and b-jet multiplicity.

Similarly,  $Z + \text{jets}$  events can mimic  $t\bar{t}$  events where the leptonic decay of a  $Z$  boson to a lepton and an anti-lepton takes place. This background can be distinguished from semi-leptonic  $t\bar{t}$  decays by vetoing on a second lepton and imposing jet multiplicity requirements. Misidentification and misreconstruction of these leptons as jets, however, can result in such events mimicking  $t\bar{t}$  events and passing the signal selection, although this contamination is small.

#### 5.1.4 QCD background

The multi-jet background from QCD events is also a significant background to this semi-leptonic  $t\bar{t}$  analysis. Gluon-gluon fusion and quark-antiquark annihilation in proton-proton collisions can produce energetic jets. Although these processes have only two jets in their final state, higher order processes, including initial state radiation and final state radiation, can also produce additional jets, leading to potential mimicking of the semi-leptonic  $t\bar{t}$  signal. The leptons required for this to happen can come from jets which are misreconstructed and misidentified as leptons, or real leptons in heavy flavour ( $b$  and  $c$  flavour) jets. Unfortunately the cross section of these processes is several orders of magnitude larger than the signal cross section. Although the lepton (either fake or real) is rarely one that passes selection, the much higher QCD cross section means that its contribution as a background is significant.

In the muon+jets channel, only highly energetic jets ( $p_T > 500 \text{ GeV}$ ) are capable of “punching through” from the calorimeters to leave tracks in the muon chambers. Such events can be removed by isolation requirements (since it deposits significant amounts of energy in the calorimeters). Events with real electrons and muons from heavy quark jets can be identified by the track quality requirements in the selection since they would not begin from the primary vertex and so would have a distinct track signature compared to prompt leptons.

On the other hand, the electron channel poses a more problematic QCD background, due mainly to the conversion of photons, whether produced at the interaction point or through subsequent decays and radiation, into electrons and positrons. The identification and removal

of such events is described in Section 3.3.3. However, the large uncertainty in the cross section of QCD events, large contamination from higher order processes with additional jets in the signal region of this analysis and the difficulty in modelling such contributions lead to significant disagreements in the numbers of events passing the signal selection in data and in simulation. Therefore, the QCD background is modelled using a data driven method.

The QCD background is difficult to model precisely because of large uncertainties on the cross sections and the significant higher contributions which can easily be mismodelled, leading to incorrect event kinematics and selection biases. Hence, the QCD background shape is modelled using a data driven method, described in Section 7.3.5 and then normalised to the number of events passing the selection process in simulation.

## 5.2 Monte Carlo Simulation

Monte Carlo event simulation is used to simulate the aforementioned signal and background processes, and to compare the theoretical knowledge of the Standard Model incorporated therein with real data. Differences between simulation and data would then indicate the presence of new physics processes which are not present in the theoretical assumptions made in the Standard Model, or perhaps that the simulation process is sub-optimal. Different event generators exist, and samples produced by the MADGRAPH, PYTHIA, POWHEG and HERWIG generators are used in this analysis.

Different generators have characteristics which optimise them for different aspects of the production chain: the initial hard process scattering of the partons in the hadrons (protons), decay showers of the resulting partons, subsequent decays of resulting hadrons and hadronisation of resulting partons, and the underlying event (the parton showers produced from soft scattering between the remaining contents of the colliding protons).

### 5.2.1 MadGraph

MADGRAPH [19], a matrix element generator, works by taking into account ext-to-leading-order Feynman diagrams for a given process and subsequently calculating the matrix elements for said diagrams over all phase space. The parton distribution functions are used to generate the incoming partons. The cross section of the process and various subprocesses and the structure and contents of the event (such as the partons present and their kinematics) are thus produced. Proton fragmentation and subsequent hadronisation are simulated using the PYTHIA generator, as explained in Section 5.2.3.

The parton showers are then matched with the matrix element partons via the MLM method [65]. This method ensures that parton showers with a highly energetic jet are not double counted. Matching is carried out between parton showers in the hadronisation and the partons from the matrix element calculations. The matching is carried out by satisfying distance requirements in  $\eta$  and  $\phi$  between the parton and parton shower. Only if the parton has a transverse energy above a certain threshold, is it considered for this matching, and if an event contains either too few or too many matching jets, it is discarded. The matching threshold is process dependent as follows:

- $t\bar{t}$ : 20 GeV
- $W + \text{jets}$ : 10 GeV
- $Z + \text{jets}$ : 10 GeV

### 5.2.2 MCatNLO

The MC@NLO [53, 55] generator is a next-to-leading-order generator. These additional corrections provide more accurate simulations of physics processes in comparison to leading-order generators by including additional partons from the initial hard process in the final state of the event.

### 5.2.3 PYTHIA

PYTHIA [87] then simulates the proton fragmentation, the subsequent hadronisation of the resulting quarks and gluons resulting from the hard interaction and the underlying event. PYTHIA is considered to be particularly good at multi-particle simulation, modelling fragmentation and hadronisation, and matching parton showers. Therefore, PYTHIA carries out these steps after the initial partons are provided by other generators in most simulated samples, if it is not already used for the whole production chain (as is common in QCD multijet simulations).

### 5.2.4 POWHEG

One problem with the MC@NLO generator is that some events are given negative weights when matching the next-to-leading-order QCD multijet calculations to parton showers. The Positive Weight Hardest Emission Generator, POWHEG [54, 80, 17], is another next-to-leading-order generator which generates the hardest processes in the event first, which avoids double counting of softer radiation produced later in the chain, which is the cause of negative event weights.

## 5.3 Theoretical Systematics

### 5.3.1 Factorisation & Matching Threshold

Systematic uncertainties are present in the choice of the threshold transverse energy above which matching of matrix-element partons to parton showers is carried out. Simulated samples in which the threshold is increased and decreased by a factor of 2 (see Table 5.1) are used to estimate the affect of this uncertainty on this analysis.

Similarly, the factorisation scale at which  $\alpha_S$  is varied up and down from the nominal value

of  $Q^2 = m^2 + \Sigma p_T^2$  by a factor of 2 to produce simulation samples to evaluate the systematic uncertainty resulting from this. The uncertainty resulting from these variations are evaluated in both  $t\bar{t}$  and  $W/Z + \text{jets}$  processes.

Process	Matching Threshold			Factorisation Scale		
	nominal / GeV	+ variation / GeV	- variation / GeV	nominal / GeV	+ variation / GeV	- variation
$t\bar{t}$	20	40	10	$Q^2 = m_T^2 + \Sigma p_T^2$	$(2Q)^2$	$(0.5Q)^2$
$W + \text{jets}$	10	20	5	$Q^2 = m_W^2 + \Sigma p_T^2$	$(2Q)^2$	$(0.5Q)^2$
$Z + \text{jets}$	10	20	5	$Q^2 = m_Z^2 + \Sigma p_T^2$	$(2Q)^2$	$(0.5Q)^2$

Table 5.1: Threshold transverse energy for matching systematic uncertainty

### 5.3.2 Detector Simulation (GEANT)

Following creation of the physics processes in proton-proton collisions, the simulated events are then put through a detector simulation to evaluate the interaction of the detector with the products of collisions. The Geometry and Tracking 4 (GEANT4) package [16, 18] is used for this purpose, which simulates what happens to particles as they travel through the geometry of the detector, including simulation of the detector components and materials and the interaction of particles with the detector such as particle tracks and energy deposits.

# 6 | b-tagging Study

Since the t-quark decays to a W boson and a b-quark, the understanding of these decay products is important in studies of  $t\bar{t}$  events. In particular, Methods to identify jets coming from a b-quark, known as b-tagging, are commonly used to increase the efficiency of  $t\text{-quark} \rightarrow b\text{-quark}W$  signal selection. CMS has several algorithms for b-tagging: TrackCounting (High Efficiency) and TrackCounting (High Purity), JetBProbability; JetProbability; SoftMuon; SoftMuonByPt; SoftMuonByIP3d; SimpleSecondaryVertex (High Efficiency); SimpleSecondaryVertex (High Purity); CombinedSecondaryVertex and CombinedSecondaryVetexMVA. These algorithms produce a discriminator output for each jet which indicates how likely it is to be a b-quark flavour jet. In all cases, a more positive discriminator value indicates a jet that is more likely to be a b-quark flavour jet.

The relatively long lifetime (of the order of  $10^{-12}\text{s}$ ) of b-quarks means that they travel a significant distance (of the order of a few mm) before decaying. This leads to events with b-jets possessing a secondary vertex distinguishable at a significant distance from the primary interaction vertex, as seen in Figure 6.1. This secondary vertex information, together with track based information such as the number of tracks in the jet, the invariant mass of the secondary vertex and the impact parameter significance (described below) of each jet track is used by the CSV algorithm to produce a discriminator ranging from 0 to 1, with larger numbers corresponding to a higher probability of a jet being a b-jet. Three b-tagging working points are used in CMS: tight, medium and loose. The medium working point is used in the different cross sections analysis, which carries a 1 % mis-tag rate (the rate at which non-b-jets are mistakenly tagged as b-jets) and approximately 70 % b-tag efficiency. The tight and loose working points have mis-tag rates of 0.1 % and 10 % respectively [36].

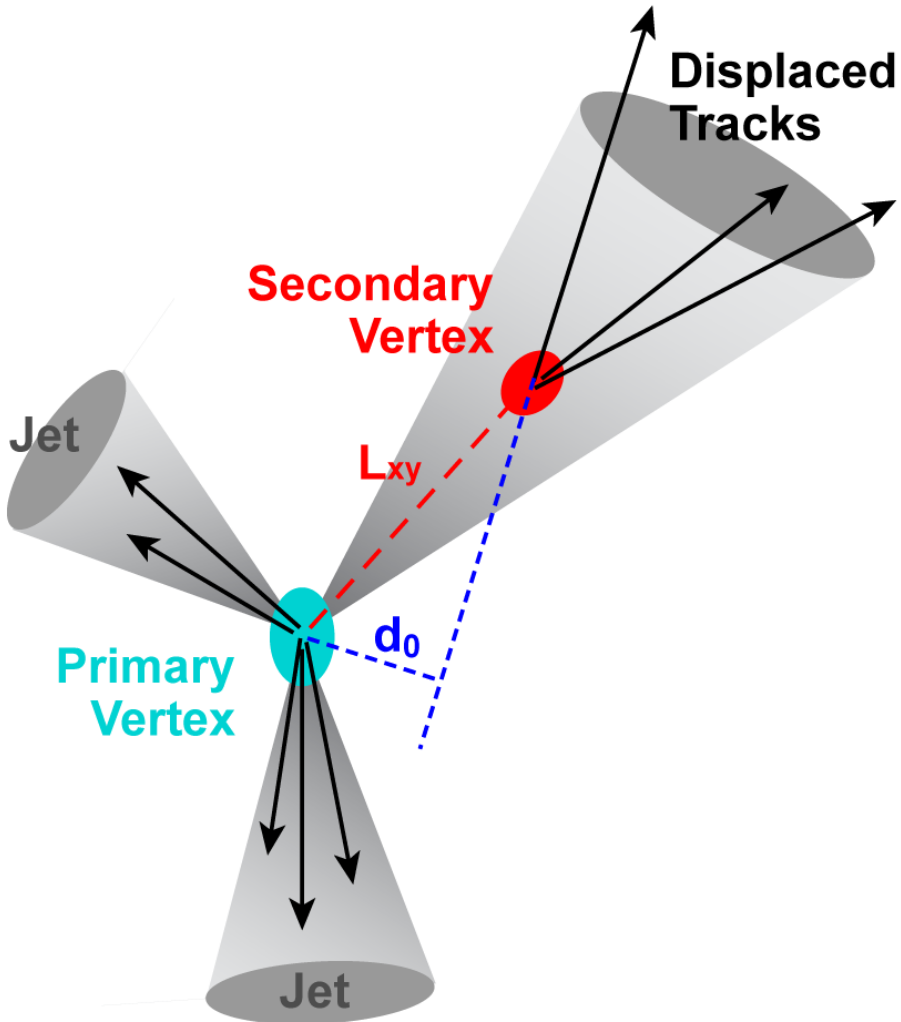


Figure 6.1: Graphical representation of an interaction originating at the primary vertex producing three jets, one of which is a b-jet with a secondary vertex [46].

## 6.1 Observables used in b-tagging algorithms

The impact parameter (IP) of a track is defined as the distance between the track and the vertex at the point of closest approach [2]. Figure 6.2 shows a schematic representation of the impact parameter for one single track. The IP measurement can be made in either the plane transverse to the beam line, or in three dimensions. The impact parameter significance ( $IP/\sigma_{IP}$ ) is often used instead as an input to b-tagging algorithms to allow for the experimental resolution. Due to the fact that the uncertainty on the IP value alone can be as large as the IP itself. The IP significance distribution of light jets ( $u, d, s$  and gluon jets) form a gaussian

about a mean of zero and width of one, with a slightly extended tail due to tracks from particles in the jet with long lifetimes. The equivalent distribution for  $c$  jets and  $b$  jets show an asymmetric distribution at positive values due to the long lifetime of B and C hadrons, making the IP significance a useful parameter to distinguish between light and heavy flavour jets [1]. The signed IP is also used, in which the sign is obtained from the sign of the scalar product of the IP vector and the jet direction, so that it is positive if the angle between the IP vector and the jet direction is less than  $90^\circ$ , and negative if the angle is greater than  $90^\circ$ . Tracks belonging in a b-jet would have an IP sign  $>0$ , since the jet direction is an estimate of the direction of travel of the B hadron. However, the sign could be inaccurately calculated in cases with badly reconstructed jet directions or primary vertices, or badly measured track parameters [1]. Another parameter based on track length, the 3D decay length significance (the ratio of the three dimensional distance between the primary vertex and the secondary vertex, and the uncertainty on this value) is also used by some b-tagging algorithms.

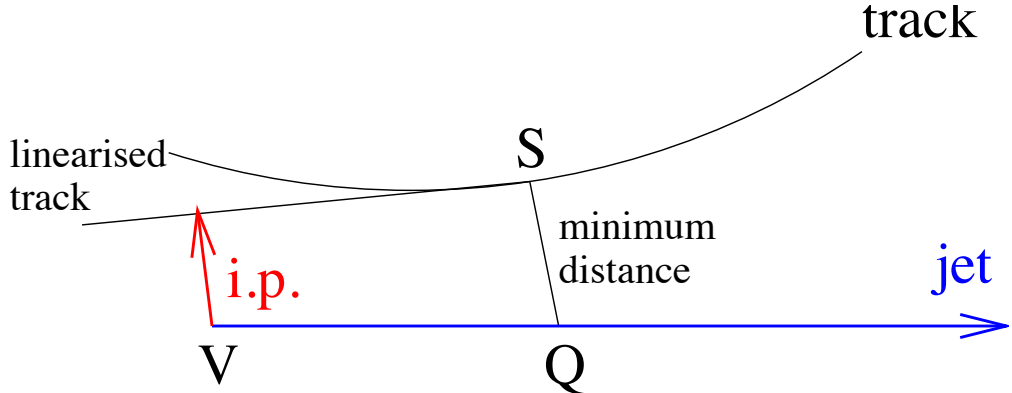


Figure 6.2: Graphical representation of a track impact parameter [2].

Identification of vertices in CMS consists of two stages: vertex finding and vertex fitting. Vertex finding deals with the creation of vertex candidates by grouping reconstructed tracks together. Vertex fitting then deals with obtaining the vertex parameters such as position of the vertex and track parameters, and the quality of the fit. An adaptive vertex fitter [91] calculates an estimate of the vertex position and weights tracks based on their compatibility with the vertex. This first fit is constrained to the interaction region to identify prompt tracks. After removing tracks with weights  $>0.5$ , subsequent fits are carried out to identify potential decay vertices, until no new vertex is identified.

## 6.2 b-tagging algorithm descriptions

### Track Counting

The simplest b-tagging algorithms available in CMS are the track counting algorithms [2], which positively identifies a b-jet if it contains N or more tracks with IP significance above some threshold value. They function by ordering all good tracks in a jet by order of decreasing IP significance, with the discriminator being the IP significance of the Nth track. The high efficiency version of this algorithm uses N=2, i.e. the second track, and the high purity version uses N=3, i.e. the third track [1].

### Jet Probability

The “jet probability” algorithms [2] produce a discriminator based on the probability that the set of tracks come from the primary vertex: a high probability would indicate that the jet is not a b-jet, which would originate at a secondary vertex. These algorithms use all tracks as input and for each track define an individual probability of coming from the primary vertex. By combining these probabilities, a jet probability is produced, and the discriminator is the negative log of this confidence level [1]. The “jet B probability” variant is based on the four most displaced tracks in the jet, since the mean number of tracks in a b jet is approximately 5 and the reconstruction of tracks within jets has an efficiency of approximately 0.8 in CMS [2]. The “jet B probability” in this case is based on the confidence level that the four most displaced tracks originate from the primary vertex.

### Soft Muon

The “soft muon” algorithms make use of global muons reconstructed in the vicinity of the reconstructed jet, which may indicate a semi-leptonic decay of B hadrons to a muon [50]. Two soft muon algorithms exist in CMS. The “soft muon by  $p_T$ ” algorithm uses the relative

$p_T$  of the muon with respect to the jet ( $p_{Trel}$ ), which is expected to be larger than that for muons in light flavour jets due to the large b-quark mass [50, 52]. A “soft muon by IP algorithm” also exists which uses the IP significance of positive IP muons. In jets containing more than one muon, the muon with the highest discriminator is used.

## Simple Secondary Vertex

The simple secondary vertex (SSV) algorithm uses the Adaptive Vertex Fitter to reconstruct the secondary vertex [91]. The discriminator is calculated based on the 3D decay length significance. If no secondary vertex is reconstructed, no discriminator is produced, meaning that the efficiency of this algorithm is limited to the maximum efficiency of secondary vertex reconstruction (approximately 65%) [36]. There are two variants of the simple secondary vertex algorithm: the high efficiency version uses vertices with at least two compatible tracks, whereas the high purity version uses vertices with at least three tracks. Since this algorithm does not directly use track-based lifetime parameters, it is less sensitive than other algorithms to tracker misalignment.

## Combined Secondary Vertex

The current CMS recommendation for physics analyses (and therefore the algorithm used in the differential cross section analysis presented in Chapters 7-9) is the Combined Secondary Vertex (CSV) algorithm [92]. This algorithm reconstructs the event vertices using the Trimmed Kalman Vertex Finder [89]. This vertex finding algorithm fits tracks to a primary vertex after removing incompatible tracks and applies cuts to these vertices in order to find a secondary vertex. The CSV algorithm then combines track-based lifetime parameters, such as IP and flight distance significance, with secondary vertex information to produce a discriminator. The increased number of input parameters means that even in cases with no reconstructed secondary vertex a discriminator can be produced, thereby increasing the maximum efficiency compared to the SSV algorithms /citeChatrchyan:2012jua. A variant

of this algorithm in which a multi-variate analysis (MVA) is performed using the CMSSW MVA Tools to produce a discriminator.

## 6.3 Performance Comparison

Distributions of the discriminators produced by the above algorithms were created for a  $t\bar{t}$  MADGRAPH Monte Carlo simulation sample (`/TTJets_TuneZ2_7TeV-madgraph-tauola/`, produced in the Fall2011 production cycle using CMSSW version 44X). A comparison of the discriminator distributions, after normalising to unit area, for the described algorithms were carried out. Figure 6.3 shows a comparison between the distributions obtained by the CSV algorithm for the different jets present in the sample: b-jets, light jets (up, down and strange flavour: uds-jets), gluon jets (g-jets) and charm flavour jets (c-jets). All distributions were normalised to unity in order to facilitate shape comparision. Equivalent plots for other algorithms are included in Figure A.1 in Appendix A. In all cases, it can be seen that higher discriminator values were produced for b-jets than for uds-jets, g-jets and c-jets, as would be expected.

## 6.4 Efficiency

Analyses in CMS make use of b-tagging algorithms by placing cuts on the discriminators. The efficiency of a cut can be defined as the ratio of number of jets passing the selection cut to the total number of jets before the selection cut. The efficiency was calculated for cut values spanning the whole range of discriminator values, thereby producing a plot of b-tag efficiency as a function of CSV discriminator cut value. Figure 6.4 shows the b-tag efficiency variation with cut value for the CSV algorithm. In practice, the aim is to acheive a high b-jet efficiency and a low efficiency for all other jet flavours, i.e. towards the bottom right of the plot. It can be seen that uds-jets and g-jets have similar rates of increase in efficiencies with respect to cut value, owing to their similar discriminator distributions. The c-jet discriminator distribution (Figure 6.3), however, has a noticeably different shape. This leads to the undesireable trend

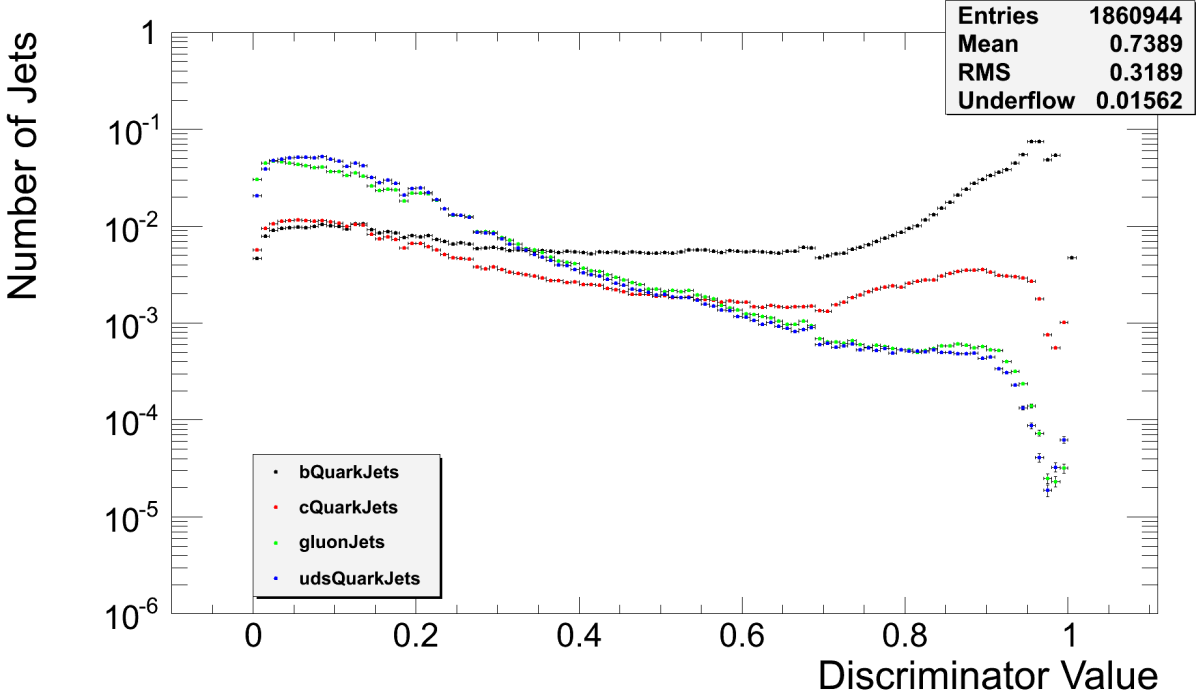


Figure 6.3: Discriminator values produced by the Combined Secondary Vertex algorithm for all b-jets, c-jets, g-jets and uds-jets after normalisation.

of higher c-jet efficiencies than for uds-jets and g-jets. Equivalent plots for other algorithms can be found in Figure A.2 in Appendix A.

## 6.5 Algorithm Comparison

The performances of the various algorithms can be compared in Figure 6.5.

It can be seen that not all algorithms reach 100% b-jet efficiency due to being inherently limited by their methods. For example, the soft muon algorithms are limited by the muon identification efficiency within b-jets and also by the branching fraction of B hadrons to muons. For instance, the soft muon algorithms all show low maximum b-jet efficiencies due to the low B hadron semi-leptonic branching ratio to muon of approximately 11% (or 20% when further decays are included such as  $b \rightarrow c \rightarrow l$ ) [52]. Similarly, the SSV algorithms are limited by the efficiency of reconstructing a secondary vertex in the jet of approximately 65%.

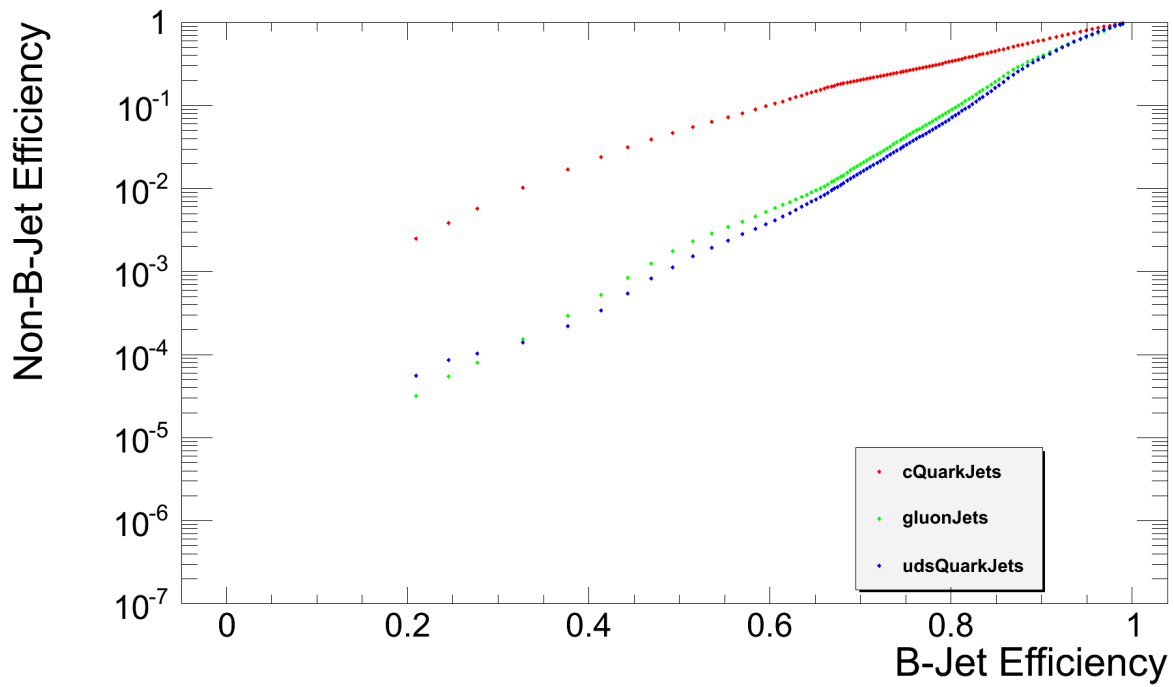


Figure 6.4: Non b-jet efficiencies as a function of b-jet efficiency for the CSV algorithm.

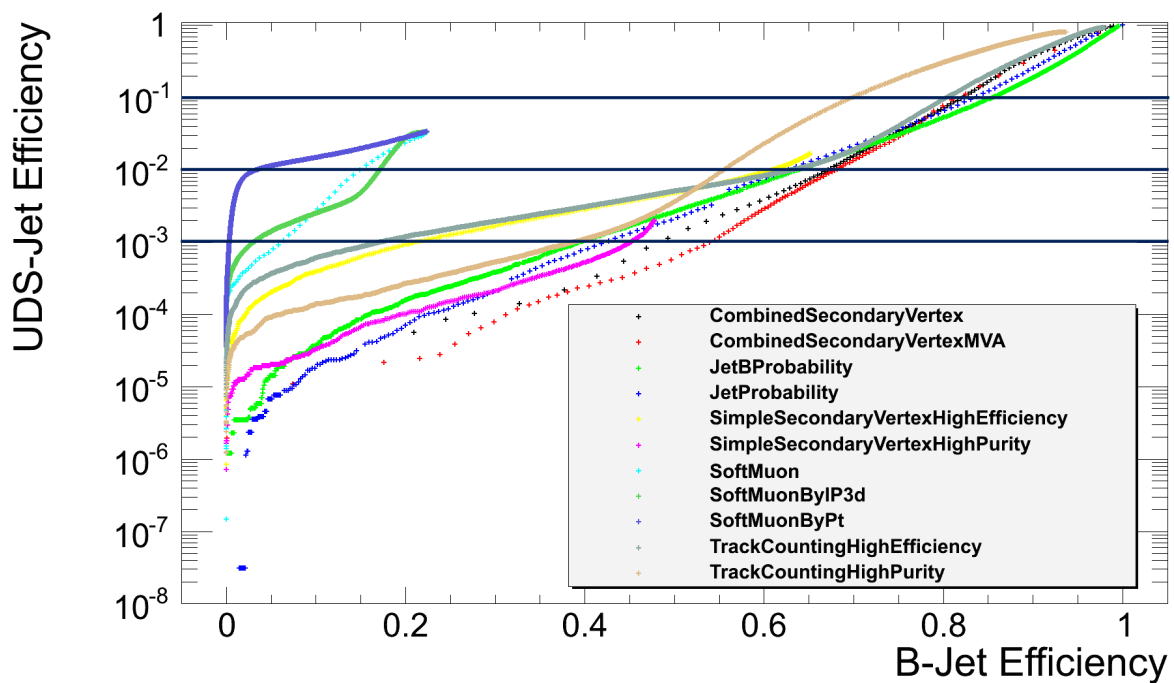


Figure 6.5: uds-jet efficiencies as a function of b-jet efficiencies for all algorithms.TODO:  
MAKE PLOT MORE LEGIBLE IF TIME PERMITS.

The 2011 and 2012 CMS recommended b-tagger is the Combined Secondary Vertex with operating point discriminator cuts of 0.244 (loose), 0.679 (medium) and 0.898 (tight) corresponding to 10%, 1% and 0.1% light jet efficiency. These cuts are indicated by the horizontal lines on Figure 6.5. It can be seen that for the tight and medium cuts, the CSV MVA algorithms provides highest b-jet efficiency and lowest light jet efficiency, followed closely by the CSV algorithm. The multiple variables that are used as input allow the CSV algorithm to produce higher efficiencies than the SSV algorithms, while the MVA analysis variant improves slightly on correctly identifying jets from b-quarks. At approximately 3% light jet efficiency, there is a convergence of many algorithms that all provide similar performance. At the loose working point also, many of the algorithms provide similar performance on b-jets, with the “jet probability” algorithms marginally outperforming the CSV algorithms. In early CMSSW versions, it was known that the jet probability algorithm provided optimal performance, leading to it being recommended for early CMS analyses. Ultimately, the CSV algorithm provides better performance in CMSSW versions after CMSSW\_2\_X\_Y, at which point it became the recommended b-tagging method.



# 7 | 7 TeV and 8 TeV Differential Cross Section Measurement: Data, Simulation and Selection

## 7.1 Outline

This chapter describes the first part of the main  $t\bar{t}$  differential cross section analysis in bins of global event variables. Following an introduction to the variables under investigation and motivations, the datasets used and the selection process is explained, including scale factors and corrections applied to ensure agreement between Monte Carlo simulation and data.

The analysis measures the normalised differential  $t\bar{t}$  cross section in the semi-leptonic channel and is carried out on 2011 and 2012 data recorded from the CMS detector. The measurement is carried out with respect to the following global, or primary, variables is carried out:

- $E_T^{\text{miss}}$ , the missing transverse energy in an event, defined as the magnitude of the missing transverse momentum vector  $\vec{p}_T^{\text{miss}}$

$$E_T^{\text{miss}} = \left[ \left( \sum_i p_x^i \right)^2 + \left( \sum_i p_y^i \right)^2 \right]^{\frac{1}{2}},$$

where  $p_x^i$  and  $p_y^i$  are momentum components of the  $i$ th object in an event, and the sums include all objects in the event.

- $H_T$ , the sum of the transverse momenta of all jets in an event

$$H_T = \sum_{\text{all jets}} p_T^{\text{jet}},$$

where the sum includes all jets with  $p_T > 20 \text{ GeV}$  and  $|\eta| < 2.5$ .

- $S_T$ , the sum of all observed transverse momenta in an event, i.e. the scalar sum of  $H_T$ ,  $E_T^{\text{miss}}$ , and lepton  $p_T$

$$S_T = H_T + E_T^{\text{miss}} + p_T^{\text{lepton}}.$$

- $p_T^W$ , the transverse momentum of the leptonically decaying W boson, obtained from  $E_T^{\text{miss}}$  and the  $p_T$  of the lepton

$$p_T^W = \sqrt{(p_x^{\text{lepton}} + p_x^{\text{miss}})^2 + (p_y^{\text{lepton}} + p_y^{\text{miss}})^2},$$

where  $p_x^{\text{lepton}}$  and  $p_y^{\text{lepton}}$  are the transverse components of  $\vec{p}^{\text{lepton}}$ , and  $p_x^{\text{miss}}$  and  $p_y^{\text{miss}}$  are the transverse components of  $\vec{p}_T^{\text{miss}}$ .

- $M_T^W$ , the transverse mass of the leptonically decaying W boson, also obtained from  $E_T^{\text{miss}}$  and the  $p_T$  of the lepton

$$M_T^W = \sqrt{E_T(\text{lepton}, E_T^{\text{miss}})^2 - (p_T^W)^2},$$

where  $E_T(\text{lepton}, E_T^{\text{miss}})$  is the scalar sum of  $E_T^{\text{miss}}$  and the transverse energy of the lepton, i.e.  $E_T^{\text{miss}} + E_T^{\text{lepton}}$

## 7.2 Data and Simulated Samples

### 7.2.1 Data

Data collected in 2011 at a centre-of-mass energy of 7 TeV and in 2012 at a centre-of-mass energy of 8 TeV are used. The datasets are determined by the triggers that were used to record them. For 7 TeV, the “ElectronHad” dataset is used in the electron channel. It was recorded with triggers that select based on a single, isolated electron and additional jets. At 8 TeV, the “SingleElectron” dataset was used for the electron channel which is based only on a single, isolated electron. In the muon channel, the “SingleMu” dataset was used for both centre-of-mass energies, requiring a single, isolated muon.

These datasets are produced from CMS data by requiring events to pass a trigger. The triggers used in both 7 TeV and 8 TeV data are shown in TableB.1 in Appendix B.1. In the electron channel, an electron plus jets trigger was used in 2011 with a requirement of electron  $E_T > 25 \text{ GeV}$  and at least three jets with  $p_T > 20 \text{ GeV}$ ; and a single electron trigger was used in 2012 with an electron  $E_T$  requirement of 27 GeV. In the muon channel, a single muon trigger was used in both data taking periods. In addition to these kinematic requirements, the triggers also have cuts for the electron on the ratio between the HCAL and the ECAL energy ( $H/E$ ), track matching with ECAL ( $\Delta\eta$  and  $\Delta\phi$ ), cluster shape ( $\sigma_{in in}$ ), ECAL isolation ( $\frac{\text{ECAL iso}}{E_T}$ ), HCAL isolation ( $\frac{\text{HCAL iso}}{E_T}$ ) and tracker isolation ( $\frac{\text{tracker iso}}{p_T}$ ). In the muon triggers, similarly, they have additional cuts on... TODO: CURRENTLY WAITING FOR EMAIL REPLY FROM MUON POG.

The datasets used are shown in Tables 7.1 and 7.2. Only data that is certified as “golden” (data taken with the CMS detector working without any major faults) is used. The masks used to filter out data taken in other periods are specified in Table B.2 in Appendix B.1.

<b>Data set name</b>	<b>Run period</b>	<b><math>L_{int}</math> / pb<math>^{-1}</math></b>	<b>Runs</b>
ElectronHad 12 Oct 2013 ReReco	Run2011A	2,333	160404--173692
ElectronHad 12 Oct 2013 ReReco	Run2011B	2,738	175833--180252
SingleMu 12 Oct 2013 ReReco	Run2011A	2,331	160404--173692
SingleMu 12 Oct 2013 ReReco	Run2011B	2,766	175833--180252

Table 7.1: 7 TeV data sets by run period with the corresponding integrated luminosities ( $L_{int}$ ) and run numbers.

<b>Data set name</b>	<b>Run period</b>	<b><math>L_{int}</math> / pb<math>^{-1}</math></b>	<b>Runs</b>
SingleElectron 22 Jan 2013 ReReco	Run2012A	883.3	190456--193621
SingleElectron 22 Jan 2013 ReReco	Run2012B	4,389.0	193834--196531
SingleElectron 22 Jan 2013 ReReco	Run2012C	7,137.0	198022--203742
SingleElectron 22 Jan 2013 ReReco	Run2012D	7,318.0	203777--208686
SingleMu 22 Jan 2013 ReReco	Run2012A	889.4	190456--193621
SingleMu 22 Jan 2013 ReReco	Run2012B	4,424.0	193834--196531
SingleMu 22 Jan 2013 ReReco	Run2012C	7,152.0	198022--203742
SingleMu 22 Jan 2013 ReReco	Run2012D	7,280.0	203777--208686

Table 7.2: 8 TeV data sets by run period with the corresponding integrated luminosities ( $L_{int}$ ) and run numbers.

### 7.2.2 Simulated Samples

The Monte Carlo generators used in this analysis are MADGRAPH [19], PYTHIA [87], POWHEG [80, 54, 17], HERWIG [60] and MC@NLO [53, 55]. See Section 5.2 for more details of these Monte Carlo generators.

The signal for this analysis is the production of a  $t\bar{t}$  pair which decays semi-leptonically, i.e. each of the t-quarks decays to a W boson and a b-jet, with one of the W bosons decaying hadronically to two jets and the other decaying leptonically to a lepton (electron or muon) and an associated neutrino. Section 5 outlines the signal and background events considered. Additional, lower energy jets, can be produced from other scatterings in the same proton-proton interaction and from gluon radiation from quarks in the decay. See Section 5 for detailed descriptions of the signal and backgrounds in this analysis.

Tables 7.3 and 7.6 show the Monte Carlo signal samples used in this analysis at 7 TeV and

8 TeV respectively. Tables 7.4 and 7.4 list the background simulation samples used. Top pair production is modelled using MADGRAPH, single top events are modelled with POWHEG, W and Z boson plus jets production is modelled using MADGRAPH and QCD multi-jet events are modelled with PYTHIA. In all cases, PYTHIA is used to model radiation and hadronisation processes. Tables 7.5 and 7.8 show the samples used to evaluate the factorisation scale, matching threshold, and top quark mass uncertainties. W + jets and Z + jets samples were not made available at 7 TeV, so the scaled distributions from 8 TeV were used, as described in Section 9.1.2.

Table 7.3: 7 TeV Monte Carlo signal datasets used for this analysis.

Process	Generator	$\sigma$ ( pb)	No. events	$\mathcal{L}_{\text{int}}$ ( fb $^{-1}$ )
t $\bar{t}$	MADGRAPH	177.31	17100187	96.4
t $\bar{t}$	MC@NLO	Not Available	-	-
t $\bar{t}$	POWHEG-PYTHIA	177.31	4833135	27.3
t $\bar{t}$	POWHEG-HERWIG	177.31	4480816	25.3

## 7.3 Selection

Selection algorithms are run on the data and samples listed in Sections 7.2 and 7.2.2 to identify t $\bar{t}$  events. The selection process is performed in two stages: a “pre-selection” using loose criteria to produce ntuples and a second full selection when processing these ntuples to produce the final sample. The selection used follows the recommended criteria by the CMS TOP Physics Analysis Group (PAG) and is the same for 7 TeV and 8 TeV.

### 7.3.1 Preselection

The preselection is performed on the AOD datasets, with the aim of making the resulting ntuples smaller in size but still versatile enough for use later in the analysis chain.

The preselection requires at least one good primary vertex with at least four degrees of freedom, located within 24 cm of the centre of the CMS detector in the  $z$  direction and within 2 cm of the centre of the beam trajectory in the transverse plane. In addition, events

are required to have at least one lepton candidate. In the case of electrons, a transverse energy of at least 30 GeV and  $|\eta| < 2.5$  and in the muon channel a transverse momentum of at least 20 GeV and  $|\eta| < 2.1$  are required.

Several filters are also applied in the preselection stage to remove events with significant levels of noise due to elements of the detector with sub-optimal performance during data-taking. These filters include an HCAL noise filter to remove events with high HCAL noise, a tracking failure filter to remove events with too few tracks, ECAL filters to remove events with signals in dead and/or noisy modules of the ECAL and a beam scraping veto which requires tracks of high purity in events with high track multiplicity.

### 7.3.2 Electron selection

The final selection in the electron+jets channel follows that recommended by the CMS TOP Physics Analysis Group (PAG). After having passed the electron trigger, events are further required to have an electron with an MVA electron identification of  $> 0.5$ , with  $E_T > 30 \text{ GeV}$  and  $|\eta| < 2.5$  (excluding the transition region between the ECAL barrel and endcap of  $1.4442 < |\eta| < 1.5660$ ). A transverse impact parameter, the distance between the electron and the primary vertex, of  $d_{xy} < 0.02 \text{ cm}$  is also required. In addition, a  $\rho$  corrected (explained in Section 3.3.2) relative isolation of  $< 0.1$ , within a cone of size  $\Delta R = 0.3$  is required and electrons that are matched to a photon conversion are rejected. A veto on additional electrons with looser identification criteria than the signal requirements mentioned here include an MVA identification of  $> 0.5$ ,  $E_T > 20 \text{ GeV}$ ,  $|\eta| < 2.5$  and a  $\rho$  corrected relative isolation of  $< 0.15$ .

### 7.3.3 Muon selection

As in the electron channel, the final selection in the muon channel is taken from the CMS TOP PAG recommendations. In this case, the muon identification requirement comprises several cuts: at least five hits in the tracker and at least one hit in the muon chambers

associated to the track, at least one layer of the muon chamber hits must be matched to a global muon (described in Section 3.3.4), and the inner track must include at least one hit in the pixel sub detector. Furthermore, the normalised chi-squared of the track fit should be less than 10. In addition, the muon identification algorithms should identify the particle as a global, particle flow (PF) muon, the muon track should pass within a z-distance of  $d_z < 0.5$  cm of the primary vertex and the transverse impact parameter is required to be  $d_{xy} < 0.2$  cm. The signal selection also requires that the muon has a  $p_T > 26$  GeV,  $|\eta| < 2.1$  and a  $\Delta\beta$  corrected (explained in Section 3.3.2) relative isolation of  $< 0.12$ , within a cone of size  $\Delta R = 0.4$ . Loose muons are vetoed, that satisfy the looser requirements of passing the particle flow identification,  $p_T > 10$  GeV,  $|\eta| < 2.5$  and a  $\Delta\beta$  corrected relative isolation  $< 0.2$ .

### 7.3.4 Jets selection

In addition to the signal lepton, all events must also have at least four particle flow jets as reconstructed using the anti- $kt$  algorithm (see Section 3.3.5) with a cone of  $\Delta R = 0.5$ . These jets are also required to have  $p_T > 30$  GeV,  $|\eta| < 2.5$ , be at least  $\Delta R = 0.3$  from the signal electron or muon and satisfy the criteria for the loose particle flow jet identification. These criteria are outlined in Section 3.3.5. Candidate particle flow jets from pileup are removed from the event; this is known as charged hadron subtraction. Events with at least four jets passing these criteria are permitted to have other lower energy jets passing the same requirements mentioned above, down to  $p_T = 20$  GeV. At least two of the four primary jets are further required to originate from b quarks (the process of identifying b jets is explained in Section 7.4.2.)

### 7.3.5 Multi-jet background selection

The QCD background is difficult to model in simulation, therefore this background distribution is modelled from data. In the electron+jets channel, a control region comprised primarily

of QCD events in the photon conversion region can be obtained by applying the full event selection with the exception of an inverted conversion veto, i.e. the veto on electrons that are matched to a photon conversion is reversed such that events will only pass the selection if they are matched to a photon conversion. The  $\geq 2$  b tags requirement is also relaxed to select only events with 0 b-tags to enrich the selection with QCD events. In order to evaluate a systematic uncertainty on the shape of this QCD background, an alternative control region is obtained by using the full signal selection but with the electron isolation requirement changed from  $< 0.1$  to  $> 0.2$ .

In the case of the muon+jets channel, the full selection is applied with the exception of the muon relative isolation requirement, which is switched from  $< 0.12$  to  $> 0.3$  and with the b tag requirement reduced to only events with 0 b tags in order to remove most other  $t\bar{t}$  background processes and produce a high purity QCD sample, as shown in Figure 7.1. In order to increase statistics the jet multiplicity requirement is reduced to require at least three jets.

Due to the low statistics of the QCD samples obtained from data, the inclusive QCD sample over all bins is used in every bin for each primary variable. The remaining contribution from  $t\bar{t}$ , single-top and  $W/Z + \text{jets}$  processes is subtracted from the data sample using the estimation from Monte Carlo simulation. The resulting template of QCD events from data is then used later in the fitting procedure, in place of the equivalent Monte Carlo template.

A comparison between data and simulation in the electron+jets QCD selections is shown in Figure 7.2. There is reasonably good agreement between the data and simulation in the conversion selection but low statistics in the simulation lead to some events with large weights, leading to peaks in the distribution. The non-isolated QCD selection shows more discrepancies between the simulation and data, but it should be noted that at  $\sqrt{s} = 7 \text{ TeV}$  the simulation does not contain the triggers used in this analysis, unlike at  $\sqrt{s} = 8 \text{ TeV}$ , therefore the simulation distribution at  $\sqrt{s} = 7 \text{ TeV}$  is not affected by the trigger isolation requirements.

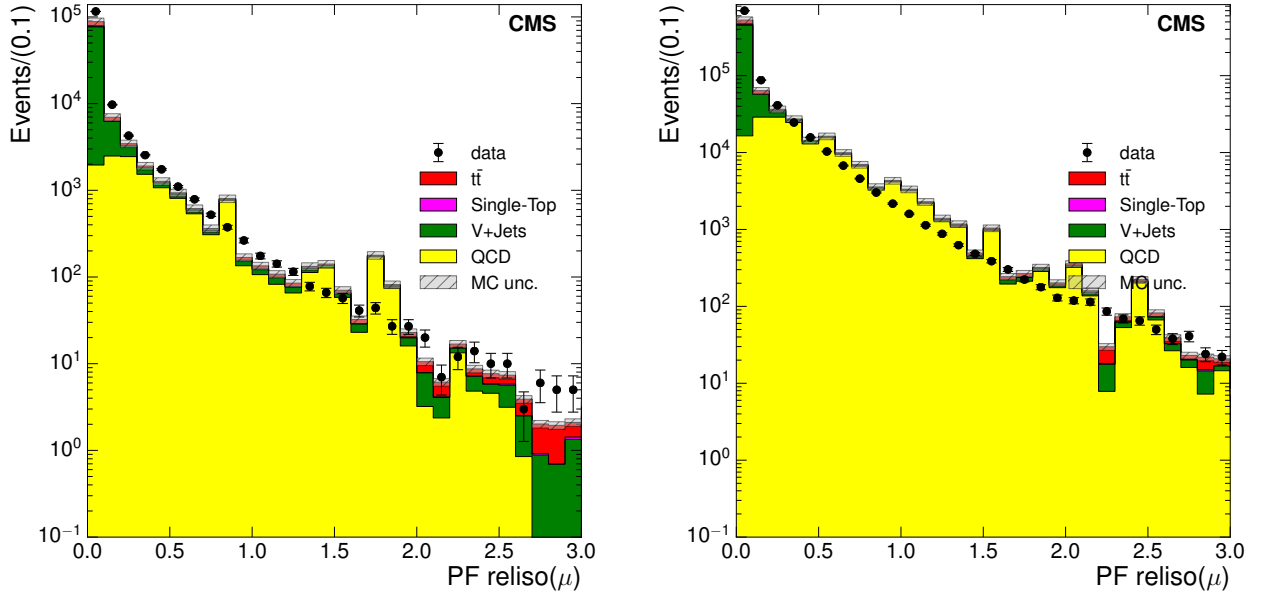


Figure 7.1: PF relative isolation distributions in the muon+jets channel, before subtraction of  $t\bar{t}$ , single top and  $V + \text{jets}$  at  $\sqrt{s} = 7 \text{ TeV}$  (left) and  $\sqrt{s} = 8 \text{ TeV}$  (right).

The true QCD background distribution is a mixture of the conversion and non-isolated distributions. A comparison of the two QCD background selections at  $\sqrt{s} = 7 \text{ TeV}$  and  $\sqrt{s} = 8 \text{ TeV}$  is also shown in the lower plots in Figure 7.2. Background events in which electrons come from jets misreconstructed as electrons or from b-quark or c-quark decays will pass the non-isolated selection, whereas conversion events in which the second electron is not rejected by the electron veto will pass the conversion selection. Another point to note is that, while the general shape of the conversion selection is expected to be the same in both signal and QCD background selections, the same may not be true of the non-isolated selection due to the isolation requirement in the signal selection. In addition, the number of events passing the QCD background selections will be very small compared to the number of events passing the signal selection, so the effect of even large uncertainties in the QCD background on the total number of events will be minimal. In the muon+jets channel, similarly, it is clear that the data and simulation are not in agreement and that there is a low amount of statistics available in simulation.

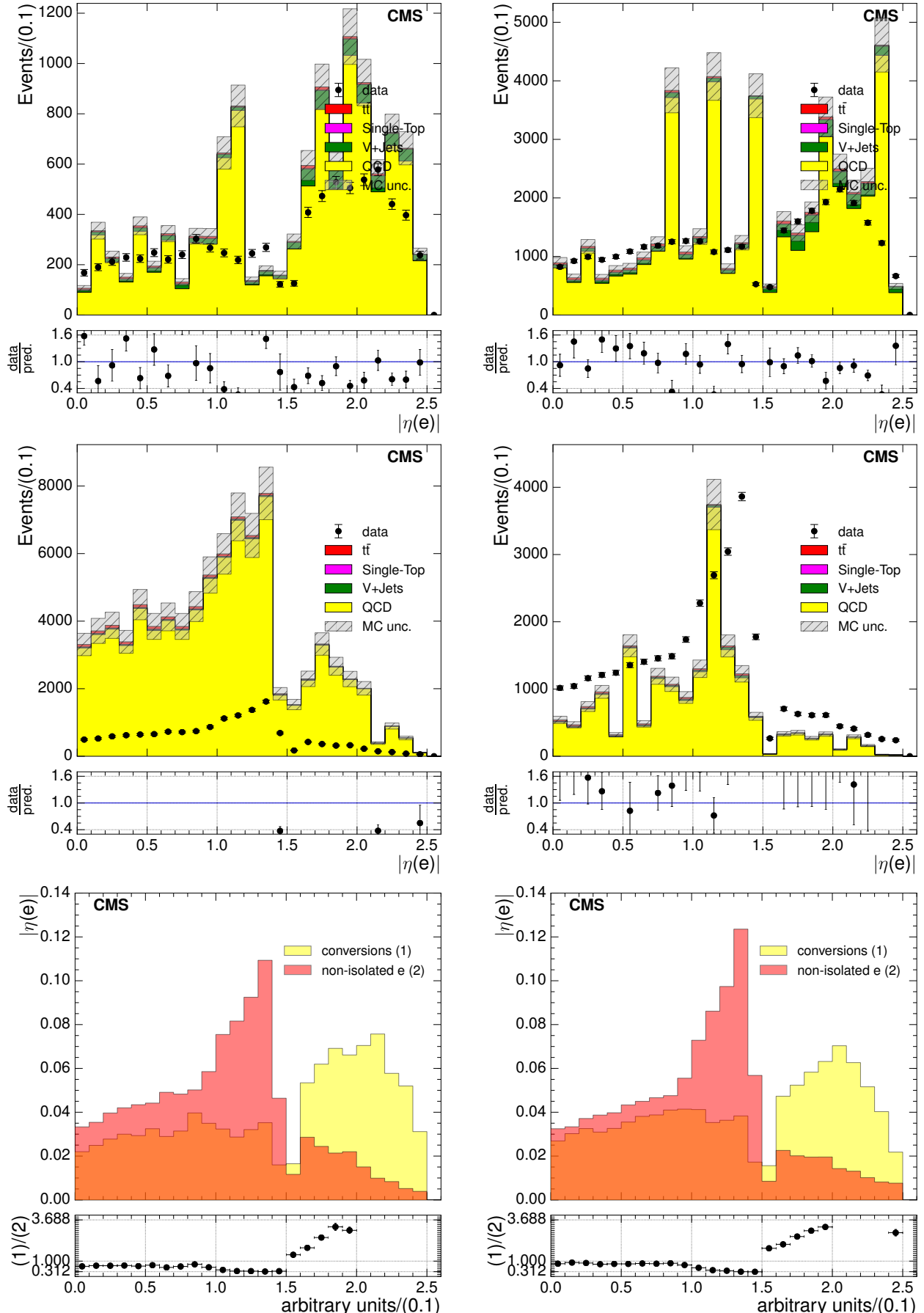


Figure 7.2: Comparison of QCD selections in the electron+jets channel at  $\sqrt{s} = 7$  TeV on the left and at  $\sqrt{s} = 8$  TeV on the right. Conversion region is shown at the top, non-isolated selection in the middle and a comparison of the two selections in data is shown in the lower plots.

## 7.4 Data-MC scale factors

There exist small but significant discrepancies between data and simulation distributions regarding pileup modelling; b tagging; trigger, identification and isolation efficiency; jet energy scale and jet energy resolution, and  $E_T^{\text{miss}}$  calculation. Scale factors and corrections are applied to both MC and data to account for these differences. The data-MC scale factors used are in accordance with the CMS TOP PAG, and the relevant corrections are implemented for 7 TeV and 8 TeV.

### 7.4.1 Pileup

Monte Carlo simulation events are produced by first creating the hard proton-proton interaction of interest in a proton bunch crossing, and then introducing the additional interactions, pileup, are added. The pileup distribution in simulation does not reflect the true distribution in data, therefore pileup reweighting is carried out. The instantaneous luminosity is used to estimate the number of pileup instances in an event at  $\sqrt{s} = 7$  TeV and  $\sqrt{s} = 8$  TeV using a tool provided by the CMS Physics Validation Group. For each number of pileup interactions in simulation, a weight is then produced to match the respective distribution in data.

The estimation of the pileup distribution in data is obtained using the instantaneous luminosity measured in each proton bunch crossing, and the total inelastic proton-proton cross section. There is an uncertainty on the measured luminosity which is currently 2.6% for 2012 data [44] and 2.2% for 2011 data [43]. The total inelastic cross section has been reported using CMS forward calorimetry [32] and by the TOTEM collaboration [20]. Based on these findings, the CMS recommended central values of 68 mb for  $\sqrt{s} = 7$  and 69.3 mb for  $\sqrt{s} = 8$  have been used, with a  $\pm 5\%$  uncertainty to account for pileup and physics modelling in simulation. The distributions of the number of reconstructed vertices before and after applying pileup reweighting in the electron+jets channel is shown in Figure 7.3, and in the muon+jets channel is shown in Figure B.1 in Appendix B.2. The distributions show good agreement

after reweighting.

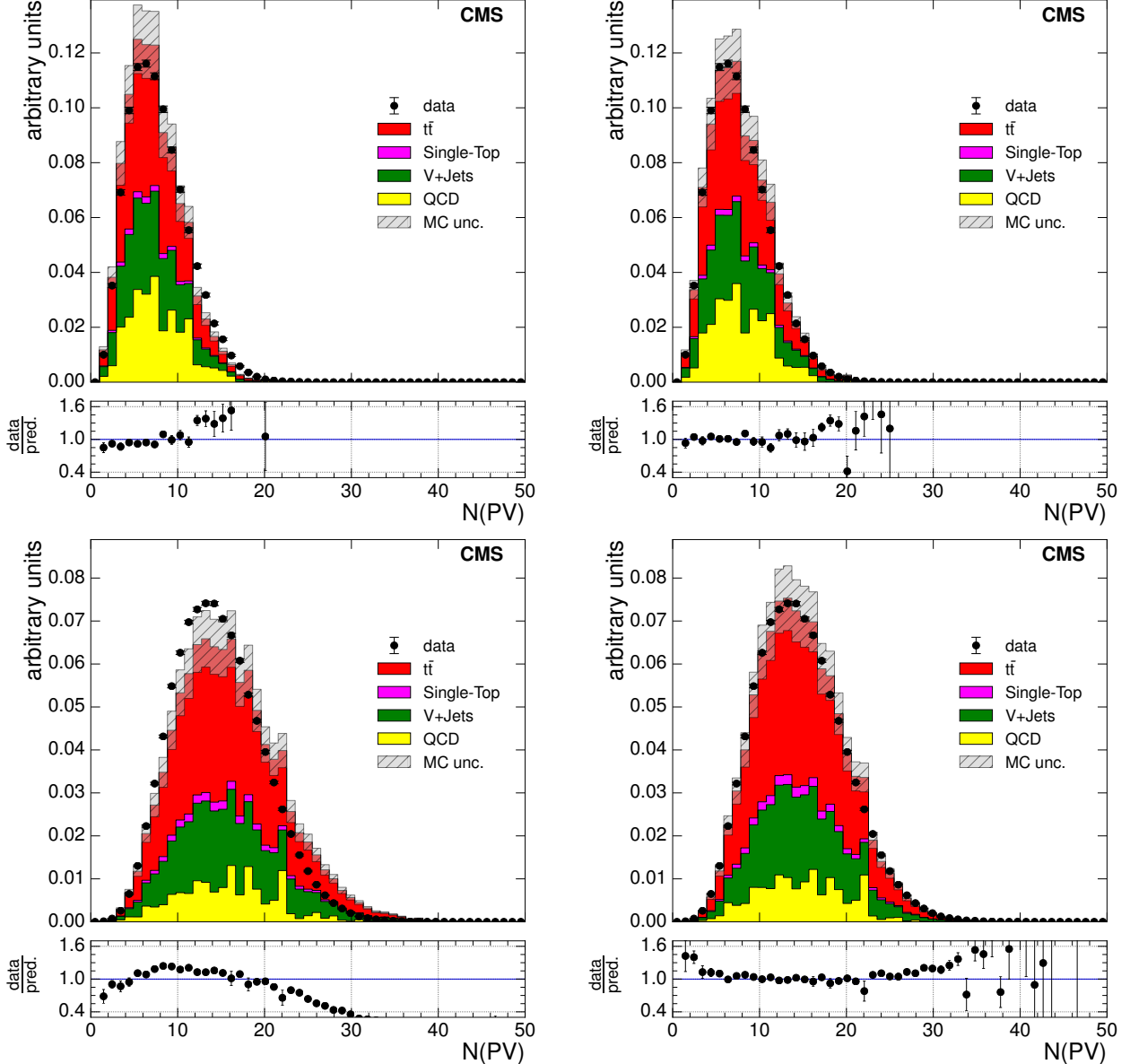


Figure 7.3: Distributions of the number of reconstructed vertices in an event in the electron+jets channel before implementing pileup reweighting (left) and after implementation (right) at  $\sqrt{s} = 7$  TeV (upper) and  $\sqrt{s} = 8$  TeV (lower). Both data and sum of MC simulations are normalised to one.

#### 7.4.2 b-tagging

The combined secondary vertex b-tagging algorithm (CSV) described in Section 3.3.5 is used in this analysis to identify jets originating from b-quarks in  $t\bar{t}$  events. The medium working point, CSVM, which corresponds to a cut on the discriminator output by the algorithm

of 0.679, is used in this analysis. Discrepancies between the b-tagging efficiency in data and Monte Carlo simulation have been noted in  $\sqrt{s} = 7 \text{ TeV}$  [36] and  $\sqrt{s} = 8 \text{ TeV}$  [5]. To account for these differences, events are reweighted based on the recommendation of the CMS b-tagging Physics Object Group (POG), with the aim of ensuring that the probability of an event passing selection criteria in simulation matches the probability of an even in data with the same jet(s) passing the same selection. The result of this reweighting in the electron+jets channel is shown in Figure 7.4, and in the muon+jets channel in Figure B.2 in Appendix B.2 . The b-tagging efficiency uncertainty is evaluated by varying the scale factors by  $\pm 1\sigma$ .

### 7.4.3 Jet Energy Scale

Jet energies are corrected to take into account energy coming from other sources. Level 1 (L1 Pileup) corrections remove energy that comes from pileup collisions, Level 2 (L2 Relative) corrections remove the dependence of jet response on  $\eta$ , and Level 3 (L3 Absolute) corrections correct for the jet response dependence on  $p_T$  [30]. These corrections are applied to both data and Monte Carlo simulation events. An additional residual correction (L2L3Residual) is applied to data only for fine tuning of the agreement between data and simulation.

Furthermore, jet energy resolution corrections are applied (known as jet smearing) to account for the fact that jet energy resolution has been measured to be worse in data than in simulation. These PF jet corrections are provided by the CMS JETMET Physics Object Group using  $0.8 \text{ fb}^{-1}$  of dijet data at  $\sqrt{s} = 7 \text{ TeV}$  [30] and  $19.7 \text{ fb}^{-1}$  of dijet data at  $\sqrt{s} = 8 \text{ TeV}$  [45].

### 7.4.4 Missing Transverse Energy Corrections

The adjustments to the jet energies as a result of the corrections mentioned in Section 7.4.3 in turn affect the distributions of  $E_T^{\text{miss}}$  and  $E_T^{\text{miss}} \phi$  in the event. Corrections known as Type-I  $E_T^{\text{miss}}$  corrections are applied to propagate these changes to the  $E_T^{\text{miss}}$  distributions. In addition, Type-0 corrections are applied to account for pileup interactions in the event,

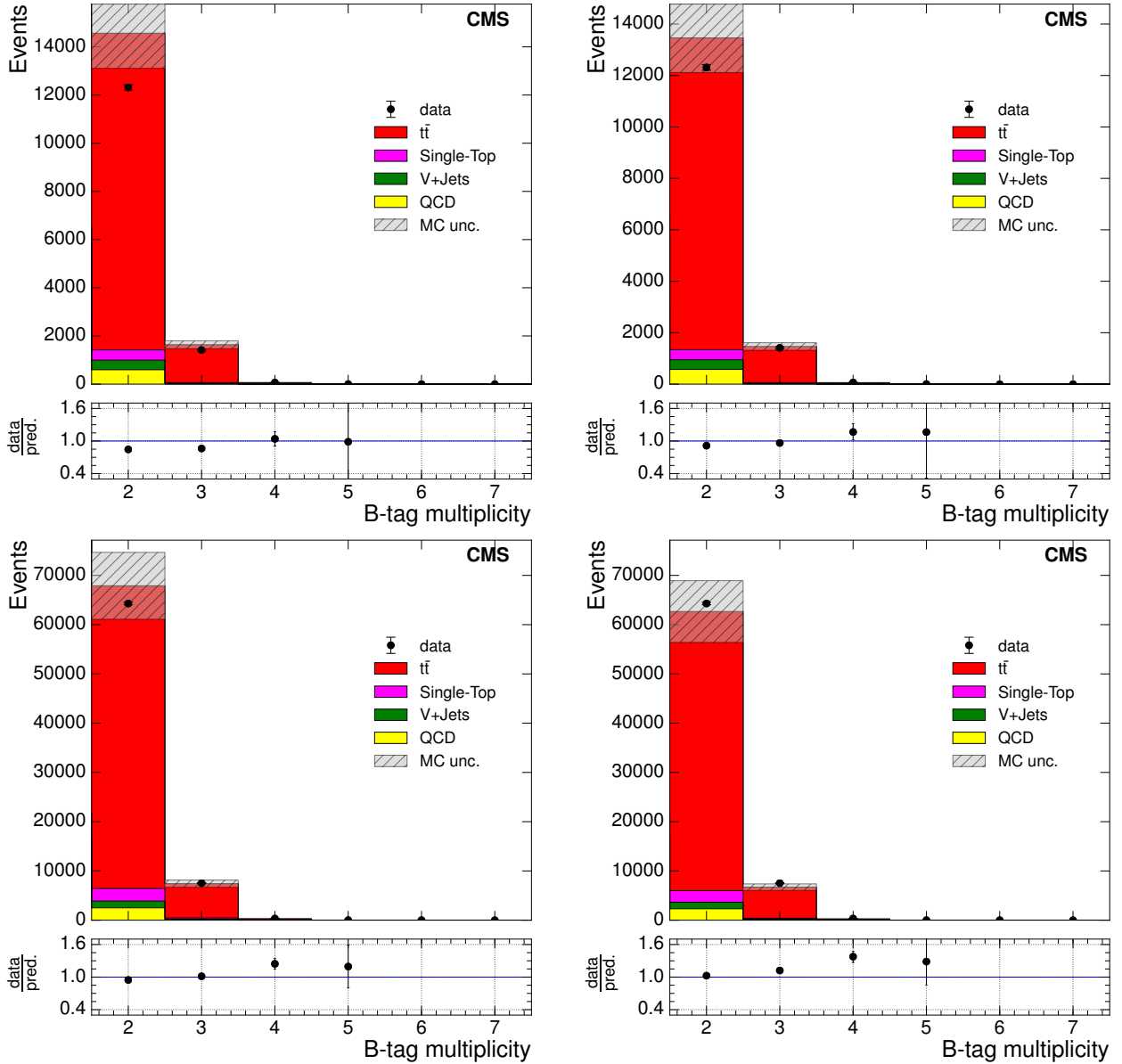


Figure 7.4: Distributions of the number of b-tags in an event in the electron+jets channel before applying b-tag scale factors (left) and after application (right) at  $\sqrt{s} = 7 \text{ TeV}$  (upper) and  $\sqrt{s} = 8 \text{ TeV}$  (lower).

and  $E_T^{\text{miss}} \phi$  corrections are applied to mitigate a known modulation of the  $E_T^{\text{miss}}$  distribution with respect to  $\phi$ .

### 7.4.5 Trigger, Lepton ID and Isolation Efficiencies and Corrections

Corrections are also required for the trigger, identification and isolation efficiencies for muons and electrons. In the muon+jets channel, the corrections were provided by the CMS muon Physics Object Group for  $\sqrt{s} = 8 \text{ TeV}$  TODO:FINDREF (ONLY A TWIKI, WOULD THIS BE OK?) and  $\sqrt{s} = 7 \text{ TeV}$  [6].

For the electron+jets channel, the corrections were provided by the CMS EGamma Physics Object Group for  $\sqrt{s} = 8 \text{ TeV}$ , TODO:FINDREF (ONLY A TWIKI, WOULD THIS BE OK?) however the corrections for the  $\sqrt{s} = 7 \text{ TeV}$  data were not provided and so were derived independently in this analysis using the same tag and probe methods as used by the EGamma POG.

The 7 TeV triggers used (ElectronHad) in this analysis were not present in the 7 TeV simulation, and so the trigger efficiency was calculated with respect to the full selection. This efficiency was then implemented in the Monte Carlo simulation, thereby imitating the trigger. It should be noted that it is assumed that the electron and hadron legs of the trigger are not correlated, since electrons are cleaned from the jet collection at HLT level.

A tag and probe method [31] was used to derive identification, isolation scale factors and electron trigger efficiencies. The full reference selection was first applied with the exception of trigger, b-tagging and electron veto requirements, while in addition, a second loose electron was required. A Z mass constraint was placed on the two electrons in the event by requiring them to have an invariant mass of between 60 GeV and 120 GeV, thus ensuring that the pair of electrons originated from a Z boson decay. The tight ('tag') electron requirements were  $p_T > 30 \text{ GeV}$ ,  $|\eta| < 0.8$ , relative isolation  $< 0.1$ , MVA identification  $> 0.9$ ,  $d_{xy} < 0.02 \text{ cm}$  and reconstructed at HLT level. The loose ('probe') electron requirements were  $p_T > 30 \text{ GeV}$ ,  $|\eta| < 2.5$  and  $d_{xy} < 2 \text{ cm}$ .

Fits were then performed, firstly of the invariant mass of all pairs of tag and probe electrons, and secondly after applying the identification and isolation criteria to the probe electrons, to the invariant mass distribution of pairs of tag and probe electrons in which the probe electron passed the identification and isolation criteria. The fit was implemented in both Monte Carlo simulation and in data, and a Breit-Wigner distribution convoluted with a Crystal Ball function is used to model the invariant mass of the tag and probe electrons, with a falling exponential used to model the background distribution. The Breit-Wigner distribution takes a form similar to that of a Gaussian distribution, with flatter tails [24]. The Crystal Ball function is also based on a Gaussian distribution, but with a power-law tail to the lower end [82, 58, 88]. Both of these functions are commonly used to model the mass peaks of resonances. The result of this fitting procedure in data can be seen in Figure 7.5.

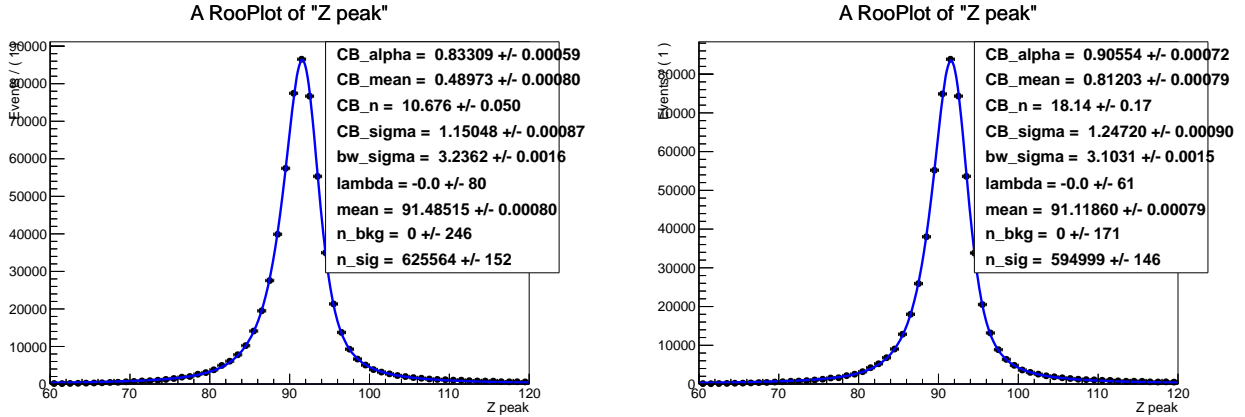


Figure 7.5: Fits of the invariant mass distribution of all tag-and-probe pairs (left) and tag-and-probe pairs in which the probe satisfies the identification and isolation criteria (right).

The efficiency of the identification and isolation process is then calculated using the numbers extracted from the fits, in bins of  $p_T$  and  $\eta$  of the probe electron, as follows:

$$\epsilon(\text{identification and isolation}) = \frac{N_{\text{probe, passing}}^{\text{fit}}}{N_{\text{probe, all}}^{\text{fit}}} \quad (7.1)$$

where  $N_{\text{probe, all}}^{\text{fit}}$  is the total number of events with tag and probe electrons and  $N_{\text{probe, passing}}^{\text{fit}}$  is the subset in which the probe passes identification and isolation criteria.

The scale factor is then calculated as the ratio between the efficiencies in simulation and in data. The efficiencies in both can be seen to be similar in Figure 7.6, leading to scale factors close to one.

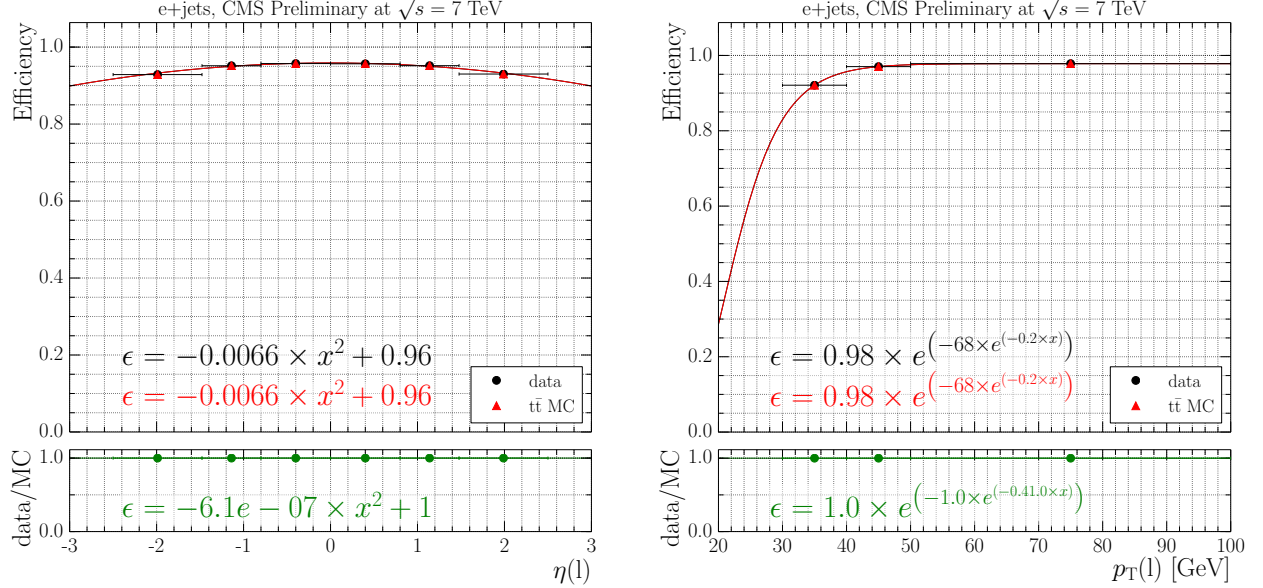


Figure 7.6: Identification and isolation efficiencies as a function of  $\eta$  and  $p_T$  in data and  $t\bar{t}$  Monte Carlo simulation.

The efficiency of the electron part of the trigger is then similarly calculated, with respect to the identification and isolation requirements, meaning the events passing the identification and isolation requirements in the previous stage are then used as the baseline for the trigger efficiency. The subset of these in which the probe electron matches a HLT electron is then used to calculate the efficiency as follows:

$$\epsilon(\text{trigger}) = \frac{N_{\text{probe, matching HLT}}^{\text{fit}}}{N_{\text{probe, identification and isolation}}^{\text{fit}}} \quad (7.2)$$

where  $N_{\text{probe, identification and isolation}}^{\text{fit}}$  is the number of events passing from equation 7.2 and  $N_{\text{probe, matching HLT}}^{\text{fit}}$  is the subset in which the probe is matched to an HLT electron object.

In order to calculate the efficiency of the hadron leg of the trigger, the full selection with only the electron part of the trigger and without b-tagging, applied to the SingleElectron dataset, is taken as the baseline. The number of these events passing the hadronic leg of the

trigger is then used to calculate the hadronic leg efficiency as follows:

$$\epsilon(\text{hadron leg}) = \frac{N_{\text{hadron leg, passing}}}{N_{\text{passing selection}}} \quad (7.3)$$

where  $N_{\text{passing selection}}$  is the number of events passing the baseline selection with the electron leg of the trigger and no b-tagging requirements, and  $N_{\text{hadron leg, passing}}$  is the subset in which the hadron leg of the trigger is satisfied.

The scale factors are produced in bins of  $p_T$  and  $\eta$  of the fourth most energetic jet, since this is the lowest energy jet that is selected. Parametrising as a function of higher energy jets would lead to a bias towards high efficiencies as the trigger will have a higher efficiency at higher jet energies.

Equivalent fit and efficiency plots for the trigger are included in Figures B.3 and B.4 in Appendix B.2. TODO:HAVE NOT INCLUDED MUON ID-ISO OR TRIGGER PLOTS ANYWHERE, ASSUMING OK WITH JUST ELECTRON PLOTS.

Table 7.4: 7 TeV Monte Carlo background datasets used for this analysis. All samples are generated inclusively if not marked otherwise (\* generator cut on in-flight-decays of b- and c-hadrons,  $\ominus$  enriched in conversion electrons;  $l$  means all leptonic decays:  $l = e, \mu, \tau$ ;  $\bullet$  generator cut on  $m_{Z/\gamma} > 50$  GeV).

Process	Generator	$\sigma$ ( pb)	No. events	$\mathcal{L}_{\text{int}}$ ( $\text{fb}^{-1}$ )
Single $\tilde{t}$ -channel ( $W \rightarrow l\nu$ )	POWHEG	64.6	3249530	50.3
Single $\bar{t} t$ -channel ( $W \rightarrow l\nu$ )	POWHEG	64.6	1813615	28.1
Single $\tilde{s}$ -channel ( $W \rightarrow l\nu$ )	POWHEG	4.21	229786	54.6
Single $\bar{t} s$ -channel ( $W \rightarrow l\nu$ )	POWHEG	4.21	138187	32.8
Single $\tilde{t}W$ -channel ( $W \rightarrow l\nu$ )	POWHEG	10.6	744859	70.3
Single $\bar{t} tW$ -channel ( $W \rightarrow l\nu$ )	POWHEG	10.6	801626	75.6
$W (\rightarrow l\nu) + 1$ Jet	MADGRAPH	4480.0	70430949	15.7
$W (\rightarrow l\nu) + 2$ Jets	MADGRAPH	1435.0	25069566	17.5
$W (\rightarrow l\nu) + 3$ Jets	MADGRAPH	304.2	6291772	20.7
$W (\rightarrow l\nu) + 4$ Jets	MADGRAPH	172.6	13240209	76.7
$Z/\gamma^* (\rightarrow l^+l^-) + \text{jets } \bullet$	MADGRAPH	3048	32846945	10.8
QCD BCtoE $p_T$ 20-30 *	PYTHIA	139299.0	1927944	$1.4 \times 10^{-2}$
QCD BCtoE $p_T$ 30-80 *	PYTHIA	143844.8	1946505	$1.4 \times 10^{-2}$
QCD BCtoE $p_T$ 80-170 *	PYTHIA	9431.1	1002427	0.1
QCD EM $p_T$ 20-30 $\ominus$	PYTHIA	2502660.0	32976415	$1.3 \times 10^{-2}$
QCD EM $p_T$ 30-80 $\ominus$	PYTHIA	3625840.0	71775065	$2.0 \times 10^{-2}$
QCD EM $p_T$ 80-170 $\ominus$	PYTHIA	142813.8	7650319	$5.4 \times 10^{-2}$
QCD EM $p_T$ 170-250 $\ominus$	PYTHIA	142813.8	2968842	$2.1 \times 10^{-2}$
QCD EM $p_T$ 250-350 $\ominus$	PYTHIA	368.0	2952960	8.0
QCD EM $p_T$ 350-inf $\ominus$	PYTHIA	55.0	2957326	53.8
$\gamma + \text{Jets HT } 40\text{-}100$	MADGRAPH	25690.0	9882860	0.4
$\gamma + \text{Jets HT } 100\text{-}200$	MADGRAPH	5213.0	1514347	0.3
$\gamma + \text{Jets HT } > 200$	MADGRAPH	798.3	9275592	11.6
QCD $\mu$ enriched $p_T$ 15-20	PYTHIA	1668096.0	1901684	$1.1 \times 10^{-3}$
QCD $\mu$ enriched $p_T$ 20-30	PYTHIA	1342184.0	10173300	$7.6 \times 10^{-3}$
QCD $\mu$ enriched $p_T$ 30-50	PYTHIA	596506.8	11610111	$1.9 \times 10^{-2}$
QCD $\mu$ enriched $p_T$ 50-80	PYTHIA	140039.55	9870031	$7.0 \times 10^{-2}$
QCD $\mu$ enriched $p_T$ 80-120	PYTHIA	28546.2	9769136	0.3
QCD $\mu$ enriched $p_T$ 120-170	PYTHIA	4692.91	7818474	1.7
QCD $\mu$ enriched $p_T$ 170-300	PYTHIA	1445.96	8116409	5.6
QCD $\mu$ enriched $p_T$ 300-470	PYTHIA	95.4464	7870002	82.5
QCD $\mu$ enriched $p_T$ 470-600	PYTHIA	7.41697	3812529	514.0
QCD $\mu$ enriched $p_T$ 600-800	PYTHIA	1.69145	4149911	2453.5
QCD $\mu$ enriched $p_T$ 800-1000	PYTHIA	0.231869	4036867	17410.1
QCD $\mu$ enriched $p_T$ 1000-inf	PYTHIA	0.053385	4133897	77435.6

Table 7.5: 7 TeV Monte Carlo systematic datasets used for this analysis. All samples are produced with the MADGRAPH generator. W + jets and Z + jets samples were not available and so have been scaled from available 8 TeV samples.

Process	Variation	Generator	$\sigma$ ( pb)	No. events	$\mathcal{L}_{\text{int}}$ ( $\text{fb}^{-1}$ )
t̄t 0.5×Q <sup>2</sup> (normalisation & factorisation scale down)	MADGRAPH 177.31		9426377		53.2
t̄t 2×Q <sup>2</sup> (normalisation & factorisation scale up)		MADGRAPH 177.31	10095984		56.9
t̄t 0.5× matching threshold (down)		MADGRAPH 177.31	4056487		22.9
t̄t 2× matching threshold (up)		MADGRAPH 177.31	16727257		94.3
t̄t 0.5× mass uncertainty (down)		MADGRAPH 177.31	4560762		25.7
t̄t 2× mass uncertainty (up)		MADGRAPH 177.31	9151264		51.6
W + jets 0.5×Q <sup>2</sup> (scale down)		MADGRAPH 31314	20121177		0.6
W + jets 2×Q <sup>2</sup> (scale up)		MADGRAPH 31314	20711338		0.7
W + jets 0.5× matching threshold (matching down)		MADGRAPH 31314	21341479		0.7
W + jets 2× matching threshold (matching up)		MADGRAPH 31314	20594331		0.7
Z + jets 0.5×Q <sup>2</sup> (scale down)		MADGRAPH 3048.0	1934895		0.6
Z + jets 2×Q <sup>2</sup> (scale up)		MADGRAPH 3048.0	2159410		0.7
Z + jets 0.5× matching threshold (matching down)		MADGRAPH 3048.0	2112383		0.7
Z + jets 2× matching threshold (matching up)		MADGRAPH 3048.0	1985526		0.7

Table 7.6: 8 TeV Monte Carlo signal datasets used for this analysis.

Process	Generator	$\sigma$ ( pb)	No. events	$\mathcal{L}_{\text{int}}$ ( $\text{fb}^{-1}$ )
t̄t	MADGRAPH	252.89	6706068	26.5
t̄t	MC@NLO	252.89	32852517	129.9
t̄t	POWHEG-PYTHIA	252.89	21675913	85.7
t̄t	POWHEG-HERWIG	252.89	27684194	109.5

Table 7.7: 8 TeV Monte Carlo background datasets used for this analysis. All samples are generated inclusively if not marked otherwise (\* generator cut on in-flight-decays of b- and c-hadrons,  $\ominus$  enriched in conversion electrons;  $l$  means all leptonic decays:  $l = e, \mu, \tau$ ; • generator cut on  $m_{Z/\gamma} > 50$  GeV).

Process	Generator	$\sigma$ ( pb)	No. events	$\mathcal{L}_{\text{int}}$ ( $\text{fb}^{-1}$ )
Single $t\bar{t}$ -channel ( $W \rightarrow l\nu$ )	POWHEG	55.531	3758221	67.7
Single $t\bar{t}$ t-channel ( $W \rightarrow l\nu$ )	POWHEG	30.0042	1906041	63.5
Single $s\bar{s}$ -channel ( $W \rightarrow l\nu$ )	POWHEG	3.89394	259960	66.8
Single $t\bar{t}$ s-channel ( $W \rightarrow l\nu$ )	POWHEG	1.75776	139974	79.6
Single $t\bar{t}W$ -channel ( $W \rightarrow l\nu$ )	POWHEG	11.1773	497657	44.5
Single $t\bar{t}$ tW-channel ( $W \rightarrow l\nu$ )	POWHEG	11.1773	473721	42.4
$W (\rightarrow l\nu) + 1$ Jet	MADGRAPH	5400.0	23129996	15.7
$W (\rightarrow l\nu) + 2$ Jets	MADGRAPH	1750.0	34027847	17.5
$W (\rightarrow l\nu) + 3$ Jets	MADGRAPH	519.0	15539463	20.7
$W (\rightarrow l\nu) + 4$ Jets	MADGRAPH	214.0	13373865	76.7
$Z/\gamma^* (\rightarrow l^+l^-) + 1$ jet•	MADGRAPH	561.0	24032529	42.8
$Z/\gamma^* (\rightarrow l^+l^-) + 2$ jets•	MADGRAPH	181.0	21840628	0.1
$Z/\gamma^* (\rightarrow l^+l^-) + 3$ jets•	MADGRAPH	51.1	10819603	0.2
$Z/\gamma^* (\rightarrow l^+l^-) + 4$ jets•	MADGRAPH	23.04	6381467	0.3
QCD BCtoE $p_T$ 20-30 *	PYTHIA	167388.0	1731522	$1.0 \times 10^{-2}$
QCD BCtoE $p_T$ 30-80 *	PYTHIA	167040.0	2037907	$1.2 \times 10^{-2}$
QCD BCtoE $p_T$ 80-170 *	PYTHIA	12981.9	1945523	0.1
QCD BCtoE $p_T$ 170-250 *	PYTHIA	632.0	1948112	3.1
QCD BCtoE $p_T$ 250-350 *	PYTHIA	103.3	2026516	19.6
QCD BCtoE $p_T$ 350-inf *	PYTHIA	23.9	1948525	81.5
QCD EM $p_T$ 20-30 $\ominus$	PYTHIA	2914860.0	34830398	$1.2 \times 10^{-2}$
QCD EM $p_T$ 30-80 $\ominus$	PYTHIA	4615893.0	32443607	$7.0 \times 10^{-3}$
QCD EM $p_T$ 80-170 $\ominus$	PYTHIA	183294.9	34024542	0.2
QCD EM $p_T$ 170-250 $\ominus$	PYTHIA	4586.5	31696985	6.9
QCD EM $p_T$ 250-350 $\ominus$	PYTHIA	556.7	33659467	60.5
QCD EM $p_T$ 350-inf $\ominus$	PYTHIA	89.1	33756727	378.8
$\gamma + \text{Jets HT } 200\text{-}400$	MADGRAPH	960.5	47316433	49.3
$\gamma + \text{Jets HT } 400\text{-inf}$	MADGRAPH	107.5	9491846	88.3
QCD $\mu$ enriched $p_T$ 15-20	PYTHIA	2738580.0	1722678	$0.6 \times 10^{-3}$
QCD $\mu$ enriched $p_T$ 20-30	PYTHIA	1865500.0	8486893	$4.5 \times 10^{-3}$
QCD $\mu$ enriched $p_T$ 30-50	PYTHIA	806298.0	9560248	$1.2 \times 10^{-2}$
QCD $\mu$ enriched $p_T$ 50-80	PYTHIA	176187.6	10365209	$5.9 \times 10^{-2}$
QCD $\mu$ enriched $p_T$ 80-120	PYTHIA	40448.0	9238622	0.2
QCD $\mu$ enriched $p_T$ 120-170	PYTHIA	7463.94	8501920	1.1
QCD $\mu$ enriched $p_T$ 170-300	PYTHIA	2299.752	7669932	3.3
QCD $\mu$ enriched $p_T$ 300-470	PYTHIA	151.8048	7832248	51.6
QCD $\mu$ enriched $p_T$ 470-600	PYTHIA	11.79648	3783066	320.7
QCD $\mu$ enriched $p_T$ 600-800	PYTHIA	2.690196	4118988	1531.1
QCD $\mu$ enriched $p_T$ 800-1000	PYTHIA	0.3687810	4099633	11116.7
QCD $\mu$ enriched $p_T$ 1000-inf	PYTHIA	0.0849078	9238622	108807.7

Table 7.8: 8 TeV Monte Carlo systematic datasets used for this analysis. All samples are produced with the MADGRAPH generator.

Process	Variation	Generator	$\sigma$ ( pb)	No. events	$\mathcal{L}_{\text{int}}$ ( $\text{fb}^{-1}$ )
$t\bar{t}$ $0.5 \times Q^2$ (normalisation & factorisation scale down)	MADGRAPH 252.89		5387169		21.3
$t\bar{t}$ $2 \times Q^2$ (normalisation & factorisation scale up)	MADGRAPH 252.89		5009481		19.8
$t\bar{t}$ $0.5 \times$ matching threshold (down)	MADGRAPH 252.89		5476715		21.7
$t\bar{t}$ $2 \times$ matching threshold (up)	MADGRAPH 252.89		5415003		21.4
$t\bar{t}$ $0.5 \times$ mass uncertainty (down)	MADGRAPH 252.89		39423535		155.9
$t\bar{t}$ $2 \times$ mass uncertainty (up)	MADGRAPH 252.89		26488957		104.7
W + jets $0.5 \times Q^2$ (scale down)	MADGRAPH 36257.2		20121177		0.6
W + jets $2 \times Q^2$ (scale up)	MADGRAPH 36257.2		20711338		0.6
W + jets $0.5 \times$ matching threshold (down)	MADGRAPH 36257.2		21341479		0.6
W + jets $2 \times$ matching threshold (up)	MADGRAPH 36257.2		20594331		0.6
Z + jets $0.5 \times Q^2$ (scale down)	MADGRAPH 3503.71		1934895		0.6
Z + jets $2 \times Q^2$ (scale up)	MADGRAPH 3503.71		2159410		0.6
Z + jets $0.5 \times$ matching threshold (down)	MADGRAPH 3503.71		2112383		0.6
Z + jets $2 \times$ matching threshold (up)	MADGRAPH 3503.71		1985526		0.6

# 8 | 7 TeV and 8 TeV Differential Cross Section Measurement: Fitting, Unfolding and Measurement

## 8.1 Data-MC Comparison

Following the full event selection, the simulated events are scaled to match the luminosity of the data using the scale factor:

$$S = \frac{\mathcal{L} \times \sigma}{N_{\text{processed}}} \quad (8.1)$$

where  $N_{\text{processed}}$  is the total number of events processed for each Monte Carlo sample and  $\sigma$  is the production cross section of each process. The numbers of events passing each selection step in data and in Monte Carlo simulation, after scaling to the measured luminosity, are shown for both the electron+jets and muon+jets channels in Table 8.1 at  $\sqrt{s} = 7 \text{ TeV}$ , and in Table 8.2 at  $\sqrt{s} = 8 \text{ TeV}$ .

The distributions of the primary variables  $E_T^{\text{miss}}$ ,  $H_T$ ,  $S_T$ ,  $p_T^W$  and  $M_T^W$  after the full selection requirements are applied are shown in Figures 8.1 and 8.2 for the electron and muon channels respectively at  $\sqrt{s} = 7 \text{ TeV}$ ; and in Figures 8.3 and 8.4 respectively at  $\sqrt{s} = 8 \text{ TeV}$ . The normalisations and shapes are all obtained from simulation except in the case of QCD which is taken from data: the conversion region is used in the electron channel and the

Table 8.1: Expected and observed event yields at several stages of the electron+jets selection (upper) and the muon+jets channel selection(lower) at  $\sqrt{s}=7$  TeV.

Selection step	t̄t + jets	W + jets	Z + jets	Single-Top	QCD	Sum MC	Data
Preselection	248837 ± 131	296487 ± 255	87027 ± 237	26397 ± 43	24578753 ± 81165	25237503 ± 81166	4928736
Event cleaning/HLT	248712 ± 131	296343 ± 255	86964 ± 237	26385 ± 43	24574668 ± 81161	25233075 ± 81162	1103841
One isolated electron	70973 ± 69	91618 ± 132	26311 ± 122	5355 ± 17	263313 ± 6601	457572 ± 6604	299020
Muon veto	67163 ± 67	91581 ± 132	26196 ± 122	5269 ± 17	263195 ± 6601	453405 ± 6604	295961
Dilepton veto	66336 ± 67	91559 ± 132	20560 ± 107	5251 ± 17	263183 ± 6601	446892 ± 6603	289456
Conversion veto	64497 ± 66	87866 ± 130	19671 ± 105	5106 ± 16	174315 ± 5761	351458 ± 5763	243472
≥ 1 jets	64497 ± 66	87866 ± 130	19671 ± 105	5106 ± 16	174315 ± 5761	351457 ± 5763	243471
≥ 2 jets	64489 ± 66	87789 ± 130	19633 ± 105	5104 ± 16	173680 ± 5748	350697 ± 5750	243446
≥ 3 jets	63514 ± 65	82167 ± 123	18188 ± 101	4912 ± 16	126305 ± 4416	295088 ± 4420	236124
≥ 4 jets	35285 ± 48	17935 ± 42	3618 ± 45	1461 ± 8	21354 ± 1507	79656 ± 1509	71414
≥ 1 b-tagged jets	29777 ± 44	2764 ± 17	562 ± 17	1160 ± 7	3601 ± 513	37864 ± 516	34671
≥ 2 b-tagged jets	13777 ± 30	326 ± 4	76 ± 6	434 ± 4	590 ± 220	15205 ± 222	13792
Selection step	t̄t + jets	W + jets	Z + jets	Single-Top	QCD	Sum MC	Data
Preselection	248280 ± 131	296599 ± 255	87128 ± 237	26362 ± 43	18658866 ± 41697	19317237 ± 41699	4201249
Event cleaning/HLT	248155 ± 131	296455 ± 255	87065 ± 237	26350 ± 43	18655836 ± 41690	19313864 ± 41692	444679
One isolated muon	74418 ± 71	93902 ± 132	22774 ± 115	5724 ± 19	45516 ± 2160	242336 ± 2168	206738
Second muon veto	73036 ± 70	93893 ± 132	14109 ± 89	5690 ± 19	44741 ± 2153	231470 ± 2161	194980
Electron veto	69681 ± 69	93852 ± 132	14020 ± 89	5615 ± 19	44666 ± 2153	227835 ± 2160	192335
≥ 1 jets	69680 ± 69	93851 ± 132	14020 ± 89	5615 ± 19	44648 ± 2153	227816 ± 2160	192335
≥ 2 jets	69675 ± 69	93791 ± 132	14007 ± 89	5613 ± 19	43404 ± 2139	226492 ± 2146	192310
≥ 3 jets	69054 ± 68	89508 ± 126	13186 ± 86	5455 ± 18	14627 ± 1059	191831 ± 1072	186061
≥ 4 jets	38222 ± 50	19234 ± 42	2707 ± 38	1573 ± 8	2028 ± 242	63766 ± 254	54684
≥ 1 b-tagged jets	32268 ± 46	2965 ± 16	463 ± 15	1250 ± 7	873 ± 148	37821 ± 157	30852
≥ 2 b-tagged jets	15016 ± 30	355 ± 5	60 ± 5	468 ± 4	180 ± 48	16081 ± 58	13128

Table 8.2: Expected and observed event yields at several stages of the electron+jets selection (upper) and the muon+jets selection (lower) at  $\sqrt{s}=8$  TeV.

Selection step	t̄t + jets	W + jets	Z + jets	Single-Top	QCD	Sum MC	Data
Preselection	1389239 ± 1071	1748404 ± 1149	385132 ± 236	170598 ± 265	131270649 ± 477929	134964023 ± 477932	13219192
Event cleaning/HLT	376950 ± 547	493785 ± 573	143253 ± 138	35559 ± 122	3844108 ± 83191	4893656 ± 83195	5952438
One isolated electron	335908 ± 515	427471 ± 520	95501 ± 111	31520 ± 115	554050 ± 27723	1444453 ± 27733	1754243
Muon veto	316823 ± 500	427354 ± 520	95069 ± 111	30820 ± 113	553991 ± 27723	1424058 ± 27733	1733585
Dilepton veto	312321 ± 497	427247 ± 520	70836 ± 96	30648 ± 113	553952 ± 27723	1395005 ± 27733	1692425
Conversion veto	304300 ± 490	411661 ± 510	68005 ± 94	29849 ± 111	309968 ± 20284	1123785 ± 20297	1447105
≥ 1 jets	304300 ± 490	411658 ± 510	68005 ± 94	29849 ± 111	309968 ± 20284	1123781 ± 20297	1447105
≥ 2 jets	304264 ± 490	411028 ± 510	67901 ± 94	29834 ± 111	307974 ± 20200	1121003 ± 20213	1446970
≥ 3 jets	299232 ± 486	372483 ± 472	61904 ± 87	28518 ± 109	226054 ± 16034	988193 ± 16049	1251530
≥ 4 jets	172557 ± 369	76326 ± 175	13484 ± 35	9524 ± 64	43901 ± 4145	315795 ± 4165	361692
≥ 1 b-tagged jets	142836 ± 332	10417 ± 65	2019 ± 13	7296 ± 55	8705 ± 1812	171275 ± 1845	181705
≥ 2 b-tagged jets	63233 ± 215	1114 ± 21	291 ± 4	2566 ± 32	2427 ± 1660	69632 ± 1675	72176
Selection step	t̄t + jets	W + jets	Z + jets	Single-Top	QCD	Sum MC	Data
Preselection	1400798 ± 1080	1765900 ± 1159	389320 ± 239	171677 ± 266	104820777 ± 238065	108548474 ± 238070	20815265
Event cleaning/HLT	469828 ± 622	669486 ± 711	153379 ± 147	46228 ± 141	1673119 ± 33684	3012042 ± 33698	3166723
One isolated muon	385092 ± 562	496720 ± 582	92752 ± 111	37012 ± 126	89801 ± 6391	1101379 ± 6444	1373749
Second muon veto	377038 ± 556	496660 ± 582	54606 ± 85	36705 ± 126	89060 ± 6380	1054070 ± 6433	1292713
Electron veto	358624 ± 542	496506 ± 582	54260 ± 85	36049 ± 124	89037 ± 6380	1034478 ± 6431	1274884
≥ 1 jets	358624 ± 542	496498 ± 582	54259 ± 85	36049 ± 124	89037 ± 6380	1034470 ± 6431	1274884
≥ 2 jets	358592 ± 542	495658 ± 581	54186 ± 85	36029 ± 124	88048 ± 6354	1032515 ± 6405	1274817
≥ 3 jets	354271 ± 539	448652 ± 534	49426 ± 78	34498 ± 122	34560 ± 2810	921409 ± 2914	1138923
≥ 4 jets	202771 ± 407	90874 ± 199	10999 ± 32	11233 ± 71	8003 ± 1304	323883 ± 1383	351087
≥ 1 b-tagged jets	168125 ± 367	12499 ± 73	1715 ± 12	8660 ± 61	4252 ± 1036	195253 ± 1104	197025
≥ 2 b-tagged jets	74995 ± 238	1367 ± 23	229 ± 4	3023 ± 35	527 ± 410	80143 ± 476	81047

non-isolated region is used in the muon channel. In general there is good agreement between data and simulation. The distributions in simulation peak at slightly higher energies because event reweighting to account for the  $p_T$  mismodelling of the top quark in simulation (see Section 9.1.2) has not yet been carried out at this stage.

## 8.2 Binning Choice

The different cross sections in this analysis are measured in bins of the primary variable distributions. The choice of bin sizes and boundaries are significant because events generated in one bin can migrate to another bin after reconstruction due to the finite resolution of the detector. This altering of the number of events, as a result of events moving into, or out of, a bin is important to understand so that the final reconstructed distribution can be deconvoluted (unfolded) to the true distribution. In light of this, the binning choice is made based on two variables defined as purity ( $p^k$ ) and stability ( $s^k$ ):

$$p^k = \frac{N_{\text{rec}\&\text{gen}}^k}{N_{\text{rec}}^k} \quad (8.2)$$

$$s^k = \frac{N_{\text{rec}\&\text{gen}}^k}{N_{\text{gen}}^k}. \quad (8.3)$$

$N_{\text{rec}\&\text{gen}}^k$  is the number of events generated and reconstructed in bin  $k$ ,  $N_{\text{rec}}^k$  is the number of events reconstructed in bin  $k$  and  $N_{\text{gen}}^k$  is the number of events generated in bin  $k$ . The stability of a bin is sensitive to the migration of events out of a bin, while the purity is sensitive to the migration of events into a bin (see Figure 8.5).

In this analysis, the bins for each primary variable distribution were chosen such that all bins have purity and stability values of 0.5 or greater, meaning that at least half of the events generated in a bin remain in that bin after reconstruction, and that at least half of the events reconstructed in a bin were generated in that bin. In order to avoid very small bins with a

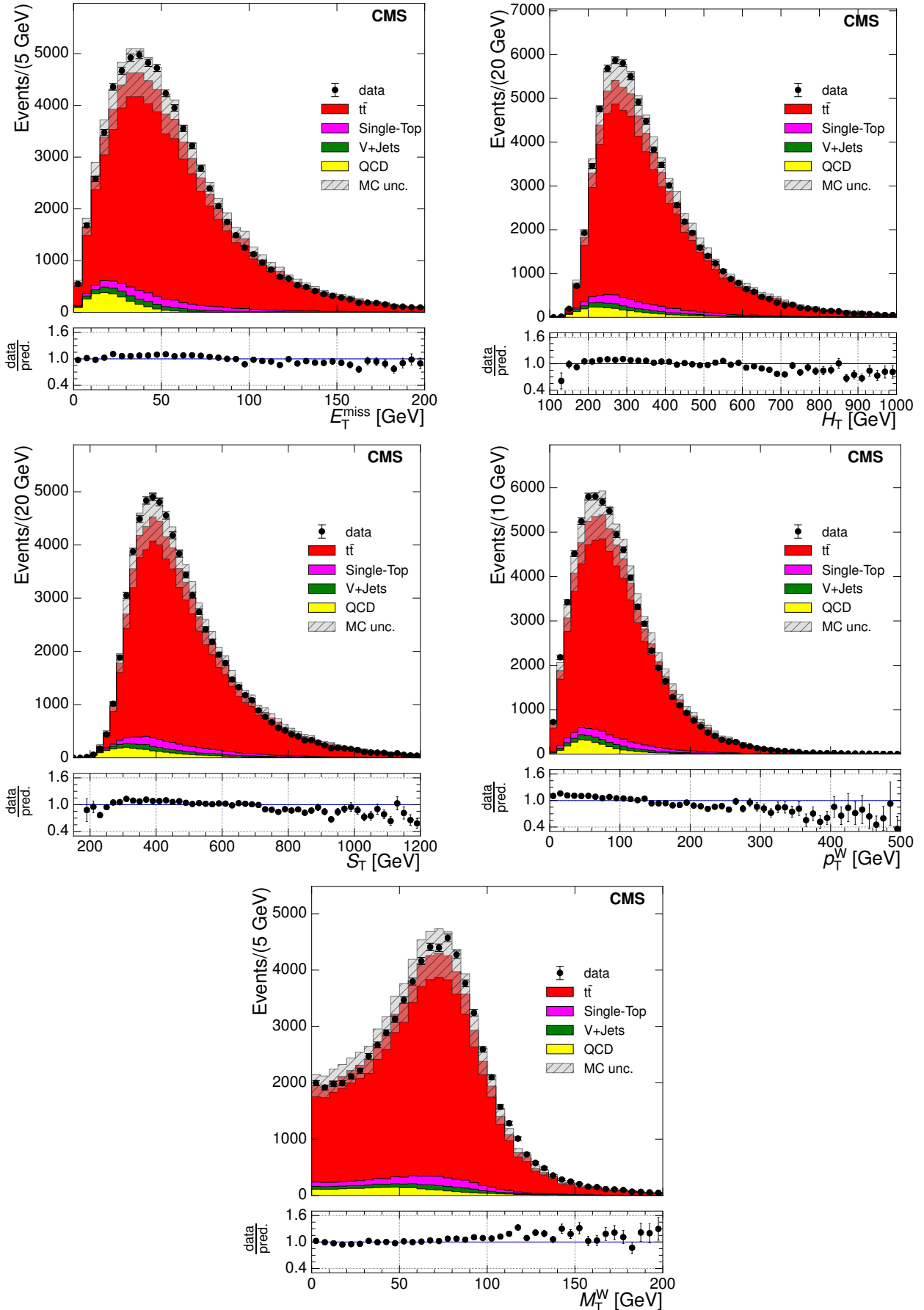


Figure 8.1: Comparison of Monte Carlo simulation to data in the electron+jets channel after final selection at  $\sqrt{s} = 7 \text{ TeV}$  for  $E_T^{\text{miss}}$  (upper left),  $H_T$  (upper right),  $S_T$  (middle left),  $p_T^W$  (middle right) and  $M_T^W$  (lower). The shaded region represents the  $t\bar{t}$  MC normalisation uncertainty. The lower plots show the ratio of the sum of simulated events to the data.

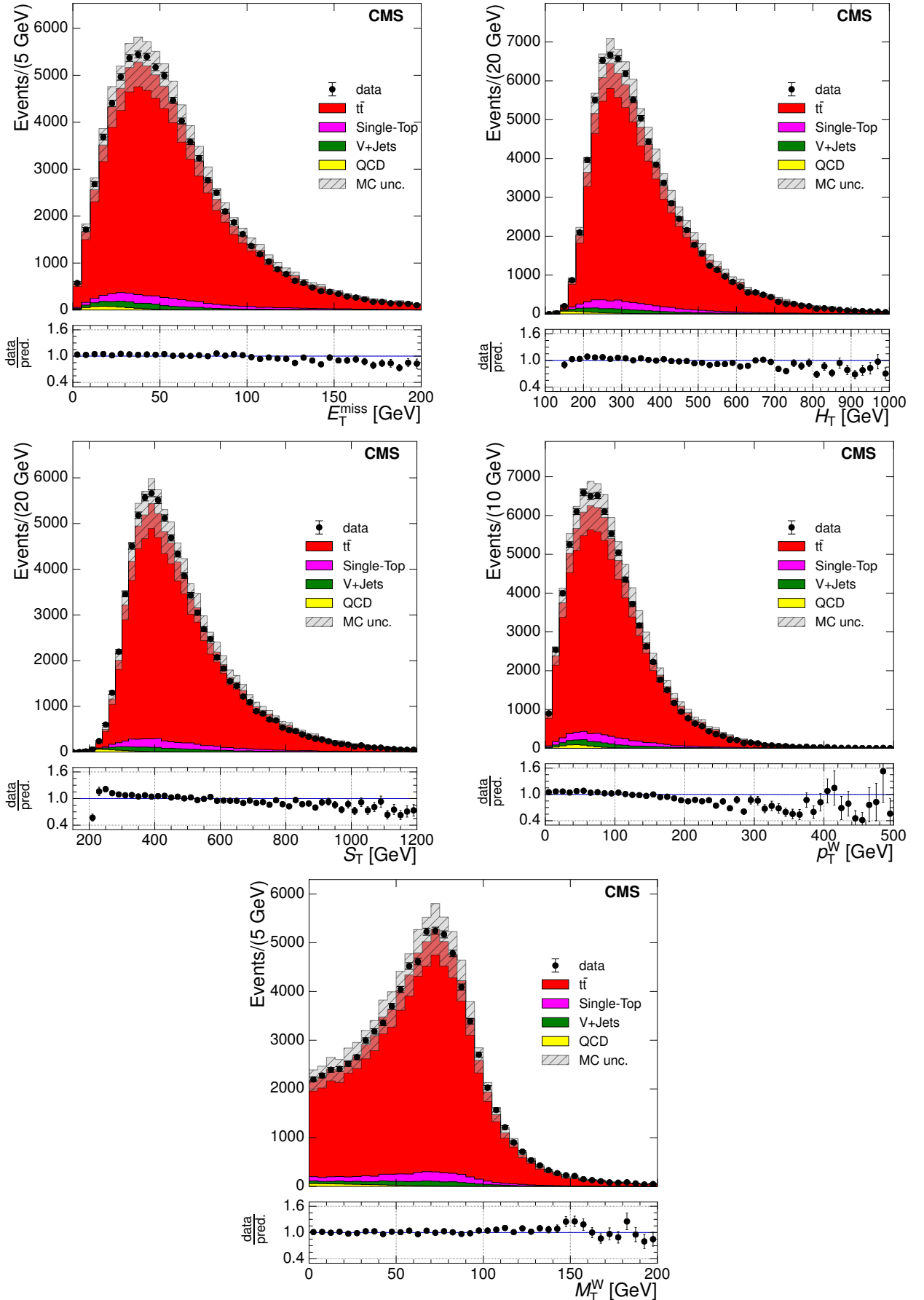


Figure 8.2: Comparison of Monte Carlo simulation to data in the muon+jets channel after final selection at  $\sqrt{s} = 7 \text{ TeV}$  for  $E_T^{\text{miss}}$  (upper-left),  $H_T$  (upper right),  $S_T$  (middle left),  $p_T^W$  (middle right) and  $M_T^W$  (lower). The shaded region represents the  $t\bar{t}$  MC normalisation uncertainty. The lower plots show the ratio of the sum of simulated events to the data.

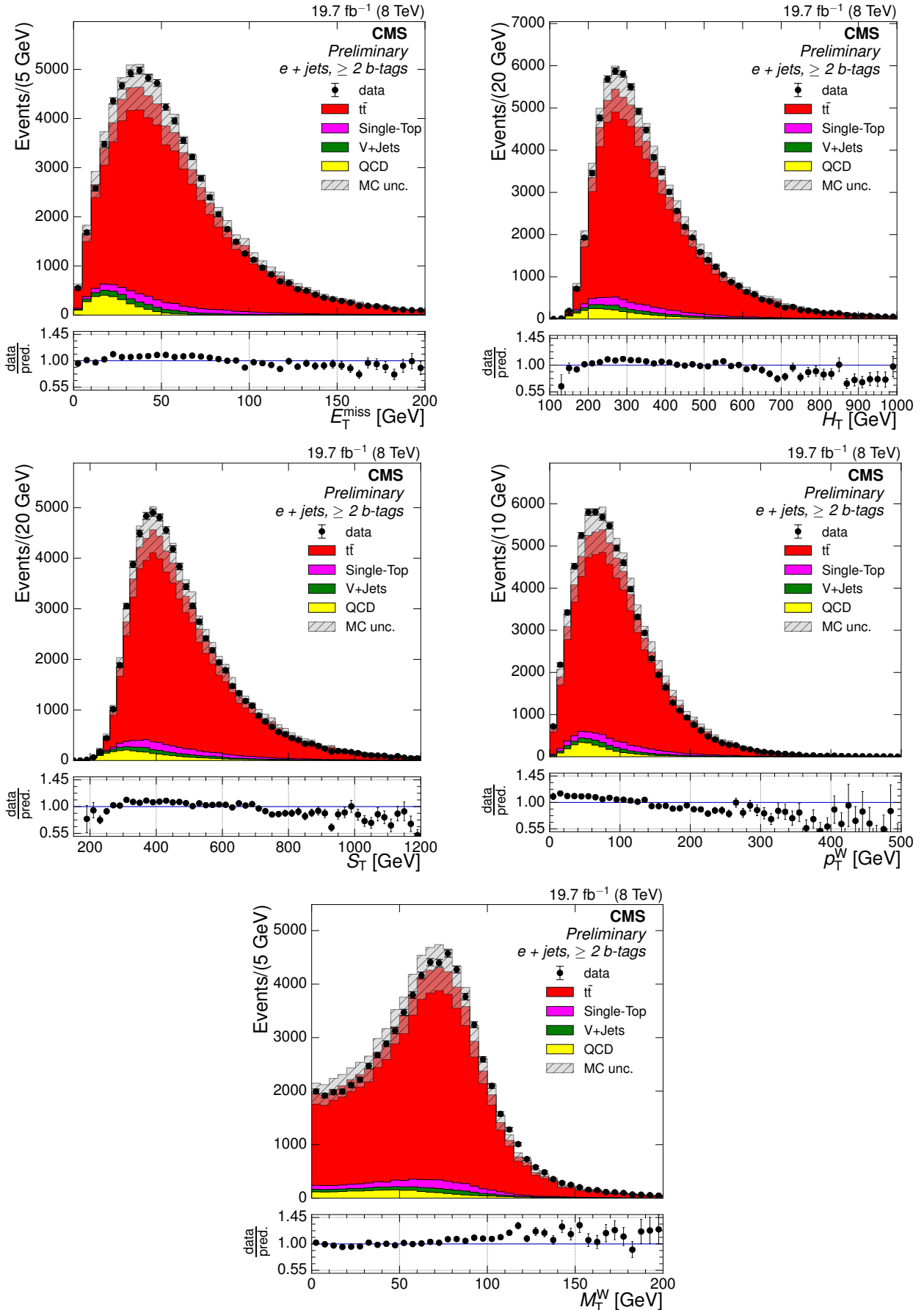


Figure 8.3: Comparison of Monte Carlo simulation to data in the electron+jets channel after final selection at  $\sqrt{s} = 8 \text{ TeV}$  for  $E_T^{\text{miss}}$  (upper left),  $H_T$  (upper right),  $S_T$  (middle left),  $p_T^W$  (middle right) and  $M_T^W$  (lower). The shaded region represents the  $t\bar{t}$  MC normalisation uncertainty. The lower plots show the ratio of the sum of simulated events to the data.

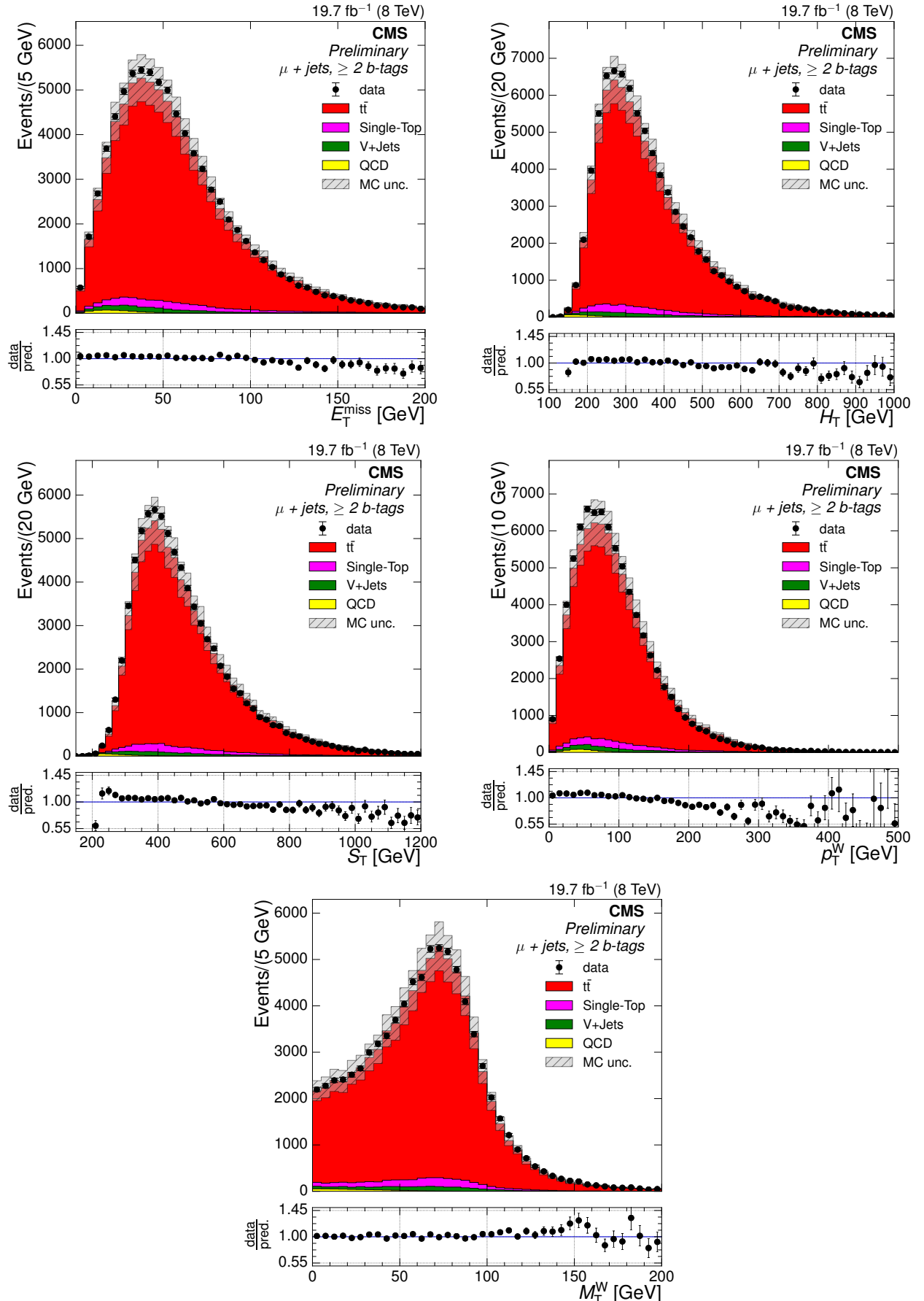


Figure 8.4: Comparison of Monte Carlo simulation to data in the muon+jets channel after final selection at  $\sqrt{s} = 8 \text{ TeV}$  for  $E_T^{\text{miss}}$  (upper-left),  $H_T$  (upper right),  $S_T$  (middle left),  $p_T^W$  (middle right) and  $M_T^W$  (lower). The shaded region represents the  $t\bar{t}$  MC normalisation uncertainty. The lower plots show the ratio of the sum of simulated events to the data.

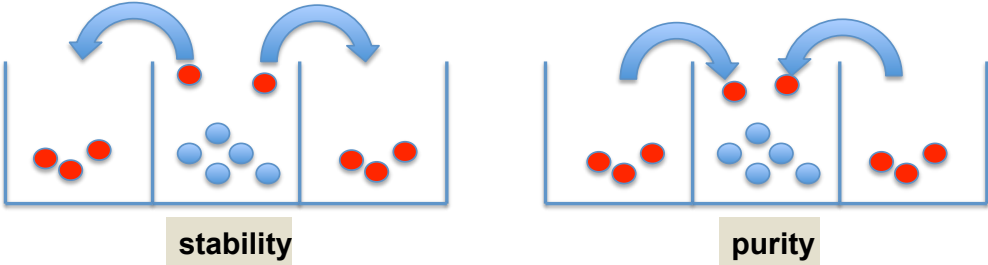


Figure 8.5: Stability quantifies the migration of events out of a bin while purity quantifies the migration of events into a bin. Both quantities compare the bin in which an event is generated to the range in which they are reconstructed.

large relative statistical error, a requirement that all bins have at least 100 events is also enforced.

The determination of the bin boundaries following these criteria is carried out simultaneously in (and therefore the binning is identical in) both centre of mass energies and both the electron+jets and muon+jets channel.

Plots of generated versus reconstructed events in simulation for all primary variables are shown in the electron+jets channel in Figure 8.6 for  $\sqrt{s} = 7 \text{ TeV}$  and in Figure 8.7 for  $\sqrt{s} = 8 \text{ TeV}$ . The corresponding plots in the muon+jets channel are shown in Figures B.5 and B.6 in Appendix B.3. The purity and stability values of the chosen bins are shown in Appendix B.4.

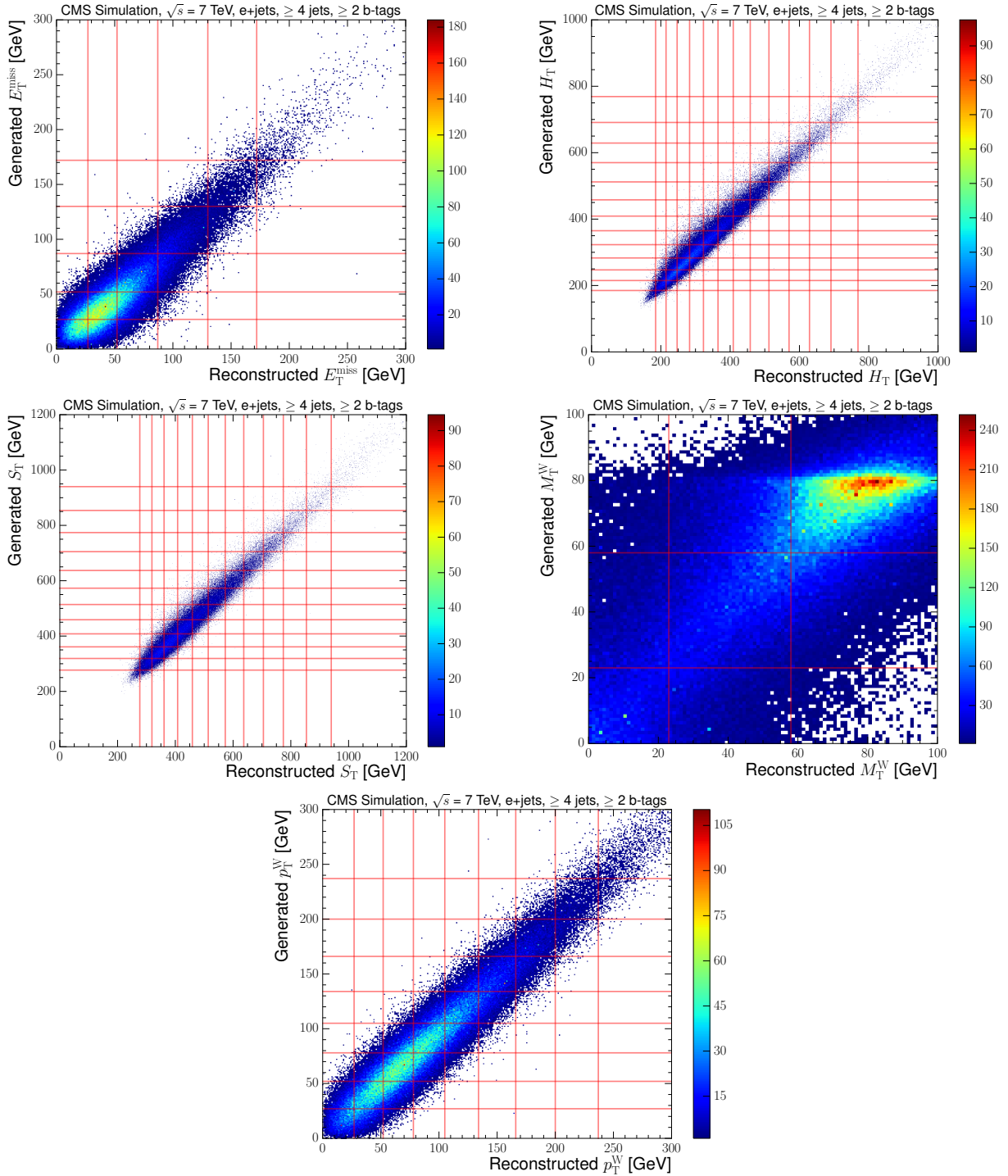


Figure 8.6: Generated versus reconstructed distributions of the primary variables  $E_T^{\text{miss}}$  (upper left),  $H_T$  (upper right),  $S_T$  (middle left),  $M_T^W$  (middle right) and  $p_T^W$  (lower) with horizontal and vertical lines representing the boundaries of the selected bins at  $\sqrt{s} = 7 \text{ TeV}$  in the electron+ jets channel. These distributions are obtained using  $t\bar{t}$  simulation.

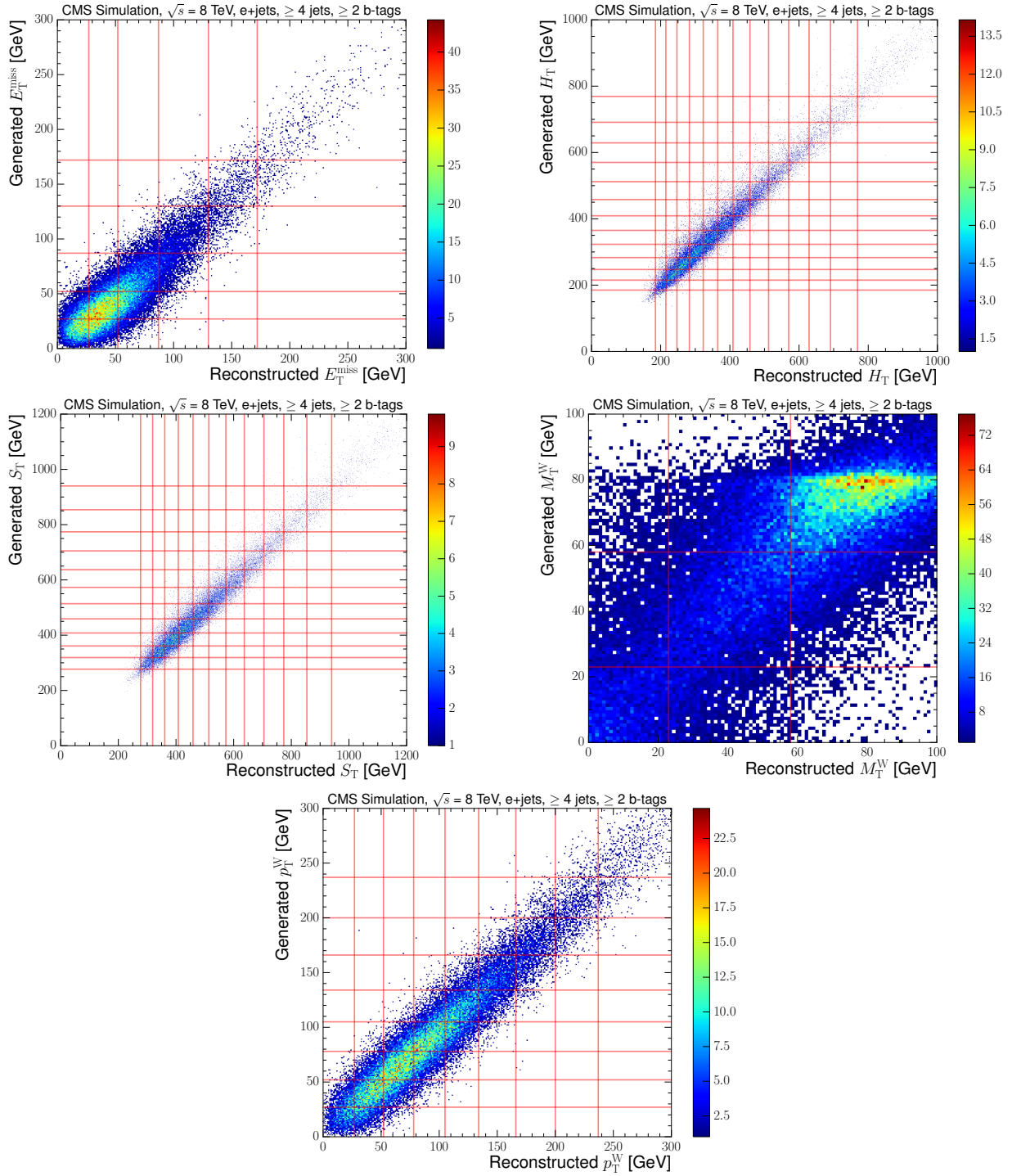


Figure 8.7: Generated versus reconstructed distributions of the primary variables  $E_T^{\text{miss}}$  (upper left),  $H_T$  (upper right),  $S_T$  (middle left),  $M_T^W$  (middle right) and  $p_T^W$  (lower) with horizontal and vertical lines representing the boundaries of the selected bins at  $\sqrt{s} = 8$  TeV in the electron+ jets channel. These distributions are obtained using  $t\bar{t}$  simulation.

## 8.3 Maximum Likelihood Fit

A maximum log likelihood fit of four templates to data in each bin of the primary variables is used to obtain the number of events from each process in each bin. Three fitting variables are used because no individual variable is able to distinguish between all four templates used in the fit:

- $t\bar{t}$
- single-top
- $V+jets$  ( $W+jets + Z+jets$ )
- QCD multi-jet

The template distributions are obtained from the following three variables: the absolute pseudorapidity of the lepton ( $|\eta|$ ), the three-dimensional angle between the lepton and the nearest b-jet ( $\alpha$ ), and the invariant mass of the three jets with the highest  $p_T$  sum ( $M3$ ).

The fit is carried out by maximising the log of the likelihood function (LL):

$$LL(x_i, d_i) = -2 \log \prod_i \frac{x_i^{d_i} \cdot e^{-x_i}}{d_i!} = -2 \sum_i \log \left( \frac{x_i^{d_i} \cdot e^{-x_i}}{d_i!} \right). \quad (8.4)$$

where  $i$  is the bin index in the template,  $x_i$  is the total of all the templates in bin  $i$ , and  $d_i$  is the observed number of data events in bin  $i$ .  $x_i$  is defined to be

$$x_i = \sum_j N_j x_{ij}, \text{ with } \sum_i x_{ij} = 1 \text{ for each process.} \quad (8.5)$$

where  $x_{ij}$  represents the templates and  $N_j$  represents the normalisations of the templates i.e. the fit parameters. Fitting using more than one fitting variable (the three aforementioned

fitting variables), the log likelihoods are summed:

$$LL(x, d) = -\frac{2}{n} \sum_{k=1,n} \log L_k \quad (8.6)$$

where  $L_k$  is the likelihood function of each of the different fit variables. Here the division by  $n$  accounts for the fact that the same information is used in all three fit variables, and so full correlation is assumed between the three fitting variables, which provides a conservative estimate of the uncertainties in the resulting fitted parameters. The fit operates by adjusting the normalisation of each template with the aim of equating  $x_i$  and  $d_i$  in each bin of each template. The starting normalisations in the templates are obtained from simulation after the full selection has been applied (this includes the QCD template, although the shape for this is obtained from data).

### 8.3.1 Choice of templates

$t\bar{t}$ , single-top and V+jets templates are taken from simulation, while the QCD template is extracted from data as described in Section 7.3.5. The W+jets and Z+jets templates are combined firstly due to the similar shapes of the distributions in these two background processes, and secondly due to limited statistics available in simulation. The four template shapes in each of the three fitting variables at  $\sqrt{s} = 7$  TeV in both channels are shown in Figure 8.8. The corresponding plots for  $\sqrt{s} = 8$  TeV are shown in Appendix B.5.

This combination of fitting variables was selected because they are only weakly correlated to the primary variables under investigation, and they show good discrimination between the four templates. Single top events have similar signatures to  $t\bar{t}$  events, with a central lepton from the decay of the single top, leading to a single top template that is similar to the  $t\bar{t}$  template in the electron  $|\eta|$  and muon  $|\eta|$  distributions. In the  $\alpha$  distribution, the similarity is attributable to the fact that the closest b-jet from the lepton is generally a b-jet from the decay of a t-quark. However, the average boost for single top events is lower than in  $t\bar{t}$

events, leading to a wider single top template. The M3 variable will be a combination of the jets from the hadronically decaying t-quark (a b-jet and two other jets from the W-boson, which may include a second b-jet) in  $t\bar{t}$  events, whereas in the other templates, M3 will simply correspond to some random combination of jets in the event. Hence, M3 shows the best discrimination between the single top and  $t\bar{t}$  templates.

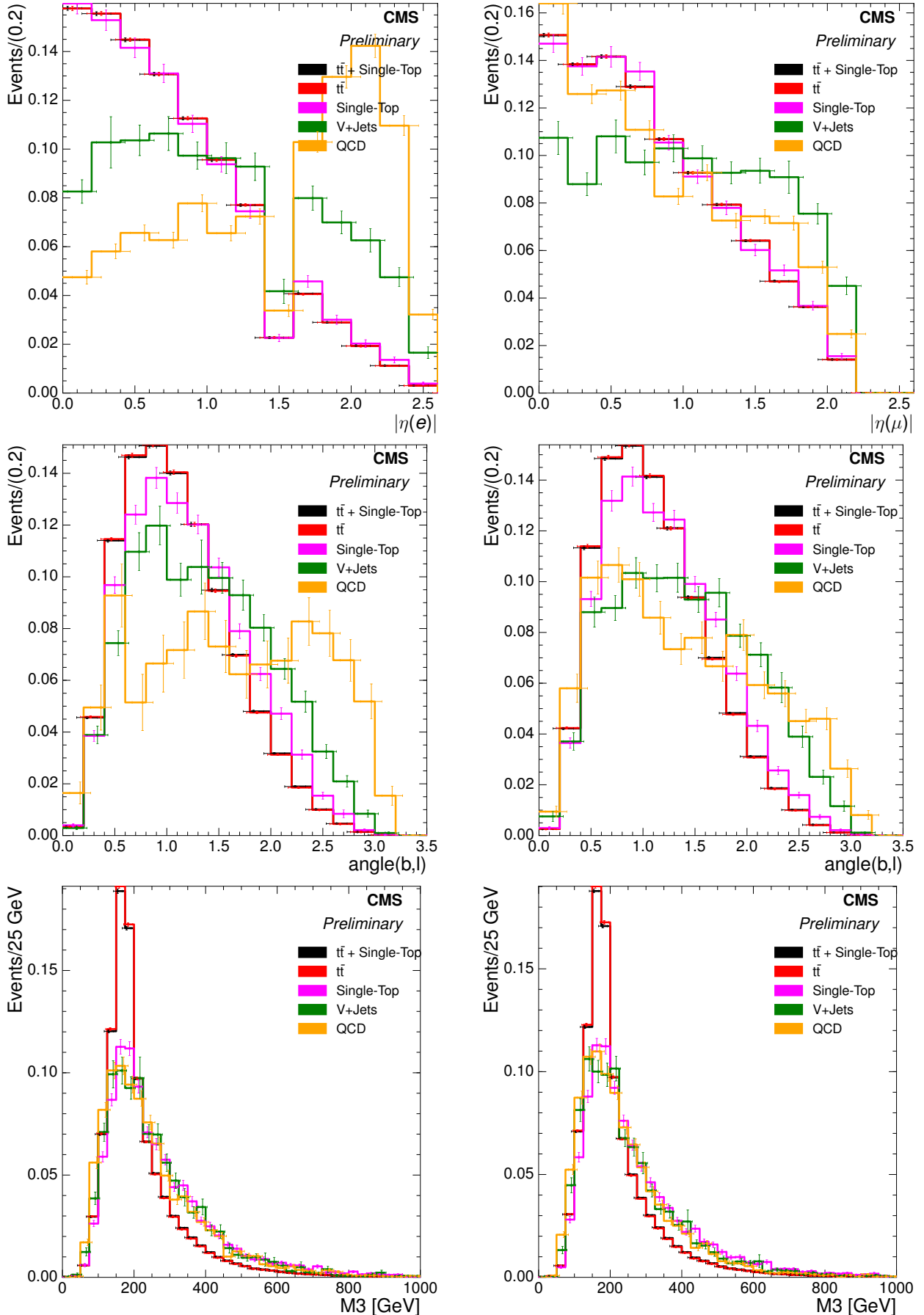


Figure 8.8: Normalised distributions of the templates for the three fit variables lepton  $|\eta|$  (upper),  $\alpha$  (middle) and  $M_3$  (lower) inclusive across all primary variable bins at  $\sqrt{s} = 7$  TeV in the electron+jets channel (left) and in the muon+jets channel (right).

The QCD templates, in particular those in higher bins of the primary variables, contain lower statistics than those in lower bins. Therefore, the inclusive QCD template shape, i.e. the QCD distribution over all bins, is used for the fitting process in every bin. Figure 8.9 shows a comparison between QCD templates at  $\sqrt{s} = 8$  TeV in the lowest three bins of the  $E_T^{\text{miss}}$  variable and also the inclusive  $E_T^{\text{miss}}$  QCD template. It can be seen that the third  $E_T^{\text{miss}}$  bin already shows large statistical errors due to low numbers of events, and that the inclusive template is largely shaped by events in the first two bins. Therefore, the inclusive QCD template is used rather than those in individual bins. Similar plots showing the same behaviour for the other primary variables at  $\sqrt{s} = 8$  TeV are shown in Appendix B.6.

An inclusive template is also used in the V+jets (W+jets + Z+jets) template for the same reason. Figure 8.10 shows a comparison between the V+jets templates at  $\sqrt{s} = 8$  TeV in each  $E_T^{\text{miss}}$  bin and also the inclusive  $E_T^{\text{miss}}$  V+jets template. As is the case for the QCD background template, it can be seen in the V+jets templates that there are diminished statistics available in higher bins, and the inclusive template shape is largely governed by the lower bins. Similar plots demonstrating the same behaviour for the other primary variables at  $\sqrt{s} = 8$  TeV are shown in Appendix B.7.

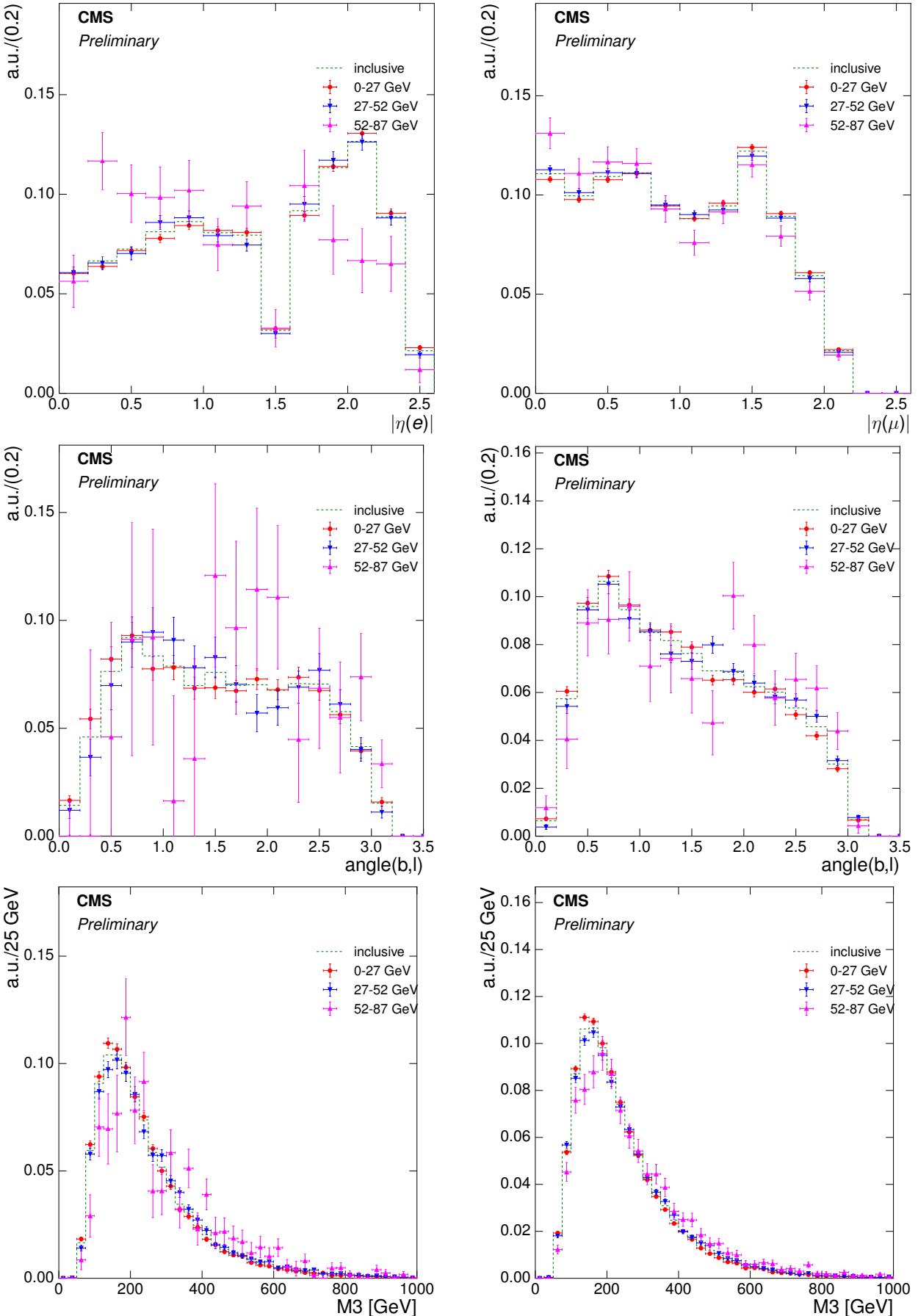


Figure 8.9: Normalised distributions of the QCD templates for the three fit variables lepton  $|\eta|$  (upper),  $\alpha$  (middle) and  $M_3$  (lower) inclusive across all  $E_T^{\text{miss}}$  bins and for the lowest three  $E_T^{\text{miss}}$  bins at  $\sqrt{s} = 8 \text{ TeV}$  in the electron+jets channel (left) and in the muon+jets channel (right).

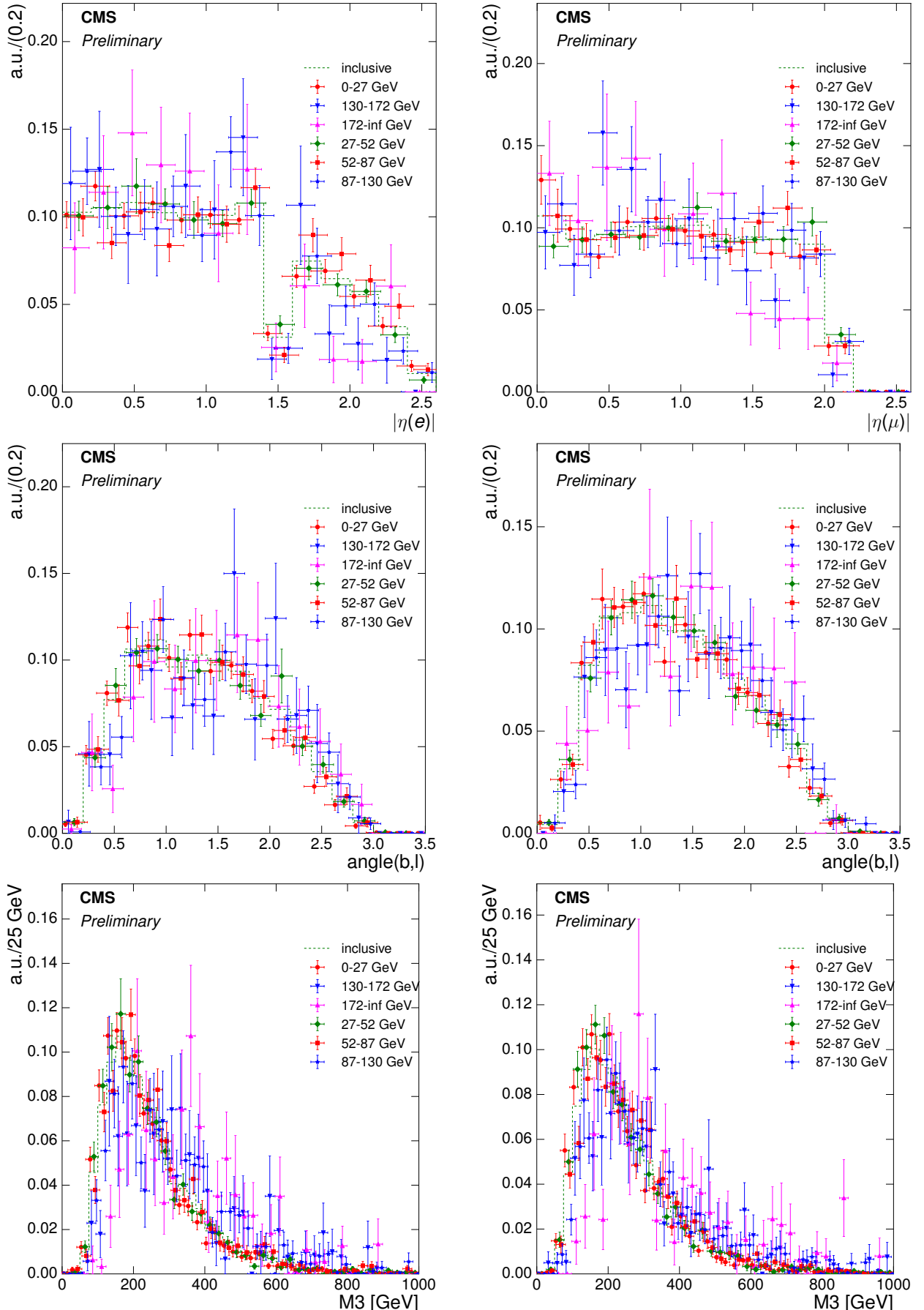


Figure 8.10: Normalised distributions of the  $V+jets$  templates for the three fit variables lepton  $|\eta|$  (upper),  $\alpha$  (middle) and  $M3$  (lower) inclusive across all  $E_T^{\text{miss}}$  bins and for the lowest three  $E_T^{\text{miss}}$  bins at  $\sqrt{s} = 8\text{ TeV}$  in the electron+jets channel (left) and in the muon+jets channel (right).

TODO: Insert Fit Template Plots?

### 8.3.2 Fit Results

The results from the fit are shown in Figures 8.11 and 8.12 for the electron and muon channels respectively at  $\sqrt{s} = 7 \text{ TeV}$ , and in Figures 8.13 and 8.14 for the electron and muon channels at  $\sqrt{s} = 8 \text{ TeV}$ . The corresponding numerical values from the fit can be found in Appendix B.8. Overall, the agreement between the data and the simulation is within the fit uncertainty.

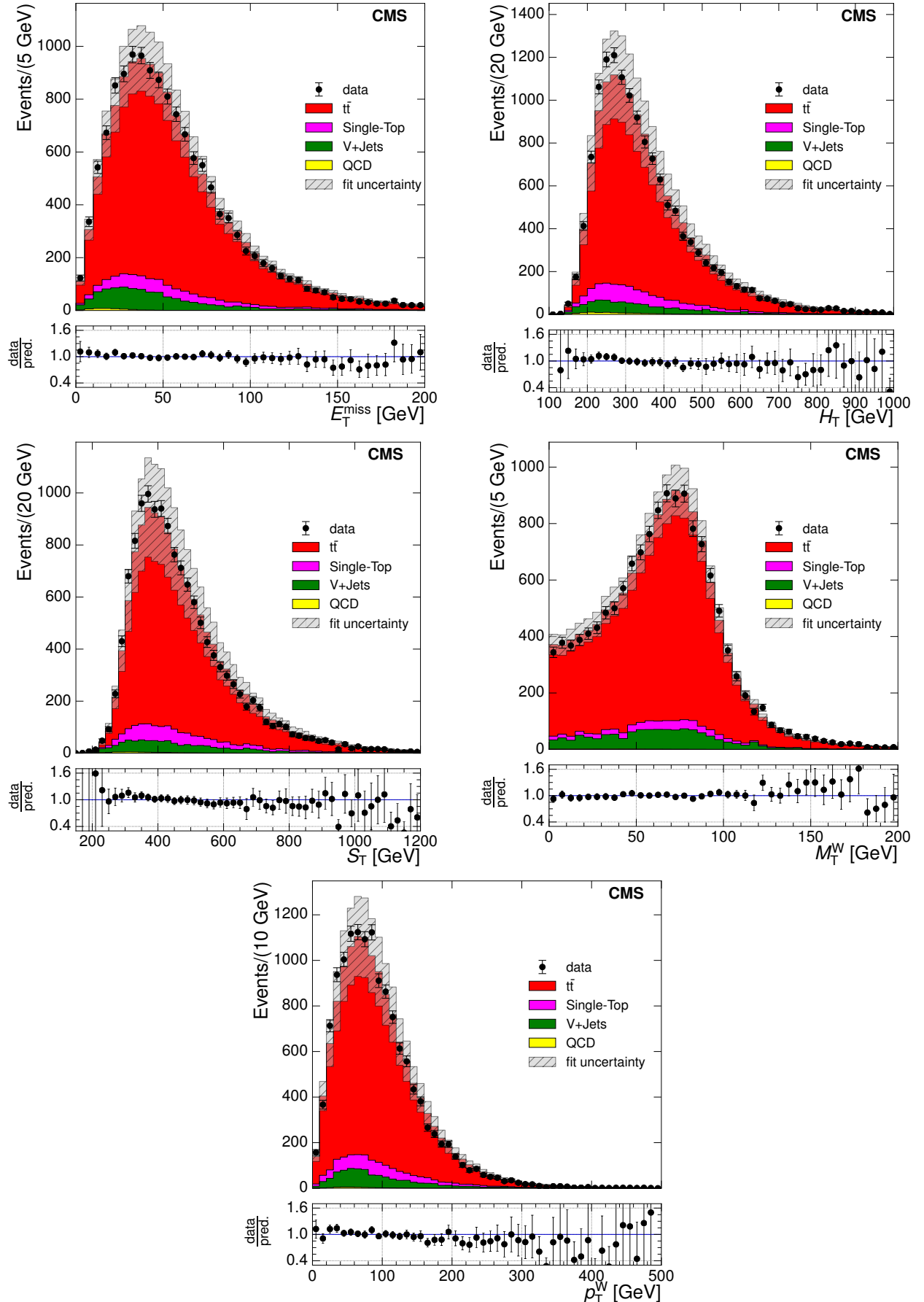


Figure 8.11: Comparison of Monte Carlo simulation to data in the electron+jets channel after fitting at  $\sqrt{s} = 7 \text{ TeV}$ .

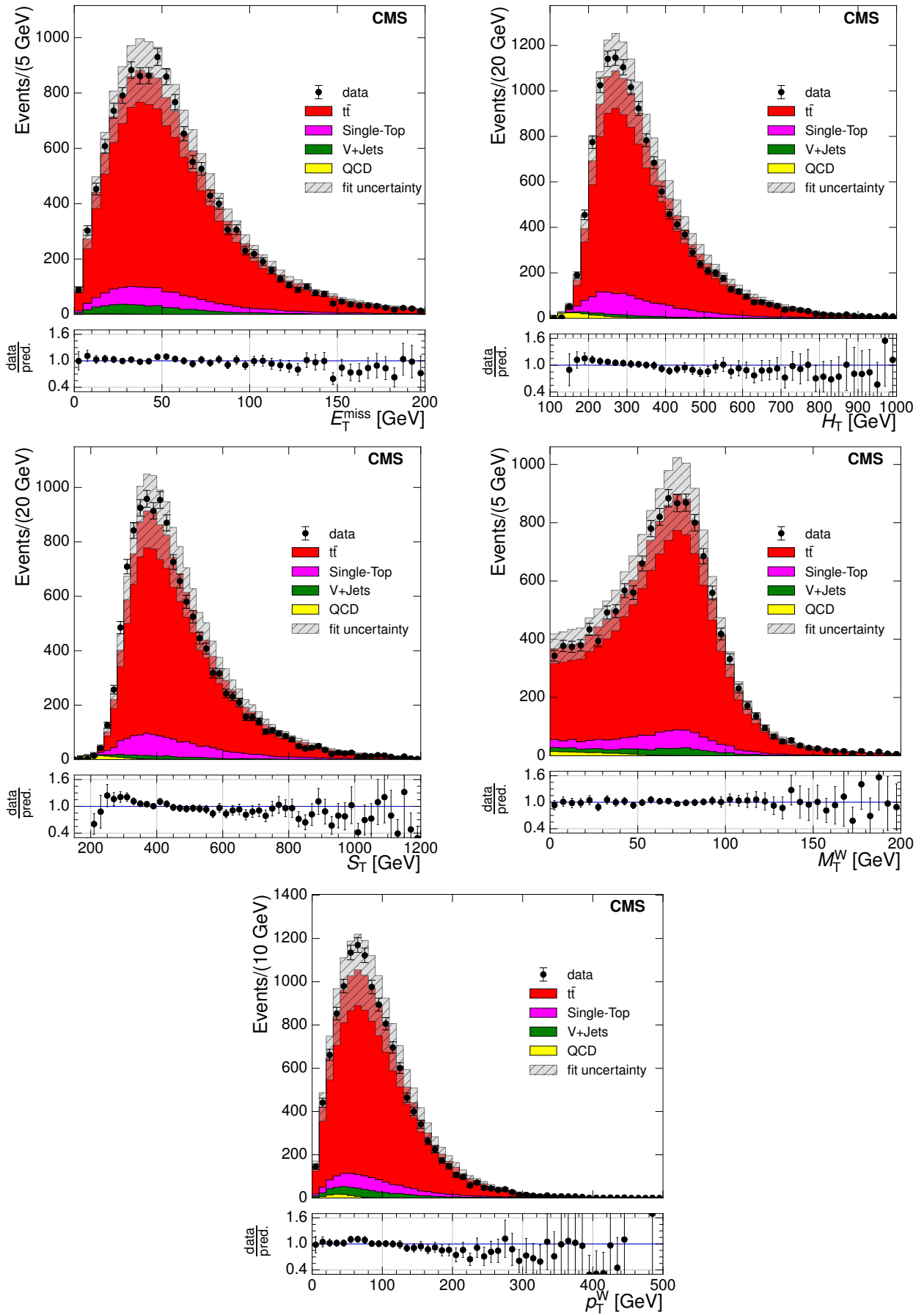


Figure 8.12: Comparison of Monte Carlo simulation to data in the muon+jets channel after fitting at  $\sqrt{s} = 7$  TeV.

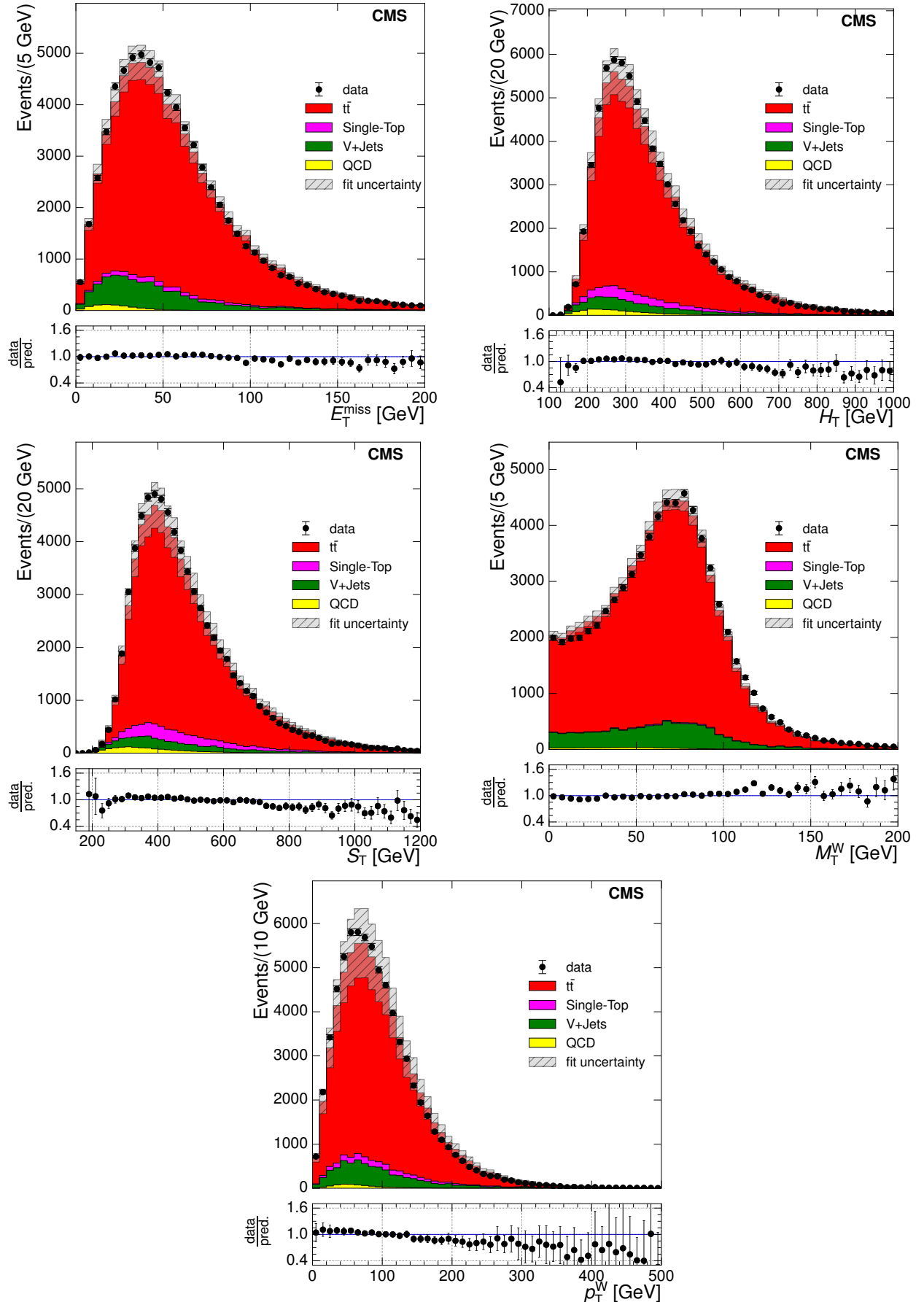


Figure 8.13: Comparison of Monte Carlo simulation to data in the electron+jets channel after fitting at  $\sqrt{s} = 8 \text{ TeV}$ .

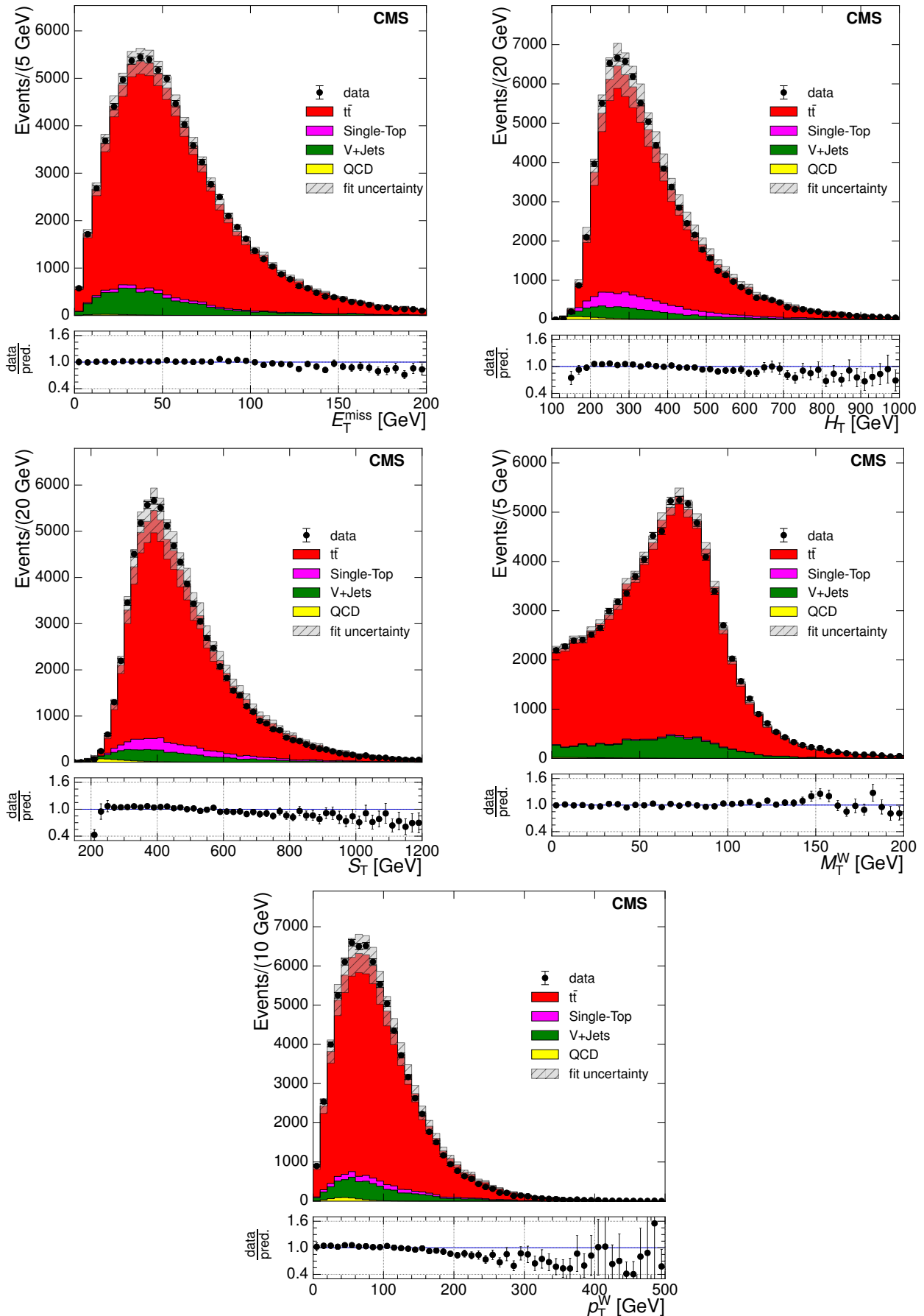


Figure 8.14: Comparison of Monte Carlo simulation to data in the muon+jets channel after fitting at  $\sqrt{s} = 8 \text{ TeV}$ .

## 8.4 Fit cross-checks

The correlations between the fitted processes,  $N_{t\bar{t}}$ ,  $N_{singletop}$ ,  $N_{V+Jets}$  and  $N_{QCD}$ , for the  $E_T^{\text{miss}}$  variable in the electron+jets channel at  $\sqrt{s} = 8 \text{ TeV}$  are shown in Figure 8.15. The equivalent plots for  $\sqrt{s} = 7 \text{ TeV}$  are shown in Figure B.16 in Appendix B.9. It can be seen that the correlation between signal and QCD remains very low for all  $E_T^{\text{miss}}$  bins. The V+jets template is negatively correlated with the QCD template in low bins, whereas this is not seen in higher bins due to these bins containing very few QCD events.

## 8.5 Background Subtraction

As a cross-check for the fitting process, an alternative method of extracting the number of  $t\bar{t}$  events using the background subtraction method. The MC predictions of single top, V+jets and QCD events is subtracted from the data in each bin to provide the  $t\bar{t}$  yield. The normalisations of these background processes is the same as previously in the fitting method, i.e. to their respective cross sections and luminosities. The resulting number of  $t\bar{t}$  events is then taken forward to the unfolding process.

## 8.6 Unfolding

The measurement of the differential cross section will be limited by the finite resolution of the detector, detector acceptance and selection efficiency, and also by the presence of a small number of dilepton and fully hadronic  $t\bar{t}$  events, and semi-leptonic events in the tau channel. In order to allow later comparison of results with theory predictions and with measurements from other experiments, deconvolution (unfolding) is employed to provide an estimate of the true distributions of the measured variables.

Generally speaking, any variable can be generated and reconstructed in simulation. Denoting the generated (“true”) distribution by a vector  $x_0$ , and the corresponding reconstructed

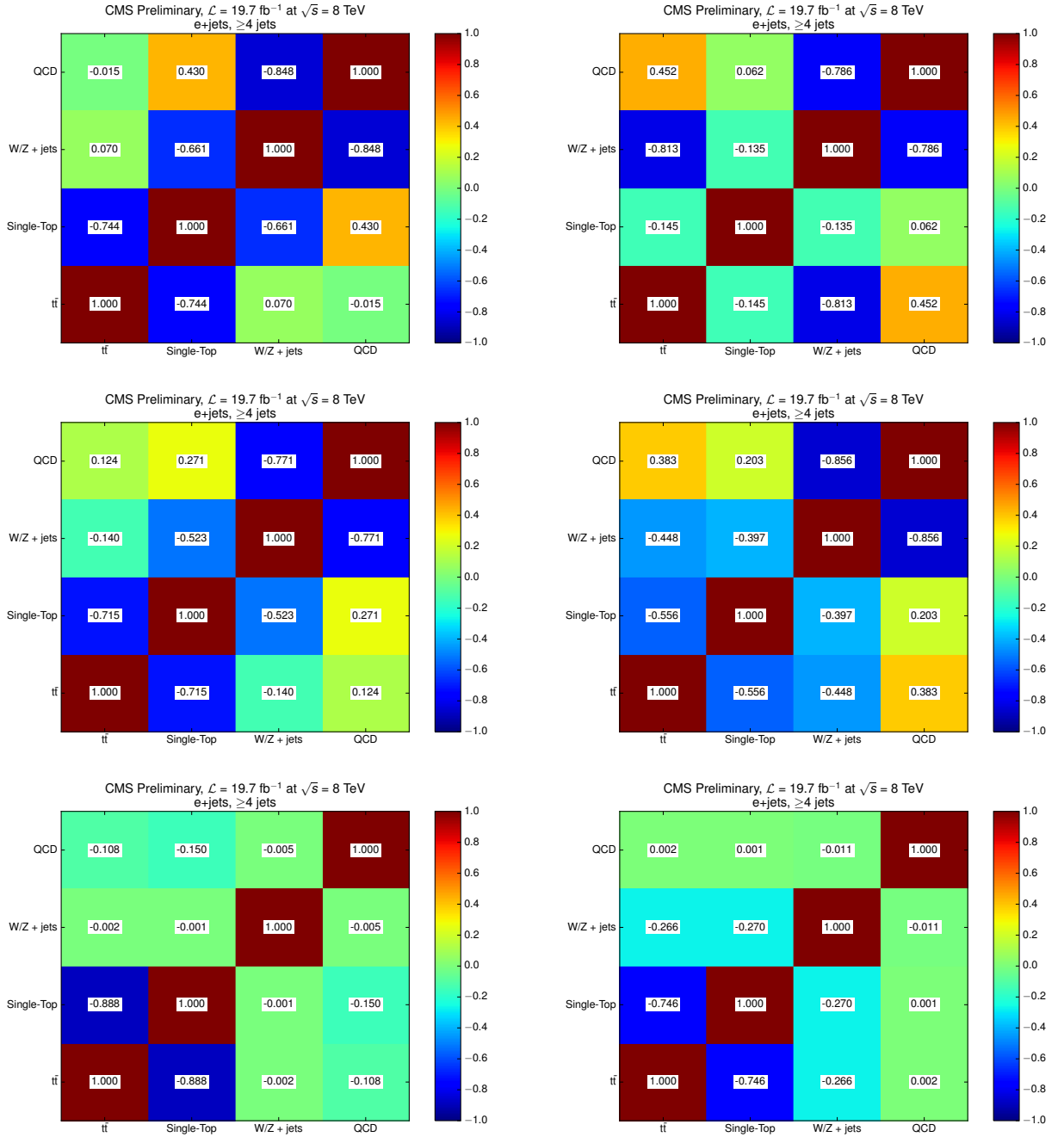


Figure 8.15: Correlation between fit processes for the  $E_T^{\text{miss}}$  variable in the electron+jets channel at  $\sqrt{s} = 8 \text{ TeV}$  in bins 0-27 GeV (upper left), 27-52 GeV (upper right), 52-87 GeV (middle left), 87-130 GeV (middle right), 130-172 GeV (lower left) and  $\geq 172 \text{ GeV}$  (lower right).

distribution by  $b_0$ , these can be related by

$$\hat{A}x_0 = b_0. \quad (8.7)$$

where  $\hat{A}$  is the response matrix, containing information about how the true distribution is reconstructed and measured as the distribution obtained in the real world. The variable in question is then measured in reality to have some distribution,  $b$ , which is then related to the true distribution by

$$\hat{A}x = b, \quad (8.8)$$

and therefore

$$b = \hat{A}^{-1}x, \quad (8.9)$$

Therefore, in this analysis, the system is solved to identify the true underlying distribution,  $x$ , using Singular Value Decomposition (SVD) [66] of the response matrix, with the RooUnfold package [15], and using regularisation overcome the problem of oscillating solutions. In SVD unfolding, the response matrix is factorised as follows:

$$\hat{A} = USV^T. \quad (8.10)$$

$S$  is a diagonal matrix with non-negative diagonal elements of dimensions  $m \times n$ , and  $U$  and  $V$  are orthogonal matrices of dimensions  $m \times m$  and  $n \times n$  respectively. The diagonal elements of  $S$  are called *singular values* of the matrix  $A$  and the columns of  $U$  and  $V$  are called the left and right *singular vectors*. The inverse of the response matrix can then be

stated as

$$\hat{A}^{-1} = VS^{-1}U^T. \quad (8.11)$$

In systems in which the response matrix,  $\hat{A}$ , is of full rank (all columns and rows are linearly independent of each other) and statistical errors in the bins of the distribution are small, the problem can be solved simply using the inverted response matrix  $\hat{A}^{-1}$ . However, in most real life cases, this is not the case, leading to unphysical fluctuations [66]. Regularisation is used in SVD unfolding to help overcome this problem using a regularisation parameter,  $k$ , which specifies the number of statistically significant terms in the system.

The value of  $k$  can be obtained by considering a measured variable that follows a smooth distribution, an *a priori* knowledge of the measured distribution, in which only the first few terms of the matrix decomposition are expected to be significant, with the contribution of higher, rapidly oscillating, terms expected to be compatible with zero [66]. The  $i$ th component of the vector  $d$ ,  $d_i$ , is the coefficient of the measured distribution  $b$ . Using  $d$ , a vector obtained by rotating the measured distribution  $b$ ,

$$d = U^T \times b. \quad (8.12)$$

A plot of  $\log|d_i|$  versus  $i$  can be plotted, where the bin number is represented by  $i$ . This will show  $d_i$  as being statistically significant, i.e.  $d_i \gg 1$ , for small  $i$ , and falling exponentially to a random Gaussian distribution about 0 for larger  $i$ . A falling exponential function plus a flat line can be fitted to this distribution, and the value of  $i$  at which the  $d_i$  changes from exponentially falling to within 10% of the flat component is taken as the value of the regularisation parameter,  $k$ , which represents the number of significant bins in the distribution [66].

The value of  $k$  should be between 2 and the number of bins in the distribution, and aims

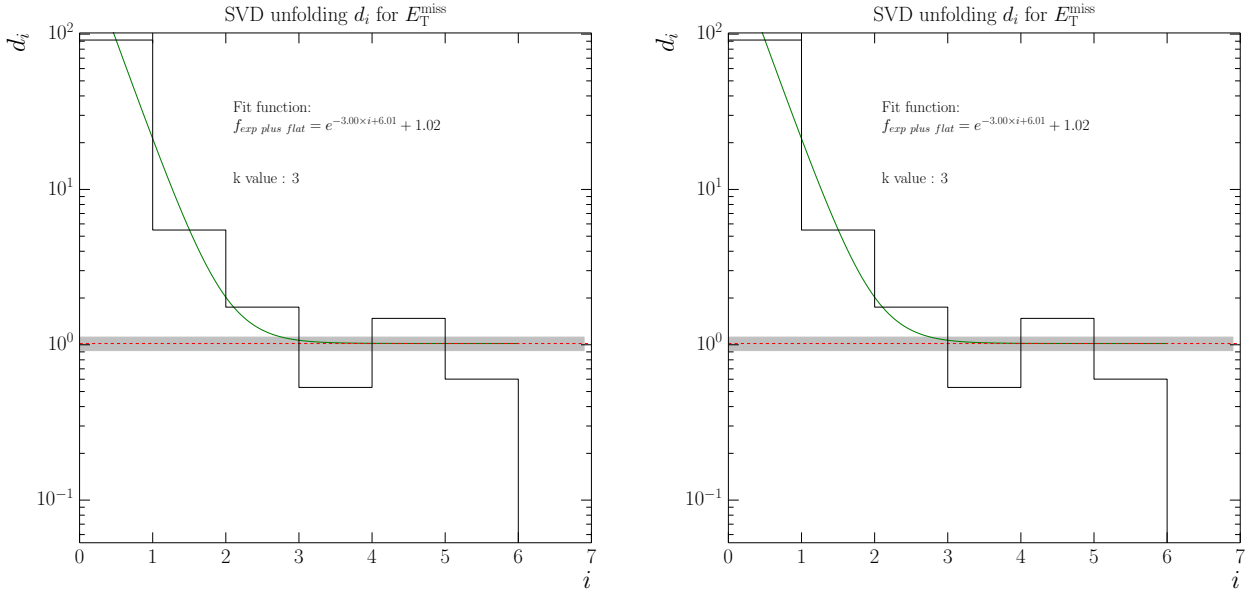


Figure 8.16:  $\log|d_i|$  plots at  $\sqrt{s} = 8$  TeV for the electron+jets channel (left) and the muon+jets channel (right).

to prevent statistical fluctuations in the distribution being interpreted as real variations in the true data. A low value of  $k$  favours the Monte Carlo truth input, while a high value of  $k$  favours the measured data which is to be unfolded. The  $\log|d_i|$  plots for  $E_T^{\text{miss}}$  variable at  $\sqrt{s} = 7$  TeV is shown in Figure 8.16. The resulting  $k$  values for both channels and both centre of mass energies are shown in Table 8.3.

The required inputs to SVD unfolding with the RooUnfold package are:

- the simulated true distribution before selection
- the simulated reconstructed distribution after selection
- the two-dimensional reconstruction matrix of the true distributions after selection versus the measured distributions after selection.

All of the above are obtained from Monte Carlo simulations of  $t\bar{t}$  events. Unfolding is carried out to the semi-leptonic phase space, where the lepton is either an electron or a muon. In the cases of  $E_T^{\text{miss}}$ ,  $p_T^W$  and  $M_T^W$ , unfolding is carried out to the full phase-space where the  $E_T^{\text{miss}}$  is defined as the  $p_T$  of the neutrino from the semi-leptonic decay; and in the cases of

variable	k-value (electron)	k-value (muon)
$\sqrt{s} = 7 \text{ TeV}$		
$E_T^{\text{miss}}$	2	2
$H_T$	3	3
$S_T$	3	3
$M_T^W$	2	2
$p_T^W$	3	3
$\sqrt{s} = 8 \text{ TeV}$		
$E_T^{\text{miss}}$	3	3
$H_T$	3	3
$S_T$	4	4
$M_T^W$	2	2
$p_T^W$	3	3

Table 8.3: Optimal  $k$ -values for all primary variables at both 7 and 8 TeV.

$H_T$  and  $S_T$ , unfolding is carried out to particle level where the jets in the true distribution have  $p_T \geq 20 \text{ GeV}$ .

Closure tests were carried out to verify the unfolding method using reconstructed simulated events as pseudo-data. A successful closure test results in the unfolded values matching the simulated truth of the same simulation sample, as can be seen in Figure 8.17 for the  $E_T^{\text{miss}}$  variable at  $\sqrt{s} = 8 \text{ TeV}$ .

The unfolding method described here was tested using toy Monte Carlo sets and producing pull distributions to investigate any potential bias in the method and to verify the unfolding error is estimated correctly. The central  $t\bar{t}$  MADGRAPH sample is used to vary the contents in each bin of each primary variable distribution based on assumed Poissonian behaviour around the observed values. 300 sets of variations (henceforth referred to as models) are created, with the truth and reconstructed distributions varied independently, while another independent variation of the reconstructed distribution is used as the pseudo-data to be unfolded. This therefore creates  $300 \times 300$  combinations of model and pseudo-data. The pull

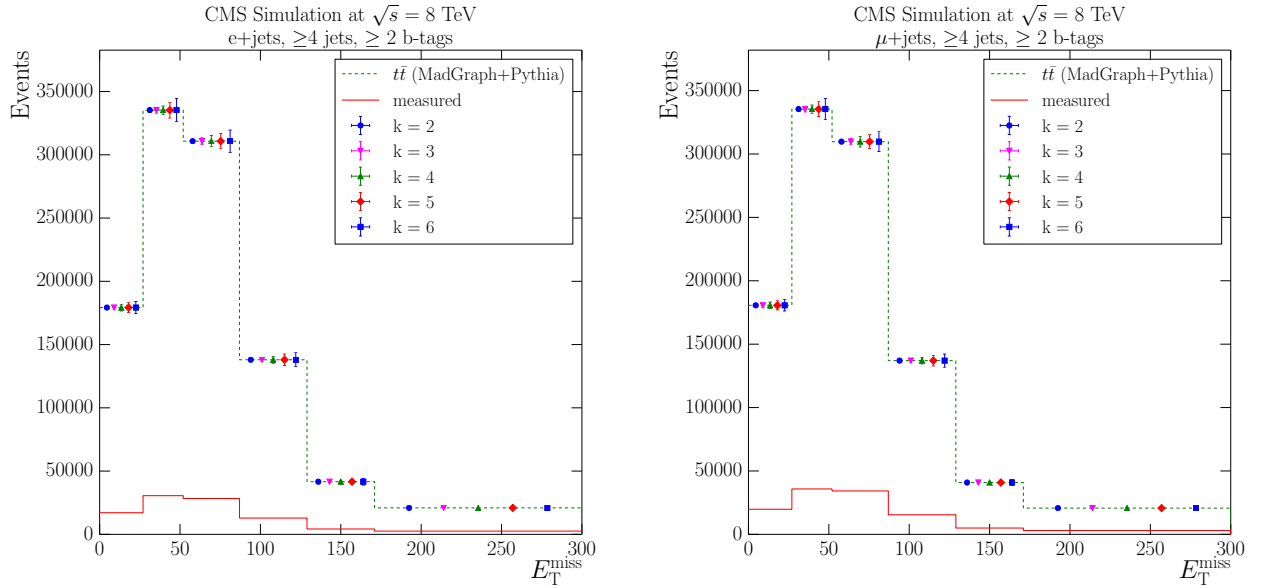


Figure 8.17: Unfolding closure tests performed by unfolding the reconstructed MADGRAPH distribution (“measured”) to generated values for the  $E_T^{\text{miss}}$  variable in the electron+jets channel (left) and the muon+jets channel (right) at  $\sqrt{s} = 8 \text{ TeV}$ .

distributions are created as follows

$$\frac{N^{\text{unfolded}} - N^{\text{true}}}{\sigma} \quad (8.13)$$

where  $N^{\text{unfolded}}$  is the number of events in the unfolded result,  $N^{\text{true}}$  is the number of events in the expected distribution after unfolding (Monte Carlo truth), and  $\sigma$  is the unfolding uncertainty. Provided the unfolding uncertainty is estimated correctly and that there is no bias in the method, the pull distribution is expected to have a Gaussian distribution around a mean of 0 and a  $\sigma$  of 1. Any bias would manifest as a pull distribution centred at a non-zero value, and any miscalculation of the unfolding uncertainty will result in a width of  $< 1$  or  $> 1$  for an overestimation or an underestimation respectively.

### 8.6.1 Measurement

The unfolded number of  $t\bar{t}$  events can now be used to calculate the normalised differential cross-section in each bin of the primary variables by first calculating the average cross-section

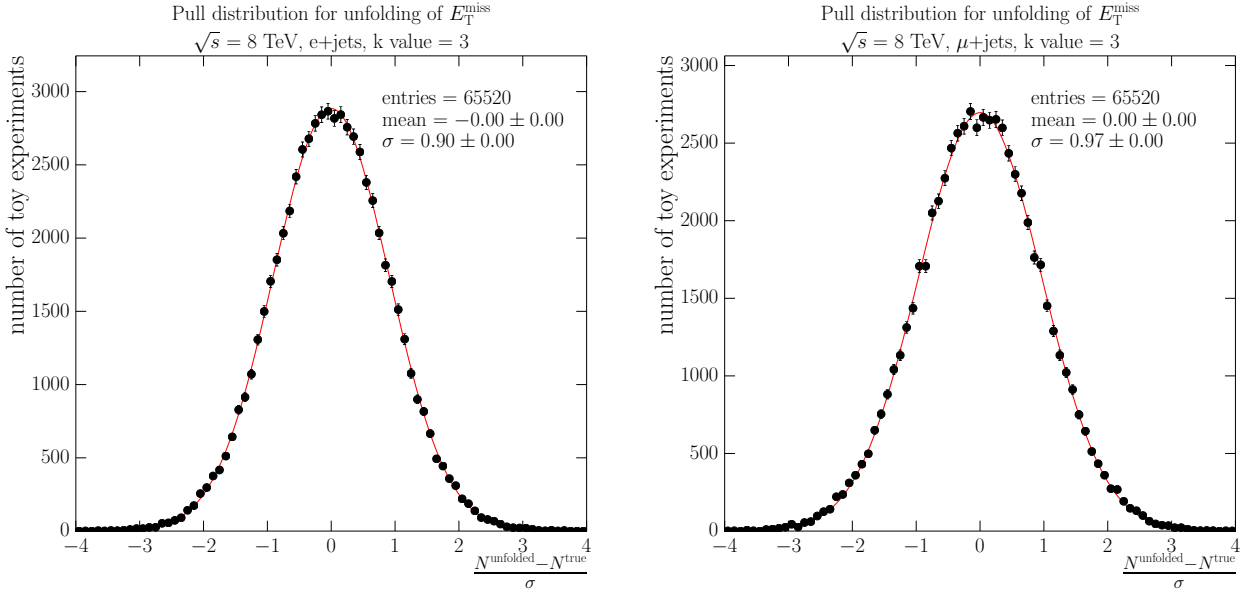


Figure 8.18: Pull distributions using toy Monte Carlo datasets for the  $E_T^{\text{miss}}$  variable using a  $k$  value of 3 in the electron+jets channel (left) and in the muon+jets channel (right) at  $\sqrt{s} = 8 \text{ TeV}$ .

in each bin using

$$\Delta\sigma_{t\bar{t}}^i = \frac{N_{t\bar{t}}^i}{\text{BR} \times \mathcal{L}}. \quad (8.14)$$

Here, the theoretical  $t\bar{t}$  semi-leptonic branching ratio is denoted by  $\text{BR}$ ,  $\epsilon$  is the total efficiency of the  $t\bar{t}$  simulation sample, and  $\mathcal{L}$  is the luminosity of the recorded dataset. Subsequently, the differential cross section in each primary variable bin is calculated by dividing by the bin width  $\Delta X$  as follows:

$$\frac{d\sigma_{t\bar{t}}^i}{dX} = \frac{\Delta\sigma_{t\bar{t}}^i}{\Delta X} = \frac{N_{t\bar{t}}^i}{\text{BR} \times \mathcal{L} \times \Delta X}. \quad (8.15)$$

Finally, the normalised differential cross section in each bin is obtained by normalising to the total measured cross section

$$\frac{1}{\sigma_{t\bar{t}}^{\text{tot}}} \frac{d\sigma_{t\bar{t}}^i}{dX} = \frac{1}{\sum_j d\sigma_{t\bar{t}}^j} \frac{d\sigma_{t\bar{t}}^j}{dX} = \frac{\text{BR} \times \mathcal{L}}{\sum_j N_{t\bar{t}}^j} \frac{N_{t\bar{t}}^i}{\text{BR} \times \mathcal{L} \times \Delta X} = \frac{1}{\sum_j N_{t\bar{t}}^j} \frac{N_{t\bar{t}}^i}{\Delta X} \quad (8.16)$$

# 9 | 7 TeV and 8 TeV Differential Cross Section Measurement: Systematic Uncertainties and Results

## 9.1 Systematic uncertainties

The systematic uncertainties in this analysis are evaluated independently, under the assumption that systematic uncertainty sources are uncorrelated, by changing the inputs by the associated uncertainties ( $-1\sigma$  and  $+1\sigma$ ) and measuring the deviation in the final result from the nominal measurement. The final result from systematic variations are generally found to be compatible with the nominal measurement within uncertainties. The uncertainties from each source are therefore symmetrised by using the maximum absolute deviation of the up or down systematic variation. The total systematic uncertainty is obtained by adding the systematic uncertainties in quadrature, and this is summed with the fitting and unfolding uncertainties to obtain the total measurement uncertainty. The normalisation of the final differential cross section will cancel systematic uncertainties that are correlated between bins of the primary variables.

In the case of experimental uncertainties, the uncertainty is calculated by changing the templates in the fitting process and/or their normalisations, and using the nominal MADGRAPH response matrix in the unfolding process. In the case of theoretical uncertainties, the central fitting templates and normalisation are used, while the response matrix information

is changed according to the systematic being investigated.

The systematic uncertainties are summarised in Tables B.27 to B.36.

### 9.1.1 Experimental Uncertainties

Jet energy scale uncertainty is evaluated as a function of jet  $p_T$  and jet  $\eta$ , and a 10% jet energy resolution uncertainty is applied. The jet energy scale (JES) directly changes the  $p_T$  of jets in the event, and also propagates to the event  $E_T^{\text{miss}}$  (see Section 7.4.4). Therefore the JES uncertainty becomes significant at higher values of the primary variables, in particular of  $E_T^{\text{miss}}$ ,  $H_T$  and  $S_T$ .

Together with jet energy scale uncertainty, the  $E_T^{\text{miss}}$  energy uncertainties are the only systematics applied to both simulation and data. These take account of uncertainty in the lepton energy, and propagates this to the  $E_T^{\text{miss}}$  in the event. While the electron and muon energy uncertainties are not dominant sources of error in this analysis, the effect of the uncertainty on tau energy has been calculated to be larger. Events with tau leptons can pass the signal selection (a component of what are known as fake events, i.e. non semi-leptonic  $t\bar{t}$  events which pass our signal selection) if they mimic the signature of an electron+jets or muon+jets  $t\bar{t}$  event:

- semi-leptonic tau, where  $\tau \rightarrow e/\mu + \bar{\nu}_{e/\mu} + \nu_\tau$  (Figure 9.1a).
- di-leptonic  $e\tau$  &  $\mu\tau$ , where  $\tau \rightarrow q\bar{q}' + \nu_\tau$  (Figure 9.1b).
- di-leptonic  $\tau\tau$ , where  $\tau \rightarrow q\bar{q}' + \nu_\tau, \tau \rightarrow e/\mu + \bar{\nu}_{e/\mu}$  (Figure 9.1c).

If, for example, the leptonically decaying W boson from a semi-leptonic  $t\bar{t}$  decay decays to a tau lepton and a tau neutrino, and the tau lepton then decays to another tau neutrino, an electron/muon and an electron neutrino/muon neutrino via a virtual W boson, such an event might fake our signal and pass the  $t\bar{t}$  signal selection. Fake events are removed by subtracting the fake distribution obtained from simulation. However, for the systematic

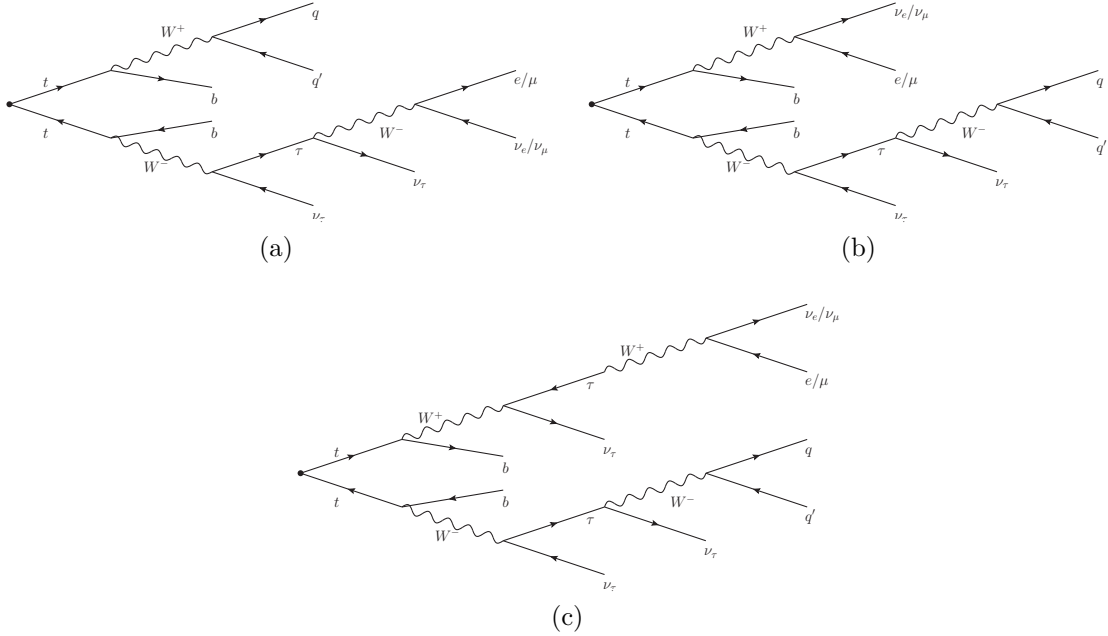


Figure 9.1: Feynman diagrams of semi-leptonic  $\tau$  events (a), dileptonic events with one  $\tau$  lepton (b) and dileptonic events with two  $\tau$  leptons (c).

measurements with the tau energy varied up and down, the same fake distribution shape is subtracted as in the nominal measurement. A comparison of the fakes and the signal  $E_T^{\text{miss}}$  distributions shapes from  $t\bar{t}$  simulation are shown on the left in Figure 9.2. It can be seen that the relative contribution from fakes increases as  $E_T^{\text{miss}}$  increases. Approximately 14% of the reconstructed  $t\bar{t}$  events in simulation are fake events (13.5% in electron channel and 13.9% in muon channel). The right hand plot in Figure 9.2 compares the normalisations of signal and fake events after selection. The effect of varying the electron and muon energies is not so pronounced because there are not many electrons or muons in the fake collection (a dileptonic  $t\bar{t}$  event with  $ee$ ,  $e\mu$  or  $\mu\mu$  would have to be misreconstructed as a semi-leptonic event for this to happen).

The difference between the tau energy down ( $-1\sigma$ ) variation and the nominal measurements in the  $E_T^{\text{miss}}$  variable before fitting and unfolding is shown in Figure 9.3. In the highest  $E_T^{\text{miss}}$  bin, the difference is approximately 6%, and this value remains approximately constant after fitting and unfolding. The significant affect of varying the tau energy is therefore unlikely to be an artifact of the fitting and/or unfolding procedure, but a real difference in the number

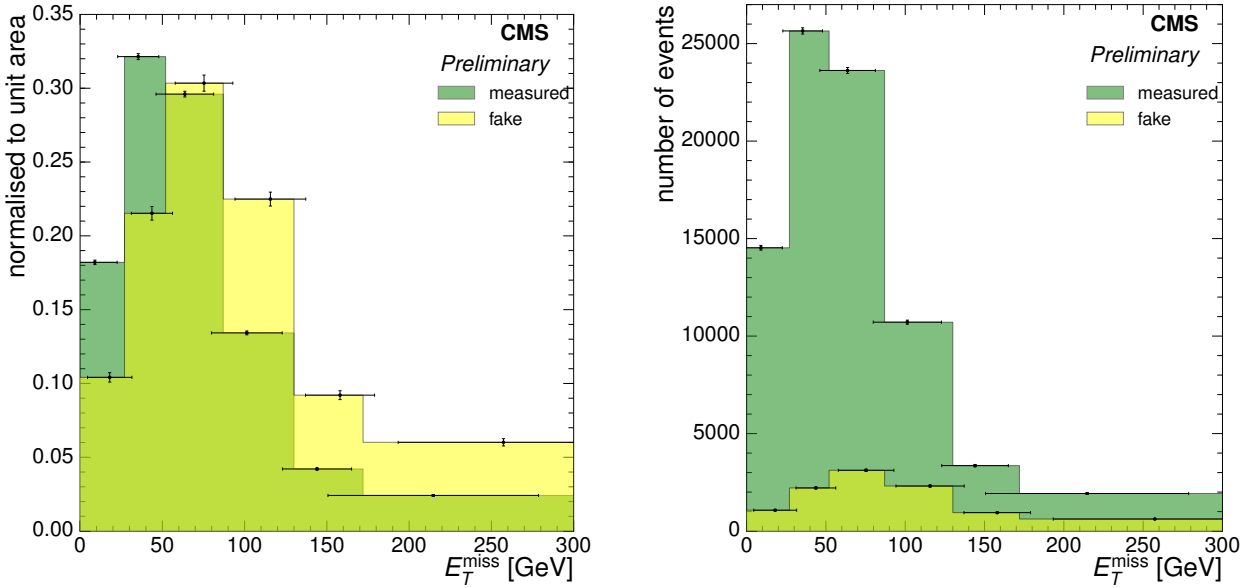


Figure 9.2: Comparison of the signal and fake distributions from semi-leptonic  $t\bar{t}$  events after selection in simulation in the electron+jets channel at  $\sqrt{s} = 8$  TeV normalised to one (left) and normalised to the numbers of events (right).

of events.

Other small sources of experimental uncertainty include the non-clustered energy uncertainty (which refers to fluctuations in deposits in the electromagnetic calorimeter that are not included in jet clusters), the matching threshold and factorisation and normalisation scale uncertainties in  $W + \text{jets}$  and  $Z + \text{jets}$  events, pileup uncertainty, the QCD template shape uncertainty, and the efficiency of electron, muon and b-tagging in the selection process.

Rate changing systematics such as the uncertainty on the luminosity and the uncertainty on the theoretical cross-sections of the signal and background processes have a negligible effect on the final result, since they cancel in the final normalised measurements.

### 9.1.2 Theoretical Uncertainties

#### 7 TeV V+Jets theory systematic template

The factorisation and normalisation scale ( $Q^2$  up/down) uncertainty is evaluated using simulation samples produced with the scale varied by factors of 2 (up) and 0.5 (down).

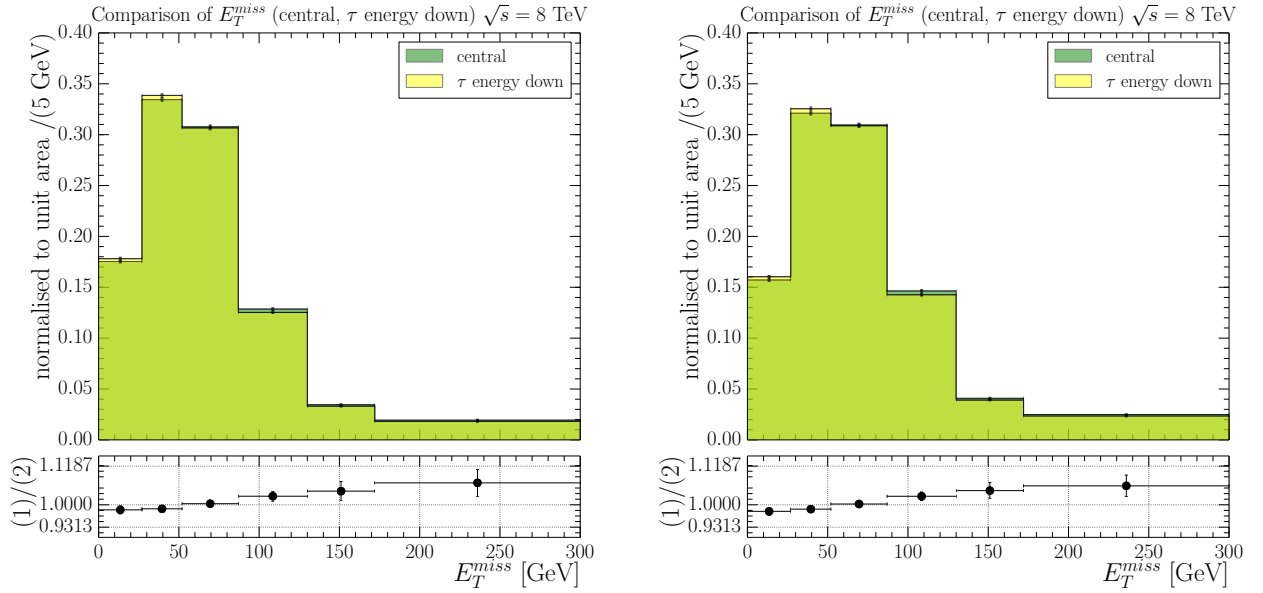


Figure 9.3: Comparison of the  $E_T^{\text{miss}}$  distributions in the nominal measurement and in the tau energy down variation before fitting and unfolding in data (left) and in  $t\bar{t}$  simulation (right) at  $\sqrt{s} = 8 \text{ TeV}$

This has been evaluated to be one of the dominating uncertainties in this analysis. The uncertainty in the matching threshold (matching up/down) for  $t\bar{t}$  events is evaluated in the same way.

Unfortunately, Monte Carlo simulation for theoretical systematic uncertainties at  $\sqrt{s} = 7 \text{ TeV}$  have not been made available for  $W+jets$  and  $Z+jets$  processes. However, it can be seen in Figure 9.4 that the  $W+jets$  template shapes at  $\sqrt{s} = 7 \text{ TeV}$  and  $\sqrt{s} = 8 \text{ TeV}$  are similar. The  $V+jets$  template shapes used to evaluate these theoretical systematics are therefore obtained from  $\sqrt{s} = 8 \text{ TeV}$  theoretical systematic datasets, and then scaled to the normalisation in the nominal sample at  $\sqrt{s} = 7 \text{ TeV}$ .

## Hadronisation Uncertainty

The uncertainty due to hadronisation modelling is evaluated by comparing a simulated sample generated using the POWHEG generator and PYTHIA to model the hadron showering (POWHEG + PYTHIA) to a sample generator using the same POWHEG generator and HERWIG to model the hadron showering (POWHEG + HERWIG). The difference

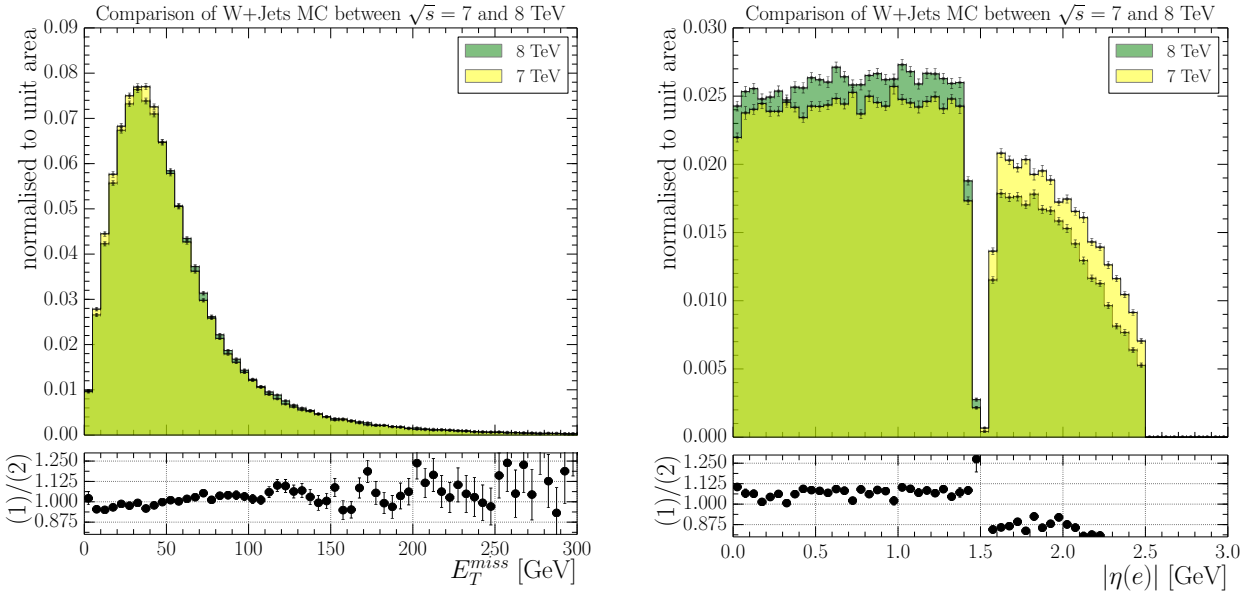


Figure 9.4: Shape comparison of W+jets templates in  $\sqrt{s} = 7$  TeV and  $\sqrt{s} = 8$  TeV Monte Carlo simulation for  $E_T^{\text{miss}}$  (left) and electron  $|\eta|$  (right) in the electron+jets channel.

between the PYTHIA and HERWIG samples is scaled to the nominal measurement and taken as the hadronisation uncertainty. All variables, and in particular those sensitive to hadronic aspects of an event such as  $H_T$  and  $S_T$ , are significantly affected by this systematic, with a larger uncertainty in lower bins of the primary variables.

## PDF Uncertainties

The proton PDF uncertainties are evaluated similarly, with 44 distinct weights from the CTEQ 6.6 PDF sets used to reweight events in the simulated samples and repeat the analysis. The top quark mass uncertainty is evaluated using  $t\bar{t}$  samples produced with two different top quark masses of 169.5 GeV and 173.5 GeV, and scaling the error obtained using these samples to the top mass uncertainty of  $\pm 1.0$  GeV.

## $t\bar{t}$ $p_T$ Mismodelling

There is a known issue with event generators mismodelling the top quark  $p_T$  distribution; the distribution of the transverse momentum of top quarks in data was found to be softer than that in simulation [37]. Scale factors have been derived to correct for this disagreement.

The effect of this correction on the nominal measurement was evaluated to be negligible for low values of the primary variables, increasing to 3–7% at higher values. The MADGRAPH simulation after applying the t-quark  $p_T$  correction is also included in the results plots (Figures 9.5 to 9.8), but this is not included as a systematic error.

The most significant shape changing uncertainties typically arise from the factorisation scale variations in the  $t\bar{t}$  process and the hadronisation.

### 9.1.3 Systematic Uncertainty Tables

Tables 9.1 and 9.2 give typical (median) relative systematic uncertainties for all systematic uncertainty sources, at  $\sqrt{s} = 7\text{ TeV}$  and  $\sqrt{s} = 8\text{ TeV}$  respectively, and are for the combined electron+jets and muon+jets channel, for the fitting method. The sources are grouped into categories, taking only the maximum relative uncertainty between a  $+1\sigma/-1\sigma$  variation of each uncertainty source. In categories containing more than one  $+1\sigma/-1\sigma$  variation pair ( $E_T^{\text{miss}}$  uncertainties: electron/muon/tau/unclustered energy; Background (other): $t\bar{t}$ /single top/V+jets/QCD cross sections and luminosity; Theoretical Systematics:  $t\bar{t}/V+\text{jets}$  matching and  $Q^2$ ), the maximum uncertainty of each  $+1\sigma/-1\sigma$  source is added in quadrature. The median values across all of the bins of a primary variable are then taken as the typical systematic uncertainties stated in the tables. Extended uncertainty tables can be found in Appendix B.10.

## 9.2 Results

The fitting and unfolding explained in Sections 8.3 and 8.6 is performed individually in the electron+jets and muon+jets channels, resulting in a number of  $t\bar{t}$  events in each channel. The measurement is then carried out as outlined in Section 8.6.1 on the numbers of events in each channel, in addition to the sum total of the two channels to calculate the cross section in the combined semi-leptonic channel. This section summarises the normalised differential cross sections for the primary variables investigated in this analysis. Figures 9.5 and 9.6

Table 9.1: Typical systematic uncertainties in percent (median values) for the normalised  $t\bar{t}$  differential cross section measurement at  $\sqrt{s} = 7$  TeV (combination of electron and muon channels). Typical values of the total systematic uncertainty are also shown.

Uncertainty source	$E_T^{\text{miss}}$	$H_T$	$S_T$	$p_T^W$	$M_T^W$
Electron trigger and selection efficiencies	< 1	1.30	1.41	< 1	< 1
Muon trigger and selection efficiencies	< 1	< 1	< 1	< 1	< 1
b-tagging	< 1	< 1	2.1	< 1	< 1
Jet Energy Scale	< 1	3.6	1.1	< 1	< 1
Jet Energy Resolution	< 1	3.1	1.6	< 1	< 1
$E_T^{\text{miss}}$ uncertainties	1.3	-	2.6	4.3	< 1
Pileup	< 1	0.1	2.4	< 1	< 1
QCD shape	< 1	< 1	2.2	< 1	< 1
Background (other)	< 1	< 1	3.6	< 1	< 1
Theoretical systematics	1.0	4.6	4.7	< 1	1.0
top mass	< 1	< 1	< 1	< 1	< 1
hadronisation	2.1	9.9	8.2	3.8	1.1
PDF uncertainties	< 1	< 1	< 1	< 1	< 1
$p_T$ reweighting	1.6	< 1	1.3	< 1	< 1
Total	3.7	12.4	14.6	6.8	2.9

show the distributions at  $\sqrt{s} = 7$  TeV; q and Figures 9.7 and 9.8 show the distributions at  $\sqrt{s} = 8$  TeV. Corresponding numerical results are included in Appendix B.11. Results plots showing the unfolded data distributions from the background subtraction method of extracting the  $t\bar{t}$  event yield are also shown in Appendix B.11.

The normalised cross section distributions are shown compared with predictions from MADGRAPH, POWHEG +PYTHIA, POWHEG +HERWIG, MC@NLO ( $\sqrt{s} = 8$  TeV only) and a MADGRAPH prediction with corrected t-quark  $p_T$  in the left hand plots. The error bars on the data points represent the statistical +unfolding (inner) and systematic uncertainties summed in quadrature (outer). In the right hand plots a comparison with the MADGRAPH prediction with matching threshold, and factorisation and renormalisation scale up and down. Ratio plots are shown below the distribution plots to allow easier comparison of the

Table 9.2: Typical systematic uncertainties in percent (median values) for the normalised  $t\bar{t}$  differential cross section measurement at  $\sqrt{s} = 8$  TeV (combination of electron and muon channels). Typical values of the total systematic uncertainty are also shown.

Uncertainty source	$E_T^{\text{miss}}$	$H_T$	$S_T$	$p_T^W$	$M_T^W$
Electron trigger and selection efficiencies	< 1	< 1	< 1	< 1	< 1
Muon trigger and selection efficiencies	< 1	< 1	< 1	< 1	< 1
b-tagging	< 1	< 1	< 1	< 1	< 1
Jet Energy Scale	< 1	1.7	1.4	0.5	0.7
Jet Energy Resolution	< 1	< 1	< 1	< 1	< 1
$E_T^{\text{miss}}$ uncertainties	2.8	-	1.0	2.4	< 1
Pileup	< 1	< 1	< 1	< 1	< 1
QCD shape	< 1	< 1	< 1	< 1	< 1
Background (other)	< 1	< 1	< 1	< 1	< 1
Theoretical systematics	7.2	5.2	3.7	3.2	1.7
Top quark mass	< 1	< 1	< 1	< 1	< 1
Hadronisation	4.2	4.6	7.2	3.0	1.4
PDF uncertainties	< 1	< 1	< 1	< 1	< 1
$p_T$ reweighting	< 1	< 1	< 1	< 1	< 1
Total	9.0	8.3	7.4	5.4	

distribution in data to the different simulations, with a line at 1.0 for reference. In the ratio plots, the grey error bands represent the statistical + unfolding uncertainty, while the yellow error bands represent the systematic uncertainties added in quadrature. The systematic uncertainties resulting from matching and factorisation and renormalisation scale are excluded from the systematic uncertainties in plots comparing the data distribution with theoretical variations. Similarly, the hadronisation uncertainty is excluded in plots comparing the data distribution with different simulation generators. It can be seen that the data distributions show softer distributions than in simulation as a result of the mismodelling of the t-quark  $p_T$  in the generators [37]. The corrected MADGRAPH distribution, however, shows good agreement with the data.

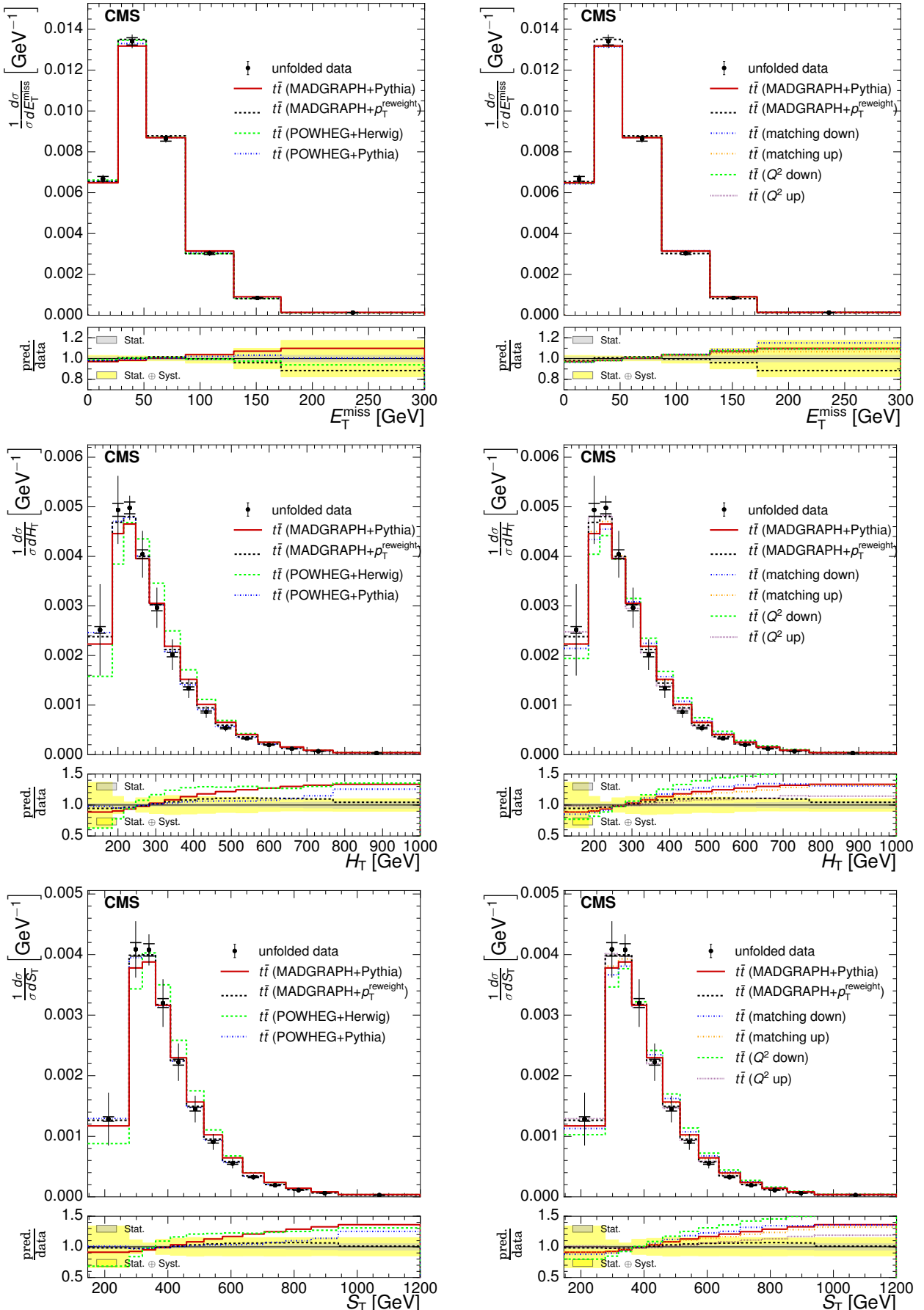


Figure 9.5: Comparison of the measured normalised differential cross section with respect to  $E_T^{\text{miss}}$  (upper),  $H_T$  (middle) and  $S_T$  (lower) to different Monte Carlo generators: MADGRAPH, POWHEG +HERWIG, POWHEG +PYTHIA and MADGRAPH corrected for top  $p_T$  mismodelling (left) and to different Monte Carlo predictions matching threshold up/down and factorisation scale up/down (right) in the combined electron+jets and muon+jets channel at 130 GeV. The plots show the ratio of predicted to data (pred./data) with statistical and systematic uncertainties.

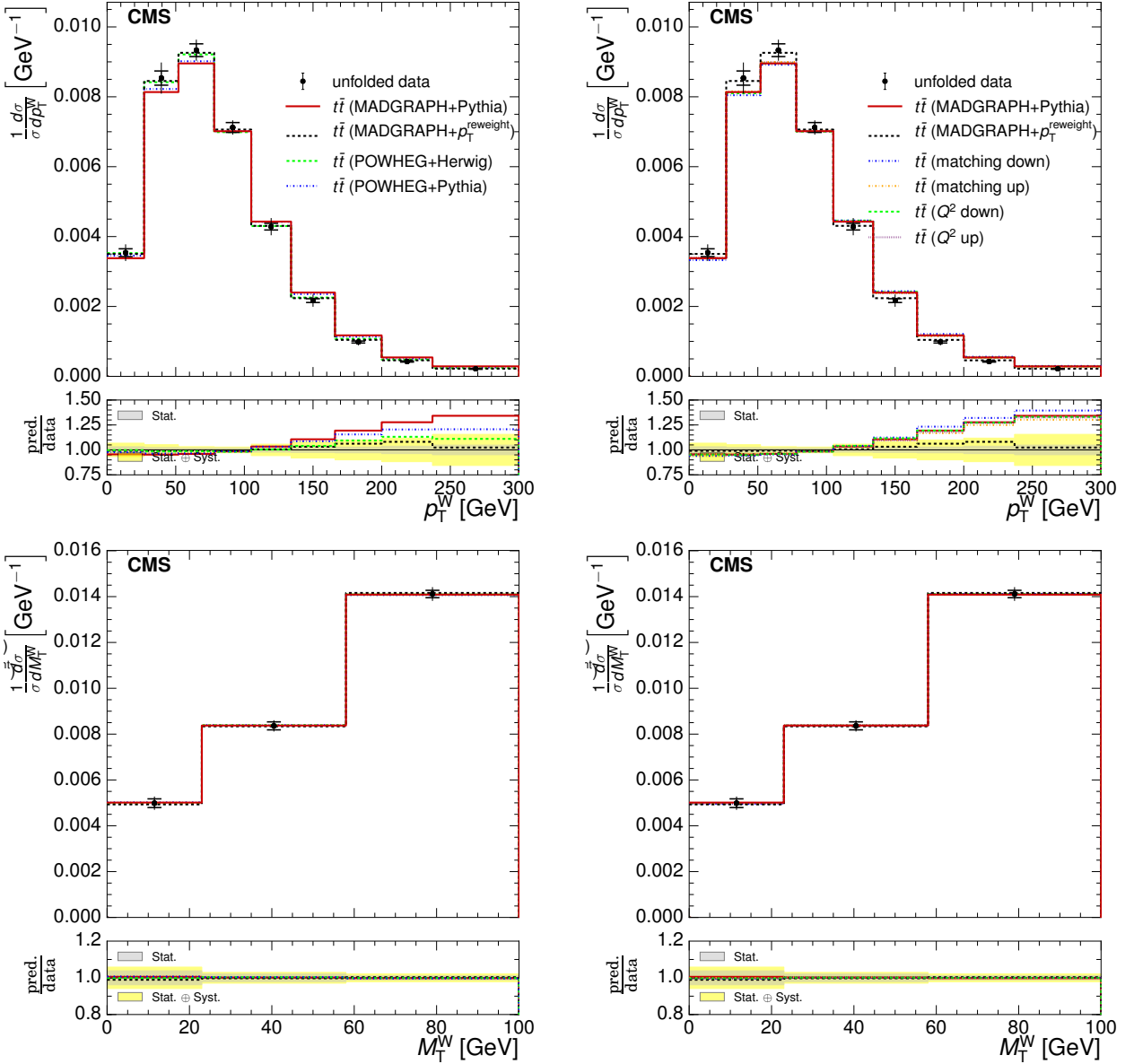


Figure 9.6: Comparison of the measured normalised differential cross section with respect to  $p_T^W$  and  $M_T^W$  to different Monte Carlo generators: MADGRAPH, POWHEG +HERWIG, POWHEG +PYTHIA and MADGRAPH corrected for top  $p_T$  mismodelling (left) and to different Monte Carlo predictions matching threshold up/down and factorisation scale up/down (right) in the combined electron+jets and muon+jets channel at  $\sqrt{s} = 7$  TeV. The lower plots show the ratio of the predictions to the data.

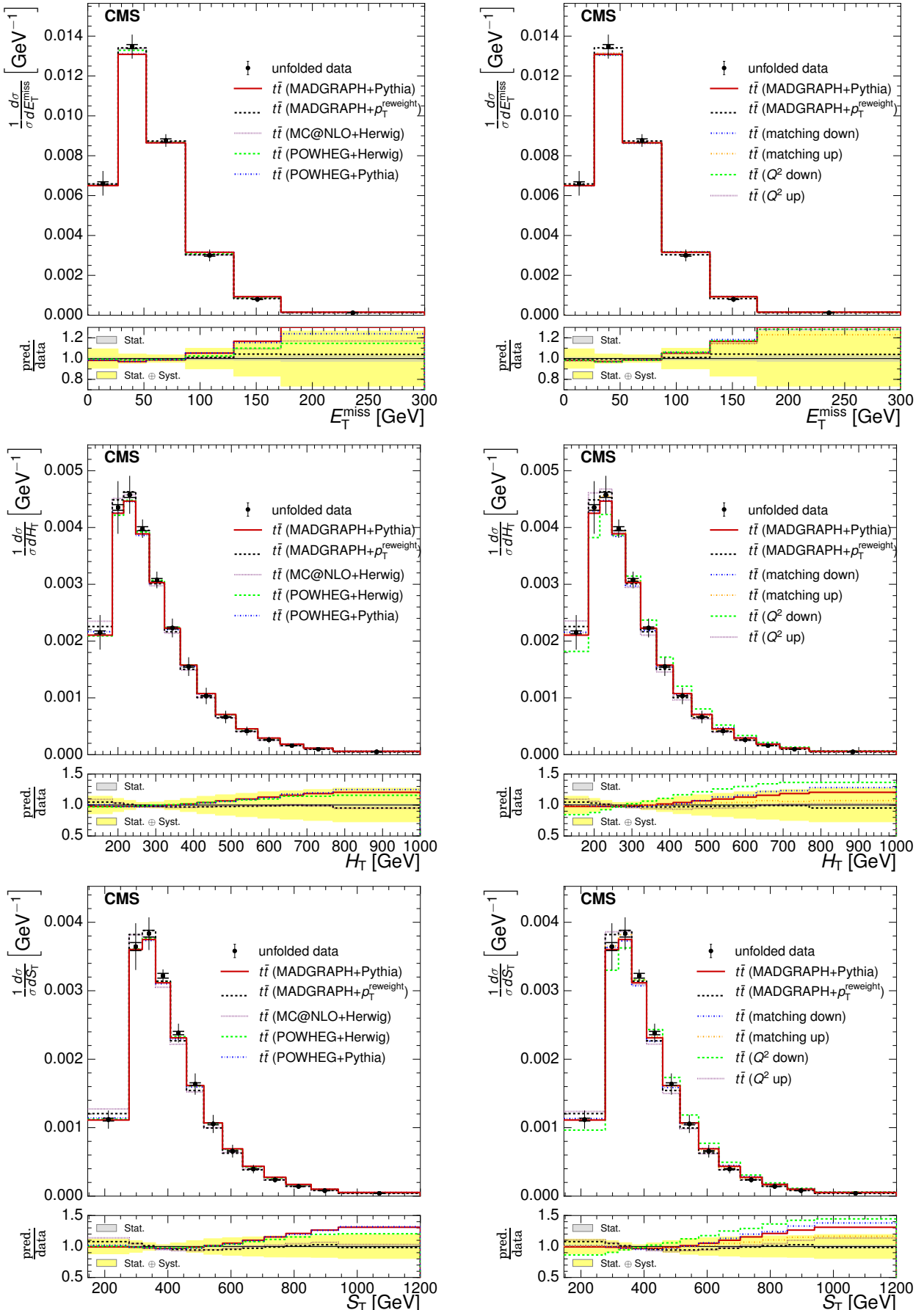


Figure 9.7: Comparison of the measured normalised differential cross section with respect to  $E_T^{\text{miss}}$ ,  $H_T$  and  $S_T$  to different Monte Carlo generators: MADGRAPH, POWHEG +HERWIG, POWHEG +PYTHIA and MADGRAPH corrected for top  $p_T$  mismodelling (left) and to different Monte Carlo predictions matching threshold up/down and factorisation scale up/down (right) in the combined electron+jets and muon+jets channel at  $\sqrt{s} = 8$  TeV. 132

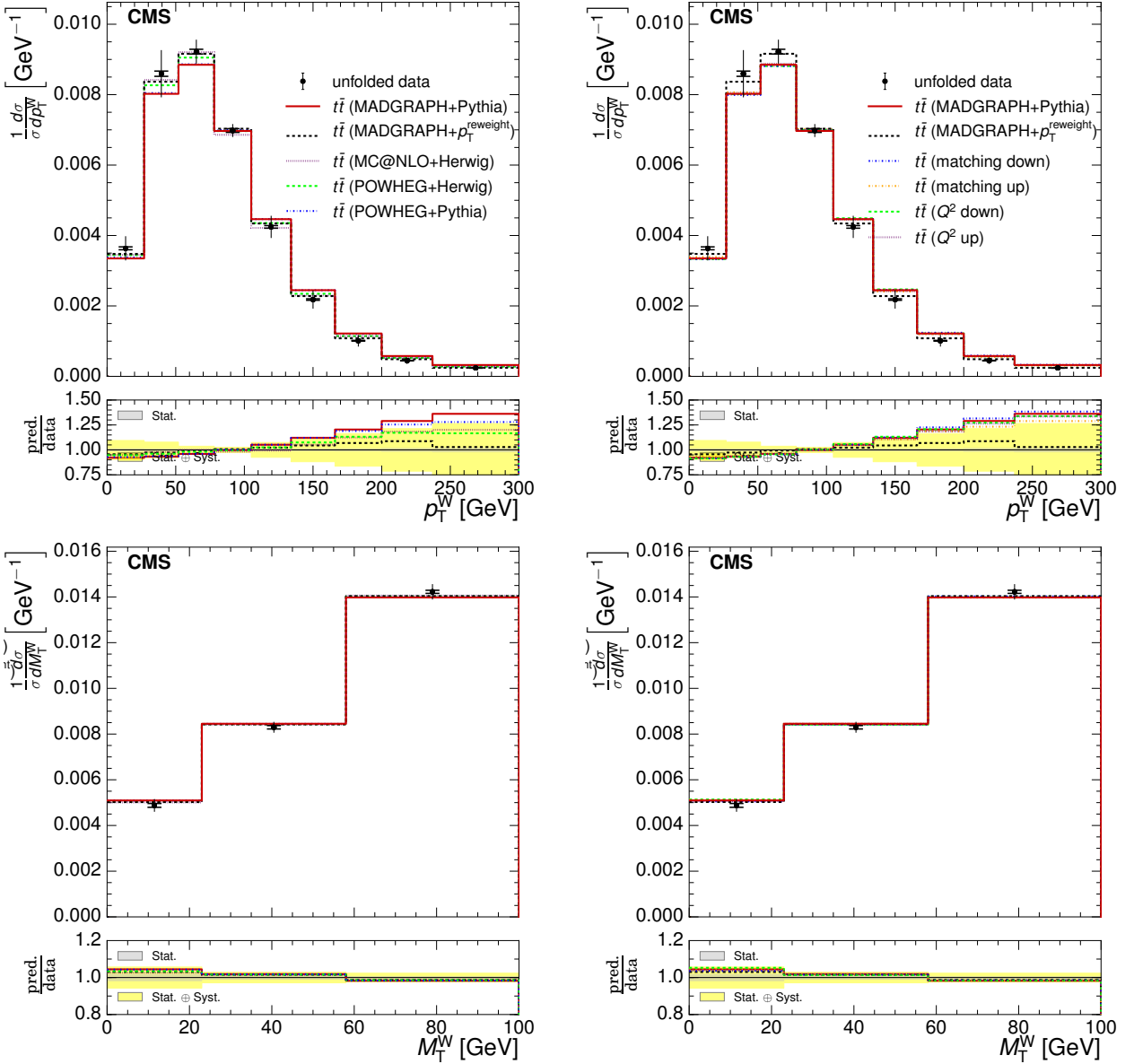


Figure 9.8: Comparison of the measured normalised differential cross section with respect to  $p_T^W$  and  $M_T^W$  to different Monte Carlo generators: MADGRAPH, POWHEG +HERWIG, POWHEG +PYTHIA and MADGRAPH corrected for top  $p_T$  mismodelling (left) and to different Monte Carlo predictions matching threshold up/down and factorisation scale up/down (right) in the combined electron+jets and muon+jets channel at  $\sqrt{s} = 8$  TeV. The lower plots show the ratio of the predictions to the data.



# 10 | Summary

This thesis has presented an overview of the theoretical background to the Standard Model, a summary of the CMS detector at the LHC, and a measurement of differential  $t\bar{t}$  cross sections with respect to global variables  $E_T^{\text{miss}}$ ,  $H_T$ ,  $S_T$ ,  $M_T^W$  and  $p_T^W$  in proton-proton collisions with  $5.0 \text{ fb}^{-1}$  of data at  $\sqrt{s}=7 \text{ TeV}$  and with  $19.7 \text{ fb}^{-1}$  of data at  $\sqrt{s}=8 \text{ TeV}$  collected with the CMS experiment at the LHC.

The main objective of these measurements is to verify the models and generators used to produce simulations of the signal and background events in CMS. This understanding provides a good basis in new physics analyses where such events constitute a significant background. In addition, the distributions under investigation would be sensitive to rare standard model processes; for example, the  $E_T^{\text{miss}}$  or  $M_T^W$  distributions would be sensitive to  $t\bar{t} + Z/W$  processes, while the  $H_T$ ,  $S_T$  and  $p_T^W$  distributions would provide information on  $t\bar{t} + X$  production where  $X$  is massive and decays to hadrons. Hints of new physics scenarios such as stop pair production may also be visible in the distributions of global variables.

The results of this analysis confirmed the previously observed characteristic of a  $p_T$  distribution that is softer in data than in the simulation. The simulated distribution corrected for this mismodelling shows good agreement with data, however. Otherwise, the data shows good general agreement with the theoretical predictions, showing that these commonly used Monte Carlo simulation generators can be used with confidence to model  $t\bar{t}$  events.

Run 2 of the LHC after Long Shutdown 1 began in June 2015 with proton-proton collisions occurring at  $\sqrt{s} = 13 \text{ TeV}$ . Further measurements of  $t\bar{t}$  events are on-going at the LHC on Run 2 data and will no doubt continue to do so. Currently an Early Analysis (analyses aimed to obtain and demonstrate that the detector and simulations are well understood at this early stage of Run 2) is being carried out by the same group that worked on the

analysis presented in this thesis on  $40 \text{ pb}^{-1}$  of LHC Run 2 data from CMS. As collision energies and luminosities at the LHC increase, the resulting higher statistics and larger cross sections in the coming years could lead to the observation of rare physics processes and/or the production of potential heavier particles than observed to date.

Run 2 is scheduled to continue until Long Shutdown 2 in 2018 when major accelerator and experiment upgrades will take place. Until then, regular technical stops, such as vacation periods, will allow for routine maintenance to be carried out. A summary of the service work carried out by the author for the CMS experiment has also been covered. Work relating to strip tracker operations and maintenance, and investigation of the new binary CBC readout chip for the strip tracker. Currently the newer CBC2 is undergoing testing, with a CBC3 already in the design stages and final testing to begin in 2018 for a scheduled installation in CMS at the HL-LHC from 2023 onwards.

# A | b-tagging Study Plots

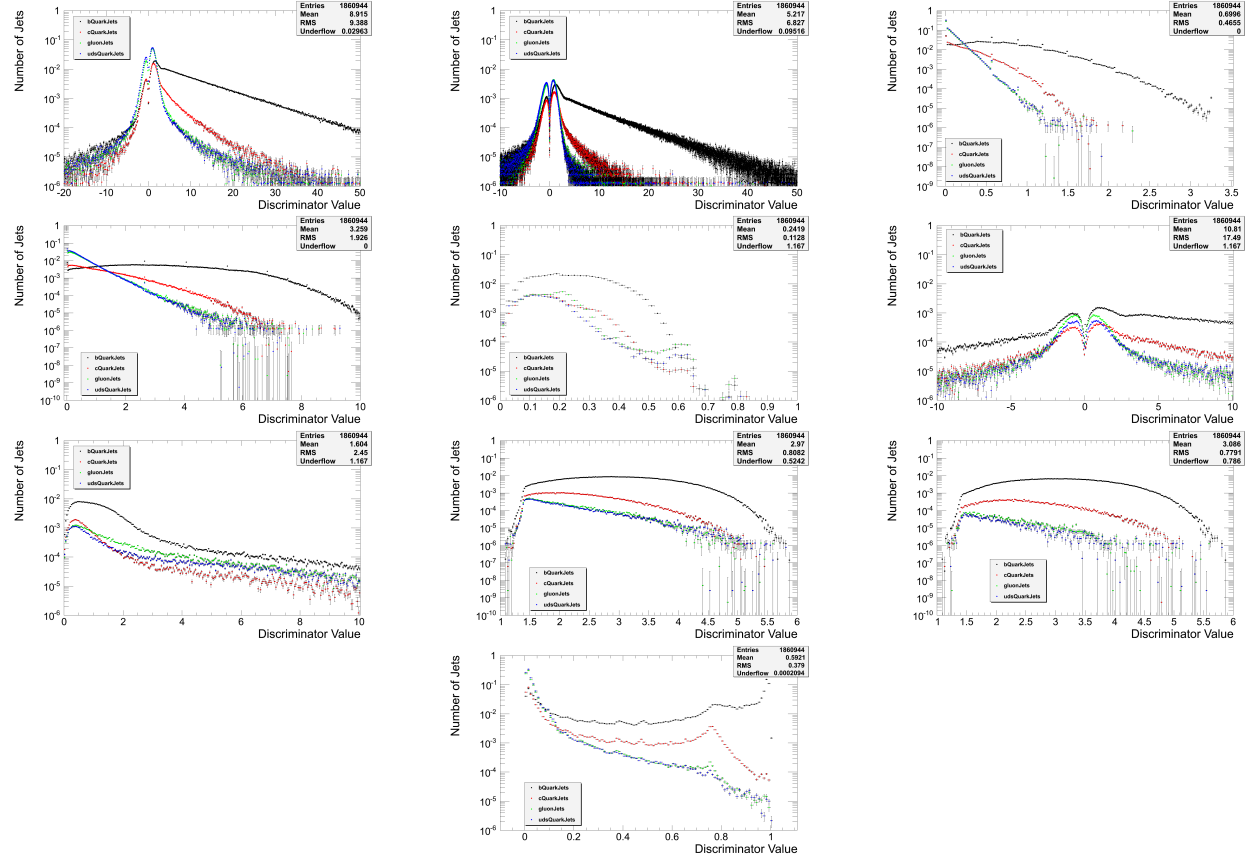


Figure A.1: Discriminator values produced by, from upper left: Track Counting High Efficiency, Track Counting High Purity, Jet Probability, JetBProbability, Soft Muon, Soft Muon by IP, Soft Muon by  $p_T$ , SSV High Efficiency, SSV High Purity and the CSV MVA algorithm for b-jets, c-jets, g-jets and uds-jets after normalisation

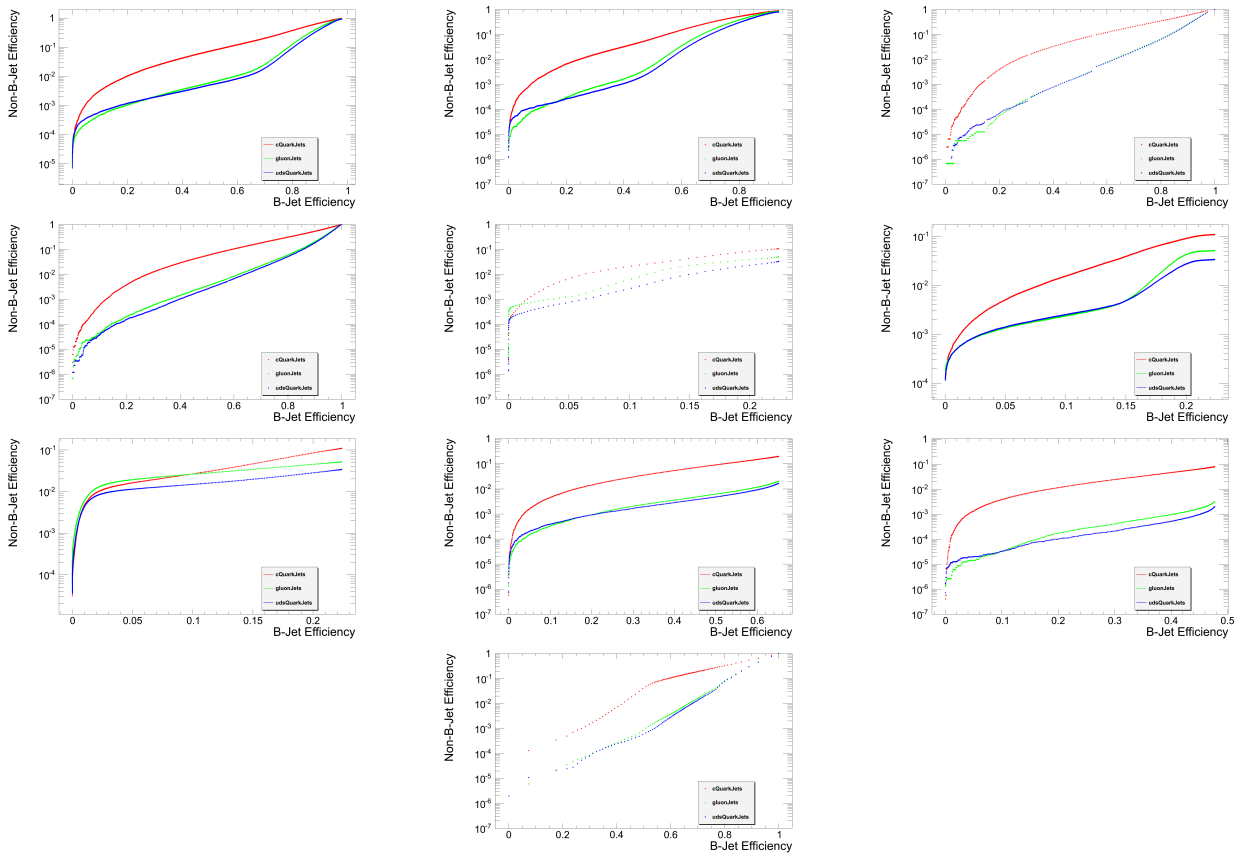


Figure A.2: c-jet, g-jet and uds-jet efficiencies as a function of b-jet efficiency for, from upper left: Track Counting High Efficiency, Track Counting High Purity, Jet Probability, JetBProbability, Soft Muon, Soft Muon by IP, Soft Muon by  $p_T$ , SSV High Efficiency, SSV High Purity and the CSV MVA algorithm.

# B | $t\bar{t}$ different cross section analysis

## B.1 Datasets in differential cross section analysis

Year	$\sqrt{s}$ ( TeV)	Channel	HLT Trigger
2011	7	electron	HLT_Ele25_CaloIdVT_TrkIdT_CentralTriJet30
2011	7	electron	HLT_Ele25_CaloIdVT_TrkIdT_TriCentralJet30
2011	7	electron	HLT_Ele25_CaloIdVT_CaloIsoT_TrkIdT_TrkIsoT_TriCentralJet30
2011	7	electron	HLT_Ele25_CaloIdVT_CaloIsoT_TrkIdT_TrkIsoT_TriCentralPFJ
2012	8	electron	HLT_Ele27_WP80
2011	7	muon	HLT_IsoMu24
2011	7	muon	HLT_IsoMu24_eta2p1
2012	8	muon	HLT_IsoMu24_eta2p1_v

Table B.1: HLT Triggers used in 2011 and 2012 data in the electron and muon channels.

Data Period	Mask
2011	Cert_160404-180252_7TeV_ReRecoNov08_Collisions11_JSON_v2.txt
2012	Cert_190456-208686_8TeV_22Jan2013ReReco_Collisions12_JSON.txt

Table B.2: JSON files used for the 2011 and 2012 data taking periods.

## B.2 Data - Monte Carlo corrections

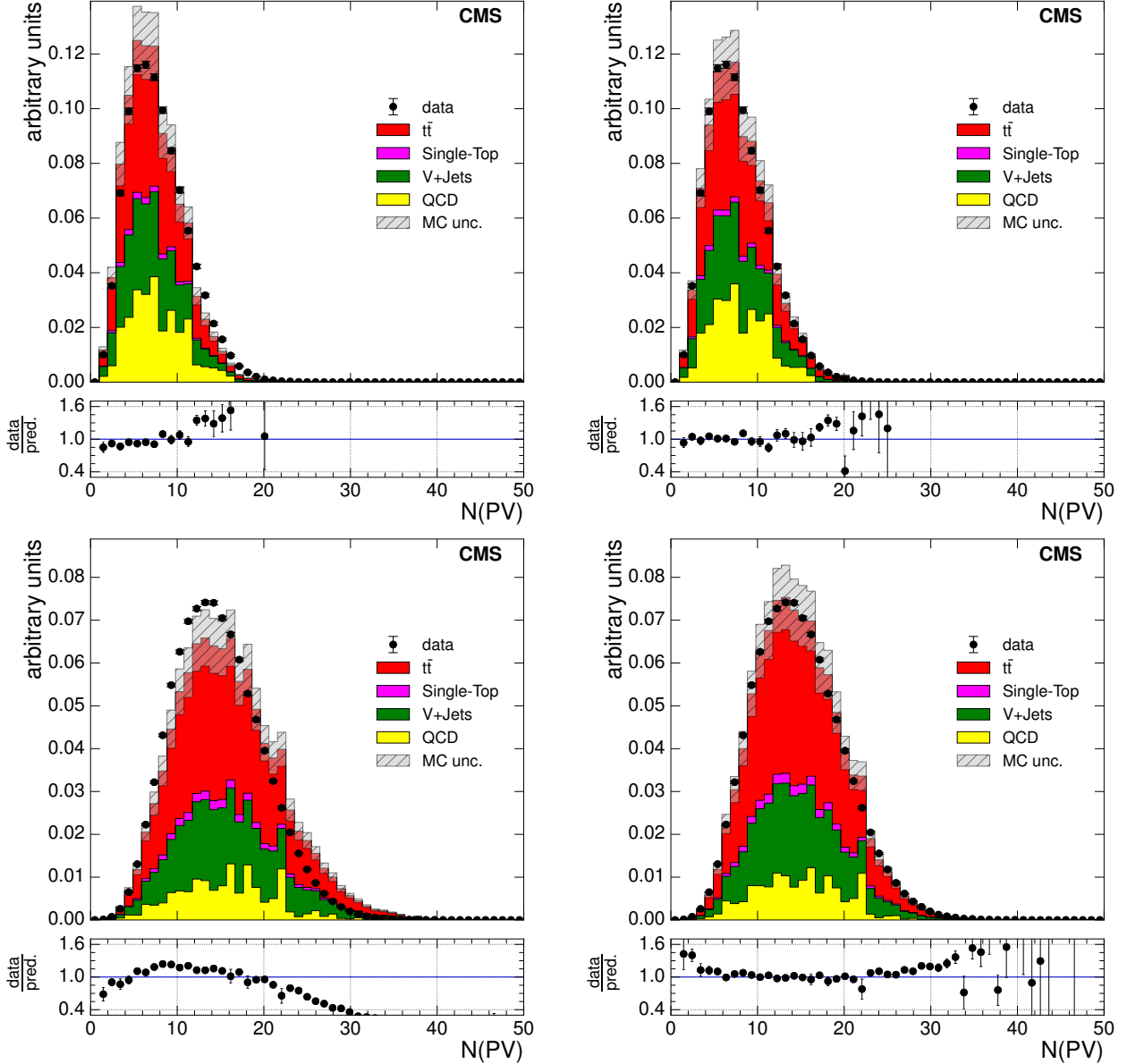


Figure B.1: Distributions of the number of reconstructed vertices in an event in the muon+jets channel before implementing pileup reweighting (left) and after implementation (right) at  $\sqrt{s} = 7\text{ TeV}$  (upper) and  $\sqrt{s} = 8\text{ TeV}$  (lower).

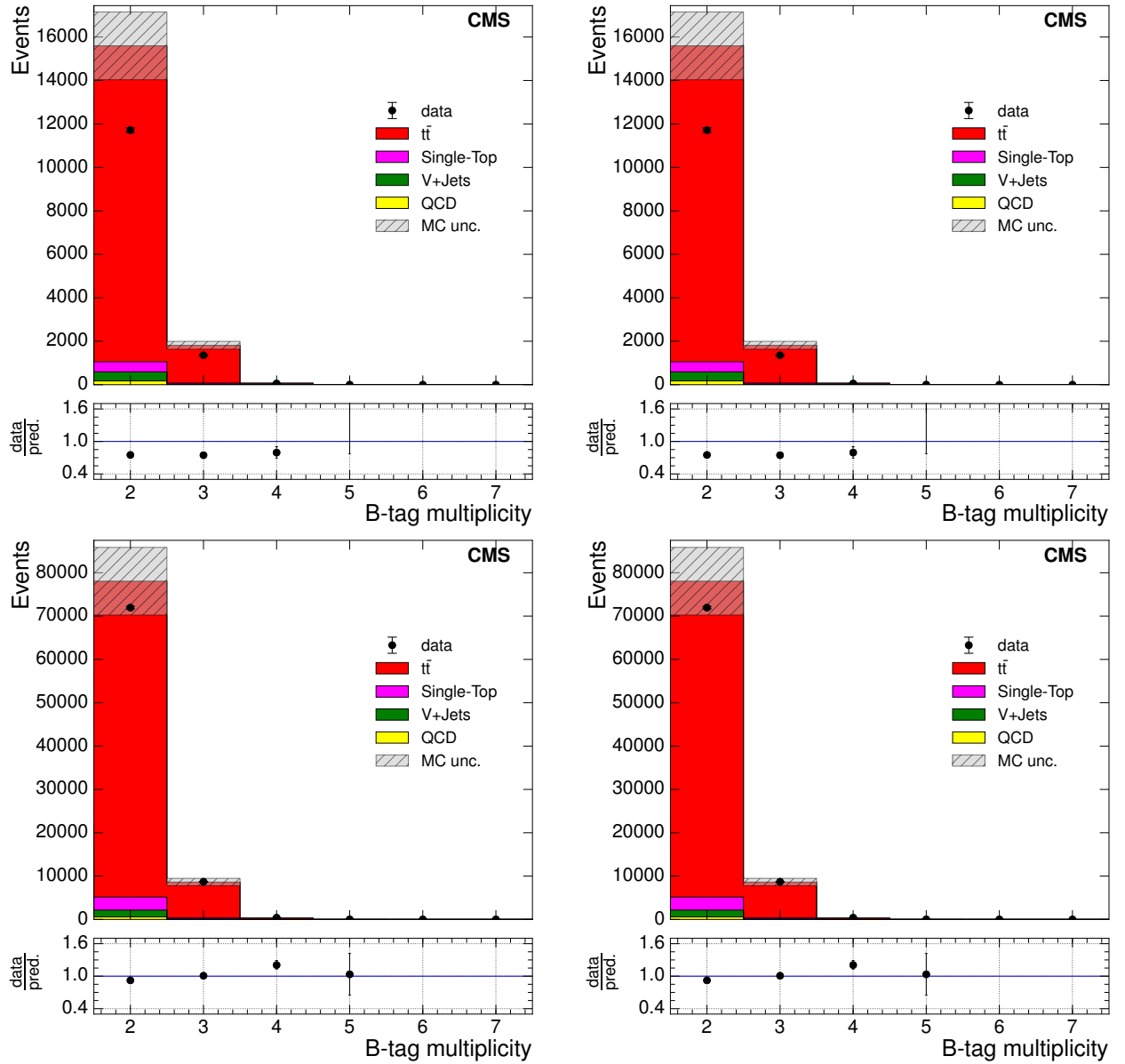


Figure B.2: Distributions of the number of b-tags in an event in the muon+jets channel before applying b-tag scale factors (left) and after application (right) at  $\sqrt{s} = 7 \text{ TeV}$  (upper) and  $\sqrt{s} = 8 \text{ TeV}$  (lower).

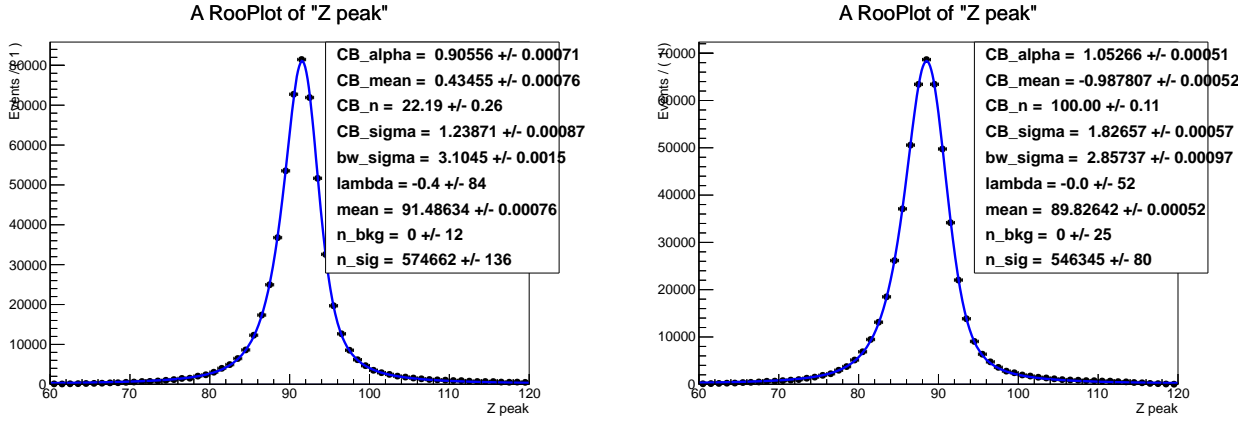


Figure B.3: Fits of the invariant mass distribution of all tag-and-probe pairs (left) and for tag-and-probe pairs in which the probe passes the trigger (right).

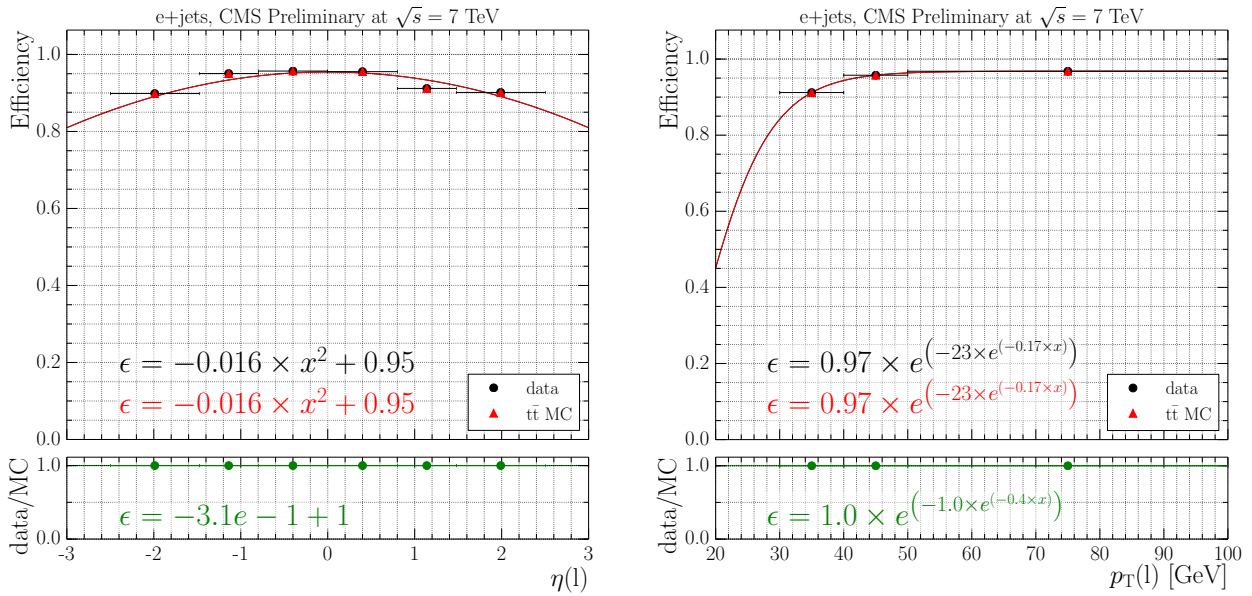


Figure B.4: Trigger efficiencies as a function of  $\eta$  and  $p_T$  in data and  $t\bar{t}$  Monte Carlo simulation.

### B.3 Binning in the muon+jets channel

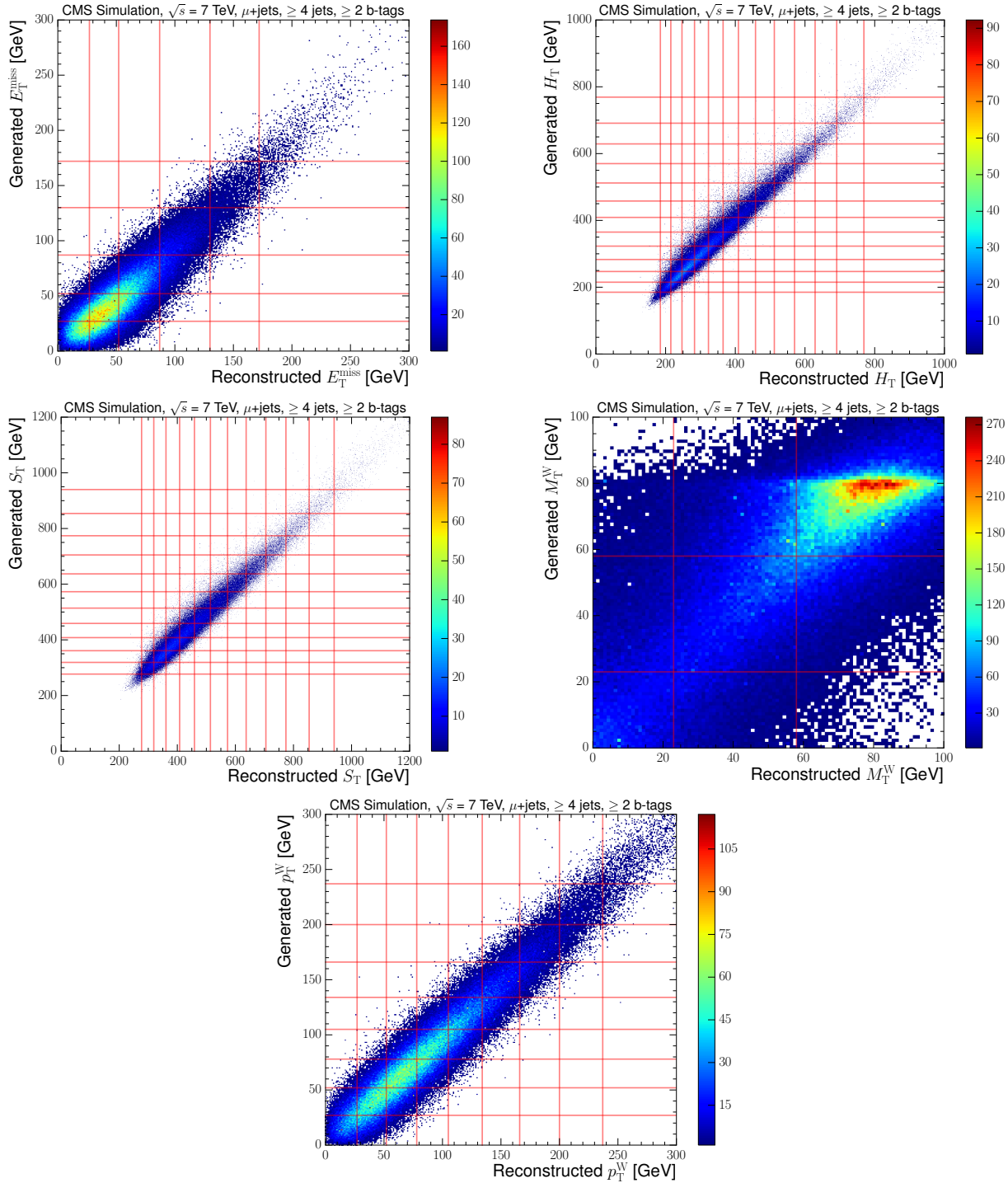


Figure B.5: Generated versus reconstructed distributions of the primary variables  $E_T^{\text{miss}}$  (upper left),  $H_T$  (upper right),  $S_T$  (middle left),  $M_T^W$  (middle right) and  $p_T^W$  (lower) with horizontal and vertical lines representing the boundaries of the selected bins at  $\sqrt{s} = 7 \text{ TeV}$  in the muon+jets channel. These distributions are obtained using  $t\bar{t}$  simulation.

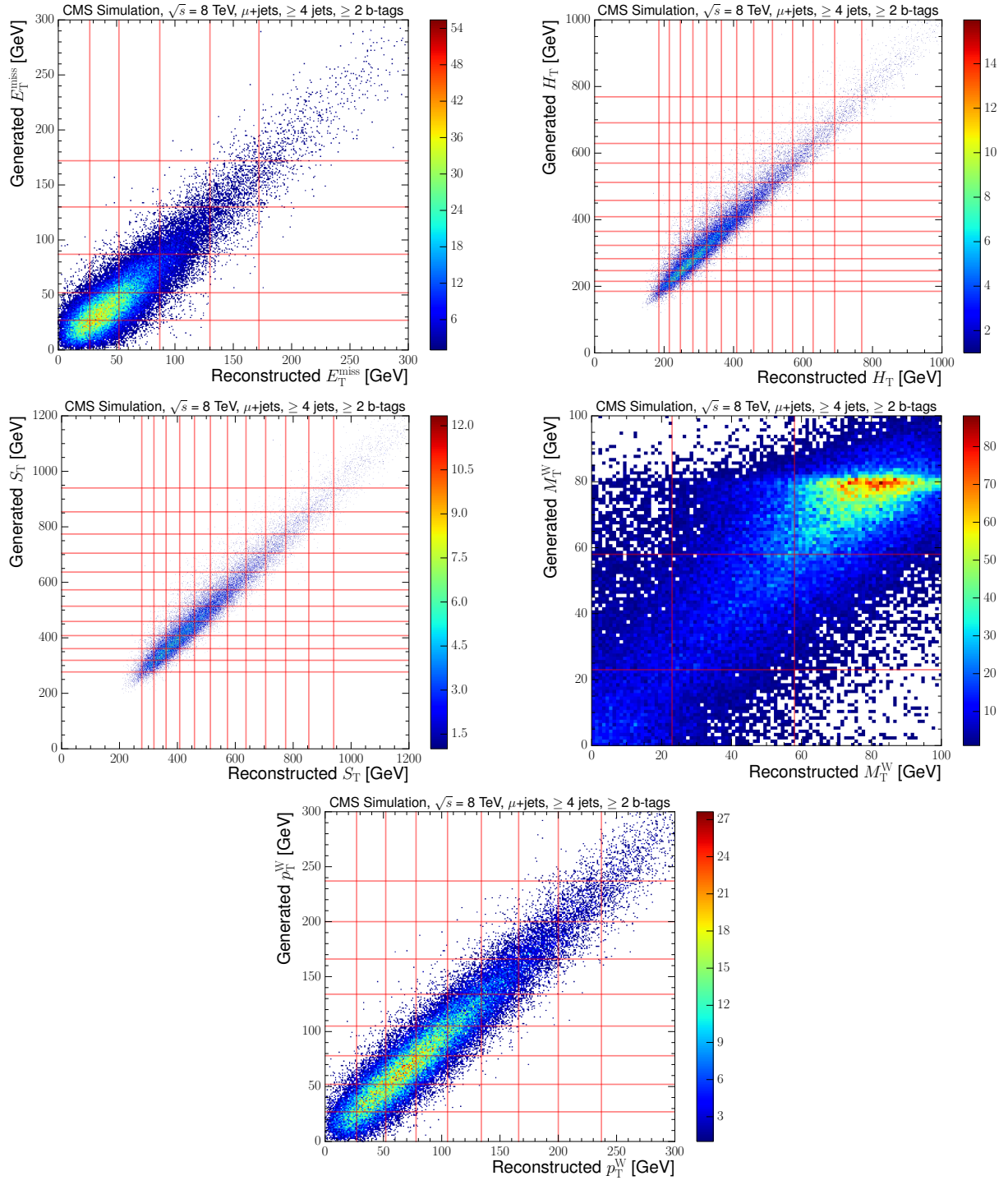


Figure B.6: Generated versus reconstructed distributions of the primary variables  $E_T^{\text{miss}}$  (upper left),  $H_T$  (upper right),  $S_T$  (middle left),  $M_T^W$  (middle right) and  $p_T^W$  (lower) with horizontal and vertical lines representing the boundaries of the selected bins at  $\sqrt{s} = 8 \text{ TeV}$  in the muon+jets channel. These distributions are obtained using  $t\bar{t}$  simulation.

## B.4 Binning choice tables

$E_T^{\text{miss}}$ bin ( GeV)	purity	stability	number of events
0 - 27	0.649	0.533	1367
27 - 52	0.588	0.538	2187
52 - 87	0.537	0.636	1691
87 - 130	0.542	0.666	660
130 - 172	0.521	0.624	179
$\geq 172$	0.711	0.824	119
$H_T$ bin ( GeV)	purity	stability	number of events
0 - 186	0.589	0.567	102
186 - 216	0.546	0.565	344
216 - 249	0.542	0.585	676
249 - 286	0.541	0.575	884
286 - 326	0.543	0.556	896
326 - 368	0.536	0.538	765
368 - 412	0.537	0.517	598
412 - 462	0.566	0.538	518
462 - 516	0.573	0.531	375
516 - 574	0.580	0.537	264
574 - 634	0.590	0.529	172
634 - 696	0.581	0.539	113
696 - 781	0.660	0.624	100
$\geq 781$	0.886	0.814	117
$S_T$ bin ( GeV)	purity	stability	number of events
0 - 277	0.565	0.550	108
277 - 319	0.564	0.549	422
319 - 361	0.538	0.543	743
361 - 408	0.530	0.547	939
408 - 459	0.527	0.539	897
459 - 514	0.534	0.536	764
514 - 573	0.539	0.530	601
573 - 637	0.548	0.532	449
637 - 705	0.548	0.534	305
705 - 774	0.540	0.523	194
774 - 854	0.576	0.566	151
854 - 946	0.613	0.580	102
$\geq 946$	0.838	0.837	133
$M_T^W$ bin ( GeV)	purity	stability	number of events
0 - 23	0.528	0.598	659
23 - 58	0.515	0.562	1557
$\geq 58$	0.845	0.786	4518
$p_T^W$ bin ( GeV)	purity	stability	number of events
0 - 27	0.597	0.549	467
27 - 52	0.551	0.526	960
52 - 78	0.550	0.540	1228
78 - 105	0.539	0.538	1107
105 - 134	0.537	0.554	857
134 - 166	0.537	0.568	570
166 - 200	0.524	0.564	314
200 - 237	0.536	0.573	177
$\geq 237$	0.707	0.789	145

Table B.3: The selected bins for the measurement in the electron channel at a centre-of-mass energy of 7 TeV. In addition to the bin ranges<sup>147</sup> the purity, stability and number of expected  $t\bar{t}$  events are shown.

$E_T^{\text{miss}}$ bin ( GeV)	purity	stability	number of events
0 - 27	0.641	0.533	1445
27 - 52	0.587	0.536	2374
52 - 87	0.552	0.638	1982
87 - 130	0.550	0.673	770
130 - 172	0.533	0.634	207
$\geq 172$	0.706	0.844	133
$H_T$ bin ( GeV)	purity	stability	number of events
0 - 186	0.595	0.568	121
186 - 216	0.543	0.563	397
216 - 249	0.545	0.583	787
249 - 286	0.541	0.576	1008
286 - 326	0.546	0.559	1010
326 - 368	0.540	0.538	841
368 - 412	0.547	0.529	675
412 - 462	0.569	0.542	558
462 - 516	0.584	0.537	406
516 - 574	0.585	0.547	281
574 - 634	0.590	0.542	181
634 - 696	0.597	0.546	119
696 - 781	0.682	0.623	105
$\geq 781$	0.885	0.818	117
$S_T$ bin ( GeV)	purity	stability	number of events
0 - 277	0.562	0.552	135
277 - 319	0.560	0.542	503
319 - 361	0.536	0.546	866
361 - 408	0.532	0.546	1056
408 - 459	0.530	0.543	1003
459 - 514	0.538	0.540	853
514 - 573	0.543	0.531	645
573 - 637	0.553	0.534	477
637 - 705	0.548	0.539	326
705 - 774	0.542	0.523	200
774 - 854	0.571	0.557	152
854 - 946	0.598	0.585	101
$\geq 946$	0.847	0.832	138
$M_T^W$ bin ( GeV)	purity	stability	number of events
0 - 23	0.535	0.608	742
23 - 58	0.523	0.574	1777
$\geq 58$	0.851	0.789	5093
$p_T^W$ bin ( GeV)	purity	stability	number of events
0 - 27	0.599	0.544	558
27 - 52	0.559	0.529	1141
52 - 78	0.549	0.539	1369
78 - 105	0.531	0.538	1190
105 - 134	0.537	0.557	928
134 - 166	0.537	0.569	610
166 - 200	0.526	0.568	336
200 - 237	0.532	0.575	183
$\geq 237$	0.689	0.794	150

Table B.4: The selected bins for the measurement in the muon channel at a centre-of-mass energy of 7 TeV. In addition to the bin ranges<sup>148</sup> the purity, stability and number of expected  $t\bar{t}$  events are shown.

$E_T^{\text{miss}}$ bin ( GeV)	purity	stability	number of events
0 - 27	0.634	0.505	6400
27 - 52	0.557	0.507	9823
52 - 87	0.503	0.606	7792
87 - 130	0.517	0.643	3239
130 - 172	0.500	0.598	904
$\geq 172$	0.700	0.840	670
$H_T$ bin ( GeV)	purity	stability	number of events
0 - 186	0.556	0.514	430
186 - 216	0.511	0.508	1408
216 - 249	0.508	0.540	2878
249 - 286	0.511	0.540	3869
286 - 326	0.502	0.524	3892
326 - 368	0.508	0.511	3463
368 - 412	0.506	0.500	2828
412 - 462	0.532	0.510	2457
462 - 516	0.534	0.509	1857
516 - 574	0.547	0.500	1256
574 - 634	0.557	0.512	902
634 - 696	0.518	0.505	584
696 - 781	0.627	0.551	572
$\geq 781$	0.872	0.815	801
$S_T$ bin ( GeV)	purity	stability	number of events
0 - 277	0.580	0.500	463
277 - 319	0.539	0.500	1769
319 - 361	0.509	0.515	3204
361 - 408	0.505	0.522	4126
408 - 459	0.501	0.514	4035
459 - 514	0.504	0.510	3532
514 - 573	0.503	0.502	2780
573 - 637	0.517	0.510	2179
637 - 705	0.517	0.504	1507
705 - 774	0.506	0.508	1039
774 - 854	0.540	0.504	769
854 - 946	0.552	0.550	551
$\geq 946$	0.842	0.831	909
$M_T^W$ bin ( GeV)	purity	stability	number of events
0 - 23	0.515	0.577	3245
23 - 58	0.507	0.541	7446
$\geq 58$	0.823	0.774	20751
$p_T^W$ bin ( GeV)	purity	stability	number of events
0 - 27	0.556	0.505	1962
27 - 52	0.531	0.507	4354
52 - 78	0.527	0.513	5536
78 - 105	0.515	0.510	5131
105 - 134	0.510	0.533	4051
134 - 166	0.518	0.546	2775
166 - 200	0.502	0.544	1590
200 - 237	0.511	0.545	903
$\geq 237$	0.683	0.790	792

Table B.5: The selected bins for the measurement in the electron channel at a centre-of-mass energy of 8 TeV. In addition to the bin ranges<sup>149</sup> the purity, stability and number of expected  $t\bar{t}$  events are shown.

$E_T^{\text{miss}}$ bin ( GeV)	purity	stability	number of events
0 - 27	0.638	0.511	7341
27 - 52	0.563	0.515	11569
52 - 87	0.526	0.610	9865
87 - 130	0.506	0.651	3814
130 - 172	0.504	0.592	1050
$\geq 172$	0.695	0.845	802
$H_T$ bin ( GeV)	purity	stability	number of events
0 - 186	0.559	0.514	527
186 - 216	0.518	0.515	1698
216 - 249	0.518	0.537	3521
249 - 286	0.507	0.548	4735
286 - 326	0.507	0.523	4725
326 - 368	0.500	0.504	4032
368 - 412	0.503	0.501	3297
412 - 462	0.536	0.503	2815
462 - 516	0.529	0.503	2087
516 - 574	0.549	0.520	1551
574 - 634	0.542	0.502	987
634 - 696	0.560	0.504	656
696 - 781	0.644	0.607	641
$\geq 781$	0.886	0.796	842
$S_T$ bin ( GeV)	purity	stability	number of events
0 - 277	0.583	0.523	629
277 - 319	0.548	0.519	2276
319 - 361	0.511	0.508	3895
361 - 408	0.504	0.522	5021
408 - 459	0.502	0.519	4855
459 - 514	0.508	0.512	4170
514 - 573	0.511	0.500	3248
573 - 637	0.502	0.504	2393
637 - 705	0.522	0.517	1766
705 - 774	0.519	0.500	1135
774 - 854	0.546	0.529	884
854 - 946	0.571	0.558	621
$\geq 946$	0.836	0.837	961
$M_T^W$ bin ( GeV)	purity	stability	number of events
0 - 23	0.506	0.589	3712
23 - 58	0.511	0.554	9078
$\geq 58$	0.836	0.774	25227
$p_T^W$ bin ( GeV)	purity	stability	number of events
0 - 27	0.589	0.520	2700
27 - 52	0.535	0.509	5484
52 - 78	0.524	0.509	6644
78 - 105	0.507	0.515	5918
105 - 134	0.509	0.526	4588
134 - 166	0.504	0.544	3012
166 - 200	0.513	0.546	1767
200 - 237	0.506	0.558	994
$\geq 237$	0.676	0.801	894

Table B.6: The selected bins for the measurement in the muon channel at a centre-of-mass energy of 8 TeV. In addition to the bin ranges<sup>150</sup> the purity, stability and number of expected  $t\bar{t}$  events are shown.

## B.5 Fitting Variable Distributions

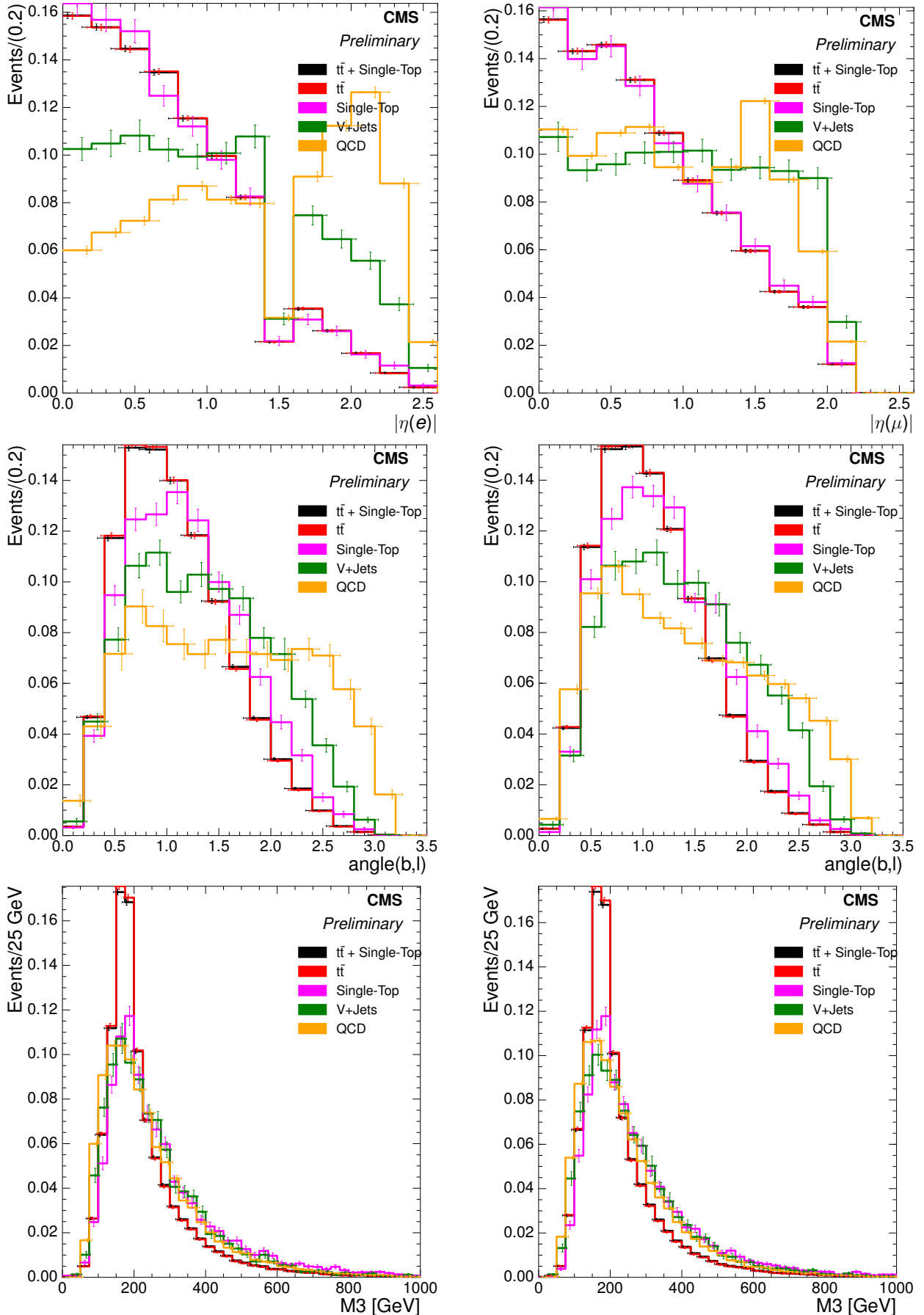


Figure B.7: Normalised distributions of the templates for the three fit variables lepton  $|\eta|$  (upper),  $\alpha$  (middle) and  $M_3$  (lower) inclusive across all primary variable bins at  $\sqrt{s} = 8$  TeV in the electron+jets channel (left) and in the muon+jets channel (right).

## B.6 Fitting variable QCD background template comparisons

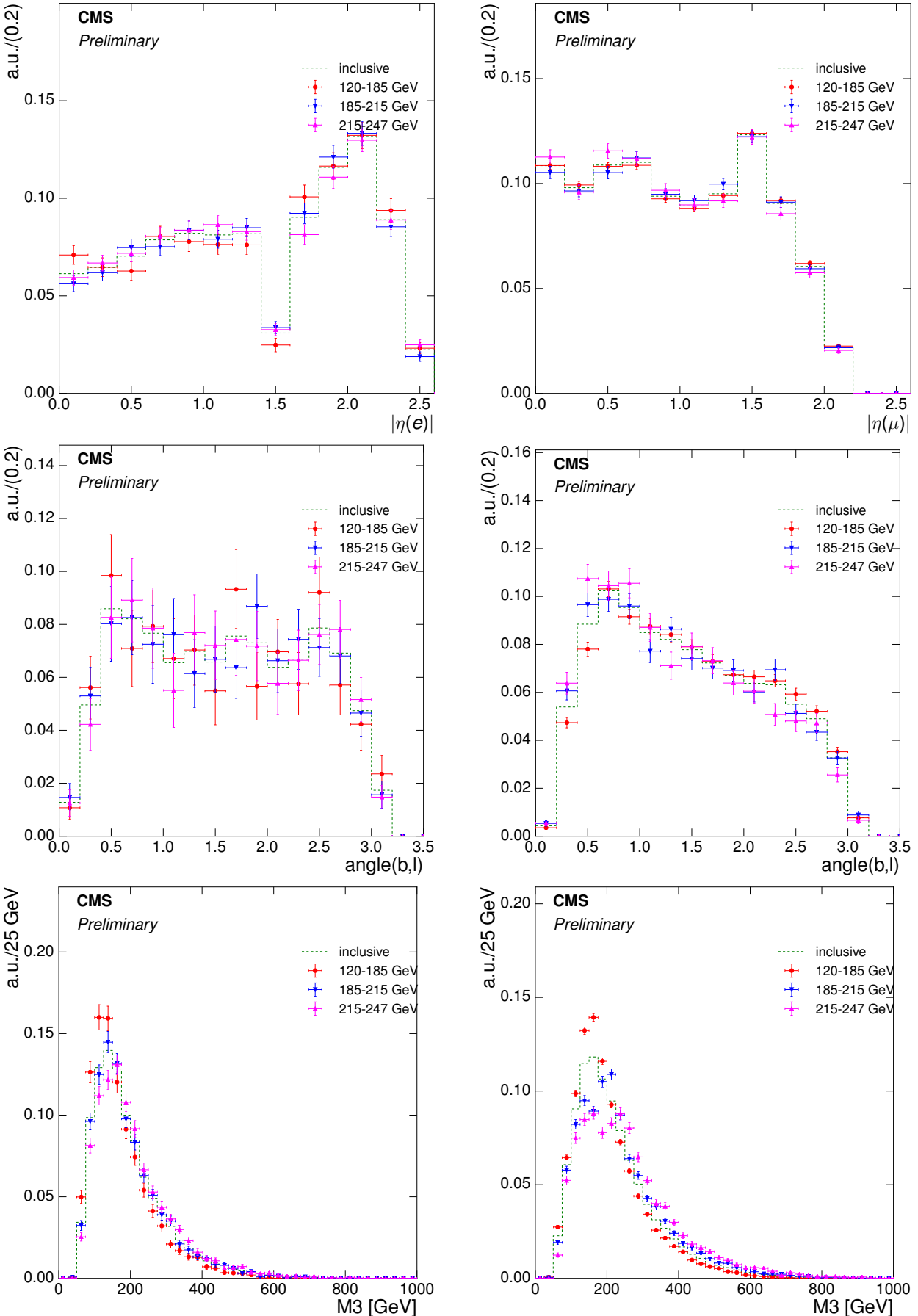


Figure B.8: Normalised distributions of the QCD templates for the three fit variables lepton  $|\eta|$  (upper),  $\alpha$  (middle) and  $M3$  (lower) inclusive across all  $H_T$  bins and for the lowest three  $H_T$  bins at  $\sqrt{s} = 8$  TeV in the electron+jets channel (left) and in the muon+jets channel (right).

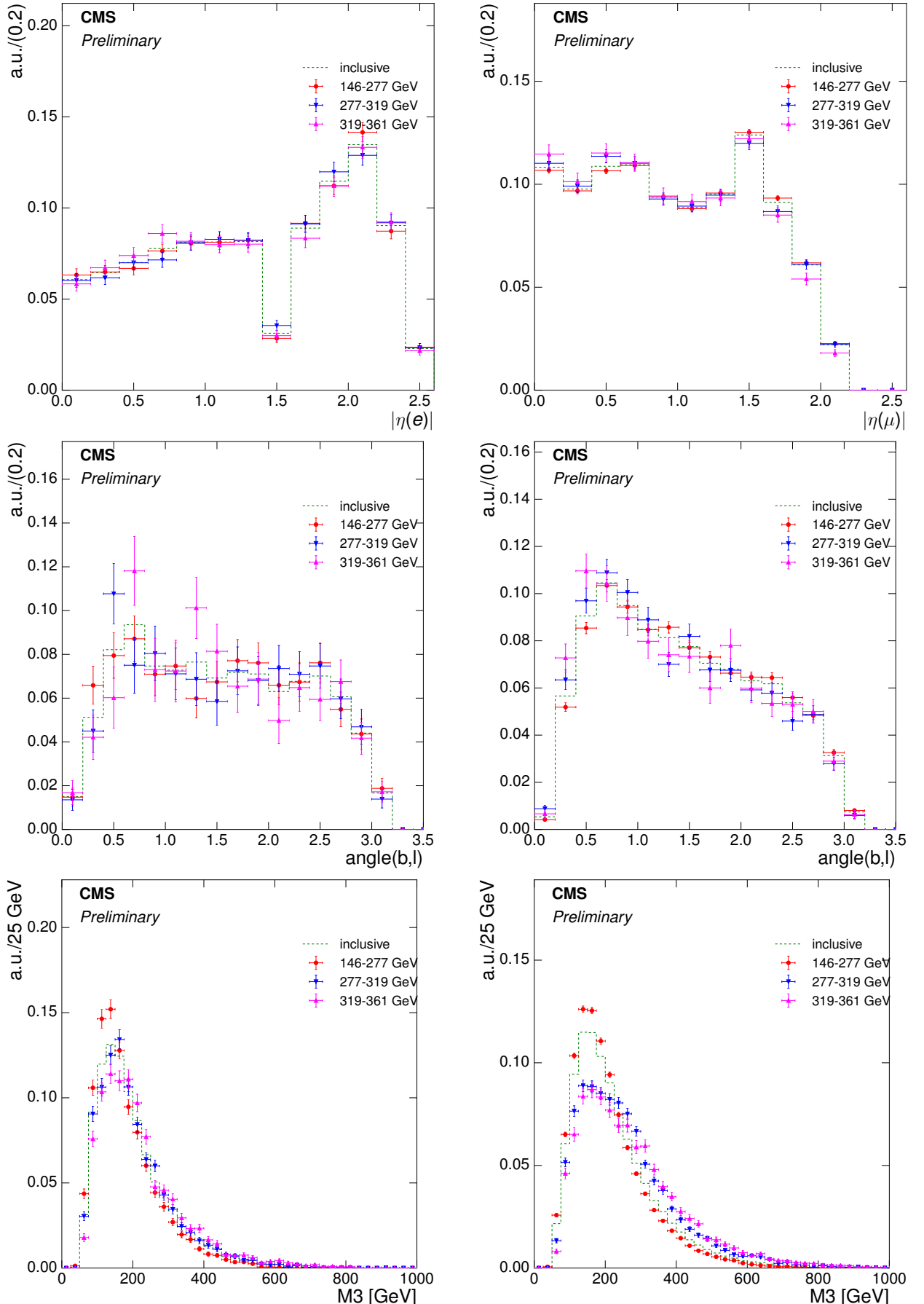


Figure B.9: Normalised distributions of the QCD templates for the three fit variables lepton  $|\eta|$  (upper),  $\alpha$  (middle) and  $M3$  (lower) inclusive across all  $S_T$  bins and for the lowest three  $S_T$  bins at  $\sqrt{s} = 8 \text{ TeV}$  in the electron+jets channel (left) and in the muon+jets channel (right).

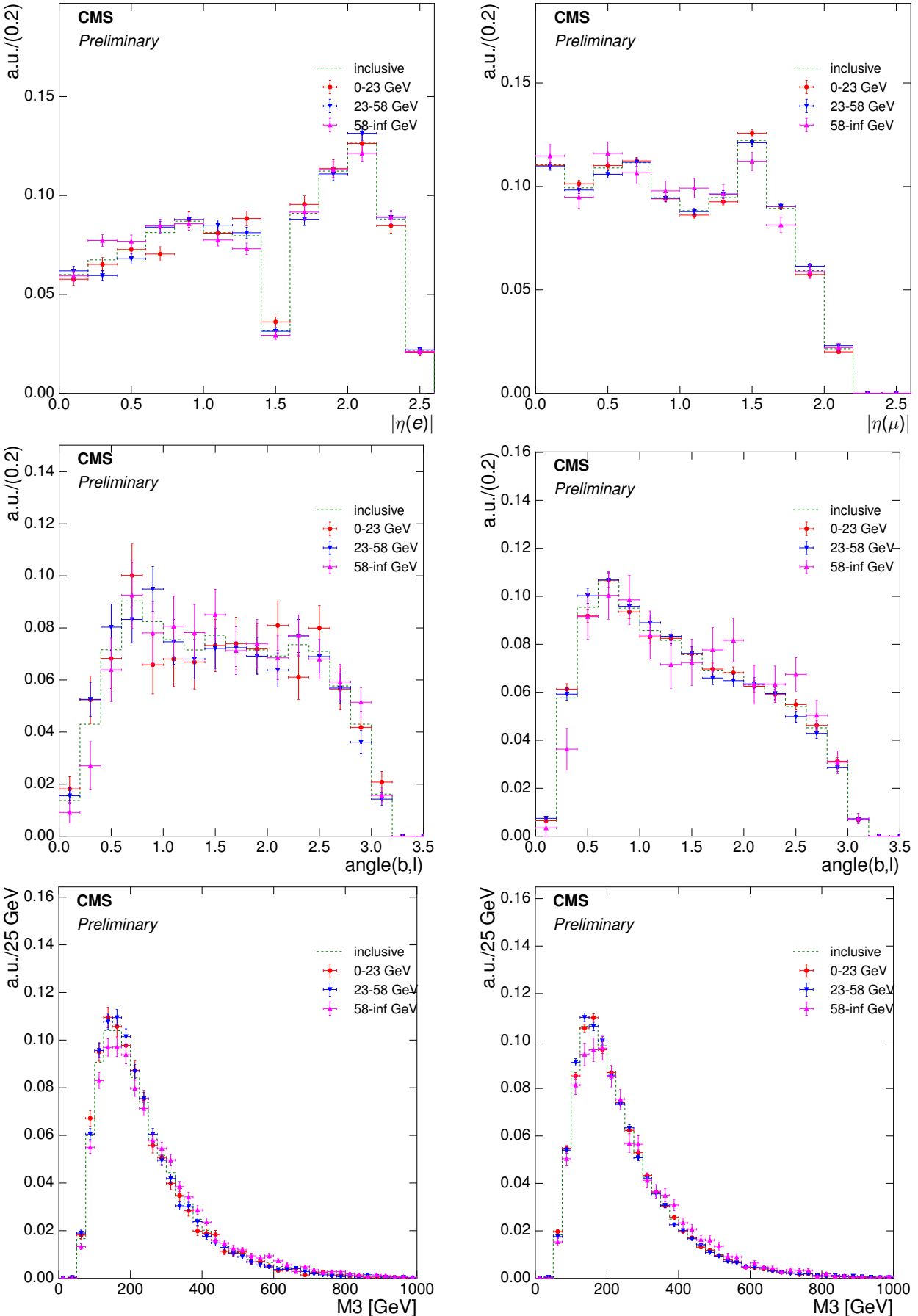


Figure B.10: Normalised distributions of the QCD templates for the three fit variables lepton  $|\eta|$  (upper),  $\alpha$  (middle) and  $M_3$  (lower) inclusive across all  $M_T^W$  bins and for the lowest three  $M_T^W$  bins at  $\sqrt{s} = 8 \text{ TeV}$  in the electron+jets channel (left) and in the muon+jets channel (right).

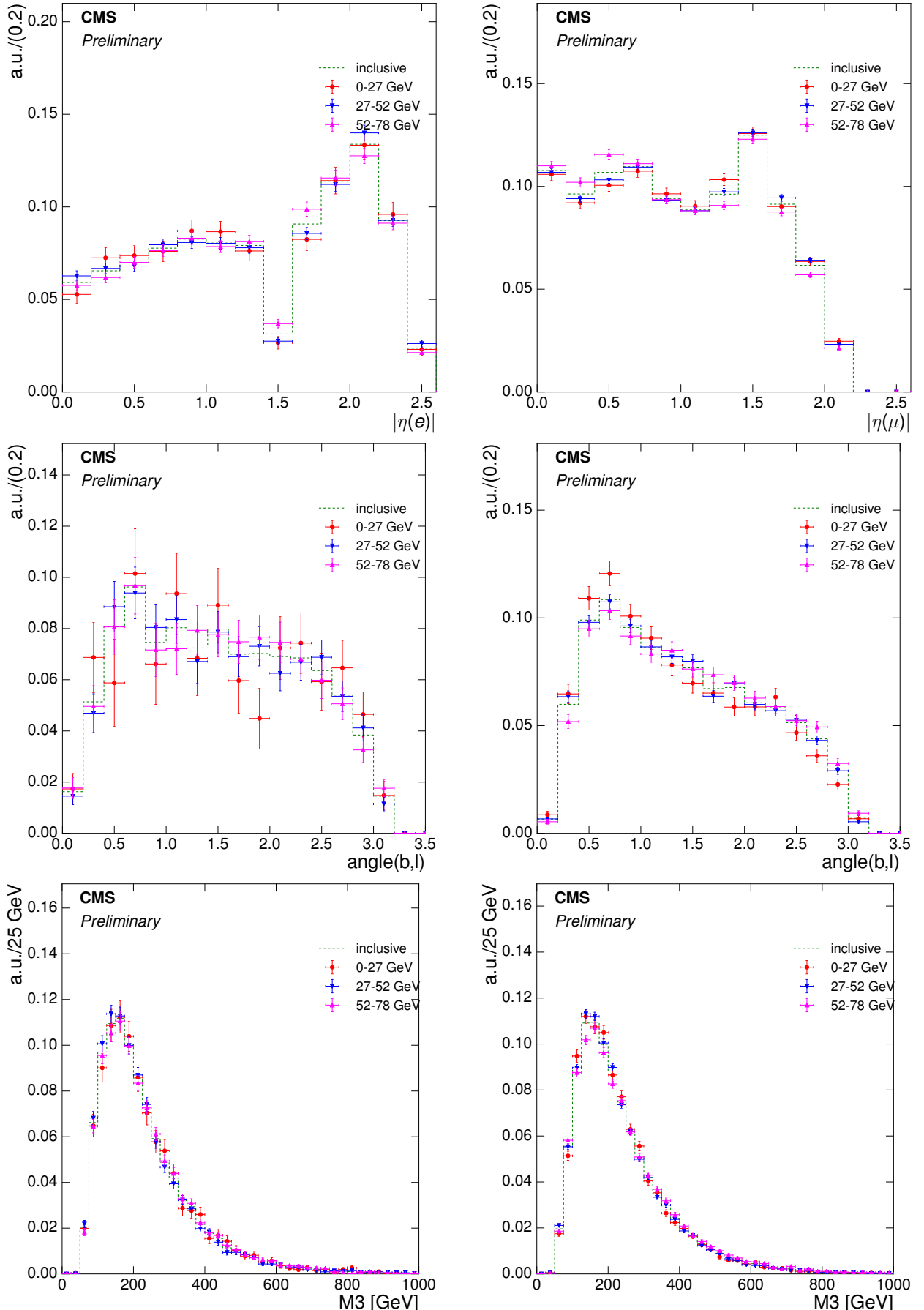


Figure B.11: Normalised distributions of the QCD templates for the three fit variables lepton  $|\eta|$  (upper),  $\alpha$  (middle) and  $M3$  (lower) inclusive across all  $p_T^W$  bins and for the lowest three  $p_T^W$  bins at  $\sqrt{s} = 8$  TeV in the electron+jets channel (left) and in the muon+jets channel (right). 157

## B.7 Fitting variable V+jets background template comparisons

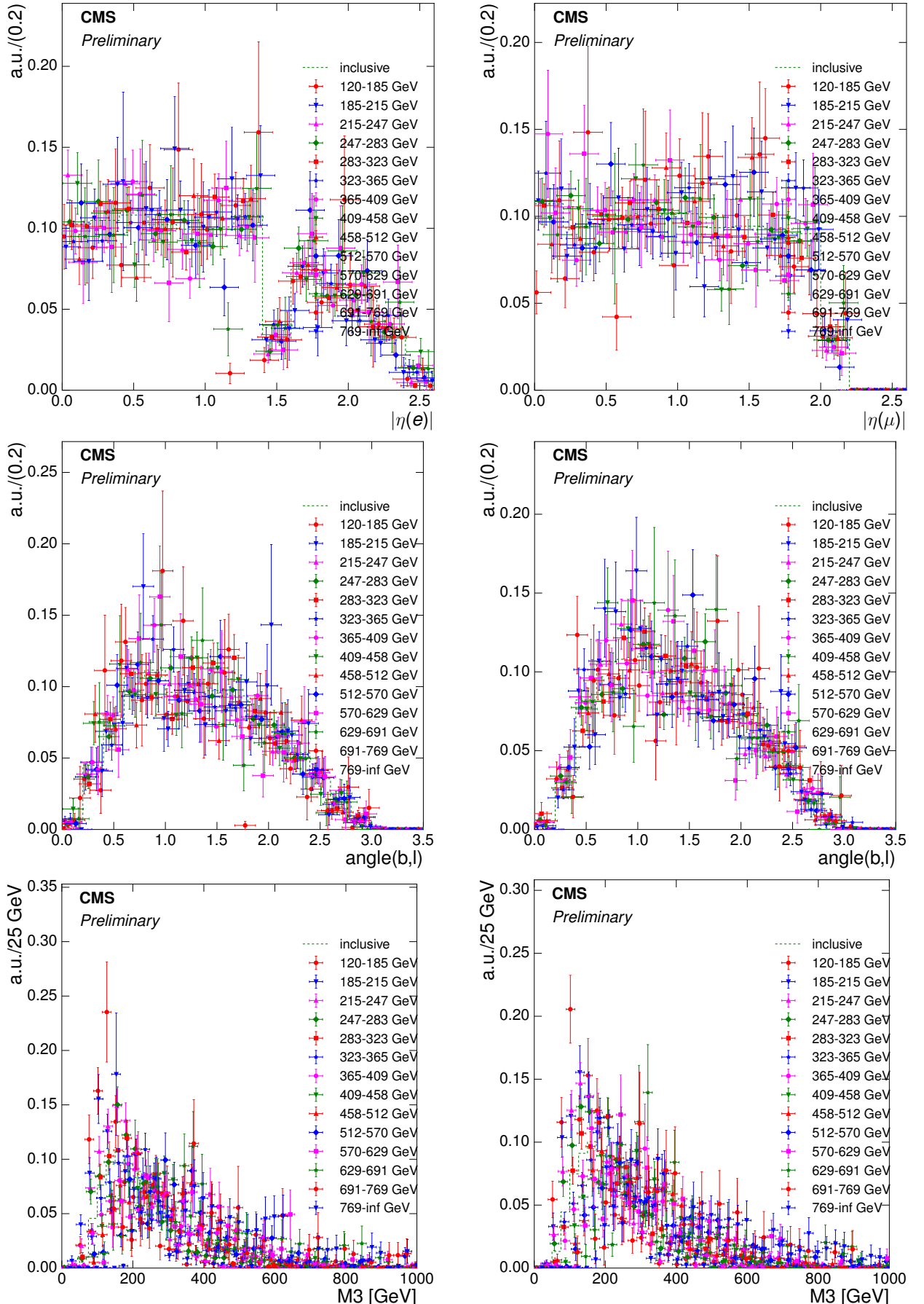


Figure B.12: Normalised distributions of the V+jets templates for the three fit variables lepton  $|\eta|$  (upper),  $\alpha$  (middle) and  $M3$  (lower) inclusive across all  $H_T$  bins and for individual  $H_T$  bins at  $\sqrt{s} = 8$  TeV in the electron+jets channel (left) and in the muon+jets channel (right).

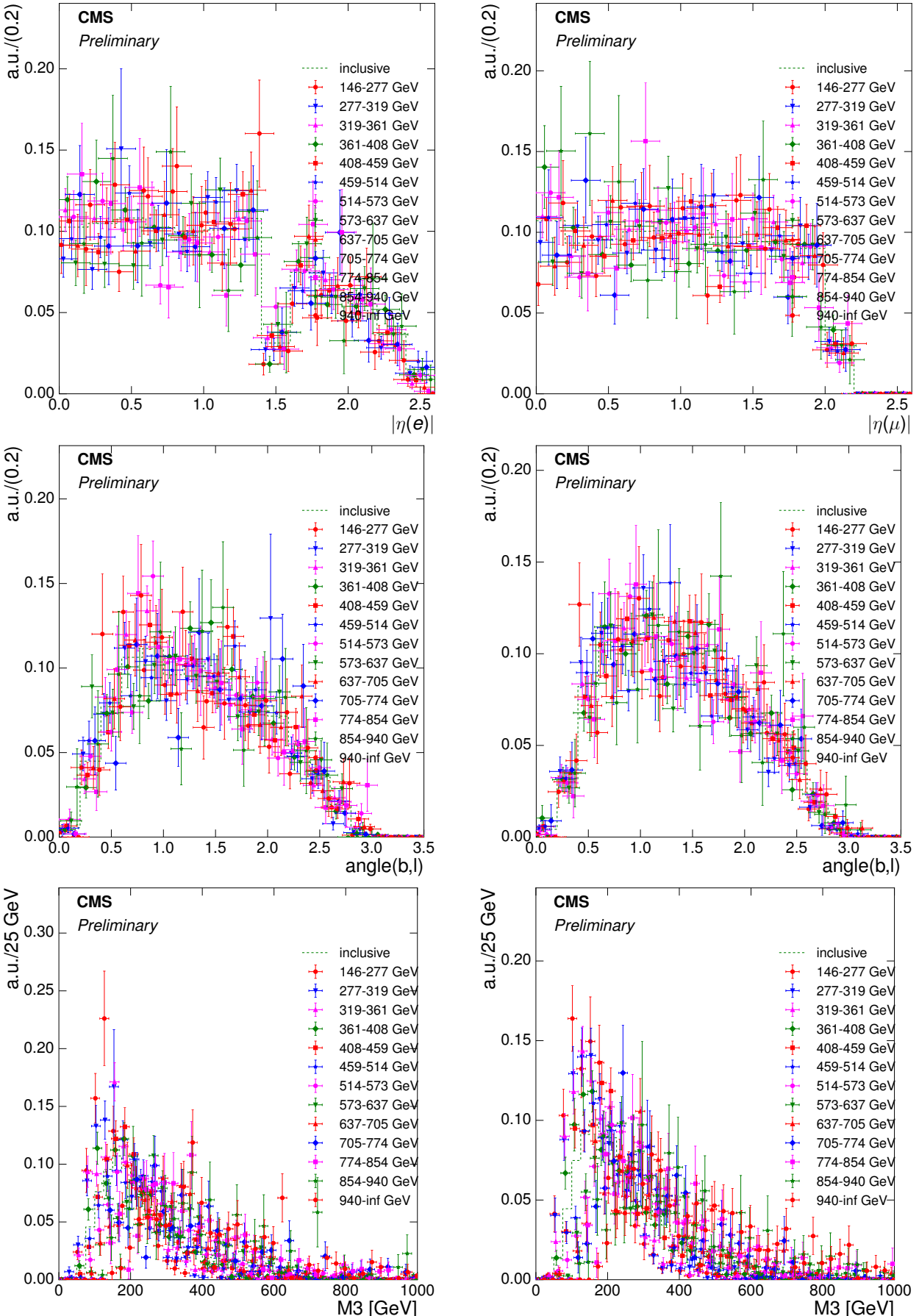


Figure B.13: Normalised distributions of the V+jets templates for the three fit variables lepton  $|\eta|$  (upper),  $\alpha$  (middle) and  $M3$  (lower) inclusive across all  $S_T$  bins and for individual  $S_T$  bins at  $\sqrt{s} = 8$  TeV in the electron+jets channel (left) and in the muon+jets channel (right).

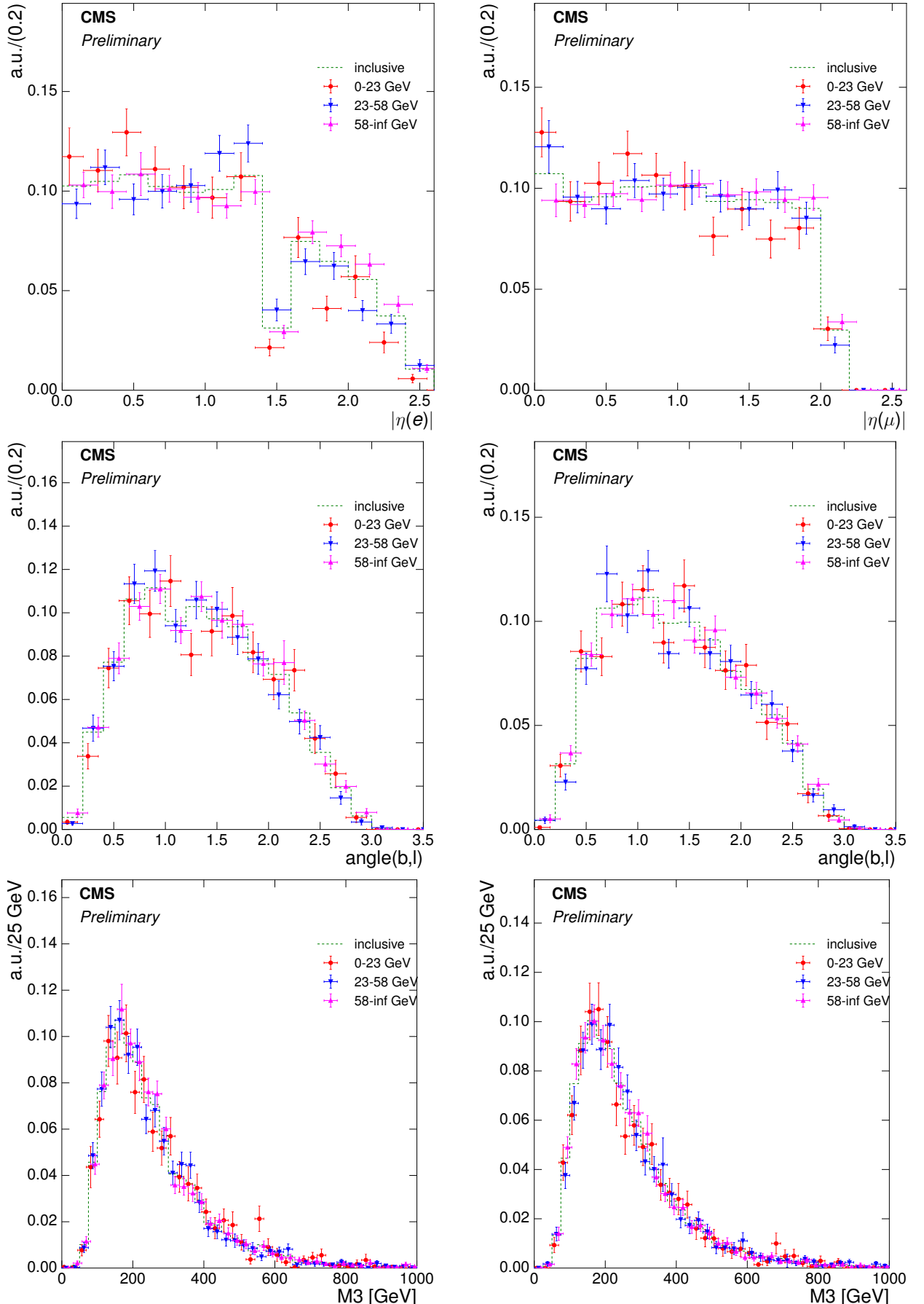


Figure B.14: Normalised distributions of the V+jets templates for the three fit variables lepton  $|\eta|$  (upper),  $\alpha$  (middle) and  $M3$  (lower) inclusive across all  $M_T^W$  bins and for individual  $M_T^W$  bins at  $\sqrt{s} = 8$  TeV in the electron+jets channel (left) and in the muon+jets channel (right).

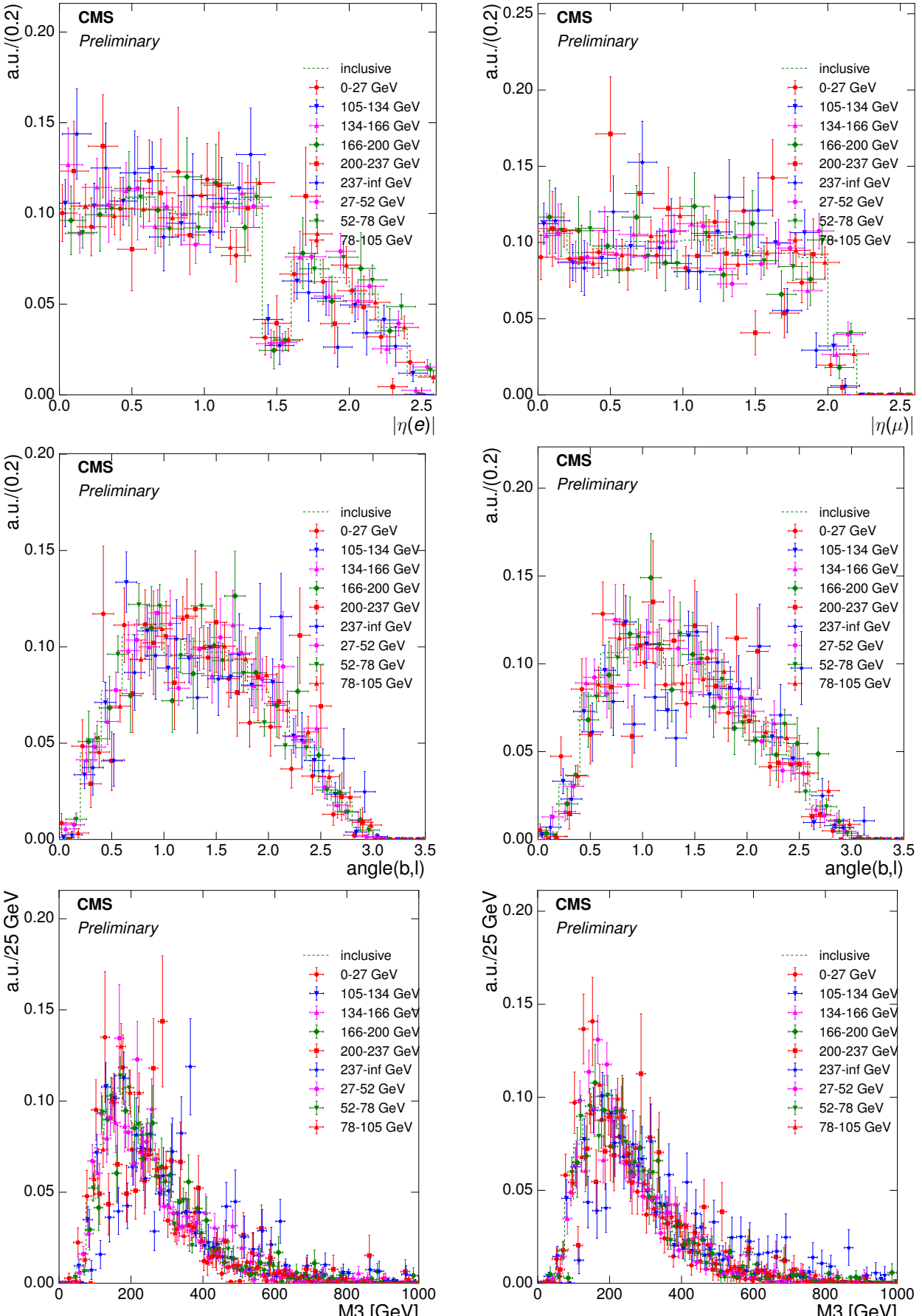


Figure B.15: Normalised distributions of the V+jets templates for the three fit variables lepton  $|\eta|$  (upper),  $\alpha$  (middle) and  $M_3$  (lower) inclusive across all  $p_T^W$  bins and for individual  $p_T^W$  bins at  $\sqrt{s} = 8$  TeV in the electron+jets channel (left) and in the muon+jets channel (right).

## B.8 Fit Results Tables

Table B.7: Fit results for the  $E_T^{\text{miss}}$  variable at a centre-of-mass energy of 7 TeV (electron channel).

Process	0–27 GeV	27–52 GeV	52–87 GeV	87–130 GeV	130–172 GeV	$\geq 172$ GeV	Total
t̄t in	2526.0 ± 41.1	4512.2 ± 54.0	4013.3 ± 55.7	1725.2 ± 33.3	518.4 ± 18.5	287.8 ± 12.2	13582.9 ± 214.8
t̄t fit	2444.9 ± 90.2	3902.5 ± 159.0	3610.7 ± 148.6	1447.3 ± 83.5	366.1 ± 34.8	202.0 ± 24.1	11973.6 ± 540.2
Single-Top in	82.4 ± 6.7	143.2 ± 8.9	120.1 ± 7.7	50.5 ± 4.9	19.6 ± 3.1	12.0 ± 2.1	427.8 ± 33.4
Single-Top fit	0.0 ± 381.7	341.0 ± 197.4	212.6 ± 181.9	82.4 ± 88.3	59.3 ± 33.1	57.1 ± 21.2	752.3 ± 903.6
W/Z + jets in	121.0 ± 8.7	138.7 ± 9.9	82.9 ± 5.9	30.9 ± 2.2	12.8 ± 0.9	9.4 ± 0.7	395.7 ± 28.3
W/Z + jets fit	403.7 ± 125.3	342.4 ± 110.5	160.7 ± 105.0	109.3 ± 58.0	0.0 ± 40.5	4.9 ± 13.6	1021.0 ± 452.9
QCD in	323.3 ± 15.0	242.9 ± 11.3	9.0 ± 0.4	1.3 ± 0.1	1.0 ± 0.0	1.0 ± 0.0	578.5 ± 26.8
QCD fit	31.4 ± 56.6	0.0 ± 25.7	0.0 ± 88.1	0.0 ± 15.5	13.6 ± 11.0	0.0 ± 82.7	45.1 ± 279.6
Sum MC in	3052.7 ± 71.5	5037.0 ± 84.1	4225.3 ± 69.7	1807.8 ± 40.5	551.8 ± 22.6	310.3 ± 15.0	14984.9 ± 303.4
Sum MC fit	2880.0 ± 653.8	4586.0 ± 492.5	3984.0 ± 523.6	1639.0 ± 245.3	439.0 ± 119.5	264.0 ± 141.6	13792.0 ± 2176.3
Data	2880.0 ± 180.1	4586.0 ± 226.1	3984.0 ± 207.8	1639.0 ± 132.0	439.0 ± 66.7	264.0 ± 49.6	13792.0 ± 862.2

Table B.8: Fit results for the  $E_T^{\text{miss}}$  variable at a centre-of-mass energy of 7 TeV (muon channel).

Process	0–27 GeV	27–52 GeV	52–87 GeV	87–130 GeV	130–172 GeV	$\geq 172$ GeV	Total
t̄t in	2697.6 ± 41.5	4877.4 ± 57.9	4542.1 ± 52.0	1983.5 ± 34.2	594.9 ± 18.8	320.7 ± 13.0	15016.1 ± 217.4
t̄t fit	2026.2 ± 122.4	3800.8 ± 157.6	3729.3 ± 145.1	1475.9 ± 85.8	413.7 ± 39.0	200.7 ± 24.9	11646.6 ± 574.9
Single-Top in	88.4 ± 6.7	150.6 ± 8.4	138.4 ± 8.4	57.6 ± 5.1	20.1 ± 3.0	13.9 ± 2.3	468.9 ± 33.9
Single-Top fit	269.5 ± 150.0	397.2 ± 203.6	200.9 ± 164.4	83.5 ± 88.4	21.4 ± 33.7	35.3 ± 24.2	1007.8 ± 664.1
W/Z + jets in	107.9 ± 6.4	144.1 ± 8.6	103.6 ± 6.2	39.0 ± 2.3	11.5 ± 0.7	10.5 ± 0.6	416.5 ± 24.8
W/Z + jets fit	178.6 ± 119.9	198.1 ± 116.8	28.8 ± 101.6	43.6 ± 62.1	0.0 ± 35.8	9.0 ± 15.9	458.0 ± 452.1
QCD in	122.6 ± 5.1	22.6 ± 0.9	34.9 ± 1.5	0.1 ± 0.0	0.1 ± 0.0	0.1 ± 0.0	180.4 ± 7.5
QCD fit	4.7 ± 335.7	0.0 ± 370.4	0.0 ± 714.2	0.0 ± 253.2	10.9 ± 20.4	0.0 ± 18.8	15.6 ± 1712.7
Sum MC in	3016.5 ± 59.8	5194.7 ± 75.9	4819.1 ± 68.1	2080.2 ± 41.6	626.5 ± 22.4	345.1 ± 15.9	16082.0 ± 283.7
Sum MC fit	2479.0 ± 727.9	4396.1 ± 848.5	3959.0 ± 1125.3	1603.0 ± 489.5	446.0 ± 128.9	245.0 ± 83.8	13128.1 ± 3403.9
Data	2479.0 ± 159.2	4396.0 ± 211.6	3959.0 ± 200.7	1603.0 ± 126.7	446.0 ± 65.9	245.0 ± 46.9	13128.0 ± 811.0

Table B.9: Fit results for the  $H_T$  variable at a centre-of-mass energy of 7 TeV (electron channel).

Process	120–185 GeV	185–215 GeV	215–247 GeV	247–283 GeV	283–323 GeV	323–365 GeV	365–409 GeV	409–458 GeV	458–512 GeV	512–570 GeV	570–629 GeV	629–691 GeV	691–769 GeV	$\geq 769$ GeV	Total
t̄t in	220.2 ± 11.4	769.6 ± 24.0	1478.9 ± 29.9	2001.7 ± 40.5	2101.2 ± 37.0	1827.6 ± 37.5	1451.0 ± 31.1	1176.7 ± 25.8	868.9 ± 23.5	602.5 ± 18.7	384.4 ± 14.7	257.2 ± 11.9	193.0 ± 10.5	249.9 ± 12.1	13582.9 ± 328.7
t̄t fit	197.0 ± 42.8	705.9 ± 72.2	1399.3 ± 91.5	1998.6 ± 110.9	1782.1 ± 89.0	1533.8 ± 71.0	1235.2 ± 66.6	934.0 ± 67.5	671.5 ± 49.7	533.4 ± 47.5	342.1 ± 34.4	200.0 ± 23.6	152.7 ± 20.1	188.2 ± 29.3	11873.8 ± 816.0
Single-Top in	12.9 ± 2.5	32.2 ± 4.2	49.4 ± 5.0	59.5 ± 5.7	64.1 ± 5.9	53.3 ± 5.4	41.4 ± 4.6	33.6 ± 4.0	27.2 ± 3.6	18.2 ± 2.9	13.0 ± 2.6	7.7 ± 1.8	6.2 ± 1.7	9.2 ± 2.0	427.8 ± 51.7
Single-Top fit	106.7 ± 45.0	120.0 ± 83.5	239.4 ± 101.8	13.1 ± 367.3	109.0 ± 121.5	48.5 ± 88.6	64.8 ± 68.8	134.0 ± 68.1	82.5 ± 46.9	31.4 ± 40.3	28.1 ± 30.7	7.2 ± 19.0	11.3 ± 18.0	45.6 ± 27.5	1041.6 ± 1127.1
W/Z + jets in	24.2 ± 1.7	34.0 ± 2.4	47.4 ± 3.4	47.3 ± 3.4	50.7 ± 3.6	43.5 ± 3.1	34.8 ± 2.5	31.8 ± 2.3	24.2 ± 1.7	22.0 ± 1.6	14.1 ± 1.0	6.1 ± 0.4	6.6 ± 0.5	9.1 ± 0.7	395.7 ± 28.3
W/Z + jets fit	0.0 ± 16.7	14.2 ± 47.5	10.2 ± 33.9	181.3 ± 65.1	218.9 ± 76.0	174.6 ± 65.4	21.3 ± 99.6	55.0 ± 36.8	50.0 ± 29.4	11.2 ± 41.9	7.8 ± 16.3	30.8 ± 14.2	0.0 ± 13.1	0.0 ± 16.6	775.4 ± 572.6
QCD in	0.3 ± 0.0	102.4 ± 4.7	46.5 ± 2.2	193.7 ± 9.0	82.0 ± 3.8	86.8 ± 4.0	13.2 ± 0.6	17.5 ± 0.8	2.8 ± 0.1	4.6 ± 0.2	13.1 ± 0.6	5.5 ± 0.3	2.0 ± 0.1	6.0 ± 0.3	576.5 ± 26.7
QCD fit	13.4 ± 10.8	11.9 ± 29.5	0.0 ± 69.3	0.0 ± 14.8	0.0 ± 90.2	0.0 ± 36.5	50.7 ± 40.1	0.0 ± 18.6	0.0 ± 10.9	17.9 ± 19.9	0.0 ± 6.9	0.0 ± 5.1	0.0 ± 1.9	7.2 ± 5.8	101.1 ± 360.4
Sum MC in	257.7 ± 15.6	938.2 ± 35.3	1622.1 ± 40.4	2302.1 ± 58.5	2298.0 ± 50.4	2011.2 ± 50.0	1540.4 ± 38.8	1259.6 ± 32.9	923.2 ± 28.9	647.3 ± 23.4	424.6 ± 19.0	276.5 ± 14.4	207.7 ± 12.8	274.1 ± 15.0	14982.9 ± 435.5
Sum MC fit	317.0 ± 115.4	852.0 ± 232.7	1649.0 ± 296.6	2193.0 ± 558.0	2110.0 ± 376.7	1757.0 ± 261.5	1372.0 ± 275.0	1123.0 ± 191.1	804.0 ± 136.8	594.0 ± 149.6	378.0 ± 88.3	238.0 ± 61.9	164.0 ± 53.1	241.0 ± 79.2	13791.9 ± 2876.0
Data	317.0 ± 61.1	852.0 ± 97.6	1649.0 ± 135.2	2193.0 ± 155.3	2110.0 ± 153.2	1757.0 ± 139.5	1372.0 ± 122.7	1123.0 ± 109.6	804.0 ± 92.2	594.0 ± 79.5	378.0 ± 62.2	238.0 ± 49.8	164.0 ± 38.8	241.0 ± 49.6	13792.0 ± 1346.4

Table B.10: Fit results for the  $H_T$  variable at a centre-of-mass energy of 7 TeV (muon channel).

Process	120–185 GeV	185–215 GeV	215–247 GeV	247–283 GeV	283–323 GeV	323–365 GeV	365–409 GeV	409–458 GeV	458–512 GeV	512–570 GeV	570–629 GeV	629–691 GeV	691–769 GeV	$\geq 769$ GeV	Total
t̄t in	253.7 ± 12.0	882.4 ± 22.4	1711.4 ± 31.2	2273.6 ± 37.9	2358.3 ± 40.4	2019.1 ± 35.9	1586.2 ± 34.1	1258.0 ± 27.4	916.9 ± 22.6	636.0 ± 18.5	400.4 ± 14.8	269.7 ± 13.0	196.2 ± 10.4	254.3 ± 12.5	15016.1 ± 333.1
t̄t fit	337.9 ± 18.7	839.0 ± 104.1	1394.6 ± 101.4	1883.0 ± 101.4	1937.2 ± 79.3	1498.0 ± 81.8	1100.7 ± 63.9	901.6 ± 55.1	595.8 ± 48.0	450.8 ± 38.7	253.6 ± 33.4	146.6 ± 24.4	112.7 ± 20.9	127.1 ± 28.9	11578.5 ± 799.9
Single-Top in	17.4 ± 3.2	35.4 ± 4.0	56.1 ± 5.3	63.2 ± 5.6	67.6 ± 6.1	55.0 ± 5.0	46.4 ± 4.6	37.4 ± 4.1	29.4 ± 3.7	19.8 ± 2.9	13.5 ± 2.4	8.0 ± 1.8	8.1 ± 1.9	11.6 ± 2.2	468.9 ± 52.8
Single-Top fit	0.0 ± 46.2	61.1 ± 110.5	90.4 ± 135.6	121.0 ± 119.8	86.6 ± 93.2	279.0 ± 77.9	157.3 ± 60.1	94.4 ± 51.2	99.2 ± 45.2	63.9 ± 35.5	50.4 ± 31.7	34.2 ± 21.9	29.0 ± 18.5	70.9 ± 28.3	1237.3 ± 875.6
W/Z + jets in	26.6 ± 1.6	37.5 ± 2.2	49.4 ± 2.9	52.9 ± 3.2	57.4 ± 3.4	47.0 ± 2.8	36.9 ± 2.2	30.0 ± 1.8	25.3 ± 1.5	17.5 ± 1.0	9.8 ± 0.6	8.1 ± 0.5	6.3 ± 0.4	11.6 ± 0.7	416.5 ± 24.8
W/Z + jets fit	0.0 ± 39.9	21.9 ± 25.0	32.3 ± 101.5	12.6 ± 248.9	62.7 ± 92.7	0.0 ± 149.0	0.0 ± 108.6	0.0 ± 36.1	0.0 ± 100.7	0.0 ± 18.6	0.0 ± 47.9	4.9 ± 50.0	7.3 ± 8.9	0.0 ± 5.3	141.7 ± 1033.1
QCD in	12.2 ± 0.5	27.3 ± 1.2	30.0 ± 1.3	42.7 ± 1.9	21.7 ± 0.9	19.8 ± 0.9	19.6 ± 0.9	1.4 ± 0.1	1.6 ± 0.1	1.8 ± 0.1	0.8 ± 0.0	0.1 ± 0.0	1.1 ± 0.0	0.3 ± 0.0	180.3 ± 7.9
QCD fit	7.2 ± 13.5	0.0 ± 26.3	106.7 ± 87.2	24.3 ± 100.8	18.6 ± 69.4	0.0 ± 97.9	0.0 ± 42.7	0.0 ± 15.8	0.0 ± 14.0	3.3 ± 12.6	0.0 ± 10.2	10.4 ± 29.6	0.0 ± 24.4	0.0 ± 3.2	170.5 ± 547.6
Sum MC in	309.9 ± 17.3	982.6 ± 29.9	1846.9 ± 40.7	2432.4 ± 48.5	2505.0 ± 50.9	2140.8 ± 44.6	1689.0 ± 41.8	1326.8 ± 33.3	973.3 ± 27.9	675.1 ± 22.6	424.5 ± 17.8	286.0 ± 15.3	211.6 ± 12.7	277.7 ± 15.4	16081.9 ± 418.7
Sum MC fit	345.0 ± 118.3	922.0 ± 265.9	1624.0 ± 425.7	2041.0 ± 570.9	2105.0 ± 334.6	1777.0 ± 406.6	1258.0 ± 275.3	996.0 ± 158.1	695.0 ± 207.9	518.0 ± 105.4	304.0 ± 123.1	196.0 ± 125.9	149.0 ± 72.7	198.0 ± 65.6	13128.0 ± 3256.2
Data	345.0 ± 59.2	922.0 ± 97.6	1624.0 ± 129.6	2041.0 ± 143.7	2105.0 ± 146.0	1777.0 ± 133.9	1258.0 ± 112.8	996.0 ± 100.5	695.0 ± 83.3	518.0 ± 71.0	304.0 ± 53.8	196.0 ± 43.3	149.0 ± 38.4	198.0 ± 43.6	13128.0 ± 1256.8

Table B.11: Fit results for the  $S_T$  variable at a centre-of-mass energy of 7 TeV (electron channel).

Process	146–277 GeV	277–319 GeV	319–361 GeV	361–408 GeV	408–459 GeV	459–514 GeV	514–573 GeV	573–637 GeV	637–705 GeV	705–774 GeV	774–854 GeV	854–940 GeV	$\geq 940$ GeV	Total
t̄t in	243.0 $\pm$ 12.7	925.4 $\pm$ 23.2	1705.6 $\pm$ 38.2	2198.3 $\pm$ 38.3	2139.4 $\pm$ 37.3	1836.8 $\pm$ 38.1	1440.0 $\pm$ 30.2	1057.2 $\pm$ 25.5	726.1 $\pm$ 20.4	466.2 $\pm$ 15.8	341.3 $\pm$ 14.1	210.2 $\pm$ 10.4	293.3 $\pm$ 12.9	13582.9 $\pm$ 317.1
t̄t fit	247.0 $\pm$ 46.2	1009.4 $\pm$ 199.6	1619.0 $\pm$ 97.4	2014.1 $\pm$ 122.4	1943.0 $\pm$ 83.4	1619.5 $\pm$ 82.4	1108.8 $\pm$ 66.6	795.9 $\pm$ 64.0	623.0 $\pm$ 41.9	344.9 $\pm$ 71.7	261.2 $\pm$ 26.4	185.7 $\pm$ 22.8	185.8 $\pm$ 26.5	11957.3 $\pm$ 951.3
Single-Top in	15.1 $\pm$ 2.8	34.2 $\pm$ 4.1	56.1 $\pm$ 5.5	61.8 $\pm$ 5.8	62.6 $\pm$ 6.0	54.6 $\pm$ 5.4	40.9 $\pm$ 4.4	31.9 $\pm$ 3.6	23.8 $\pm$ 3.4	16.4 $\pm$ 2.8	11.1 $\pm$ 2.2	7.4 $\pm$ 1.8	11.9 $\pm$ 2.2	427.8 $\pm$ 50.1
Single-Top fit	70.6 $\pm$ 53.4	0.0 $\pm$ 2172.9	152.3 $\pm$ 114.4	48.2 $\pm$ 174.0	86.9 $\pm$ 105.7	21.8 $\pm$ 102.5	155.6 $\pm$ 69.8	169.7 $\pm$ 64.4	77.8 $\pm$ 38.8	40.9 $\pm$ 32.9	59.8 $\pm$ 24.3	25.3 $\pm$ 20.9	62.7 $\pm$ 25.5	971.6 $\pm$ 2999.4
W/Z + jets in	29.3 $\pm$ 2.1	41.3 $\pm$ 3.0	45.7 $\pm$ 3.3	51.1 $\pm$ 3.7	52.3 $\pm$ 3.7	39.4 $\pm$ 2.8	38.6 $\pm$ 2.8	28.2 $\pm$ 2.0	25.3 $\pm$ 1.8	15.4 $\pm$ 1.1	10.4 $\pm$ 0.7	6.8 $\pm$ 0.5	12.0 $\pm$ 0.9	395.7 $\pm$ 28.3
W/Z + jets fit	8.2 $\pm$ 31.4	103.5 $\pm$ 95.8	86.7 $\pm$ 46.7	198.7 $\pm$ 87.8	142.1 $\pm$ 69.8	159.7 $\pm$ 61.2	59.5 $\pm$ 44.5	3.0 $\pm$ 416.6	0.0 $\pm$ 999.9	39.0 $\pm$ 142.0	0.0 $\pm$ 53.6	0.0 $\pm$ 22.2	0.0 $\pm$ 390.9	800.5 $\pm$ 2462.5
QCD in	3.1 $\pm$ 0.1	146.2 $\pm$ 6.8	43.6 $\pm$ 2.0	234.5 $\pm$ 10.9	79.1 $\pm$ 3.7	10.6 $\pm$ 0.5	16.5 $\pm$ 0.8	14.3 $\pm$ 0.7	4.0 $\pm$ 0.2	8.7 $\pm$ 0.4	7.8 $\pm$ 0.4	3.5 $\pm$ 0.2	4.7 $\pm$ 0.2	576.5 $\pm$ 26.7
QCD fit	25.2 $\pm$ 21.3	1.0 $\pm$ 206.6	0.0 $\pm$ 60.7	0.0 $\pm$ 32.3	0.0 $\pm$ 20.0	0.0 $\pm$ 47.1	0.0 $\pm$ 26.6	24.5 $\pm$ 31.8	5.2 $\pm$ 9.8	0.2 $\pm$ 514.4	0.0 $\pm$ 3.5	0.0 $\pm$ 5.4	6.5 $\pm$ 6.1	62.6 $\pm$ 985.6
Sum MC in	290.4 $\pm$ 17.7	1147.1 $\pm$ 37.1	1851.0 $\pm$ 49.0	2545.7 $\pm$ 58.6	2333.4 $\pm$ 50.7	1941.3 $\pm$ 46.8	1536.0 $\pm$ 38.2	1131.6 $\pm$ 31.9	779.3 $\pm$ 25.9	506.7 $\pm$ 20.1	370.6 $\pm$ 17.5	228.0 $\pm$ 12.9	321.9 $\pm$ 16.1	14982.9 $\pm$ 422.3
Sum MC fit	351.0 $\pm$ 152.3	1114.0 $\pm$ 2674.9	1858.0 $\pm$ 319.3	2261.0 $\pm$ 416.5	2172.0 $\pm$ 278.9	1801.0 $\pm$ 293.3	1324.0 $\pm$ 207.4	993.0 $\pm$ 576.7	706.0 $\pm$ 1090.5	425.0 $\pm$ 760.9	321.0 $\pm$ 107.8	211.0 $\pm$ 71.3	255.0 $\pm$ 449.1	13792.0 $\pm$ 7398.8
Data	351.0 $\pm$ 64.6	1114.0 $\pm$ 113.2	1858.0 $\pm$ 143.3	2261.0 $\pm$ 158.2	2172.0 $\pm$ 154.8	1801.0 $\pm$ 141.3	1324.0 $\pm$ 119.1	993.0 $\pm$ 102.0	706.0 $\pm$ 86.0	425.0 $\pm$ 66.6	321.0 $\pm$ 54.5	211.0 $\pm$ 46.3	255.0 $\pm$ 50.2	13792.0 $\pm$ 1300.1

Table B.12: Fit results for the  $S_T$  variable at a centre-of-mass energy of 7 TeV (muon channel).

Process	146–277 GeV	277–319 GeV	319–361 GeV	361–408 GeV	408–459 GeV	459–514 GeV	514–573 GeV	573–637 GeV	637–705 GeV	705–774 GeV	774–854 GeV	854–940 GeV	$\geq 940$ GeV	Total
t̄t in	305.9 $\pm$ 13.3	1099.3 $\pm$ 25.8	1979.3 $\pm$ 33.4	2478.8 $\pm$ 39.3	2392.5 $\pm$ 41.7	2008.9 $\pm$ 37.6	1522.1 $\pm$ 30.1	1115.1 $\pm$ 25.3	772.0 $\pm$ 21.3	483.2 $\pm$ 16.1	350.4 $\pm$ 13.8	213.5 $\pm$ 10.5	295.2 $\pm$ 13.4	15016.1 $\pm$ 321.6
t̄t fit	313.1 $\pm$ 53.1	1116.8 $\pm$ 92.5	1713.7 $\pm$ 89.1	1927.7 $\pm$ 105.7	1857.9 $\pm$ 83.2	1396.0 $\pm$ 87.2	1084.6 $\pm$ 64.4	813.8 $\pm$ 52.6	512.4 $\pm$ 44.6	345.3 $\pm$ 31.8	218.7 $\pm$ 26.3	117.8 $\pm$ 22.2	149.5 $\pm$ 26.4	11567.2 $\pm$ 779.1
Single-Top in	18.3 $\pm$ 3.2	42.7 $\pm$ 4.6	57.8 $\pm$ 5.3	71.6 $\pm$ 6.3	64.6 $\pm$ 5.4	56.6 $\pm$ 5.1	46.4 $\pm$ 4.6	35.7 $\pm$ 3.9	24.6 $\pm$ 3.4	15.9 $\pm$ 2.6	11.9 $\pm$ 2.2	8.4 $\pm$ 1.8	14.4 $\pm$ 2.3	468.9 $\pm$ 50.9
Single-Top fit	47.3 $\pm$ 54.3	48.3 $\pm$ 102.8	87.6 $\pm$ 118.4	197.6 $\pm$ 132.2	181.1 $\pm$ 83.9	257.5 $\pm$ 98.0	111.4 $\pm$ 60.4	57.2 $\pm$ 48.7	63.6 $\pm$ 44.1	34.6 $\pm$ 29.4	50.7 $\pm$ 26.3	32.0 $\pm$ 20.6	67.5 $\pm$ 25.6	1236.6 $\pm$ 844.8
W/Z + jets in	30.2 $\pm$ 1.8	45.8 $\pm$ 2.7	53.8 $\pm$ 3.2	55.2 $\pm$ 3.3	55.6 $\pm$ 3.3	45.7 $\pm$ 2.7	38.6 $\pm$ 2.3	24.3 $\pm$ 1.4	22.1 $\pm$ 1.3	15.6 $\pm$ 0.9	9.6 $\pm$ 0.6	6.5 $\pm$ 0.4	13.6 $\pm$ 0.8	416.5 $\pm$ 24.8
W/Z + jets fit	0.0 $\pm$ 15.6	41.5 $\pm$ 61.3	43.7 $\pm$ 61.2	83.7 $\pm$ 66.0	0.0 $\pm$ 90.6	14.6 $\pm$ 54.8	0.0 $\pm$ 20.3	0.0 $\pm$ 35.1	5.0 $\pm$ 25.7	2.1 $\pm$ 24.7	1.6 $\pm$ 27.4	10.1 $\pm$ 9.3	0.0 $\pm$ 3.8	202.3 $\pm$ 495.9
QCD in	39.5 $\pm$ 1.7	15.2 $\pm$ 0.6	57.3 $\pm$ 2.4	24.5 $\pm$ 1.0	17.2 $\pm$ 0.7	19.6 $\pm$ 0.8	3.9 $\pm$ 0.2	1.0 $\pm$ 0.0	0.8 $\pm$ 0.0	0.1 $\pm$ 0.0	1.1 $\pm$ 0.0	0.1 $\pm$ 0.0	0.2 $\pm$ 0.0	180.4 $\pm$ 7.6
QCD fit	12.6 $\pm$ 16.7	24.4 $\pm$ 65.5	0.0 $\pm$ 122.8	0.0 $\pm$ 68.1	85.0 $\pm$ 43.1	0.0 $\pm$ 169.6	0.0 $\pm$ 12.4	0.0 $\pm$ 13.0	0.0 $\pm$ 755.8	0.0 $\pm$ 17.3	0.0 $\pm$ 427.0	0.0 $\pm$ 30.1	0.0 $\pm$ 2.3	121.9 $\pm$ 1743.7
Sum MC in	393.9 $\pm$ 20.0	1202.9 $\pm$ 33.8	2148.2 $\pm$ 44.4	2630.1 $\pm$ 50.0	2529.9 $\pm$ 51.2	2130.7 $\pm$ 46.2	1611.1 $\pm$ 37.2	1176.1 $\pm$ 30.7	819.4 $\pm$ 26.0	514.8 $\pm$ 19.6	373.0 $\pm$ 16.7	228.5 $\pm$ 12.7	323.5 $\pm$ 16.5	16082.0 $\pm$ 404.9
Sum MC fit	373.0 $\pm$ 139.7	1231.0 $\pm$ 322.0	1845.0 $\pm$ 391.6	2209.0 $\pm$ 372.0	2124.0 $\pm$ 300.8	1668.0 $\pm$ 409.7	1196.0 $\pm$ 157.5	871.0 $\pm$ 149.3	581.0 $\pm$ 870.2	382.0 $\pm$ 103.3	271.0 $\pm$ 507.0	160.0 $\pm$ 82.2	217.0 $\pm$ 58.1	13128.0 $\pm$ 3863.5
Data	373.0 $\pm$ 62.2	1231.0 $\pm$ 112.7	1845.0 $\pm$ 138.4	2209.0 $\pm$ 149.7	2124.0 $\pm$ 147.1	1668.0 $\pm$ 129.1	1196.0 $\pm$ 109.7	871.0 $\pm$ 92.7	581.0 $\pm$ 75.9	382.0 $\pm$ 60.5	271.0 $\pm$ 51.4	160.0 $\pm$ 38.9	217.0 $\pm$ 45.1	13128.0 $\pm$ 1213.5

Table B.13: Fit results for the  $p_T^W$  variable at a centre-of-mass energy of 7 TeV (electron channel).

Process	0--27 GeV	27--52 GeV	52--78 GeV	78--105 GeV	105--134 GeV	134--166 GeV	166--200 GeV	200--237 GeV	$\geq 237$ GeV	Total
t̄t in	953.0 $\pm$ 26.1	2150.1 $\pm$ 35.2	2788.4 $\pm$ 45.5	2617.7 $\pm$ 40.9	2058.0 $\pm$ 37.0	1379.9 $\pm$ 34.1	782.4 $\pm$ 22.0	431.9 $\pm$ 15.5	421.8 $\pm$ 14.8	13582.9 $\pm$ 270.9
t̄t fit	821.0 $\pm$ 63.4	2182.9 $\pm$ 125.8	2544.3 $\pm$ 132.8	2380.5 $\pm$ 119.5	1781.9 $\pm$ 92.8	1139.6 $\pm$ 71.2	548.8 $\pm$ 51.9	296.2 $\pm$ 31.4	277.4 $\pm$ 26.2	11972.7 $\pm$ 715.1
Single-Top in	30.0 $\pm$ 4.1	67.8 $\pm$ 6.1	80.6 $\pm$ 6.8	78.7 $\pm$ 6.4	61.7 $\pm$ 5.6	43.3 $\pm$ 4.6	26.5 $\pm$ 3.3	17.2 $\pm$ 2.7	22.0 $\pm$ 2.8	427.8 $\pm$ 42.4
Single-Top fit	12.8 $\pm$ 112.3	17.6 $\pm$ 311.9	159.1 $\pm$ 179.7	207.9 $\pm$ 134.8	108.6 $\pm$ 105.5	68.5 $\pm$ 77.6	110.2 $\pm$ 54.0	88.8 $\pm$ 29.7	93.6 $\pm$ 24.4	867.1 $\pm$ 1029.8
W/Z + jets in	28.0 $\pm$ 2.0	73.6 $\pm$ 5.3	89.0 $\pm$ 6.4	66.7 $\pm$ 4.8	48.3 $\pm$ 3.5	34.9 $\pm$ 2.5	22.7 $\pm$ 1.6	14.3 $\pm$ 1.0	18.3 $\pm$ 1.3	395.7 $\pm$ 28.3
W/Z + jets fit	146.2 $\pm$ 50.4	264.5 $\pm$ 80.0	122.8 $\pm$ 155.1	104.6 $\pm$ 78.9	116.5 $\pm$ 67.9	111.9 $\pm$ 51.8	46.2 $\pm$ 67.3	0.0 $\pm$ 6.1	0.0 $\pm$ 12.3	912.7 $\pm$ 569.8
QCD in	6.0 $\pm$ 0.3	95.9 $\pm$ 4.4	95.7 $\pm$ 4.4	268.5 $\pm$ 12.4	85.2 $\pm$ 3.9	15.9 $\pm$ 0.7	3.2 $\pm$ 0.1	2.2 $\pm$ 0.1	3.9 $\pm$ 0.2	576.5 $\pm$ 26.7
QCD fit	0.0 $\pm$ 42.3	0.0 $\pm$ 71.6	32.8 $\pm$ 54.2	0.0 $\pm$ 14.7	0.0 $\pm$ 18.7	0.0 $\pm$ 39.5	6.8 $\pm$ 30.8	0.0 $\pm$ 5.6	0.0 $\pm$ 5.2	39.6 $\pm$ 282.8
Sum MC in	1017.0 $\pm$ 32.4	2387.4 $\pm$ 51.0	3053.6 $\pm$ 63.1	3031.6 $\pm$ 64.5	2253.1 $\pm$ 50.0	1474.0 $\pm$ 42.0	834.8 $\pm$ 27.1	465.6 $\pm$ 19.3	465.9 $\pm$ 19.1	14982.9 $\pm$ 368.4
Sum MC fit	980.0 $\pm$ 268.5	2465.0 $\pm$ 589.4	2859.0 $\pm$ 521.8	2693.0 $\pm$ 347.9	2007.0 $\pm$ 284.9	1320.0 $\pm$ 240.1	712.0 $\pm$ 204.0	385.0 $\pm$ 72.8	371.0 $\pm$ 68.2	13792.0 $\pm$ 2597.6
Data	980.0 $\pm$ 105.9	2465.0 $\pm$ 168.1	2859.0 $\pm$ 177.5	2693.0 $\pm$ 171.1	2007.0 $\pm$ 147.4	1320.0 $\pm$ 118.8	712.0 $\pm$ 86.4	385.0 $\pm$ 60.3	371.0 $\pm$ 58.5	13792.0 $\pm$ 1094.1

Table B.14: Fit results for the  $p_T^W$  variable at a centre-of-mass energy of 7 TeV (muon channel).

Process	0--27 GeV	27--52 GeV	52--78 GeV	78--105 GeV	105--134 GeV	134--166 GeV	166--200 GeV	200--237 GeV	$\geq 237$ GeV	Total
t̄t in	1123.0 $\pm$ 27.5	2494.5 $\pm$ 38.8	3109.7 $\pm$ 46.3	2846.6 $\pm$ 40.7	2224.3 $\pm$ 37.9	1487.2 $\pm$ 30.4	843.1 $\pm$ 21.4	457.2 $\pm$ 16.4	430.6 $\pm$ 15.5	15016.1 $\pm$ 274.8
t̄t fit	840.6 $\pm$ 64.9	1962.2 $\pm$ 118.8	2766.6 $\pm$ 141.1	2204.6 $\pm$ 118.1	1763.2 $\pm$ 91.6	1084.0 $\pm$ 71.8	569.9 $\pm$ 48.6	278.9 $\pm$ 31.4	269.0 $\pm$ 26.2	11739.0 $\pm$ 712.6
Single-Top in	34.2 $\pm$ 4.1	78.6 $\pm$ 6.9	92.3 $\pm$ 6.8	85.6 $\pm$ 6.4	64.2 $\pm$ 5.4	46.5 $\pm$ 4.5	28.1 $\pm$ 3.4	15.7 $\pm$ 2.4	23.9 $\pm$ 2.8	468.9 $\pm$ 42.7
Single-Top fit	48.7 $\pm$ 74.0	246.6 $\pm$ 140.4	46.9 $\pm$ 164.3	236.8 $\pm$ 143.3	53.6 $\pm$ 103.3	71.1 $\pm$ 67.7	59.6 $\pm$ 45.8	34.9 $\pm$ 30.1	43.7 $\pm$ 25.4	842.0 $\pm$ 794.3
W/Z + jets in	39.5 $\pm$ 2.4	75.4 $\pm$ 4.5	89.8 $\pm$ 5.4	68.3 $\pm$ 4.1	52.4 $\pm$ 3.1	38.4 $\pm$ 2.3	19.2 $\pm$ 1.1	14.3 $\pm$ 0.9	19.1 $\pm$ 1.1	416.5 $\pm$ 24.8
W/Z + jets fit	77.4 $\pm$ 80.6	71.9 $\pm$ 147.0	183.3 $\pm$ 168.4	48.6 $\pm$ 86.8	77.2 $\pm$ 73.9	0.0 $\pm$ 109.0	0.0 $\pm$ 16.2	0.0 $\pm$ 21.5	5.3 $\pm$ 14.2	463.8 $\pm$ 717.6
QCD in	3.8 $\pm$ 0.2	85.7 $\pm$ 3.6	51.7 $\pm$ 2.2	20.2 $\pm$ 0.8	1.1 $\pm$ 0.0	17.0 $\pm$ 0.7	0.7 $\pm$ 0.0	0.1 $\pm$ 0.0	0.1 $\pm$ 0.0	180.4 $\pm$ 7.5
QCD fit	50.3 $\pm$ 67.6	1.4 $\pm$ 3131.1	4.2 $\pm$ 911.5	0.0 $\pm$ 54.1	0.0 $\pm$ 63.5	15.9 $\pm$ 34.7	8.4 $\pm$ 15.5	3.2 $\pm$ 13.6	0.0 $\pm$ 8.4	83.4 $\pm$ 4300.0
Sum MC in	1200.6 $\pm$ 34.1	2734.1 $\pm$ 53.8	3343.4 $\pm$ 60.6	3020.7 $\pm$ 52.0	2342.0 $\pm$ 46.5	1589.1 $\pm$ 37.9	891.1 $\pm$ 26.0	487.3 $\pm$ 19.6	473.7 $\pm$ 19.5	16082.0 $\pm$ 350.0
Sum MC fit	1017.0 $\pm$ 287.2	2282.1 $\pm$ 3537.4	3001.0 $\pm$ 1385.3	2490.0 $\pm$ 402.3	1894.0 $\pm$ 332.3	1171.0 $\pm$ 283.2	638.0 $\pm$ 126.1	317.0 $\pm$ 96.6	318.0 $\pm$ 74.2	13128.1 $\pm$ 6524.5
Data	1017.0 $\pm$ 102.8	2282.0 $\pm$ 152.9	3001.0 $\pm$ 175.6	2490.0 $\pm$ 159.4	1894.0 $\pm$ 138.0	1171.0 $\pm$ 107.1	638.0 $\pm$ 78.3	317.0 $\pm$ 54.8	318.0 $\pm$ 54.2	13128.0 $\pm$ 1023.1

Table B.15: Fit results for the  $M_T^W$  variable at a centre-of-mass energy of 7 TeV (electron channel).

Process	0--23 GeV	23--58 GeV	$\geq 58$ GeV	Total
t̄t in	1734.8 ± 37.6	3862.1 ± 49.1	7985.4 ± 74.2	13582.3 ± 160.8
t̄t fit	1411.7 ± 85.9	3451.4 ± 145.5	7204.3 ± 215.0	12067.4 ± 446.4
Single-Top in	52.9 ± 5.1	126.8 ± 8.3	248.1 ± 11.4	427.8 ± 24.7
Single-Top fit	27.6 ± 100.7	151.2 ± 172.1	318.0 ± 264.4	496.8 ± 537.2
W/Z + jets in	58.4 ± 4.2	119.7 ± 8.6	217.6 ± 15.6	395.7 ± 28.3
W/Z + jets fit	242.8 ± 123.3	348.4 ± 103.7	608.6 ± 145.8	1199.8 ± 372.9
QCD in	163.4 ± 7.6	223.6 ± 10.4	189.4 ± 8.8	576.5 ± 26.7
QCD fit	27.9 ± 45.6	0.0 ± 37.5	0.0 ± 34.6	27.9 ± 117.7
Sum MC in	2009.5 ± 54.4	4332.3 ± 76.3	8640.5 ± 110.0	14982.3 ± 240.6
Sum MC fit	1710.0 ± 355.4	3951.0 ± 458.9	8131.0 ± 659.8	13792.0 ± 1474.1
Data	1710.0 ± 138.3	3951.0 ± 208.3	8131.0 ± 298.4	13792.0 ± 645.0

Table B.16: Fit results for the  $M_T^W$  variable at a centre-of-mass energy of 7 TeV (muon channel).

Process	0--23 GeV	23--58 GeV	$\geq 58$ GeV	Total
t̄t in	1937.1 ± 35.5	4372.8 ± 54.9	8706.2 ± 72.1	15016.1 ± 162.5
t̄t fit	1612.1 ± 68.2	3424.7 ± 136.2	6685.5 ± 215.8	11722.2 ± 420.1
Single-Top in	63.2 ± 5.6	137.3 ± 7.9	268.4 ± 11.6	468.9 ± 25.1
Single-Top fit	0.0 ± 581.2	137.4 ± 165.6	777.2 ± 265.1	914.5 ± 1011.9
W/Z + jets in	65.9 ± 3.9	118.2 ± 7.0	232.4 ± 13.9	416.5 ± 24.8
W/Z + jets fit	121.9 ± 62.3	232.9 ± 110.9	18.6 ± 757.6	373.4 ± 930.8
QCD in	58.5 ± 2.4	106.7 ± 4.5	15.1 ± 0.6	180.3 ± 7.5
QCD fit	0.0 ± 95.8	0.0 ± 55.7	117.8 ± 158.0	117.8 ± 309.5
Sum MC in	2124.6 ± 47.5	4735.1 ± 74.4	9222.1 ± 98.2	16081.8 ± 220.0
Sum MC fit	1734.0 ± 807.5	3795.0 ± 468.3	7599.0 ± 1396.5	13128.0 ± 2672.2
Data	1734.0 ± 132.8	3795.0 ± 197.7	7599.0 ± 276.5	13128.0 ± 607.0

Table B.17: Fit results for the  $E_T^{\text{miss}}$  variable at a centre-of-mass energy of 8 TeV (electron channel).

Process	0--27 GeV	27--52 GeV	52--87 GeV	87--130 GeV	130--172 GeV	$\geq 172$ GeV	Total
t̄t in	11394.8 $\pm$ 297.5	20257.4 $\pm$ 397.5	18771.6 $\pm$ 379.9	8534.4 $\pm$ 253.3	2662.8 $\pm$ 141.6	1612.1 $\pm$ 108.5	63233.1 $\pm$ 1578.2
t̄t fit	11258.8 $\pm$ 307.4	21023.0 $\pm$ 265.5	19133.9 $\pm$ 359.0	7721.3 $\pm$ 207.2	2394.7 $\pm$ 92.0	1212.7 $\pm$ 58.0	62744.4 $\pm$ 1289.2
Single-Top in	470.0 $\pm$ 44.6	804.0 $\pm$ 58.5	729.8 $\pm$ 55.0	348.6 $\pm$ 38.9	124.1 $\pm$ 21.9	90.5 $\pm$ 18.7	2566.9 $\pm$ 237.6
Single-Top fit	610.9 $\pm$ 421.8	0.0 $\pm$ 6921.1	380.7 $\pm$ 413.8	305.3 $\pm$ 199.2	100.3 $\pm$ 85.8	127.1 $\pm$ 52.8	1524.3 $\pm$ 8094.5
W/Z + jets in	418.9 $\pm$ 22.7	493.4 $\pm$ 26.8	309.9 $\pm$ 16.8	110.9 $\pm$ 6.0	37.4 $\pm$ 2.0	35.1 $\pm$ 1.9	1405.6 $\pm$ 76.2
W/Z + jets fit	2165.4 $\pm$ 396.9	2845.1 $\pm$ 346.6	1638.9 $\pm$ 366.8	469.8 $\pm$ 264.5	0.0 $\pm$ 71.6	66.1 $\pm$ 30.8	7185.4 $\pm$ 1477.3
QCD in	2285.7 $\pm$ 54.4	104.0 $\pm$ 2.5	35.5 $\pm$ 0.8	0.8 $\pm$ 0.0	1.0 $\pm$ 0.0	0.4 $\pm$ 0.0	2427.4 $\pm$ 57.8
QCD fit	443.8 $\pm$ 160.7	112.9 $\pm$ 147.8	11.6 $\pm$ 333.2	77.4 $\pm$ 107.0	76.0 $\pm$ 24.4	0.0 $\pm$ 23.7	721.7 $\pm$ 796.9
Sum MC in	14569.4 $\pm$ 419.3	21658.8 $\pm$ 485.2	19846.7 $\pm$ 452.6	8994.7 $\pm$ 298.2	2825.3 $\pm$ 165.5	1738.1 $\pm$ 129.0	69633.0 $\pm$ 1949.8
Sum MC fit	14478.9 $\pm$ 1286.9	23981.0 $\pm$ 7681.0	21165.0 $\pm$ 1472.8	8573.9 $\pm$ 777.9	2570.9 $\pm$ 273.8	1406.0 $\pm$ 165.3	72175.7 $\pm$ 11657.7
Data	14479.0 $\pm$ 402.7	23981.0 $\pm$ 513.6	21165.0 $\pm$ 476.2	8574.0 $\pm$ 301.0	2571.0 $\pm$ 162.1	1406.0 $\pm$ 118.1	72176.0 $\pm$ 1973.6

Table B.18: Fit results for the  $E_T^{\text{miss}}$  variable at a centre-of-mass energy of 8 TeV (muon channel).

Process	0--27 GeV	27--52 GeV	52--87 GeV	87--130 GeV	130--172 GeV	$\geq 172$ GeV	Total
t̄t in	13206.5 $\pm$ 318.6	23819.0 $\pm$ 428.4	22684.5 $\pm$ 416.1	10234.5 $\pm$ 279.2	3132.3 $\pm$ 153.1	1918.5 $\pm$ 117.3	74995.1 $\pm$ 1712.8
t̄t fit	12976.6 $\pm$ 179.3	23608.5 $\pm$ 428.3	22339.7 $\pm$ 413.8	9636.1 $\pm$ 215.5	2774.5 $\pm$ 108.0	1343.1 $\pm$ 69.8	72678.4 $\pm$ 1414.7
Single-Top in	539.8 $\pm$ 47.6	892.7 $\pm$ 60.6	894.2 $\pm$ 60.9	417.6 $\pm$ 41.8	161.0 $\pm$ 26.2	118.7 $\pm$ 22.5	3024.0 $\pm$ 259.5
Single-Top fit	0.0 $\pm$ 193.8	680.4 $\pm$ 539.3	58.4 $\pm$ 1080.7	194.1 $\pm$ 237.3	13.5 $\pm$ 198.0	206.7 $\pm$ 65.0	1153.1 $\pm$ 2314.1
W/Z + jets in	407.9 $\pm$ 20.2	566.7 $\pm$ 28.1	372.4 $\pm$ 18.4	143.3 $\pm$ 7.1	64.2 $\pm$ 3.2	42.3 $\pm$ 2.1	1596.7 $\pm$ 79.1
W/Z + jets fit	1904.6 $\pm$ 272.5	2174.5 $\pm$ 396.5	2037.9 $\pm$ 279.9	627.6 $\pm$ 251.6	229.7 $\pm$ 101.8	73.2 $\pm$ 37.7	7047.5 $\pm$ 1340.0
QCD in	440.9 $\pm$ 6.0	43.4 $\pm$ 0.6	42.5 $\pm$ 0.6	0.1 $\pm$ 0.0	0.5 $\pm$ 0.0	0.1 $\pm$ 0.0	527.6 $\pm$ 7.2
QCD fit	62.8 $\pm$ 206.5	34.6 $\pm$ 315.9	0.0 $\pm$ 135.1	59.2 $\pm$ 157.5	11.4 $\pm$ 52.3	0.0 $\pm$ 82.9	168.1 $\pm$ 950.3
Sum MC in	14595.0 $\pm$ 392.5	25321.8 $\pm$ 517.6	23993.6 $\pm$ 496.0	10795.5 $\pm$ 328.2	3357.9 $\pm$ 182.4	2079.5 $\pm$ 141.9	80143.4 $\pm$ 2058.6
Sum MC fit	14944.0 $\pm$ 852.1	26498.0 $\pm$ 1680.1	24436.1 $\pm$ 1909.5	10517.0 $\pm$ 861.9	3029.0 $\pm$ 460.2	1623.0 $\pm$ 255.4	81047.1 $\pm$ 6019.1
Data	14944.0 $\pm$ 392.0	26498.0 $\pm$ 520.6	24436.0 $\pm$ 499.9	10517.0 $\pm$ 325.7	3029.0 $\pm$ 174.3	1623.0 $\pm$ 125.6	81047.0 $\pm$ 2038.2

Table B.19: Fit results for the  $H_T$  variable at a centre-of-mass energy of 8 TeV (electron channel).

Process	120–185 GeV	185–215 GeV	215–247 GeV	247–283 GeV	283–323 GeV	323–365 GeV	365–409 GeV	409–458 GeV	458–512 GeV	512–570 GeV	570–629 GeV	629–691 GeV	691–769 GeV	$\geq 769$ GeV	Total
t̄t in	937.5 ± 85.8	3148.7 ± 156.7	6333.1 ± 223.2	8687.4 ± 259.1	9454.1 ± 270.1	8327.7 ± 253.4	6889.5 ± 231.1	5669.7 ± 207.2	4326.6 ± 181.5	2961.6 ± 150.2	2066.7 ± 125.1	1465.1 ± 105.4	1104.5 ± 90.2	1815.9 ± 116.3	63233.1 ± 2455.3
t̄t fit	1071.7 ± 67.9	3100.1 ± 176.4	7037.8 ± 110.8	9677.3 ± 138.5	9700.1 ± 207.8	8309.8 ± 167.0	6494.9 ± 171.0	5399.5 ± 143.9	4263.9 ± 122.9	3005.0 ± 104.6	1828.2 ± 75.7	1289.0 ± 48.1	898.4 ± 47.0	1388.5 ± 72.3	63464.3 ± 1653.8
Single-Top in	64.0 ± 16.4	182.6 ± 27.7	260.2 ± 33.0	360.2 ± 39.7	359.2 ± 38.0	297.8 ± 35.8	279.6 ± 34.3	210.7 ± 29.8	164.2 ± 25.9	128.9 ± 23.4	78.9 ± 17.9	52.9 ± 14.1	47.3 ± 13.0	80.3 ± 17.9	2566.9 ± 366.8
Single-Top fit	38.9 ± 69.0	517.5 ± 220.5	0.0 ± 155.1	0.0 ± 875.3	333.0 ± 270.7	540.9 ± 205.6	874.3 ± 185.9	334.2 ± 145.7	140.1 ± 112.1	75.8 ± 93.9	210.1 ± 65.7	67.4 ± 39.1	88.1 ± 40.2	137.5 ± 64.8	3357.9 ± 2543.6
W/Z + jets in	95.7 ± 5.2	124.4 ± 6.7	166.0 ± 9.0	191.1 ± 10.4	172.8 ± 9.4	144.5 ± 7.8	121.6 ± 6.6	104.3 ± 5.7	84.1 ± 4.6	60.1 ± 3.3	41.6 ± 2.3	33.0 ± 1.8	25.1 ± 1.4	41.1 ± 2.2	1405.6 ± 76.2
W/Z + jets fit	0.0 ± 37.3	121.4 ± 128.9	280.7 ± 160.5	665.1 ± 183.3	884.5 ± 272.8	861.4 ± 156.4	304.7 ± 181.8	397.4 ± 143.6	88.1 ± 135.5	149.0 ± 106.8	43.7 ± 59.7	0.0 ± 46.9	80.2 ± 51.5	3876.1 ± 1727.1	
QCD in	2.6 ± 0.1	17.4 ± 0.4	1827.4 ± 43.5	221.1 ± 5.3	47.8 ± 1.1	32.6 ± 0.8	41.1 ± 1.0	123.8 ± 2.9	30.5 ± 0.7	12.1 ± 0.3	21.7 ± 0.5	11.1 ± 0.3	19.2 ± 0.5	18.9 ± 0.5	2427.4 ± 57.8
QCD fit	178.5 ± 27.1	287.0 ± 75.5	329.5 ± 102.3	228.7 ± 99.8	167.3 ± 109.1	0.0 ± 145.6	21.2 ± 71.2	28.9 ± 59.4	91.9 ± 64.9	36.1 ± 53.4	28.0 ± 28.8	29.6 ± 15.0	42.5 ± 13.4	8.8 ± 31.6	1477.8 ± 897.3
Sum MC in	1099.8 ± 107.4	3473.2 ± 191.6	8586.7 ± 308.7	9459.9 ± 314.5	10033.9 ± 318.7	8847.7 ± 297.8	7331.8 ± 273.0	6108.5 ± 245.5	4605.5 ± 212.7	3162.7 ± 177.1	2208.9 ± 145.7	1562.1 ± 121.5	1196.2 ± 105.0	1956.1 ± 136.9	69633.0 ± 2956.2
Sum MC fit	1289.0 ± 201.3	4026.0 ± 601.3	7648.0 ± 528.7	10571.0 ± 1296.9	11085.0 ± 860.5	9712.0 ± 674.6	7695.0 ± 609.9	6160.0 ± 492.6	4584.0 ± 435.4	3266.0 ± 358.8	2110.0 ± 229.9	1386.0 ± 149.1	1029.0 ± 162.6	1615.0 ± 220.2	72176.1 ± 6821.9
Data	1289.0 ± 122.5	4026.0 ± 213.0	7648.0 ± 292.2	10571.0 ± 339.5	11085.0 ± 349.0	9712.0 ± 323.9	7695.0 ± 286.5	6160.0 ± 256.1	4584.0 ± 219.4	3266.0 ± 186.4	2110.0 ± 149.0	1386.0 ± 120.1	1029.0 ± 104.2	1615.0 ± 130.6	72176.0 ± 3092.5

Table B.20: Fit results for the  $H_T$  variable at a centre-of-mass energy of 8 TeV (muon channel).

Process	120–185 GeV	185–215 GeV	215–247 GeV	247–283 GeV	283–323 GeV	323–365 GeV	365–409 GeV	409–458 GeV	458–512 GeV	512–570 GeV	570–629 GeV	629–691 GeV	691–769 GeV	$\geq 769$ GeV	Total
t̄t in	1092.4 ± 92.3	3830.8 ± 171.8	7685.2 ± 242.5	10846.7 ± 288.8	11271.8 ± 294.2	10014.3 ± 276.9	8183.4 ± 250.4	6533.5 ± 222.4	5036.2 ± 195.2	3579.8 ± 164.9	2347.3 ± 133.4	1507.1 ± 106.1	1227.8 ± 95.8	1838.7 ± 117.5	74995.1 ± 2652.1
t̄t fit	1069.3 ± 81.0	3678.4 ± 198.3	7970.7 ± 284.4	10932.2 ± 139.4	10967.8 ± 269.3	9560.9 ± 202.1	7915.8 ± 167.8	5851.0 ± 153.5	4404.6 ± 135.7	2977.4 ± 105.9	1912.9 ± 83.0	1386.4 ± 60.4	1046.2 ± 53.1	1446.3 ± 73.3	71155.9 ± 2007.3
Single-Top in	88.6 ± 18.7	195.9 ± 28.5	338.8 ± 37.7	374.5 ± 39.4	428.9 ± 42.5	380.3 ± 39.7	312.5 ± 35.6	259.8 ± 32.8	189.5 ± 27.6	144.4 ± 24.7	96.0 ± 20.1	70.5 ± 17.2	57.6 ± 15.1	86.7 ± 18.5	3024.0 ± 398.2
Single-Top fit	248.5 ± 83.4	671.1 ± 219.9	410.2 ± 369.8	0.0 ± 805.2	1029.7 ± 346.2	535.0 ± 267.0	143.3 ± 191.0	793.0 ± 153.2	446.6 ± 132.3	357.8 ± 92.1	214.4 ± 75.2	123.5 ± 52.5	2.5 ± 191.2	117.2 ± 68.9	5092.8 ± 3048.1
W/Z + jets in	101.3 ± 5.0	143.7 ± 7.1	172.3 ± 8.5	200.6 ± 9.9	209.1 ± 10.4	179.3 ± 8.9	144.4 ± 7.2	117.4 ± 5.8	97.1 ± 4.8	65.0 ± 3.2	52.6 ± 2.6	37.4 ± 1.9	25.8 ± 1.3	50.8 ± 2.5	1596.7 ± 79.1
W/Z + jets fit	72.2 ± 85.0	0.0 ± 59.6	391.0 ± 221.4	982.7 ± 214.9	585.5 ± 176.0	718.5 ± 237.8	672.4 ± 194.1	188.0 ± 97.3	224.7 ± 81.5	155.8 ± 56.0	85.7 ± 42.2	73.0 ± 46.8	78.2 ± 26.4	20.2 ± 61.7	4248.1 ± 1600.8
QCD in	1.0 ± 0.0	408.5 ± 5.8	28.0 ± 0.4	18.9 ± 0.3	1.0 ± 0.0	7.5 ± 0.1	1.0 ± 0.0	5.4 ± 0.1	11.8 ± 0.2	7.9 ± 0.1	14.1 ± 0.2	16.3 ± 0.2	7.7 ± 0.1	1.3 ± 0.0	530.4 ± 7.5
QCD fit	58.0 ± 83.1	215.6 ± 69.5	76.9 ± 159.0	97.2 ± 176.3	0.0 ± 477.2	6.6 ± 587.6	39.5 ± 111.3	0.0 ± 51.8	0.0 ± 60.9	0.0 ± 80.2	0.0 ± 885.9	13.1 ± 28.9	0.0 ± 22.5	43.3 ± 48.6	550.2 ± 2842.7
Sum MC in	1283.3 ± 116.1	4578.9 ± 213.2	8224.3 ± 289.2	11440.7 ± 338.4	11910.9 ± 347.1	10581.4 ± 325.6	8641.4 ± 293.2	6916.2 ± 261.1	5334.6 ± 227.7	3797.1 ± 192.9	2510.0 ± 156.3	1631.3 ± 125.4	1318.9 ± 112.2	1977.4 ± 138.5	80146.2 ± 3136.9
Sum MC fit	1448.0 ± 332.6	4565.0 ± 547.3	8848.9 ± 1034.6	12012.1 ± 1335.8	12583.0 ± 1268.7	10821.0 ± 1294.5	8771.0 ± 664.2	6832.0 ± 455.8	5112.0 ± 410.5	3491.0 ± 334.2	2213.0 ± 1086.3	1596.0 ± 188.6	1127.0 ± 293.1	1627.0 ± 252.6	81047.0 ± 9498.8
Data	1448.0 ± 123.2	4565.0 ± 217.3	8849.0 ± 301.6	12012.0 ± 351.4	12583.0 ± 358.7	10821.0 ± 332.3	8771.0 ± 298.7	6832.0 ± 262.3	5112.0 ± 227.2	3491.0 ± 188.2	2213.0 ± 149.1	1596.0 ± 126.2	1127.0 ± 106.7	1627.0 ± 126.2	81047.0 ± 3169.1

Table B.21: Fit results for the  $S_T$  variable at a centre-of-mass energy of 8 TeV (electron channel).

Process	146–277 GeV	277–319 GeV	319–361 GeV	361–408 GeV	408–459 GeV	459–514 GeV	514–573 GeV	573–637 GeV	637–705 GeV	705–774 GeV	774–854 GeV	854–940 GeV	$\geq 940$ GeV	Total
t̄t in	946.0 $\pm$ 87.2	3777.2 $\pm$ 171.5	7287.4 $\pm$ 239.9	9617.1 $\pm$ 273.1	9713.1 $\pm$ 273.6	8539.6 $\pm$ 256.1	6791.6 $\pm$ 227.5	5216.9 $\pm$ 199.3	3637.8 $\pm$ 166.4	2574.4 $\pm$ 139.5	1838.8 $\pm$ 117.3	1237.2 $\pm$ 94.8	2056.0 $\pm$ 122.6	63233.1 $\pm$ 2368.9
t̄t fit	1066.4 $\pm$ 80.3	4208.8 $\pm$ 192.0	7559.1 $\pm$ 243.6	10629.2 $\pm$ 151.9	9980.6 $\pm$ 202.8	8411.8 $\pm$ 186.3	6401.4 $\pm$ 171.3	4962.8 $\pm$ 143.5	3510.8 $\pm$ 112.5	2237.7 $\pm$ 85.8	1524.8 $\pm$ 59.5	954.0 $\pm$ 48.7	1560.5 $\pm$ 65.4	63007.8 $\pm$ 1743.6
Single-Top in	67.0 $\pm$ 16.8	186.6 $\pm$ 27.6	281.6 $\pm$ 34.7	374.4 $\pm$ 39.3	361.5 $\pm$ 39.2	304.1 $\pm$ 35.9	270.3 $\pm$ 33.3	220.0 $\pm$ 30.5	155.8 $\pm$ 25.6	103.9 $\pm$ 21.1	85.7 $\pm$ 18.7	52.3 $\pm$ 14.3	103.6 $\pm$ 20.3	2566.9 $\pm$ 357.2
Single-Top fit	167.4 $\pm$ 80.9	309.7 $\pm$ 220.2	551.9 $\pm$ 322.4	0.0 $\pm$ 333.2	116.7 $\pm$ 254.4	600.2 $\pm$ 224.4	617.1 $\pm$ 180.1	664.1 $\pm$ 147.6	444.2 $\pm$ 106.9	205.7 $\pm$ 84.4	167.6 $\pm$ 53.9	128.3 $\pm$ 45.2	224.3 $\pm$ 61.8	4197.3 $\pm$ 2115.5
W/Z + jets in	108.1 $\pm$ 5.9	141.1 $\pm$ 7.6	176.8 $\pm$ 9.6	197.5 $\pm$ 10.7	169.7 $\pm$ 9.2	147.1 $\pm$ 8.0	119.5 $\pm$ 6.5	102.9 $\pm$ 5.6	71.6 $\pm$ 3.9	47.3 $\pm$ 2.6	44.6 $\pm$ 2.4	27.0 $\pm$ 1.5	52.4 $\pm$ 2.8	1405.6 $\pm$ 76.2
W/Z + jets fit	0.0 $\pm$ 171.0	47.1 $\pm$ 146.2	425.7 $\pm$ 216.2	631.1 $\pm$ 203.2	1228.2 $\pm$ 231.7	619.9 $\pm$ 244.3	414.5 $\pm$ 186.8	81.0 $\pm$ 83.0	0.0 $\pm$ 39.6	0.0 $\pm$ 107.6	27.3 $\pm$ 52.0	0.0 $\pm$ 46.0	0.0 $\pm$ 56.4	3474.8 $\pm$ 1784.0
QCD in	8.4 $\pm$ 0.2	1757.3 $\pm$ 41.8	134.9 $\pm$ 3.2	192.2 $\pm$ 4.6	44.0 $\pm$ 1.0	38.0 $\pm$ 0.9	128.6 $\pm$ 3.1	29.8 $\pm$ 0.7	20.8 $\pm$ 0.5	19.0 $\pm$ 0.5	17.3 $\pm$ 0.4	19.8 $\pm$ 0.5	17.2 $\pm$ 0.4	2427.4 $\pm$ 57.8
QCD fit	257.2 $\pm$ 31.9	387.4 $\pm$ 89.5	260.4 $\pm$ 102.1	261.8 $\pm$ 107.3	4.5 $\pm$ 323.7	32.1 $\pm$ 91.7	30.9 $\pm$ 75.6	0.0 $\pm$ 79.0	84.0 $\pm$ 29.7	68.6 $\pm$ 24.9	25.3 $\pm$ 25.7	39.8 $\pm$ 14.0	44.2 $\pm$ 16.1	1496.3 $\pm$ 1011.3
Sum MC in	1129.4 $\pm$ 110.1	5862.2 $\pm$ 248.5	7880.7 $\pm$ 287.4	10381.2 $\pm$ 327.7	10288.3 $\pm$ 323.0	9028.8 $\pm$ 300.9	7310.0 $\pm$ 270.4	5569.5 $\pm$ 236.1	3886.1 $\pm$ 196.3	2744.6 $\pm$ 163.6	1986.4 $\pm$ 138.8	1336.3 $\pm$ 111.0	2229.2 $\pm$ 146.1	69633.0 $\pm$ 2860.1
Sum MC fit	1491.0 $\pm$ 364.2	4953.0 $\pm$ 647.9	8797.1 $\pm$ 884.3	11522.0 $\pm$ 795.6	11330.0 $\pm$ 1012.7	9664.0 $\pm$ 746.7	7463.9 $\pm$ 613.8	5708.0 $\pm$ 453.1	4039.0 $\pm$ 288.7	2512.0 $\pm$ 302.7	1745.0 $\pm$ 191.2	1122.0 $\pm$ 153.9	1829.0 $\pm$ 199.7	72176.2 $\pm$ 6654.4
Data	1491.0 $\pm$ 133.1	4953.0 $\pm$ 237.2	8797.0 $\pm$ 313.0	11522.0 $\pm$ 355.2	11330.0 $\pm$ 351.5	9664.0 $\pm$ 322.3	7464.0 $\pm$ 282.5	5708.0 $\pm$ 244.1	4039.0 $\pm$ 206.4	2512.0 $\pm$ 162.4	1745.0 $\pm$ 134.9	1122.0 $\pm$ 108.3	1829.0 $\pm$ 136.8	72176.0 $\pm$ 2987.6

Table B.22: Fit results for the  $S_T$  variable at a centre-of-mass energy of 8 TeV (muon channel).

Process	146–277 GeV	277–319 GeV	319–361 GeV	361–408 GeV	408–459 GeV	459–514 GeV	514–573 GeV	573–637 GeV	637–705 GeV	705–774 GeV	774–854 GeV	854–940 GeV	$\geq 940$ GeV	Total
t̄t in	1308.6 $\pm$ 101.5	4828.7 $\pm$ 193.7	8949.3 $\pm$ 262.8	11773.4 $\pm$ 300.8	11661.3 $\pm$ 298.9	10029.2 $\pm$ 277.1	7959.9 $\pm$ 246.2	5966.6 $\pm$ 212.4	4245.7 $\pm$ 178.9	2786.3 $\pm$ 144.3	2065.1 $\pm$ 124.2	1313.2 $\pm$ 99.4	2107.8 $\pm$ 123.8	74995.1 $\pm$ 2564.1
t̄t fit	1361.6 $\pm$ 99.9	4983.2 $\pm$ 202.9	9217.9 $\pm$ 363.6	11693.6 $\pm$ 271.8	11405.1 $\pm$ 253.6	9817.7 $\pm$ 202.3	7764.1 $\pm$ 184.3	5374.4 $\pm$ 149.9	3516.8 $\pm$ 119.7	2394.0 $\pm$ 90.7	1767.1 $\pm$ 69.0	1076.0 $\pm$ 48.8	1599.7 $\pm$ 68.7	71971.1 $\pm$ 2125.3
Single-Top in	89.5 $\pm$ 18.9	219.7 $\pm$ 30.5	360.3 $\pm$ 38.4	429.6 $\pm$ 42.0	422.2 $\pm$ 41.8	370.2 $\pm$ 39.2	315.7 $\pm$ 36.4	237.0 $\pm$ 31.4	178.6 $\pm$ 26.9	122.3 $\pm$ 22.5	92.1 $\pm$ 20.0	70.6 $\pm$ 16.8	116.2 $\pm$ 21.7	3024.0 $\pm$ 386.5
Single-Top fit	418.1 $\pm$ 109.6	447.5 $\pm$ 253.0	129.5 $\pm$ 443.4	546.0 $\pm$ 328.1	490.6 $\pm$ 349.4	93.5 $\pm$ 251.2	188.6 $\pm$ 206.0	586.1 $\pm$ 158.7	596.8 $\pm$ 115.1	194.4 $\pm$ 87.7	161.2 $\pm$ 63.5	76.9 $\pm$ 43.8	125.2 $\pm$ 64.9	4054.4 $\pm$ 2474.5
W/Z + jets in	115.7 $\pm$ 5.7	164.1 $\pm$ 8.1	183.0 $\pm$ 9.1	220.4 $\pm$ 10.9	199.9 $\pm$ 9.9	176.4 $\pm$ 8.7	141.7 $\pm$ 7.0	119.7 $\pm$ 5.9	83.1 $\pm$ 4.1	60.2 $\pm$ 3.0	41.1 $\pm$ 2.0	31.4 $\pm$ 1.6	60.0 $\pm$ 3.0	1596.7 $\pm$ 79.1
W/Z + jets fit	8.7 $\pm$ 259.4	136.3 $\pm$ 143.2	735.4 $\pm$ 229.8	707.6 $\pm$ 254.7	984.1 $\pm$ 273.4	947.7 $\pm$ 169.8	408.3 $\pm$ 126.1	91.5 $\pm$ 90.2	110.4 $\pm$ 65.8	116.6 $\pm$ 46.7	0.0 $\pm$ 140.8	77.9 $\pm$ 82.7	45.3 $\pm$ 62.3	4369.7 $\pm$ 1944.9
QCD in	408.5 $\pm$ 5.6	1.0 $\pm$ 0.0	1.0 $\pm$ 0.0	18.9 $\pm$ 0.3	35.4 $\pm$ 0.5	5.4 $\pm$ 0.1	5.7 $\pm$ 0.1	15.2 $\pm$ 0.2	12.9 $\pm$ 0.2	16.3 $\pm$ 0.2	7.7 $\pm$ 0.1	1.0 $\pm$ 0.0	1.3 $\pm$ 0.0	530.4 $\pm$ 7.3
QCD fit	182.7 $\pm$ 95.6	120.1 $\pm$ 114.8	89.2 $\pm$ 169.1	212.8 $\pm$ 191.5	5.2 $\pm$ 1056.3	0.0 $\pm$ 91.3	0.0 $\pm$ 72.2	0.0 $\pm$ 69.2	0.0 $\pm$ 101.1	0.0 $\pm$ 65.1	17.7 $\pm$ 17.3	2.2 $\pm$ 478.9	21.8 $\pm$ 47.3	651.8 $\pm$ 2569.9
Sum MC in	1922.3 $\pm$ 131.8	5213.5 $\pm$ 232.3	9493.6 $\pm$ 310.2	12442.3 $\pm$ 354.0	12318.8 $\pm$ 351.1	10581.2 $\pm$ 325.1	8423.0 $\pm$ 289.7	6338.6 $\pm$ 250.0	4520.2 $\pm$ 210.1	2985.2 $\pm$ 170.1	2206.0 $\pm$ 146.4	1416.2 $\pm$ 117.8	2285.3 $\pm$ 148.4	80146.2 $\pm$ 3036.9
Sum MC fit	1971.0 $\pm$ 564.5	5687.0 $\pm$ 714.0	10172.0 $\pm$ 1205.9	13160.0 $\pm$ 1046.1	12884.9 $\pm$ 1932.6	10859.0 $\pm$ 714.6	8361.0 $\pm$ 588.6	6052.0 $\pm$ 468.0	4224.0 $\pm$ 401.6	2705.0 $\pm$ 290.1	1946.0 $\pm$ 290.7	1233.0 $\pm$ 654.3	1792.0 $\pm$ 243.3	81047.0 $\pm$ 9114.5
Data	1971.0 $\pm$ 144.0	5687.0 $\pm$ 243.2	10172.0 $\pm$ 324.3	13160.0 $\pm$ 367.7	12885.0 $\pm$ 363.1	10859.0 $\pm$ 332.2	8361.0 $\pm$ 290.6	6052.0 $\pm$ 246.6	4224.0 $\pm$ 206.4	2705.0 $\pm$ 165.0	1946.0 $\pm$ 138.4	1233.0 $\pm$ 110.4	1792.0 $\pm$ 131.4	81047.0 $\pm$ 3036.1

Table B.23: Fit results for the  $p_T^W$  variable at a centre-of-mass energy of 8 TeV (electron channel).

Process	0--27 GeV	27--52 GeV	52--78 GeV	78--105 GeV	105--134 GeV	134--166 GeV	166--200 GeV	200--237 GeV	$\geq 237$ GeV	Total
t̄t in	4063.8 ± 178.3	9575.7 ± 274.6	12466.8 ± 311.8	12054.9 ± 304.4	9721.1 ± 273.6	6755.9 ± 225.8	3958.3 ± 171.7	2289.9 ± 129.7	2346.9 ± 128.0	63233.1 ± 1997.8
t̄t fit	4381.0 ± 159.3	10707.3 ± 189.9	12562.1 ± 298.2	12407.8 ± 206.1	9614.2 ± 232.1	6076.1 ± 179.5	3434.6 ± 126.2	1867.7 ± 76.3	1811.4 ± 61.0	62862.3 ± 1528.7
Single-Top in	144.4 ± 24.6	362.1 ± 38.4	461.3 ± 43.5	437.1 ± 43.1	393.5 ± 40.8	289.3 ± 35.8	185.6 ± 27.5	120.5 ± 22.5	173.2 ± 26.5	2566.9 ± 302.8
Single-Top fit	125.3 ± 152.4	0.0 ± 1691.4	577.1 ± 377.9	0.0 ± 665.0	351.1 ± 262.5	218.1 ± 203.0	249.3 ± 126.6	259.3 ± 75.6	298.5 ± 57.0	2078.7 ± 3611.4
W/Z + jets in	112.1 ± 6.1	249.4 ± 13.5	292.8 ± 15.9	246.7 ± 13.4	184.1 ± 10.0	127.5 ± 6.9	74.3 ± 4.0	48.4 ± 2.6	70.4 ± 3.8	1405.6 ± 76.2
W/Z + jets fit	581.7 ± 176.4	1129.6 ± 256.9	1781.6 ± 346.7	1408.3 ± 270.2	748.8 ± 298.8	682.9 ± 150.0	221.5 ± 139.2	0.0 ± 4263.1	0.0 ± 35.6	6554.4 ± 5936.9
QCD in	20.4 ± 0.5	150.6 ± 3.6	1811.5 ± 43.1	164.9 ± 3.9	52.4 ± 1.2	177.2 ± 4.2	19.3 ± 0.5	10.7 ± 0.3	20.4 ± 0.5	2427.4 ± 57.8
QCD fit	79.0 ± 80.5	188.2 ± 114.7	167.2 ± 128.2	134.9 ± 114.1	8.8 ± 334.1	0.0 ± 8816.9	29.5 ± 58.5	34.0 ± 29.1	39.1 ± 17.9	680.8 ± 9694.1
Sum MC in	4340.7 ± 209.5	10337.8 ± 330.1	15032.3 ± 414.3	12903.5 ± 364.7	10351.0 ± 325.6	7349.9 ± 272.8	4237.5 ± 203.7	2469.5 ± 155.1	2610.8 ± 158.8	69633.0 ± 2434.6
Sum MC fit	5167.0 ± 568.6	12025.1 ± 2252.9	15088.0 ± 1151.0	13951.1 ± 1255.5	10723.0 ± 1127.5	6977.0 ± 9349.4	3935.0 ± 450.6	2161.0 ± 4444.2	2149.0 ± 171.4	72176.2 ± 20771.1
Data	5167.0 ± 241.9	12025.0 ± 365.6	15088.0 ± 408.6	13951.0 ± 389.9	10723.0 ± 337.9	6977.0 ± 271.7	3935.0 ± 201.7	2161.0 ± 147.2	2149.0 ± 144.2	72176.0 ± 2508.7

Table B.24: Fit results for the  $p_T^W$  variable at a centre-of-mass energy of 8 TeV (muon channel).

Process	0--27 GeV	27--52 GeV	52--78 GeV	78--105 GeV	105--134 GeV	134--166 GeV	166--200 GeV	200--237 GeV	$\geq 237$ GeV	Total
t̄t in	5359.1 ± 204.0	12104.9 ± 307.4	15135.4 ± 341.7	14178.5 ± 329.0	11157.9 ± 291.2	7537.5 ± 238.6	4379.9 ± 181.3	2488.1 ± 134.4	2653.8 ± 136.8	74995.1 ± 2164.4
t̄t fit	5523.7 ± 110.1	12780.5 ± 176.2	14949.0 ± 354.0	13818.3 ± 340.9	10693.5 ± 168.2	7116.8 ± 206.6	3701.0 ± 118.1	1994.8 ± 79.5	1957.0 ± 70.7	72534.6 ± 1624.2
Single-Top in	204.1 ± 28.4	449.7 ± 42.5	559.3 ± 48.7	534.4 ± 47.1	439.8 ± 42.4	314.4 ± 36.7	188.7 ± 28.2	126.7 ± 23.1	206.8 ± 29.2	3024.0 ± 326.2
Single-Top fit	0.0 ± 658.0	0.0 ± 138.4	565.5 ± 480.5	214.8 ± 439.8	0.0 ± 2205.0	363.6 ± 249.7	483.7 ± 128.7	188.2 ± 84.7	209.1 ± 72.1	2024.9 ± 4457.0
W/Z + jets in	131.6 ± 6.5	289.6 ± 14.3	329.6 ± 16.3	281.7 ± 13.9	190.9 ± 9.5	153.2 ± 7.6	84.9 ± 4.2	59.1 ± 2.9	76.2 ± 3.8	1596.7 ± 79.1
W/Z + jets fit	574.2 ± 98.0	1139.1 ± 237.7	1533.5 ± 260.9	1361.7 ± 359.5	1014.7 ± 242.4	179.1 ± 239.3	14.1 ± 376.4	119.0 ± 56.1	12.9 ± 198.7	5948.4 ± 2069.0
QCD in	5.7 ± 0.1	422.6 ± 5.8	5.7 ± 0.1	39.1 ± 0.5	19.7 ± 0.3	34.0 ± 0.5	0.5 ± 0.0	0.1 ± 0.0	0.1 ± 0.0	527.6 ± 7.2
QCD fit	0.0 ± 23.1	55.4 ± 158.1	0.0 ± 104.4	97.2 ± 209.3	119.9 ± 173.5	181.6 ± 146.0	64.2 ± 94.1	0.0 ± 18.0	21.0 ± 81.9	539.3 ± 1008.5
Sum MC in	5700.5 ± 239.1	13266.8 ± 370.0	16030.0 ± 406.7	15033.8 ± 390.6	11808.2 ± 343.3	8039.2 ± 283.4	4654.0 ± 213.7	2674.0 ± 160.5	2936.9 ± 169.7	80143.4 ± 2576.9
Sum MC fit	6098.0 ± 889.2	13975.1 ± 710.3	17048.0 ± 1199.9	15492.0 ± 1349.6	11828.0 ± 2789.1	7841.0 ± 841.6	4263.0 ± 717.3	2302.1 ± 238.4	2200.0 ± 423.4	81047.2 ± 9158.7
Data	6098.0 ± 251.0	13975.0 ± 380.4	17048.0 ± 419.8	15492.0 ± 398.0	11828.0 ± 346.0	7841.0 ± 279.4	4263.0 ± 205.4	2302.0 ± 150.2	2200.0 ± 143.1	81047.0 ± 2573.4

Table B.25: Fit results for the  $M_T^W$  variable at a centre-of-mass energy of 8 TeV (electron channel).

Process	0--23 GeV	23--58 GeV	$\geq 58$ GeV	Total
t̄t in	$8261.6 \pm 252.9$	$17940.6 \pm 372.0$	$37026.8 \pm 533.7$	$63229.0 \pm 1158.5$
t̄t fit	$8012.3 \pm 211.3$	$17460.8 \pm 329.3$	$38017.8 \pm 364.2$	$63491.0 \pm 904.8$
Single-Top in	$348.2 \pm 39.1$	$733.5 \pm 55.9$	$1485.2 \pm 78.9$	$2566.9 \pm 174.0$
Single-Top fit	$26.9 \pm 506.0$	$245.5 \pm 395.8$	$0.1 \pm 4833.9$	$272.5 \pm 5735.7$
W/Z + jets in	$220.2 \pm 11.9$	$403.2 \pm 21.9$	$782.2 \pm 42.4$	$1405.6 \pm 76.2$
W/Z + jets fit	$959.9 \pm 292.4$	$1784.9 \pm 403.2$	$5102.4 \pm 487.8$	$7847.2 \pm 1183.4$
QCD in	$67.7 \pm 1.6$	$1961.0 \pm 46.7$	$398.7 \pm 9.5$	$2427.4 \pm 57.8$
QCD fit	$169.8 \pm 111.3$	$371.9 \pm 146.7$	$21.8 \pm 479.5$	$563.6 \pm 737.5$
Sum MC in	$8897.6 \pm 305.6$	$21038.3 \pm 496.4$	$39693.0 \pm 664.5$	$69628.8 \pm 1466.5$
Sum MC fit	$9169.0 \pm 1121.0$	$19863.0 \pm 1275.0$	$43142.2 \pm 6165.4$	$72174.2 \pm 8561.4$
Data	$9169.0 \pm 316.6$	$19863.0 \pm 465.2$	$43142.0 \pm 684.4$	$72174.0 \pm 1466.2$

Table B.26: Fit results for the  $M_T^W$  variable at a centre-of-mass energy of 8 TeV (muon channel).

Process	0--23 GeV	23--58 GeV	$\geq 58$ GeV	Total
t̄t in	$9827.5 \pm 274.7$	$21864.3 \pm 409.9$	$43303.4 \pm 574.6$	$74995.1 \pm 1259.2$
t̄t fit	$9392.8 \pm 239.2$	$21147.1 \pm 240.7$	$42723.5 \pm 560.5$	$73263.4 \pm 1040.4$
Single-Top in	$409.5 \pm 41.6$	$903.5 \pm 61.7$	$1710.9 \pm 84.0$	$3024.0 \pm 187.3$
Single-Top fit	$82.7 \pm 277.9$	$0.0 \pm 313.9$	$303.9 \pm 700.1$	$386.6 \pm 1291.9$
W/Z + jets in	$239.4 \pm 11.9$	$490.2 \pm 24.3$	$867.1 \pm 42.9$	$1596.7 \pm 79.1$
W/Z + jets fit	$1131.5 \pm 290.2$	$2366.8 \pm 220.4$	$3720.6 \pm 382.0$	$7218.8 \pm 892.7$
QCD in	$67.7 \pm 0.9$	$458.8 \pm 6.3$	$0.9 \pm 0.0$	$527.4 \pm 7.2$
QCD fit	$178.0 \pm 179.9$	$0.0 \pm 537.4$	$0.1 \pm 177.1$	$178.2 \pm 894.4$
Sum MC in	$10544.1 \pm 329.1$	$23716.8 \pm 502.1$	$45882.3 \pm 701.5$	$80143.2 \pm 1532.8$
Sum MC fit	$10785.1 \pm 987.2$	$23514.0 \pm 1312.3$	$46748.0 \pm 1819.7$	$81047.1 \pm 4119.3$
Data	$10785.0 \pm 333.0$	$23514.0 \pm 491.1$	$46748.0 \pm 689.2$	$81047.0 \pm 1513.3$

## B.9 Fit correlations

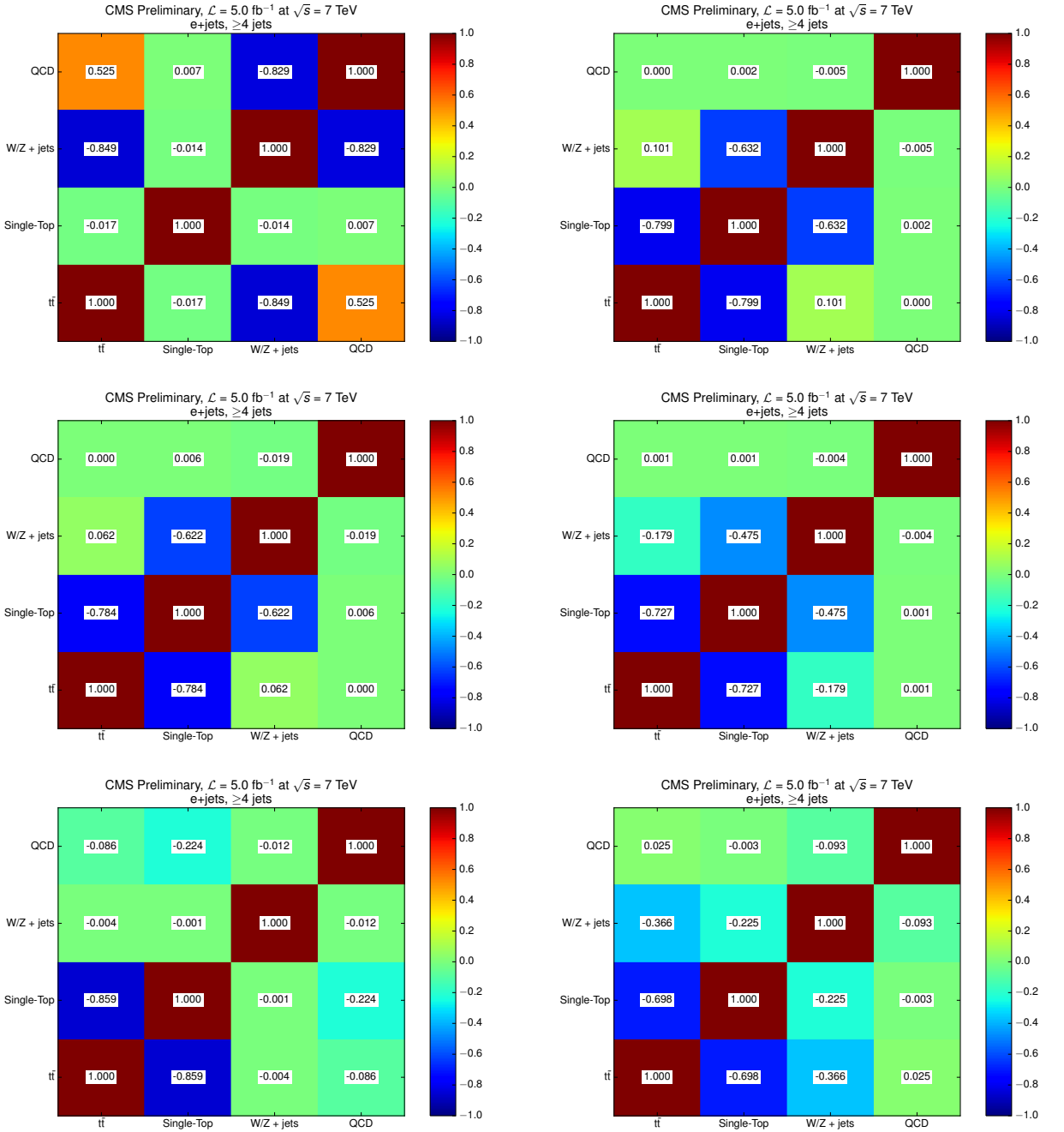


Figure B.16: Correlation between fit processes for the  $E_T^{\text{miss}}$  variable in the electron+jets channel at  $\sqrt{s} = 7 \text{ TeV}$  in bins 0-27 GeV (upper left), 27-52 GeV (upper right), 52-87 GeV (middle left), 87-130 GeV (middle right), 130-172 GeV (lower left) and  $\geq 172 \text{ GeV}$  (lower right).

## B.10 Systematic Uncertainties

Table B.27: Systematic uncertainties for the normalised  $t\bar{t}$  cross section measurement with respect to  $E_T^{\text{miss}}$  variable at a centre-of-mass energy of 7 TeV (combination of electron and muon channels).

Uncertainty source	0–27 GeV	27–52 GeV	52–87 GeV	87–130 GeV	130–172 GeV	$\geq 172$ GeV
b-tagging efficiency $-1\sigma$ (%)	0.03	0.01	-0.01	-0.03	-0.05	-0.07
b-tagging efficiency $+1\sigma$ (%)	-0.03	-0.01	0.01	0.03	0.05	0.07
Electron efficiency $-1\sigma$ (%)	-0.00	0.00	0.00	-0.00	-0.00	-0.01
Electron efficiency $+1\sigma$ (%)	0.01	0.01	-0.01	-0.02	-0.01	0.01
Jet energy resolution $-1\sigma$ (%)	-0.00	-0.02	-0.02	0.04	0.14	0.25
Jet energy resolution $+1\sigma$ (%)	0.06	0.03	-0.01	-0.08	-0.14	-0.17
Jet energy scale $-1\sigma$ (%)	-0.18	-0.11	0.03	0.25	0.51	0.72
Jet energy scale $+1\sigma$ (%)	-0.11	0.02	0.10	-0.01	-0.23	-0.43
Muon efficiency $-1\sigma$ (%)	-0.00	-0.00	0.00	0.00	0.01	0.01
Muon efficiency $+1\sigma$ (%)	0.00	0.00	-0.00	-0.00	-0.00	-0.01
PDF uncertainty $-1\sigma$ (%)	1.23	0.57	0.49	0.68	0.65	2.08
PDF uncertainty $+1\sigma$ (%)	1.23	0.57	0.49	0.68	0.65	2.08
Pile-up $-1\sigma$ (%)	-0.00	-0.00	0.00	0.01	0.01	0.01
Pile-up $+1\sigma$ (%)	0.04	0.03	-0.01	-0.05	-0.10	-0.13
QCD cross section $+1\sigma$ (%)	0.00	0.00	0.00	-0.00	-0.00	-0.00
QCD cross section $-1\sigma$ (%)	0.16	-0.02	-0.13	-0.02	0.24	0.49
QCD shape uncertainty (%)	0.02	0.01	-0.01	-0.02	-0.03	-0.04
Single top cross section $+1\sigma$ (%)	-0.00	-0.00	0.00	0.00	0.00	-0.00
Single top cross section $-1\sigma$ (%)	-0.00	0.00	0.00	0.00	-0.00	-0.00
$t\bar{t}$ cross section $+1\sigma$ (%)	0.00	0.00	0.00	-0.00	-0.00	-0.00
$t\bar{t}$ cross section $-1\sigma$ (%)	0.00	0.00	-0.00	-0.00	-0.00	-0.00
$t\bar{t}$ (top mass down) (%)	-0.02	0.02	0.10	-0.18	-0.26	-0.02
$t\bar{t}$ (top mass up) (%)	0.20	-0.16	0.02	-0.17	1.07	-0.20
$t\bar{t}$ (matching down) (%)	0.03	0.14	-0.00	-0.66	-0.21	2.55
$t\bar{t}$ (matching up) (%)	-0.07	-0.12	0.34	0.06	-0.86	-1.57
$t\bar{t}$ ( $Q^2$ down) (%)	-0.09	0.08	0.20	-0.37	-0.24	-1.04
$t\bar{t}$ ( $Q^2$ up) (%)	-0.57	0.03	0.38	-0.26	0.09	0.38
V+jets cross section $+1\sigma$ (%)	-0.00	-0.00	0.00	0.00	0.00	0.00
V+jets cross section $-1\sigma$ (%)	0.00	0.00	0.00	-0.00	-0.00	-0.00
V+jets (matching down) (%)	-0.31	-0.14	0.11	0.33	0.51	0.63
V+jets (matching up) (%)	-0.42	-0.18	0.16	0.42	0.58	0.69
V+jets ( $Q^2$ down) (%)	-0.62	-0.28	0.21	0.66	1.00	1.25
V+jets ( $Q^2$ up) (%)	-0.39	-0.17	0.14	0.41	0.60	0.72
Hadronisation uncertainty (%)	1.08	1.27	0.14	2.84	6.22	7.31
Luminosity $+1\sigma$ (%)	0.00	0.00	-0.00	-0.00	-0.00	-0.00
Luminosity $-1\sigma$ (%)	0.00	0.00	-0.00	-0.00	-0.00	-0.00
Electron energy $-1\sigma$ (%)	-0.07	-0.05	0.01	0.10	0.20	0.27
Electron energy $+1\sigma$ (%)	0.03	0.02	-0.00	-0.05	-0.10	-0.14
Muon energy $-1\sigma$ (%)	0.00	-0.00	-0.00	0.00	0.01	0.02
Muon energy $+1\sigma$ (%)	0.03	0.02	-0.01	-0.04	-0.07	-0.10
Tau energy $-1\sigma$ (%)	1.09	0.61	-0.27	-1.36	-2.45	-3.33
Tau energy $+1\sigma$ (%)	-1.07	-0.61	0.24	1.37	2.51	3.41
Unclustered energy $-1\sigma$ (%)	0.29	0.19	-0.05	-0.41	-0.79	-1.11
Unclustered energy $+1\sigma$ (%)	-0.17	-0.11	0.02	0.24	0.48	0.66
$p_T(t, \bar{t})$ reweighting (%)	0.91	1.36	1.41	1.86	6.51	14.73
Total (%)	3.03	2.49	2.15	4.36	9.94	17.53

Table B.28: Systematic uncertainties for the normalised  $t\bar{t}$  cross section measurement with respect to  $H_T$  variable at a centre-of-mass energy of 7 TeV (combination of electron and muon channels).

Uncertainty source	120–185 GeV	185–215 GeV	215–247 GeV	247–283 GeV	283–323 GeV	323–365 GeV	365–409 GeV	409–458 GeV	458–512 GeV	512–570 GeV	570–629 GeV	629–691 GeV	691–769 GeV	$\geq 769$ GeV
b-tagging efficiency $-1\sigma$ (%)	-0.02	-0.02	-0.02	-0.03	-0.03	-0.01	0.01	0.06	0.11	0.16	0.20	0.24	0.26	0.27
b-tagging efficiency $+1\sigma$ (%)	0.02	0.02	0.02	0.02	0.01	0.00	-0.02	-0.06	-0.10	-0.14	-0.17	-0.20	-0.21	-0.22
Electron efficiency $-1\sigma$ (%)	-0.23	-0.23	-0.21	-0.14	0.02	0.22	0.41	0.56	0.66	0.72	0.75	0.74	0.74	0.74
Electron efficiency $+1\sigma$ (%)	0.65	0.62	0.55	0.35	-0.07	-0.60	-1.10	-1.50	-1.78	-1.94	-1.99	-1.95	-1.89	-1.83
Jet energy resolution $-1\sigma$ (%)	0.67	0.53	0.29	-0.02	-0.33	-0.60	-0.81	-0.90	-0.90	-0.80	-0.66	-0.50	-0.35	-0.21
Jet energy resolution $+1\sigma$ (%)	-3.46	-2.71	-1.41	0.16	1.72	3.01	3.88	4.29	4.32	4.08	3.66	3.21	2.76	2.44
Jet energy scale $-1\sigma$ (%)	-3.16	-2.47	-1.27	0.11	1.37	2.41	3.24	3.87	4.28	4.49	4.55	4.53	4.39	4.25
Jet energy scale $+1\sigma$ (%)	-1.54	-1.00	-0.13	0.67	1.09	1.23	1.16	0.94	0.57	0.10	-0.48	-1.07	-1.60	-1.99
Muon efficiency $-1\sigma$ (%)	0.02	0.01	0.00	-0.00	-0.01	-0.01	-0.02	-0.02	-0.01	-0.01	0.00	0.01	0.02	0.03
Muon efficiency $+1\sigma$ (%)	0.00	0.00	0.00	0.00	0.00	0.00	0.00	-0.00	-0.01	-0.01	-0.02	-0.03	-0.03	-0.04
PDF uncertainty $-1\sigma$ (%)	0.79	0.32	0.34	0.48	0.61	0.81	0.63	0.63	0.79	1.02	1.27	1.41	1.58	1.21
PDF uncertainty $+1\sigma$ (%)	0.79	0.32	0.34	0.48	0.61	0.81	0.63	0.63	0.79	1.02	1.27	1.41	1.58	1.21
Pile-up $-1\sigma$ (%)	0.05	0.02	-0.02	-0.07	-0.09	-0.07	-0.01	0.08	0.16	0.23	0.28	0.32	0.32	0.30
Pile-up $+1\sigma$ (%)	-0.13	-0.09	-0.01	0.06	0.12	0.12	0.08	0.03	-0.01	-0.05	-0.07	-0.08	-0.07	-0.04
QCD cross section $+1\sigma$ (%)	-0.01	-0.01	-0.01	-0.00	0.00	0.01	0.01	0.01	0.02	0.02	0.02	0.02	0.02	0.02
QCD cross section $-1\sigma$ (%)	-2.11	-1.44	-0.26	1.05	1.81	1.93	1.56	0.95	0.21	-0.54	-1.23	-1.80	-2.27	-2.63
QCD shape uncertainty (%)	0.10	0.09	0.07	0.04	-0.01	-0.08	-0.14	-0.18	-0.21	-0.24	-0.27	-0.31	-0.36	-0.41
Single top cross section $+1\sigma$ (%)	-0.00	-0.00	-0.00	-0.00	-0.00	0.00	0.00	0.00	0.01	0.01	0.01	0.01	0.01	0.01
Single top cross section $-1\sigma$ (%)	-0.01	-0.01	-0.00	-0.00	0.00	0.01	0.01	0.01	0.01	0.01	0.01	0.01	0.01	0.01
$t\bar{t}$ cross section $+1\sigma$ (%)	0.00	0.00	-0.00	-0.00	-0.00	-0.00	0.00	0.00	0.00	0.00	0.00	0.00	0.00	0.00
$t\bar{t}$ cross section $-1\sigma$ (%)	0.01	0.00	-0.00	-0.01	-0.01	-0.01	-0.00	-0.00	0.00	0.00	0.01	0.01	0.01	0.01
$t\bar{t}$ (top mass down) (%)	-0.12	0.11	-0.10	0.20	-0.01	-0.00	0.02	-0.07	-0.14	-0.11	-0.03	0.20	0.12	-0.27
$t\bar{t}$ (top mass up) (%)	0.11	0.09	-0.17	0.39	-0.46	0.40	-0.22	-0.29	0.28	-0.79	-1.67	0.18	1.16	0.21
$t\bar{t}$ (matching down) (%)	-1.21	-0.21	-0.38	0.72	0.58	0.73	0.36	1.69	0.26	-0.56	-0.08	0.14	-1.38	-3.95
$t\bar{t}$ (matching up) (%)	-1.26	-0.44	-0.01	0.88	0.14	0.23	0.33	1.21	0.43	-0.17	-0.41	-0.19	1.66	3.68
$t\bar{t}$ ( $Q^2$ down) (%)	-7.76	-4.32	-0.85	2.30	3.62	5.13	5.49	5.26	4.81	4.33	2.72	2.50	3.04	2.12
$t\bar{t}$ ( $Q^2$ up) (%)	5.26	2.43	-0.12	-1.07	-2.97	-3.04	-3.31	-2.32	-1.89	-2.29	-2.20	-2.36	0.53	-0.66
V+jets cross section $+1\sigma$ (%)	-0.00	-0.00	-0.00	0.00	0.00	0.01	0.01	0.01	0.01	0.02	0.02	0.02	0.02	0.02
V+jets cross section $-1\sigma$ (%)	-0.01	-0.01	-0.00	-0.00	0.00	0.01	0.01	0.01	0.01	0.02	0.02	0.01	0.01	0.01
V+jets (matching down) (%)	-0.41	-0.42	-0.40	-0.26	0.04	0.41	0.76	1.03	1.21	1.31	1.37	1.39	1.42	1.44
V+jets (matching up) (%)	0.87	0.59	0.15	-0.24	-0.46	-0.54	-0.57	-0.60	-0.69	-0.80	-0.86	-0.85	-0.80	-0.74
V+jets ( $Q^2$ down) (%)	1.19	0.79	0.14	-0.49	-0.90	-1.02	-0.92	-0.68	-0.36	0.00	0.39	0.73	1.04	1.28
V+jets ( $Q^2$ up) (%)	-0.16	-0.21	-0.26	-0.23	-0.07	0.19	0.47	0.70	0.84	0.89	0.89	0.86	0.84	0.84
Hadronisation uncertainty (%)	35.19	12.24	3.66	11.03	12.62	13.45	11.89	10.16	8.63	9.66	7.04	5.77	5.05	1.15
Luminosity $+1\sigma$ (%)	0.02	0.01	0.01	-0.00	-0.01	-0.01	-0.02	-0.02	-0.02	-0.02	-0.01	-0.01	-0.01	-0.01
Luminosity $-1\sigma$ (%)	0.01	0.01	0.00	-0.00	-0.01	-0.01	-0.02	-0.02	-0.02	-0.01	-0.01	-0.01	-0.00	-0.00
$p_T(t, \bar{t})$ reweighting (%)	1.91	0.76	0.22	0.96	1.22	1.06	0.57	0.05	0.57	0.84	0.93	0.65	0.01	4.85
Total (%)	36.64	13.90	4.91	11.68	13.72	15.32	14.41	13.34	12.03	12.69	10.37	9.60	9.73	10.04

Table B.29: Systematic uncertainties for the normalised  $t\bar{t}$  cross section measurement with respect to  $S_T$  variable at a centre-of-mass energy of 7 TeV (combination of electron and muon channels).

Uncertainty source	146–277 GeV	277–319 GeV	319–361 GeV	361–408 GeV	408–459 GeV	459–514 GeV	514–573 GeV	573–637 GeV	637–705 GeV	705–774 GeV	774–854 GeV	854–940 GeV	$\geq 940$ GeV
b-tagging efficiency $-1\sigma$ (%)	0.05	0.05	0.04	0.02	-0.03	-0.09	-0.17	-0.21	-0.20	-0.12	0.06	0.27	0.46
b-tagging efficiency $+1\sigma$ (%)	1.78	1.41	0.64	-0.26	-1.07	-1.67	-2.09	-2.43	-2.72	-2.89	-2.96	-2.93	-2.85
Electron efficiency $-1\sigma$ (%)	0.33	0.27	0.13	-0.03	-0.18	-0.31	-0.42	-0.52	-0.60	-0.64	-0.61	-0.55	-0.48
Electron efficiency $+1\sigma$ (%)	1.41	1.11	0.47	-0.29	-0.97	-1.43	-1.66	-1.76	-1.79	-1.70	-1.50	-1.22	-0.96
Jet energy resolution $-1\sigma$ (%)	1.17	0.96	0.54	-0.04	-0.69	-1.27	-1.69	-1.94	-2.06	-2.05	-1.94	-1.77	-1.58
Jet energy resolution $+1\sigma$ (%)	-0.06	-0.03	0.00	0.04	0.08	0.09	0.01	-0.15	-0.26	-0.22	-0.01	0.31	0.62
Jet energy scale $-1\sigma$ (%)	0.38	0.26	0.04	-0.17	-0.36	-0.46	-0.42	-0.25	0.03	0.31	0.52	0.68	0.86
Jet energy scale $+1\sigma$ (%)	0.47	0.49	0.48	0.30	-0.05	-0.52	-1.13	-1.76	-2.24	-2.39	-2.22	-1.90	-1.62
Muon efficiency $-1\sigma$ (%)	-0.00	-0.00	-0.00	-0.00	-0.00	-0.00	0.00	0.01	0.01	0.02	0.03	0.03	0.03
Muon efficiency $+1\sigma$ (%)	0.00	0.00	0.00	0.00	0.00	-0.00	-0.00	-0.01	-0.02	-0.03	-0.03	-0.04	-0.05
PDF uncertainty $-1\sigma$ (%)	0.88	0.48	0.39	0.51	0.82	0.94	0.77	0.77	0.93	1.30	1.66	1.71	1.49
PDF uncertainty $+1\sigma$ (%)	0.88	0.48	0.39	0.51	0.82	0.94	0.77	0.77	0.93	1.30	1.66	1.71	1.49
Pile-up $-1\sigma$ (%)	0.13	0.12	0.08	0.06	0.04	-0.01	-0.12	-0.31	-0.57	-0.85	-1.12	-1.35	-1.50
Pile-up $+1\sigma$ (%)	2.08	1.65	0.76	-0.31	-1.31	-2.04	-2.54	-2.90	-3.12	-3.13	-2.96	-2.68	-2.40
QCD cross section $+1\sigma$ (%)	-0.05	-0.04	-0.02	0.01	0.03	0.05	0.06	0.06	0.07	0.07	0.06	0.06	0.05
QCD cross section $-1\sigma$ (%)	3.33	2.76	1.61	-0.03	-1.76	-3.31	-4.64	-5.78	-6.63	-7.10	-7.20	-7.04	-6.77
QCD shape uncertainty (%)	1.84	1.48	0.71	-0.21	-1.06	-1.73	-2.23	-2.67	-3.02	-3.26	-3.37	-3.41	-3.37
Single top cross section $+1\sigma$ (%)	1.59	1.25	0.56	-0.25	-0.99	-1.51	-1.86	-2.12	-2.31	-2.41	-2.43	-2.37	-2.27
Single top cross section $-1\sigma$ (%)	1.77	1.40	0.63	-0.28	-1.11	-1.70	-2.08	-2.37	-2.57	-2.67	-2.68	-2.61	-2.50
$t\bar{t}$ cross section $+1\sigma$ (%)	1.61	1.27	0.56	-0.27	-1.02	-1.55	-1.88	-2.12	-2.29	-2.37	-2.36	-2.30	-2.19
$t\bar{t}$ cross section $-1\sigma$ (%)	1.78	1.41	0.63	-0.28	-1.10	-1.70	-2.10	-2.39	-2.61	-2.73	-2.74	-2.68	-2.57
$t\bar{t}$ (top mass down) (%)	-0.13	-0.08	0.00	0.05	0.22	0.07	-0.10	-0.20	0.07	0.22	0.29	0.40	0.13
$t\bar{t}$ (top mass up) (%)	-0.35	-0.41	0.06	0.40	0.20	0.26	-0.52	0.82	-0.23	-0.41	1.44	0.97	1.00
$t\bar{t}$ (matching down) (%)	-0.85	-0.53	-0.17	0.59	0.95	0.91	0.72	0.05	-1.26	0.89	0.28	-2.05	-2.88
$t\bar{t}$ (matching up) (%)	-1.04	-0.47	0.37	0.34	0.32	0.32	0.31	0.20	0.18	1.02	0.78	1.94	2.98
$t\bar{t}$ ( $Q^2$ down) (%)	-8.15	-4.40	0.17	3.23	4.38	5.37	5.75	4.98	3.97	4.55	3.03	2.71	2.13
$t\bar{t}$ ( $Q^2$ up) (%)	5.43	2.06	-0.32	-2.00	-2.96	-3.20	-3.46	-2.03	-1.93	-1.14	-1.21	0.16	0.38
V+jets cross section $+1\sigma$ (%)	-0.02	-0.01	0.01	0.02	0.03	0.03	0.01	-0.02	-0.06	-0.10	-0.11	-0.12	-0.11
V+jets cross section $-1\sigma$ (%)	1.61	1.27	0.57	-0.25	-0.99	-1.53	-1.89	-2.15	-2.36	-2.47	-2.49	-2.43	-2.33
V+jets (matching down) (%)	-1.03	-0.83	-0.43	0.12	0.70	1.18	1.46	1.48	1.35	1.21	1.11	1.07	1.08
V+jets (matching up) (%)	0.03	0.01	-0.04	-0.05	0.05	0.16	0.15	0.01	-0.18	-0.35	-0.48	-0.56	-0.59
V+jets ( $Q^2$ down) (%)	-1.47	-1.21	-0.69	0.03	0.89	1.66	2.19	2.44	2.47	2.38	2.24	2.11	2.02
V+jets ( $Q^2$ up) (%)	-1.25	-1.05	-0.63	-0.01	0.73	1.42	1.91	2.15	2.22	2.23	2.19	2.16	2.14
Hadronisation uncertainty (%)	31.86	8.22	5.00	11.50	12.05	12.01	9.33	8.68	7.20	6.45	6.24	5.07	0.42
Luminosity $+1\sigma$ (%)	1.76	1.40	0.63	-0.28	-1.09	-1.69	-2.08	-2.37	-2.58	-2.70	-2.71	-2.64	-2.53
Luminosity $-1\sigma$ (%)	1.74	1.38	0.61	-0.28	-1.09	-1.67	-2.04	-2.31	-2.50	-2.60	-2.60	-2.53	-2.43
Electron energy $-1\sigma$ (%)	1.65	1.30	0.58	-0.28	-1.03	-1.55	-1.89	-2.17	-2.40	-2.52	-2.53	-2.46	-2.35
Electron energy $+1\sigma$ (%)	0.33	0.27	0.15	-0.02	-0.18	-0.33	-0.47	-0.60	-0.65	-0.62	-0.52	-0.41	-0.31
Muon energy $-1\sigma$ (%)	0.01	0.01	0.01	-0.00	-0.02	-0.03	-0.03	-0.02	0.00	0.03	0.06	0.08	0.11
Muon energy $+1\sigma$ (%)	0.04	0.04	0.03	0.02	-0.00	-0.03	-0.05	-0.09	-0.13	-0.19	-0.24	-0.29	-0.32
Tau energy $-1\sigma$ (%)	0.90	0.73	0.38	-0.08	-0.52	-0.85	-1.09	-1.31	-1.55	-1.77	-1.89	-1.87	-1.80
Tau energy $+1\sigma$ (%)	1.35	1.04	0.37	-0.40	-1.03	-1.38	-1.47	-1.44	-1.29	-1.02	-0.69	-0.39	-0.15
Unclustered energy $-1\sigma$ (%)	0.21	0.18	0.08	-0.03	-0.14	-0.18	-0.20	-0.24	-0.33	-0.44	-0.55	-0.64	-0.68
Unclustered energy $+1\sigma$ (%)	0.66	0.55	0.31	-0.02	-0.35	-0.65	-0.91	-1.17	-1.38	-1.46	-1.35	-1.14	-0.92
$p_T(t, \bar{t})$ reweighting (%)	2.98	1.24	0.20	1.25	1.67	1.61	1.32	0.88	0.53	0.21	0.24	1.29	6.80
Total (%)	33.95	11.40	6.31	12.31	13.90	15.22	14.45	14.82	14.64	15.11	14.87	14.42	14.91

Table B.30: Systematic uncertainties for the normalised  $t\bar{t}$  cross section measurement with respect to  $p_T^W$  variable at a centre-of-mass energy of 7 TeV (combination of electron and muon channels).

Uncertainty source	0--27 GeV	27--52 GeV	52--78 GeV	78--105 GeV	105--134 GeV	134--166 GeV	166--200 GeV	200--237 GeV	$\geq 237$ GeV
b-tagging efficiency $-1\sigma$ (%)	0.06	0.05	0.03	-0.01	-0.06	-0.09	-0.12	-0.14	-0.16
b-tagging efficiency $+1\sigma$ (%)	-0.23	-0.20	-0.09	0.06	0.21	0.32	0.40	0.45	0.48
Electron efficiency $-1\sigma$ (%)	-0.02	-0.02	-0.01	0.01	0.02	0.02	0.02	0.01	0.01
Electron efficiency $+1\sigma$ (%)	-1.13	-0.63	-0.10	0.26	0.54	0.85	1.22	1.56	1.80
Jet energy resolution $-1\sigma$ (%)	0.39	0.21	-0.07	-0.30	-0.37	-0.12	0.39	0.96	1.44
Jet energy resolution $+1\sigma$ (%)	0.56	0.40	0.07	-0.23	-0.44	-0.48	-0.43	-0.35	-0.31
Jet energy scale $-1\sigma$ (%)	0.29	-0.02	-0.31	-0.31	-0.02	0.46	1.02	1.51	1.82
Jet energy scale $+1\sigma$ (%)	0.60	0.85	0.76	0.10	-0.90	-1.93	-2.81	-3.38	-3.63
Muon efficiency $-1\sigma$ (%)	-0.00	-0.00	-0.00	-0.00	0.00	0.00	0.01	0.02	0.02
Muon efficiency $+1\sigma$ (%)	0.01	0.01	0.00	-0.00	-0.01	-0.01	-0.02	-0.02	-0.03
PDF uncertainty $-1\sigma$ (%)	1.07	0.63	0.10	0.45	0.38	0.96	1.15	1.38	1.25
PDF uncertainty $+1\sigma$ (%)	1.07	0.63	0.10	0.45	0.38	0.96	1.15	1.38	1.25
Pile-up $-1\sigma$ (%)	-0.65	-0.45	-0.14	0.18	0.47	0.70	0.82	0.84	0.82
Pile-up $+1\sigma$ (%)	-0.32	-0.17	0.01	0.10	0.12	0.14	0.23	0.36	0.45
QCD cross section $+1\sigma$ (%)	0.07	0.07	0.06	-0.01	-0.09	-0.16	-0.20	-0.22	-0.23
QCD cross section $-1\sigma$ (%)	1.89	1.43	0.39	-0.79	-1.56	-1.86	-1.81	-1.61	-1.42
QCD shape uncertainty (%)	0.05	0.05	0.04	0.02	-0.03	-0.11	-0.20	-0.28	-0.34
Single top cross section $+1\sigma$ (%)	0.02	0.01	-0.01	-0.01	-0.01	-0.00	0.00	0.00	0.01
Single top cross section $-1\sigma$ (%)	0.19	0.13	0.03	-0.08	-0.14	-0.17	-0.17	-0.16	-0.15
$t\bar{t}$ cross section $+1\sigma$ (%)	-0.58	-0.20	0.23	0.38	0.27	-0.08	-0.60	-1.12	-1.51
$t\bar{t}$ cross section $-1\sigma$ (%)	0.02	0.02	0.01	-0.01	-0.02	-0.03	-0.03	-0.03	-0.03
$t\bar{t}$ (top mass down) (%)	-0.09	-0.14	0.04	-0.03	0.07	0.29	0.09	0.15	0.24
$t\bar{t}$ (top mass up) (%)	0.26	-0.14	-0.02	-0.30	0.42	0.08	-0.36	-0.25	1.83
$t\bar{t}$ (matching down) (%)	0.45	0.44	0.22	-0.45	-0.75	-0.62	0.59	0.27	0.48
$t\bar{t}$ (matching up) (%)	-0.12	-0.11	0.02	-0.15	0.17	0.18	-0.13	0.96	1.12
$t\bar{t}$ ( $Q^2$ down) (%)	0.33	-0.15	-0.06	-0.53	0.20	0.71	0.47	0.85	1.04
$t\bar{t}$ ( $Q^2$ up) (%)	-0.13	-0.58	0.09	0.22	0.15	0.03	0.32	1.43	1.25
V+jets cross section $+1\sigma$ (%)	0.02	0.02	0.00	-0.01	-0.02	-0.02	-0.03	-0.03	-0.03
V+jets cross section $-1\sigma$ (%)	0.03	0.02	0.01	-0.01	-0.02	-0.03	-0.04	-0.04	-0.04
V+jets (matching down) (%)	0.02	-0.02	-0.02	0.02	0.08	0.07	-0.04	-0.22	-0.39
V+jets (matching up) (%)	0.45	0.28	0.08	-0.07	-0.20	-0.39	-0.69	-1.00	-1.25
V+jets ( $Q^2$ down) (%)	-0.03	-0.13	-0.17	-0.01	0.23	0.39	0.37	0.26	0.14
V+jets ( $Q^2$ up) (%)	0.32	0.20	0.04	-0.11	-0.26	-0.34	-0.22	-0.02	0.18
Hadronisation uncertainty (%)	3.13	2.89	2.04	1.02	3.75	5.46	6.72	7.62	9.73
Luminosity $+1\sigma$ (%)	0.01	0.01	0.00	-0.01	-0.01	-0.01	-0.01	-0.01	-0.01
Luminosity $-1\sigma$ (%)	0.03	0.02	0.00	-0.01	-0.02	-0.02	-0.03	-0.02	-0.02
Electron energy $-1\sigma$ (%)	-0.55	-0.39	-0.14	0.11	0.35	0.59	0.85	1.11	1.33
Electron energy $+1\sigma$ (%)	0.37	0.24	0.06	-0.07	-0.17	-0.32	-0.53	-0.83	-1.13
Muon energy $-1\sigma$ (%)	-0.14	-0.12	-0.07	0.01	0.12	0.23	0.32	0.40	0.48
Muon energy $+1\sigma$ (%)	0.19	0.13	0.03	-0.06	-0.14	-0.18	-0.19	-0.18	-0.16
Tau energy $-1\sigma$ (%)	3.55	2.62	0.97	-0.88	-2.56	-3.95	-5.15	-6.36	-7.53
Tau energy $+1\sigma$ (%)	-0.74	-0.87	-0.91	-0.48	0.58	2.25	4.31	6.20	7.54
Unclustered energy $-1\sigma$ (%)	2.37	1.57	0.30	-0.83	-1.64	-2.07	-2.17	-2.03	-1.76
Unclustered energy $+1\sigma$ (%)	-0.44	-0.32	-0.11	0.14	0.36	0.47	0.53	0.52	0.40
$p_T(t, \bar{t})$ reweighting (%)	1.10	0.14	0.75	0.22	0.10	0.07	0.21	0.20	5.96
Total (%)	6.76	5.23	3.23	2.88	5.74	8.13	9.98	11.82	15.61

Table B.31: Systematic uncertainties for the normalised  $t\bar{t}$  cross section measurement with respect to  $M_T^W$  variable at a centre-of-mass energy of 7 TeV (combination of electron and muon channels).

Uncertainty source	0--23 GeV	23--58 GeV	$\geq 58$ GeV
b-tagging efficiency $-1\sigma$ (%)	0.08	0.03	-0.03
b-tagging efficiency $+1\sigma$ (%)	-0.06	-0.02	0.02
Electron efficiency $-1\sigma$ (%)	0.01	0.00	-0.00
Electron efficiency $+1\sigma$ (%)	-0.68	-0.27	0.27
Jet energy resolution $-1\sigma$ (%)	-0.58	-0.19	0.21
Jet energy resolution $+1\sigma$ (%)	-0.47	-0.00	0.09
Jet energy scale $-1\sigma$ (%)	-1.48	-0.44	0.50
Jet energy scale $+1\sigma$ (%)	-1.13	-0.39	0.41
Muon efficiency $-1\sigma$ (%)	0.02	0.01	-0.01
Muon efficiency $+1\sigma$ (%)	-0.02	-0.01	0.01
PDF uncertainty $-1\sigma$ (%)	1.23	0.82	0.64
PDF uncertainty $+1\sigma$ (%)	1.23	0.82	0.64
Pile-up $-1\sigma$ (%)	-0.36	-0.08	0.11
Pile-up $+1\sigma$ (%)	-0.00	-0.03	0.02
QCD cross section $+1\sigma$ (%)	0.00	0.00	-0.00
QCD cross section $-1\sigma$ (%)	-0.41	-0.14	0.15
QCD shape uncertainty (%)	-0.15	-0.05	0.06
Single top cross section $+1\sigma$ (%)	0.01	0.00	-0.00
Single top cross section $-1\sigma$ (%)	0.01	0.00	-0.00
$t\bar{t}$ cross section $+1\sigma$ (%)	0.00	0.00	-0.00
$t\bar{t}$ cross section $-1\sigma$ (%)	0.01	0.00	-0.00
$t\bar{t}$ (top mass down) (%)	0.00	0.06	-0.03
$t\bar{t}$ (top mass up) (%)	-0.32	0.21	-0.04
$t\bar{t}$ (matching down) (%)	-0.95	0.02	0.17
$t\bar{t}$ (matching up) (%)	-0.29	0.31	-0.10
$t\bar{t}$ ( $Q^2$ down) (%)	0.40	0.47	-0.31
$t\bar{t}$ ( $Q^2$ up) (%)	-1.25	-0.00	0.24
V+jets cross section $+1\sigma$ (%)	0.00	-0.00	-0.00
V+jets cross section $-1\sigma$ (%)	0.01	0.00	-0.00
V+jets (matching down) (%)	1.19	0.45	-0.45
V+jets (matching up) (%)	-0.49	-0.17	0.18
V+jets ( $Q^2$ down) (%)	1.74	0.67	-0.67
V+jets ( $Q^2$ up) (%)	1.65	0.69	-0.66
Hadronisation uncertainty (%)	1.88	1.10	0.91
Luminosity $+1\sigma$ (%)	0.01	0.00	-0.00
Luminosity $-1\sigma$ (%)	0.00	0.00	-0.00
Electron energy $-1\sigma$ (%)	1.20	0.52	-0.49
Electron energy $+1\sigma$ (%)	-0.78	-0.38	0.34
Muon energy $-1\sigma$ (%)	0.05	0.03	-0.03
Muon energy $+1\sigma$ (%)	-0.17	-0.07	0.07
Tau energy $-1\sigma$ (%)	-1.92	-0.64	0.69
Tau energy $+1\sigma$ (%)	0.67	0.18	-0.22
Unclustered energy $-1\sigma$ (%)	-0.32	-0.24	0.18
Unclustered energy $+1\sigma$ (%)	1.32	0.38	-0.44
$p_T(t, \bar{t})$ reweighting (%)	181	0.76	0.42
Total (%)		5.85	2.94
			2.13

Table B.32: Systematic uncertainties for the normalised  $t\bar{t}$  cross section measurement with respect to  $E_T^{\text{miss}}$  variable at a centre-of-mass energy of 8 TeV (combination of electron and muon channels).

Uncertainty source	0--27 GeV	27--52 GeV	52--87 GeV	87--130 GeV	130--172 GeV	$\geq 172$ GeV
b-tagging efficiency $-1\sigma$ (%)	0.07	0.03	-0.03	-0.07	-0.06	-0.02
b-tagging efficiency $+1\sigma$ (%)	-0.32	-0.16	0.18	0.40	0.24	-0.16
Electron efficiency $-1\sigma$ (%)	-0.03	-0.02	0.02	0.03	0.03	0.04
Electron efficiency $+1\sigma$ (%)	-0.19	-0.10	0.10	0.21	0.23	0.21
Jet energy resolution $-1\sigma$ (%)	0.13	-0.12	-0.13	0.19	0.59	0.92
Jet energy resolution $+1\sigma$ (%)	-0.26	-0.07	0.11	0.12	0.30	0.75
Jet energy scale $-1\sigma$ (%)	-0.11	-0.55	-0.17	0.99	2.26	3.43
Jet energy scale $+1\sigma$ (%)	0.09	0.12	0.01	-0.33	-0.44	-0.14
Muon efficiency $-1\sigma$ (%)	0.01	0.00	-0.01	-0.01	0.02	0.06
Muon efficiency $+1\sigma$ (%)	-0.01	-0.00	0.01	0.01	-0.02	-0.06
PDF uncertainty $-1\sigma$ (%)	0.56	0.19	0.24	0.43	0.82	0.75
PDF uncertainty $+1\sigma$ (%)	0.56	0.19	0.24	0.43	0.82	0.75
Pile-up $-1\sigma$ (%)	-0.18	-0.13	0.10	0.26	0.27	0.26
Pile-up $+1\sigma$ (%)	0.09	0.05	-0.08	-0.21	0.16	0.81
QCD cross section $+1\sigma$ (%)	0.00	0.00	-0.00	-0.00	-0.00	-0.00
QCD cross section $-1\sigma$ (%)	-3.01	-1.88	0.51	3.62	9.03	15.97
QCD shape uncertainty (%)	0.23	0.06	-0.11	-0.21	-0.12	0.06
Single top cross section $+1\sigma$ (%)	-0.00	-0.00	0.00	0.00	0.00	-0.00
Single top cross section $-1\sigma$ (%)	0.00	0.00	-0.00	-0.00	-0.00	0.00
$t\bar{t}$ cross section $+1\sigma$ (%)	-0.00	-0.00	0.00	0.00	-0.00	-0.01
$t\bar{t}$ cross section $-1\sigma$ (%)	0.00	0.00	-0.00	-0.00	-0.00	0.01
$t\bar{t}$ (top mass down) (%)	-0.39	-0.03	0.08	0.26	0.41	0.43
$t\bar{t}$ (top mass up) (%)	0.38	-0.07	-0.26	-0.10	0.95	1.16
$t\bar{t}$ (matching down) (%)	0.82	0.03	-0.40	0.05	-0.64	-1.31
$t\bar{t}$ (matching up) (%)	-0.85	-0.61	0.04	1.90	2.35	1.39
$t\bar{t}$ ( $Q^2$ down) (%)	7.37	2.72	-2.98	-6.29	-9.25	-12.96
$t\bar{t}$ ( $Q^2$ up) (%)	-0.15	-0.19	-0.06	0.41	0.64	2.22
V+jets cross section $+1\sigma$ (%)	0.00	0.00	0.00	-0.00	-0.00	-0.01
V+jets cross section $-1\sigma$ (%)	0.00	0.00	-0.00	-0.00	0.00	0.01
V+jets (matching down) (%)	-0.99	-0.55	0.45	1.28	1.36	1.03
V+jets (matching up) (%)	-0.26	-0.27	0.22	0.51	0.21	-0.32
V+jets ( $Q^2$ down) (%)	-1.21	-0.48	0.62	1.18	0.89	0.29
V+jets ( $Q^2$ up) (%)	-0.92	-0.44	0.45	1.04	0.92	0.60
Hadronisation uncertainty (%)	3.30	2.19	0.93	5.16	7.94	11.30
Luminosity $+1\sigma$ (%)	0.00	0.00	-0.00	-0.00	0.00	0.01
Luminosity $-1\sigma$ (%)	-0.00	-0.00	0.00	0.00	0.01	0.01
Electron energy $-1\sigma$ (%)	-0.15	-0.17	0.03	0.32	0.62	0.87
Electron energy $+1\sigma$ (%)	-0.07	0.00	0.08	-0.03	-0.12	-0.19
Muon energy $-1\sigma$ (%)	0.05	-0.01	-0.05	0.00	0.11	0.24
Muon energy $+1\sigma$ (%)	-0.05	0.01	0.03	0.01	-0.07	-0.16
Tau energy $-1\sigma$ (%)	2.14	1.05	-0.65	-2.37	-4.18	-6.05
Tau energy $+1\sigma$ (%)	-2.13	-1.33	0.54	2.86	5.28	7.44
Unclustered energy $-1\sigma$ (%)	1.22	0.48	-0.43	-1.24	-1.75	-1.94
Unclustered energy $+1\sigma$ (%)	-1.13	-0.55	0.40	1.22	1.93	2.65
$p_T(t, \bar{t})$ reweighting (%)	0.86	0.69	0.74	0.79	2.55	7.89
Total (%)	9.34	4.48	3.63	9.90	16.86	26.54

Table B.33: Systematic uncertainties for the normalised  $t\bar{t}$  cross section measurement with respect to  $H_T$  variable at a centre-of-mass energy of 8 TeV (combination of electron and muon channels).

Uncertainty source	120–185 GeV	185–215 GeV	215–247 GeV	247–283 GeV	283–323 GeV	323–365 GeV	365–409 GeV	409–458 GeV	458–512 GeV	512–570 GeV	570–629 GeV	629–691 GeV	691–769 GeV	$\geq 769$ GeV
b-tagging efficiency $-1\sigma$ (%)	0.02	0.01	0.01	0.00	-0.00	-0.01	-0.03	-0.03	-0.03	-0.02	-0.01	0.01	0.02	0.03
b-tagging efficiency $+1\sigma$ (%)	-0.03	-0.02	-0.01	-0.00	0.01	0.03	0.04	0.04	0.03	0.02	0.00	-0.02	-0.04	-0.06
Electron efficiency $-1\sigma$ (%)	-0.00	-0.00	-0.00	-0.00	-0.00	-0.00	0.00	0.01	0.01	0.01	0.01	0.02	0.02	0.02
Electron efficiency $+1\sigma$ (%)	-0.07	-0.07	-0.07	-0.06	-0.02	0.04	0.10	0.15	0.19	0.21	0.23	0.24	0.24	0.24
Jet energy resolution $-1\sigma$ (%)	-0.25	-0.26	-0.26	-0.24	-0.07	0.14	0.34	0.51	0.64	0.77	0.90	1.03	1.14	1.23
Jet energy resolution $+1\sigma$ (%)	0.01	0.00	-0.01	0.01	0.07	0.11	0.08	0.00	-0.09	-0.18	-0.28	-0.39	-0.48	-0.54
Jet energy scale $-1\sigma$ (%)	-1.44	-1.26	-0.89	-0.39	0.22	0.85	1.43	1.92	2.32	2.51	2.55	2.46	2.33	2.23
Jet energy scale $+1\sigma$ (%)	-0.16	-0.12	-0.03	0.08	0.27	0.39	0.36	0.18	-0.09	-0.44	-0.84	-1.27	-1.63	-1.89
Muon efficiency $-1\sigma$ (%)	-0.01	-0.01	-0.01	-0.01	-0.00	0.01	0.01	0.02	0.03	0.03	0.04	0.05	0.05	0.06
Muon efficiency $+1\sigma$ (%)	0.01	0.01	0.01	0.01	0.00	-0.01	-0.01	-0.02	-0.02	-0.03	-0.03	-0.04	-0.05	-0.05
PDF uncertainty $-1\sigma$ (%)	0.44	0.39	0.32	0.28	0.24	0.18	0.34	0.56	0.80	1.25	1.54	1.88	2.04	0.90
PDF uncertainty $+1\sigma$ (%)	0.44	0.39	0.32	0.28	0.24	0.18	0.34	0.56	0.80	1.25	1.54	1.88	2.04	0.90
Pile-up $-1\sigma$ (%)	-0.16	-0.19	-0.23	-0.25	-0.14	0.05	0.28	0.50	0.67	0.80	0.89	0.95	0.99	1.01
Pile-up $+1\sigma$ (%)	-0.05	-0.03	0.01	0.04	0.06	0.05	0.02	-0.02	-0.07	-0.10	-0.12	-0.13	-0.14	-0.13
QCD cross section $+1\sigma$ (%)	-0.00	-0.00	0.00	0.00	0.00	0.00	-0.00	-0.00	-0.00	-0.00	-0.00	-0.00	-0.00	-0.00
QCD cross section $-1\sigma$ (%)	-9.85	-8.55	-5.96	-2.33	1.73	5.53	8.64	11.32	13.74	16.10	18.38	20.52	22.45	23.93
QCD shape uncertainty (%)	-0.30	-0.25	-0.16	-0.03	0.12	0.24	0.31	0.34	0.33	0.30	0.24	0.18	0.12	0.08
Single top cross section $+1\sigma$ (%)	-0.00	-0.00	-0.00	-0.00	-0.00	-0.00	0.00	0.00	0.00	0.00	0.00	0.01	0.01	0.01
Single top cross section $-1\sigma$ (%)	-0.00	-0.00	-0.00	-0.00	-0.00	0.00	0.00	0.00	0.00	0.00	0.00	0.00	0.00	0.00
$t\bar{t}$ cross section $+1\sigma$ (%)	-0.00	-0.00	-0.00	-0.00	0.00	0.00	0.00	0.00	0.00	0.00	0.00	-0.00	-0.00	-0.00
$t\bar{t}$ cross section $-1\sigma$ (%)	0.00	0.00	0.00	-0.00	-0.00	-0.00	-0.00	-0.00	0.00	0.00	0.00	0.00	0.00	0.01
$t\bar{t}$ (top mass down) (%)	1.77	0.19	-0.43	-0.62	-0.43	-0.42	-0.30	0.10	0.09	0.28	0.13	0.53	-0.23	-2.44
$t\bar{t}$ (top mass up) (%)	-2.31	-0.86	0.63	0.67	1.08	0.59	0.38	1.12	0.91	0.95	0.15	0.97	-1.20	-7.22
$t\bar{t}$ (matching down) (%)	3.57	2.12	1.35	-0.21	-1.28	-1.77	-2.77	-3.35	-2.60	-1.40	-3.25	-2.09	-4.27	-2.79
$t\bar{t}$ (matching up) (%)	-1.44	-1.23	0.03	0.29	0.99	0.68	0.49	0.44	1.02	0.71	0.15	1.82	-0.24	0.33
$t\bar{t}$ ( $Q^2$ down) (%)	-8.03	-4.88	-1.11	1.79	4.07	4.25	4.15	4.75	4.11	3.18	1.90	1.46	0.11	-1.91
$t\bar{t}$ ( $Q^2$ up) (%)	4.85	2.57	0.87	-0.84	-1.74	-2.27	-2.39	-3.21	-2.55	-3.36	-4.11	-0.72	-1.09	-1.72
V+jets cross section $+1\sigma$ (%)	-0.00	-0.00	0.00	0.00	0.00	0.00	-0.00	-0.00	-0.00	-0.00	-0.00	-0.00	0.00	0.00
V+jets cross section $-1\sigma$ (%)	-0.00	-0.00	-0.00	-0.00	-0.00	-0.00	-0.00	0.00	0.00	0.01	0.01	0.01	0.01	0.02
V+jets (matching down) (%)	-1.15	-1.05	-0.83	-0.50	0.01	0.62	1.24	1.79	2.23	2.51	2.64	2.67	2.64	2.61
V+jets (matching up) (%)	-0.44	-0.40	-0.33	-0.20	0.08	0.41	0.69	0.81	0.78	0.64	0.45	0.26	0.11	0.01
V+jets ( $Q^2$ down) (%)	-0.73	-0.68	-0.58	-0.41	-0.07	0.39	0.86	1.25	1.55	1.76	1.88	1.95	1.99	2.00
V+jets ( $Q^2$ up) (%)	-1.02	-0.95	-0.77	-0.50	-0.04	0.52	1.11	1.65	2.10	2.43	2.60	2.64	2.62	2.59
Hadronisation uncertainty (%)	1.13	2.96	3.29	2.32	0.27	1.74	3.66	5.46	6.60	7.17	7.54	7.48	7.96	9.89
Luminosity $+1\sigma$ (%)	0.00	0.00	-0.00	-0.00	-0.00	-0.00	-0.00	-0.00	0.00	0.00	0.00	0.01	0.01	0.01
Luminosity $-1\sigma$ (%)	-0.00	-0.00	-0.00	-0.00	-0.00	-0.00	0.00	0.00	0.00	0.00	0.00	0.00	0.00	0.00
$p_T(t, \bar{t})$ reweighting (%)	0.51	0.29	0.55	0.57	0.37	0.06	0.46	1.00	1.36	1.65	1.68	1.76	1.03	3.59
Total (%)	14.15	10.65	7.31	4.09	4.77	7.42	10.63	14.02	16.53	18.81	21.32	22.81	24.91	27.17

Table B.34: Systematic uncertainties for the normalised  $t\bar{t}$  cross section measurement with respect to  $S_T$  variable at a centre-of-mass energy of 8 TeV (combination of electron and muon channels).

Uncertainty source	146–277 GeV	277–319 GeV	319–361 GeV	361–408 GeV	408–459 GeV	459–514 GeV	514–573 GeV	573–637 GeV	637–705 GeV	705–774 GeV	774–854 GeV	854–940 GeV	$\geq 940$ GeV
b-tagging efficiency $-1\sigma$ (%)	0.07	0.07	0.06	0.02	-0.03	-0.07	-0.10	-0.13	-0.16	-0.18	-0.20	-0.23	-0.25
b-tagging efficiency $+1\sigma$ (%)	-0.04	-0.05	-0.04	-0.02	0.01	0.04	0.07	0.10	0.12	0.13	0.15	0.16	0.18
Electron efficiency $-1\sigma$ (%)	0.02	0.02	0.00	-0.02	-0.02	-0.02	-0.01	0.00	0.01	0.01	0.01	0.01	0.01
Electron efficiency $+1\sigma$ (%)	-0.01	-0.00	0.01	0.02	0.02	0.00	-0.02	-0.03	-0.04	-0.04	-0.04	-0.04	-0.04
Jet energy resolution $-1\sigma$ (%)	0.67	0.52	0.26	0.01	-0.28	-0.60	-0.85	-1.00	-1.02	-0.79	-0.38	0.15	0.59
Jet energy resolution $+1\sigma$ (%)	-0.21	-0.10	0.07	0.09	-0.01	-0.08	0.01	0.23	0.44	0.45	0.29	0.00	-0.26
Jet energy scale $-1\sigma$ (%)	-0.91	-0.91	-0.85	-0.47	0.23	0.80	1.38	2.07	2.58	3.02	3.15	3.02	3.01
Jet energy scale $+1\sigma$ (%)	0.56	0.38	0.14	-0.02	-0.17	-0.39	-0.49	-0.43	-0.42	-0.58	-0.82	-1.21	-1.59
Muon efficiency $-1\sigma$ (%)	0.01	0.01	0.00	-0.01	-0.01	-0.01	-0.01	-0.00	0.01	0.03	0.05	0.06	0.08
Muon efficiency $+1\sigma$ (%)	-0.01	-0.00	-0.00	0.01	0.01	0.01	0.01	-0.00	-0.01	-0.03	-0.04	-0.05	-0.07
PDF uncertainty $-1\sigma$ (%)	0.48	0.45	0.33	0.18	0.16	0.35	0.52	0.69	0.91	1.26	1.78	2.30	1.63
PDF uncertainty $+1\sigma$ (%)	0.48	0.45	0.33	0.18	0.16	0.35	0.52	0.69	0.91	1.26	1.78	2.30	1.63
Pile-up $-1\sigma$ (%)	0.19	0.10	-0.04	-0.14	-0.14	-0.06	0.02	0.08	0.13	0.06	-0.03	-0.05	-0.01
Pile-up $+1\sigma$ (%)	-0.21	-0.12	0.01	0.13	0.16	0.10	0.02	-0.04	-0.07	-0.01	0.08	0.10	0.05
QCD cross section $+1\sigma$ (%)	0.01	0.01	0.01	-0.00	-0.01	-0.01	-0.01	-0.01	-0.01	-0.01	-0.01	-0.01	-0.02
QCD cross section $-1\sigma$ (%)	-8.32	-6.90	-3.94	0.27	4.51	6.54	7.71	9.02	10.32	11.47	12.64	14.05	15.46
QCD shape uncertainty (%)	0.22	0.17	0.03	-0.13	-0.14	-0.08	-0.02	0.01	-0.04	-0.18	-0.35	-0.53	-0.65
Single top cross section $+1\sigma$ (%)	0.00	0.00	0.00	-0.00	-0.00	-0.00	-0.00	-0.00	-0.00	-0.00	-0.00	-0.00	-0.01
Single top cross section $-1\sigma$ (%)	0.01	0.01	0.01	-0.00	-0.01	-0.01	-0.01	-0.01	-0.01	-0.01	-0.01	-0.01	-0.01
$t\bar{t}$ cross section $+1\sigma$ (%)	0.01	0.01	0.01	-0.00	-0.01	-0.01	-0.01	-0.01	-0.01	-0.01	-0.01	-0.01	-0.01
$t\bar{t}$ cross section $-1\sigma$ (%)	0.01	0.01	0.01	-0.00	-0.01	-0.01	-0.01	-0.01	-0.01	-0.01	-0.01	-0.01	-0.01
$t\bar{t}$ (top mass down) (%)	1.16	-0.36	-0.57	-0.25	0.10	-0.10	0.06	-0.10	0.03	0.25	0.36	0.98	-0.29
$t\bar{t}$ (top mass up) (%)	-1.24	0.42	1.19	0.72	0.15	-0.72	-0.52	-1.13	-0.59	-1.08	-0.55	1.87	-2.84
$t\bar{t}$ (matching down) (%)	2.65	1.73	0.72	-0.11	-1.26	-1.92	-2.13	-2.45	-1.81	-1.99	-4.58	-3.05	-3.50
$t\bar{t}$ (matching up) (%)	-1.70	-0.94	0.44	0.90	0.84	0.21	0.08	-0.35	0.56	0.21	1.10	2.64	2.22
$t\bar{t}$ ( $Q^2$ down) (%)	-4.81	-1.10	1.28	2.06	2.11	0.85	1.36	-0.04	0.40	-1.64	-1.03	-0.82	-2.31
$t\bar{t}$ ( $Q^2$ up) (%)	3.15	0.90	-0.14	-0.70	-0.85	-1.61	-0.82	-2.11	-1.55	-0.80	-2.32	-0.56	0.45
V+jets cross section $+1\sigma$ (%)	0.01	0.01	0.01	-0.00	-0.01	-0.01	-0.01	-0.01	-0.01	-0.01	-0.01	-0.01	-0.01
V+jets cross section $-1\sigma$ (%)	0.01	0.01	0.01	-0.00	-0.01	-0.01	-0.01	-0.01	-0.01	-0.01	-0.01	-0.01	-0.01
V+jets (matching down) (%)	-0.78	-0.83	-0.84	-0.52	0.23	1.09	1.69	1.98	2.04	1.99	1.88	1.79	1.73
V+jets (matching up) (%)	-0.88	-0.86	-0.74	-0.25	0.62	1.37	1.66	1.57	1.24	0.82	0.41	0.09	-0.12
V+jets ( $Q^2$ down) (%)	-0.90	-0.91	-0.84	-0.44	0.37	1.22	1.76	1.95	1.91	1.79	1.63	1.53	1.54
V+jets ( $Q^2$ up) (%)	-0.85	-0.88	-0.84	-0.47	0.27	1.06	1.58	1.86	2.01	2.14	2.30	2.49	2.66
Hadronisation uncertainty (%)	5.03	5.37	3.73	0.73	2.38	5.73	8.74	9.40	10.10	10.95	8.49	7.15	8.22
Luminosity $+1\sigma$ (%)	0.01	0.01	0.01	-0.00	-0.01	-0.01	-0.01	-0.01	-0.01	-0.01	-0.01	-0.01	-0.02
Luminosity $-1\sigma$ (%)	0.01	0.01	0.01	-0.00	-0.01	-0.01	-0.01	-0.01	-0.01	-0.01	-0.01	-0.01	-0.01
Electron energy $-1\sigma$ (%)	0.16	0.10	-0.00	-0.08	-0.12	-0.12	-0.06	0.02	0.07	0.06	0.01	-0.08	-0.15
Electron energy $+1\sigma$ (%)	0.00	0.03	0.06	0.04	-0.02	-0.05	-0.03	-0.03	-0.07	-0.12	-0.15	-0.16	-0.16
Muon energy $-1\sigma$ (%)	0.09	0.06	0.00	-0.05	-0.06	-0.06	-0.04	-0.01	0.00	-0.01	-0.01	0.01	0.03
Muon energy $+1\sigma$ (%)	0.05	0.05	0.03	0.00	-0.03	-0.05	-0.07	-0.07	-0.06	-0.04	-0.05	-0.08	-0.11
Tau energy $-1\sigma$ (%)	0.94	0.74	0.39	-0.04	-0.42	-0.72	-0.91	-1.05	-1.18	-1.28	-1.29	-1.29	-1.23
Tau energy $+1\sigma$ (%)	-0.62	-0.51	-0.29	-0.05	0.18	0.42	0.64	0.84	1.01	1.14	1.33	1.49	1.53
Unclustered energy $-1\sigma$ (%)	0.34	0.32	0.25	0.07	-0.18	-0.38	-0.48	-0.52	-0.56	-0.60	-0.60	-0.58	-0.58
Unclustered energy $+1\sigma$ (%)	0.13	0.04	-0.09	-0.18	-0.16	-0.07	0.05	0.19	0.31	0.42	0.54	0.57	0.55
$p_T(t, \bar{t})$ reweighting (%)	0.53	0.43	0.49	0.22	0.08	0.30	0.46	0.62	0.68	0.81	1.10	1.14	4.18
Total (%)	11.89	9.38	6.23	2.90	5.78	9.51	12.54	14.23	15.49	16.96	17.06	17.45	19.37

Table B.35: Systematic uncertainties for the normalised  $t\bar{t}$  cross section measurement with respect to  $p_T^W$  variable at a centre-of-mass energy of 8 TeV (combination of electron and muon channels).

Uncertainty source	0–27 GeV	27–52 GeV	52–78 GeV	78–105 GeV	105–134 GeV	134–166 GeV	166–200 GeV	200–237 GeV	$\geq 237$ GeV
b-tagging efficiency $-1\sigma$ (%)	0.08	0.06	0.03	-0.01	-0.05	-0.11	-0.17	-0.24	-0.30
b-tagging efficiency $+1\sigma$ (%)	-0.11	-0.09	-0.04	0.02	0.08	0.14	0.20	0.24	0.27
Electron efficiency $-1\sigma$ (%)	0.01	0.00	-0.01	-0.01	-0.00	0.01	0.02	0.02	0.02
Electron efficiency $+1\sigma$ (%)	-0.86	-0.62	-0.13	0.39	0.69	0.75	0.67	0.51	0.34
Jet energy resolution $-1\sigma$ (%)	0.40	0.24	-0.01	-0.19	-0.23	-0.19	-0.16	-0.18	-0.25
Jet energy resolution $+1\sigma$ (%)	-0.29	-0.17	-0.00	0.11	0.21	0.27	0.17	-0.06	-0.32
Jet energy scale $-1\sigma$ (%)	-0.27	-0.32	-0.34	-0.22	0.13	0.79	1.73	2.61	3.18
Jet energy scale $+1\sigma$ (%)	-0.49	-0.33	-0.02	0.29	0.45	0.33	0.04	-0.26	-0.46
Muon efficiency $-1\sigma$ (%)	-0.02	-0.01	-0.01	-0.00	0.01	0.03	0.05	0.08	0.10
Muon efficiency $+1\sigma$ (%)	0.02	0.02	0.01	0.00	-0.01	-0.03	-0.06	-0.09	-0.12
PDF uncertainty $-1\sigma$ (%)	0.50	0.25	0.22	0.10	0.30	0.48	0.78	1.07	0.69
PDF uncertainty $+1\sigma$ (%)	0.50	0.25	0.22	0.10	0.30	0.48	0.78	1.07	0.69
Pile-up $-1\sigma$ (%)	-0.81	-0.58	-0.13	0.34	0.64	0.76	0.73	0.58	0.39
Pile-up $+1\sigma$ (%)	0.18	0.10	0.01	-0.04	-0.06	-0.10	-0.21	-0.34	-0.46
QCD cross section $+1\sigma$ (%)	0.00	0.00	-0.00	-0.00	-0.00	-0.00	0.00	0.00	0.00
QCD cross section $-1\sigma$ (%)	-8.07	-6.29	-2.55	2.08	5.76	9.14	12.84	16.68	20.00
QCD shape uncertainty (%)	-0.15	-0.11	-0.03	0.04	0.12	0.17	0.18	0.17	0.15
Single top cross section $+1\sigma$ (%)	0.00	0.00	0.00	-0.00	-0.00	-0.00	-0.00	-0.00	-0.00
Single top cross section $-1\sigma$ (%)	0.00	0.00	0.00	0.00	-0.00	-0.00	-0.00	-0.01	-0.00
$t\bar{t}$ cross section $+1\sigma$ (%)	-0.00	-0.00	-0.00	0.00	0.00	0.01	0.00	-0.00	-0.01
$t\bar{t}$ cross section $-1\sigma$ (%)	0.00	0.00	0.00	-0.00	-0.00	-0.00	-0.00	-0.00	-0.00
$t\bar{t}$ (top mass down) (%)	0.03	-0.06	-0.09	0.02	-0.01	0.10	0.39	0.29	0.32
$t\bar{t}$ (top mass up) (%)	-0.76	-0.47	0.03	0.41	-0.15	0.54	1.14	0.92	1.05
$t\bar{t}$ (matching down) (%)	-0.13	0.18	0.04	0.40	-0.27	-0.77	0.01	-0.38	-1.15
$t\bar{t}$ (matching up) (%)	-0.33	-0.70	-0.64	0.64	0.61	0.47	1.87	0.96	1.83
$t\bar{t}$ ( $Q^2$ down) (%)	3.11	2.81	0.99	-0.36	-2.53	-4.09	-6.03	-8.38	-9.23
$t\bar{t}$ ( $Q^2$ up) (%)	-0.24	-0.01	-0.00	0.41	-0.35	-0.57	0.08	0.54	1.39
V+jets cross section $+1\sigma$ (%)	0.00	0.00	0.00	0.00	-0.00	-0.01	-0.01	-0.01	-0.01
V+jets cross section $-1\sigma$ (%)	0.00	0.00	0.00	-0.00	-0.00	-0.00	-0.00	-0.00	-0.00
V+jets (matching down) (%)	-0.24	-0.36	-0.32	0.07	0.61	0.89	0.75	0.30	-0.22
V+jets (matching up) (%)	-0.25	-0.29	-0.20	0.13	0.55	0.69	0.36	-0.28	-0.94
V+jets ( $Q^2$ down) (%)	-0.33	-0.40	-0.32	0.08	0.62	0.94	0.84	0.45	0.01
V+jets ( $Q^2$ up) (%)	-0.10	-0.27	-0.34	-0.02	0.49	0.81	0.76	0.47	0.14
Hadronisation uncertainty (%)	2.30	2.79	1.98	0.75	3.06	4.92	5.97	7.85	10.28
Luminosity $+1\sigma$ (%)	-0.00	-0.00	-0.00	0.00	0.00	0.00	0.00	-0.00	-0.01
Luminosity $-1\sigma$ (%)	0.00	0.00	0.00	-0.00	-0.00	-0.00	-0.01	-0.01	-0.01
Electron energy $-1\sigma$ (%)	-0.71	-0.52	-0.15	0.26	0.59	0.75	0.74	0.65	0.56
Electron energy $+1\sigma$ (%)	0.36	0.26	0.10	-0.08	-0.26	-0.42	-0.53	-0.63	-0.71
Muon energy $-1\sigma$ (%)	0.02	0.02	0.01	-0.01	0.00	0.01	-0.05	-0.15	-0.25
Muon energy $+1\sigma$ (%)	0.18	0.14	0.04	-0.05	-0.11	-0.16	-0.25	-0.39	-0.54
Tau energy $-1\sigma$ (%)	2.06	1.59	0.74	-0.28	-1.39	-2.63	-3.95	-5.19	-6.19
Tau energy $+1\sigma$ (%)	-1.12	-0.99	-0.70	-0.11	0.81	1.99	3.27	4.55	5.64
Unclustered energy $-1\sigma$ (%)	1.05	0.79	0.32	-0.24	-0.78	-1.27	-1.67	-1.93	-2.05
Unclustered energy $+1\sigma$ (%)	-0.55	-0.44	-0.25	0.07	0.48	0.86	1.09	1.19	1.23
$p_T(t, \bar{t})$ reweighting (%)	0.51	0.34	0.65	0.11	0.40	0.45	0.26	0.35	6.93
Total (%)	9.46	7.80	3.69	2.64	7.43	11.87	16.32	21.32	26.46

Table B.36: Systematic uncertainties for the normalised  $t\bar{t}$  cross section measurement with respect to  $M_T^W$  variable at a centre-of-mass energy of 8 TeV (combination of electron and muon channels).

Uncertainty source	0--23 GeV	23--58 GeV	$\geq 58$ GeV
b-tagging efficiency $-1\sigma$ (%)	-0.04	-0.01	0.01
b-tagging efficiency $+1\sigma$ (%)	-0.01	-0.01	0.01
Electron efficiency $-1\sigma$ (%)	0.03	0.01	-0.01
Electron efficiency $+1\sigma$ (%)	0.19	0.07	-0.07
Jet energy resolution $-1\sigma$ (%)	0.54	0.26	-0.23
Jet energy resolution $+1\sigma$ (%)	0.22	0.10	-0.09
Jet energy scale $-1\sigma$ (%)	1.63	0.70	-0.65
Jet energy scale $+1\sigma$ (%)	0.03	0.01	-0.01
Muon efficiency $-1\sigma$ (%)	0.02	0.01	-0.01
Muon efficiency $+1\sigma$ (%)	-0.02	-0.01	0.01
PDF uncertainty $-1\sigma$ (%)	0.14	0.27	0.15
PDF uncertainty $+1\sigma$ (%)	0.14	0.27	0.15
Pile-up $-1\sigma$ (%)	0.51	0.23	-0.21
Pile-up $+1\sigma$ (%)	0.08	0.04	-0.04
QCD cross section $+1\sigma$ (%)	-0.01	-0.00	0.00
QCD cross section $-1\sigma$ (%)	1.23	0.46	-0.46
QCD shape uncertainty (%)	-0.67	-0.28	0.26
Single top cross section $+1\sigma$ (%)	-0.00	-0.00	0.00
Single top cross section $-1\sigma$ (%)	-0.00	-0.00	0.00
$t\bar{t}$ cross section $+1\sigma$ (%)	0.00	0.00	-0.00
$t\bar{t}$ cross section $-1\sigma$ (%)	0.00	0.00	-0.00
$t\bar{t}$ (top mass down) (%)	0.06	0.13	-0.07
$t\bar{t}$ (top mass up) (%)	0.10	0.04	-0.04
$t\bar{t}$ (matching down) (%)	-0.32	-0.01	0.06
$t\bar{t}$ (matching up) (%)	1.11	0.29	-0.35
$t\bar{t}$ ( $Q^2$ down) (%)	-1.56	-1.31	0.93
$t\bar{t}$ ( $Q^2$ up) (%)	-0.57	-0.14	0.18
V+jets cross section $+1\sigma$ (%)	0.00	0.00	-0.00
V+jets cross section $-1\sigma$ (%)	0.00	0.00	-0.00
V+jets (matching down) (%)	1.95	0.77	-0.74
V+jets (matching up) (%)	1.13	0.45	-0.43
V+jets ( $Q^2$ down) (%)	1.36	0.53	-0.51
V+jets ( $Q^2$ up) (%)	1.66	0.64	-0.62
Hadronisation uncertainty (%)	2.87	1.44	1.26
Luminosity $+1\sigma$ (%)	0.00	0.00	-0.00
Luminosity $-1\sigma$ (%)	-0.00	-0.00	0.00
Electron energy $-1\sigma$ (%)	0.70	0.31	-0.28
Electron energy $+1\sigma$ (%)	-0.42	-0.16	0.15
Muon energy $-1\sigma$ (%)	0.18	0.09	-0.08
Muon energy $+1\sigma$ (%)	-0.14	-0.06	0.05
Tau energy $-1\sigma$ (%)	-1.08	-0.41	0.40
Tau energy $+1\sigma$ (%)	0.85	0.38	-0.34
Unclustered energy $-1\sigma$ (%)	-0.29	-0.06	0.09
Unclustered energy $+1\sigma$ (%)	1.17	0.50	-0.46
$p_T(t, \bar{t})$ reweighting (%)	186	1.20	0.73
Total (%)		5.71	2.86
			0.58

## B.11 Results

### B.11.1 7 TeV

Table B.37: Normalised  $t\bar{t}$  cross section measurement with respect to  $E_T^{\text{miss}}$  variable at a centre-of-mass energy of 7 TeV (combination of electron and muon channels). The errors shown are combined statistical, fit and unfolding errors ( $\dagger$ ) and systematic uncertainty (\*).

$E_T^{\text{miss}}$ bin [ GeV ]	$\sigma_{\text{meas}} (\times 10^3)$
0--27 GeV	$6.68 \pm 0.12^\dagger \pm 0.16^* (3.03\%)$
27--52 GeV	$13.41 \pm 0.18^\dagger \pm 0.28^* (2.49\%)$
52--87 GeV	$8.64 \pm 0.12^\dagger \pm 0.14^* (2.15\%)$
87--130 GeV	$3.03 \pm 0.06^\dagger \pm 0.12^* (4.36\%)$
130--172 GeV	$0.84 \pm 0.02^\dagger \pm 0.08^* (9.94\%)$
$\geq 172$ GeV	$0.13 \pm 0.00^\dagger \pm 0.02^* (17.53\%)$

Table B.38: Normalised  $t\bar{t}$  cross section measurement with respect to  $H_T$  variable at a centre-of-mass energy of 7 TeV (combination of electron and muon channels). The errors shown are combined statistical, fit and unfolding errors ( $\dagger$ ) and systematic uncertainty (\*).

$H_T$ bin [ GeV ]	$\sigma_{\text{meas}} (\times 10^3)$
120--185 GeV	$2.52 \pm 0.07^\dagger \pm 0.92^* (36.64\%)$
185--215 GeV	$4.94 \pm 0.13^\dagger \pm 0.67^* (13.90\%)$
215--247 GeV	$4.98 \pm 0.12^\dagger \pm 0.21^* (4.91\%)$
247--283 GeV	$4.04 \pm 0.09^\dagger \pm 0.46^* (11.68\%)$
283--323 GeV	$2.96 \pm 0.06^\dagger \pm 0.40^* (13.72\%)$
323--365 GeV	$2.02 \pm 0.04^\dagger \pm 0.31^* (15.32\%)$
365--409 GeV	$1.34 \pm 0.03^\dagger \pm 0.19^* (14.41\%)$
409--458 GeV	$0.86 \pm 0.02^\dagger \pm 0.11^* (13.34\%)$
458--512 GeV	$0.54 \pm 0.01^\dagger \pm 0.06^* (12.03\%)$
512--570 GeV	$0.33 \pm 0.01^\dagger \pm 0.04^* (12.69\%)$
570--629 GeV	$0.20 \pm 0.01^\dagger \pm 0.02^* (10.37\%)$
629--691 GeV	$0.12 \pm 0.00^\dagger \pm 0.01^* (9.60\%)$
691--769 GeV	$0.07 \pm 0.00^\dagger \pm 0.01^* (9.73\%)$
$\geq 769$ GeV	$0.03 \pm 0.00^\dagger \pm 0.00^* (10.04\%)$

Table B.39: Normalised  $t\bar{t}$  cross section measurement with respect to  $S_T$  variable at a centre-of-mass energy of 7 TeV (combination of electron and muon channels). The errors shown are combined statistical, fit and unfolding errors ( $\dagger$ ) and systematic uncertainty (\*).

$S_T$ bin [ GeV ]	$\sigma_{meas} (\times 10^3)$
146--277 GeV	$1.28 \pm 0.04^\dagger \pm 0.43^* (33.95\%)$
277--319 GeV	$4.09 \pm 0.11^\dagger \pm 0.45^* (11.40\%)$
319--361 GeV	$4.08 \pm 0.10^\dagger \pm 0.24^* (6.31\%)$
361--408 GeV	$3.20 \pm 0.07^\dagger \pm 0.39^* (12.31\%)$
408--459 GeV	$2.22 \pm 0.05^\dagger \pm 0.31^* (13.90\%)$
459--514 GeV	$1.45 \pm 0.03^\dagger \pm 0.22^* (15.22\%)$
514--573 GeV	$0.91 \pm 0.02^\dagger \pm 0.13^* (14.45\%)$
573--637 GeV	$0.55 \pm 0.01^\dagger \pm 0.08^* (14.82\%)$
637--705 GeV	$0.33 \pm 0.01^\dagger \pm 0.05^* (14.64\%)$
705--774 GeV	$0.19 \pm 0.01^\dagger \pm 0.03^* (15.11\%)$
774--854 GeV	$0.11 \pm 0.00^\dagger \pm 0.02^* (14.87\%)$
854--940 GeV	$0.06 \pm 0.00^\dagger \pm 0.01^* (14.42\%)$
$\geq 940$ GeV	$0.03 \pm 0.00^\dagger \pm 0.00^* (14.91\%)$

Table B.40: Normalised  $t\bar{t}$  cross section measurement with respect to  $M_T^W$  variable at a centre-of-mass energy of 7 TeV (combination of electron and muon channels). The errors shown are combined statistical, fit and unfolding errors ( $\dagger$ ) and systematic uncertainty (\*).

$M_T^W$ bin [ GeV ]	$\sigma_{meas} (\times 10^3)$
0--23 GeV	$4.98 \pm 0.19^\dagger \pm 0.22^* (5.85\%)$
23--58 GeV	$8.36 \pm 0.17^\dagger \pm 0.17^* (2.94\%)$
$\geq 58$ GeV	$14.11 \pm 0.16^\dagger \pm 0.25^* (2.13\%)$

Table B.41: Normalised  $t\bar{t}$  cross section measurement with respect to  $p_T^W$  variable at a centre-of-mass energy of 7 TeV (combination of electron and muon channels). The errors shown are combined statistical, fit and unfolding errors ( $\dagger$ ) and systematic uncertainty (\*).

$p_T^W$ bin [ GeV ]	$\sigma_{meas} (\times 10^3)$
0--27 GeV	$3.54 \pm 0.11^\dagger \pm 0.21^* (6.76\%)$
27--52 GeV	$8.54 \pm 0.20^\dagger \pm 0.40^* (5.23\%)$
52--78 GeV	$9.33 \pm 0.18^\dagger \pm 0.24^* (3.23\%)$
78--105 GeV	$7.12 \pm 0.14^\dagger \pm 0.15^* (2.88\%)$
105--134 GeV	$4.28 \pm 0.10^\dagger \pm 0.23^* (5.74\%)$
134--166 GeV	$2.17 \pm 0.05^\dagger \pm 0.17^* (8.13\%)$
166--200 GeV	$0.98 \pm 0.03^\dagger \pm 0.09^* (9.98\%)$
200--237 GeV	$0.42 \pm 0.02^\dagger \pm 0.05^* (11.82\%)$
$\geq 237$ GeV	$0.21 \pm 0.01^\dagger \pm 0.03^* (15.61\%)$

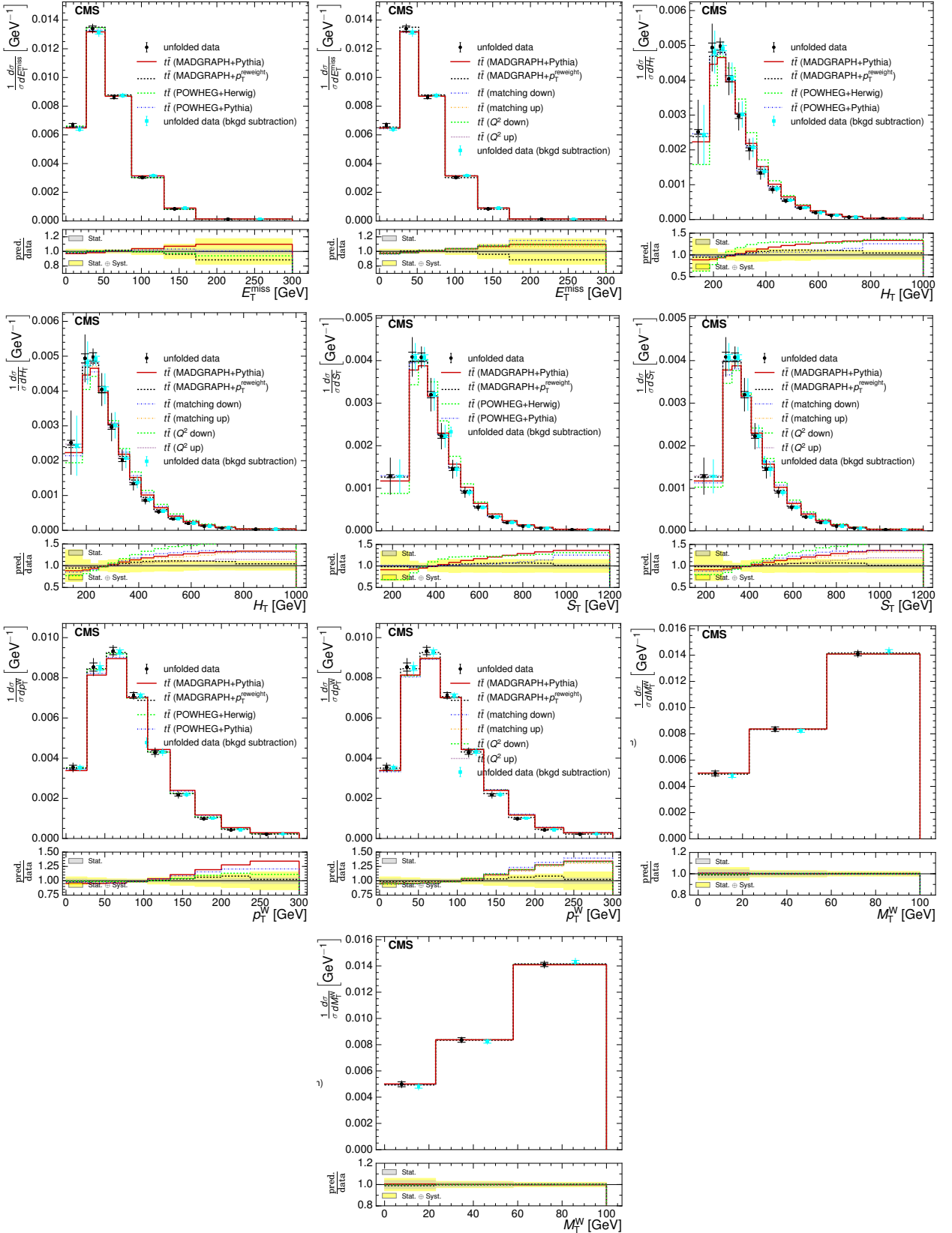


Figure B.17: Comparison of the measured normalised differential cross section, including from the background subtraction method, with respect to  $E_T^{\text{miss}}$ ,  $H_T$ ,  $S_T$ ,  $p_T^W$  and  $M_T^W$  to different Monte Carlo generators: MADGRAPH, POWHEG +HERWIG, POWHEG +PYTHIA and MADGRAPH corrected for top  $p_T$  mismodelling (left) and to different Monte Carlo predictions matching threshold up/down and factorisation scale up/down (right) in the combined electron+jets and muon+jets channel at  $\sqrt{s} = 7 \text{ TeV}$ . The lower plots show the ratio of the predictions to the data.

## B.11.2 8 TeV

Table B.42: Normalised  $t\bar{t}$  cross section measurement with respect to  $E_T^{\text{miss}}$  variable at a centre-of-mass energy of 8 TeV (combination of electron and muon channels). The errors shown are combined statistical, fit and unfolding errors ( $\dagger$ ) and systematic uncertainty (\*).

$E_T^{\text{miss}}$ bin [ GeV ]	$\sigma_{\text{meas}} (\times 10^3)$
0--27 GeV	$6.62 \pm 0.08^\dagger \pm 0.61^* (9.34\%)$
27--52 GeV	$13.47 \pm 0.10^\dagger \pm 0.60^* (4.48\%)$
52--87 GeV	$8.76 \pm 0.08^\dagger \pm 0.31^* (3.63\%)$
87--130 GeV	$3.00 \pm 0.04^\dagger \pm 0.29^* (9.90\%)$
130--172 GeV	$0.80 \pm 0.01^\dagger \pm 0.13^* (16.86\%)$
$\geq 172$ GeV	$0.12 \pm 0.00^\dagger \pm 0.03^* (26.54\%)$

Table B.43: Normalised  $t\bar{t}$  cross section measurement with respect to  $H_T$  variable at a centre-of-mass energy of 8 TeV (combination of electron and muon channels). The errors shown are combined statistical, fit and unfolding errors ( $\dagger$ ) and systematic uncertainty (\*).

$H_T$ bin [ GeV ]	$\sigma_{\text{meas}} (\times 10^3)$
120--185 GeV	$2.15 \pm 0.03^\dagger \pm 0.30^* (14.15\%)$
185--215 GeV	$4.35 \pm 0.05^\dagger \pm 0.46^* (10.65\%)$
215--247 GeV	$4.58 \pm 0.05^\dagger \pm 0.33^* (7.31\%)$
247--283 GeV	$3.98 \pm 0.04^\dagger \pm 0.16^* (4.09\%)$
283--323 GeV	$3.08 \pm 0.02^\dagger \pm 0.14^* (4.77\%)$
323--365 GeV	$2.23 \pm 0.02^\dagger \pm 0.16^* (7.42\%)$
365--409 GeV	$1.55 \pm 0.01^\dagger \pm 0.16^* (10.63\%)$
409--458 GeV	$1.03 \pm 0.01^\dagger \pm 0.14^* (14.02\%)$
458--512 GeV	$0.66 \pm 0.01^\dagger \pm 0.11^* (16.53\%)$
512--570 GeV	$0.41 \pm 0.00^\dagger \pm 0.08^* (18.81\%)$
570--629 GeV	$0.26 \pm 0.00^\dagger \pm 0.06^* (21.32\%)$
629--691 GeV	$0.16 \pm 0.00^\dagger \pm 0.04^* (22.81\%)$
691--769 GeV	$0.10 \pm 0.00^\dagger \pm 0.02^* (24.91\%)$
$\geq 769$ GeV	$0.05 \pm 0.00^\dagger \pm 0.01^* (27.17\%)$

Table B.44: Normalised  $t\bar{t}$  cross section measurement with respect to  $S_T$  variable at a centre-of-mass energy of 8 TeV (combination of electron and muon channels). The errors shown are combined statistical, fit and unfolding errors ( $\dagger$ ) and systematic uncertainty (\*).

$S_T$ bin [ GeV ]	$\sigma_{meas} (\times 10^3)$
146--277 GeV	$1.12 \pm 0.02^\dagger \pm 0.13^* (11.89\%)$
277--319 GeV	$3.64 \pm 0.06^\dagger \pm 0.34^* (9.38\%)$
319--361 GeV	$3.83 \pm 0.05^\dagger \pm 0.23^* (6.23\%)$
361--408 GeV	$3.22 \pm 0.03^\dagger \pm 0.09^* (2.90\%)$
408--459 GeV	$2.38 \pm 0.02^\dagger \pm 0.14^* (5.78\%)$
459--514 GeV	$1.64 \pm 0.02^\dagger \pm 0.15^* (9.51\%)$
514--573 GeV	$1.05 \pm 0.01^\dagger \pm 0.13^* (12.54\%)$
573--637 GeV	$0.66 \pm 0.01^\dagger \pm 0.09^* (14.23\%)$
637--705 GeV	$0.40 \pm 0.01^\dagger \pm 0.06^* (15.49\%)$
705--774 GeV	$0.24 \pm 0.00^\dagger \pm 0.04^* (16.96\%)$
774--854 GeV	$0.14 \pm 0.00^\dagger \pm 0.02^* (17.06\%)$
854--940 GeV	$0.08 \pm 0.00^\dagger \pm 0.01^* (17.45\%)$
$\geq 940$ GeV	$0.04 \pm 0.00^\dagger \pm 0.01^* (19.37\%)$

Table B.45: Normalised  $t\bar{t}$  cross section measurement with respect to  $M_T^W$  variable at a centre-of-mass energy of 8 TeV (combination of electron and muon channels). The errors shown are combined statistical, fit and unfolding errors ( $\dagger$ ) and systematic uncertainty (\*).

$M_T^W$ bin [ GeV ]	$\sigma_{meas} (\times 10^3)$
0--23 GeV	$4.88 \pm 0.08^\dagger \pm 0.27^* (5.71\%)$
23--58 GeV	$8.30 \pm 0.07^\dagger \pm 0.23^* (2.86\%)$
$\geq 58$ GeV	$14.22 \pm 0.07^\dagger \pm 0.33^* (2.37\%)$

Table B.46: Normalised  $t\bar{t}$  cross section measurement with respect to  $p_T^W$  variable at a centre-of-mass energy of 8 TeV (combination of electron and muon channels). The errors shown are combined statistical, fit and unfolding errors ( $\dagger$ ) and systematic uncertainty (\*).

$p_T^W$ bin [ GeV ]	$\sigma_{meas} (\times 10^3)$
0--27 GeV	$3.64 \pm 0.04^\dagger \pm 0.34^* (9.46\%)$
27--52 GeV	$8.59 \pm 0.07^\dagger \pm 0.67^* (7.80\%)$
52--78 GeV	$9.22 \pm 0.07^\dagger \pm 0.33^* (3.69\%)$
78--105 GeV	$6.98 \pm 0.05^\dagger \pm 0.18^* (2.64\%)$
105--134 GeV	$4.24 \pm 0.04^\dagger \pm 0.31^* (7.43\%)$
134--166 GeV	$2.18 \pm 0.02^\dagger \pm 0.26^* (11.87\%)$
166--200 GeV	$1.01 \pm 0.01^\dagger \pm 0.16^* (16.32\%)$
200--237 GeV	$0.45 \pm 0.01^\dagger \pm 0.10^* (21.32\%)$
$\geq 237$ GeV	$0.24 \pm 0.00^\dagger \pm 0.06^* (26.46\%)$

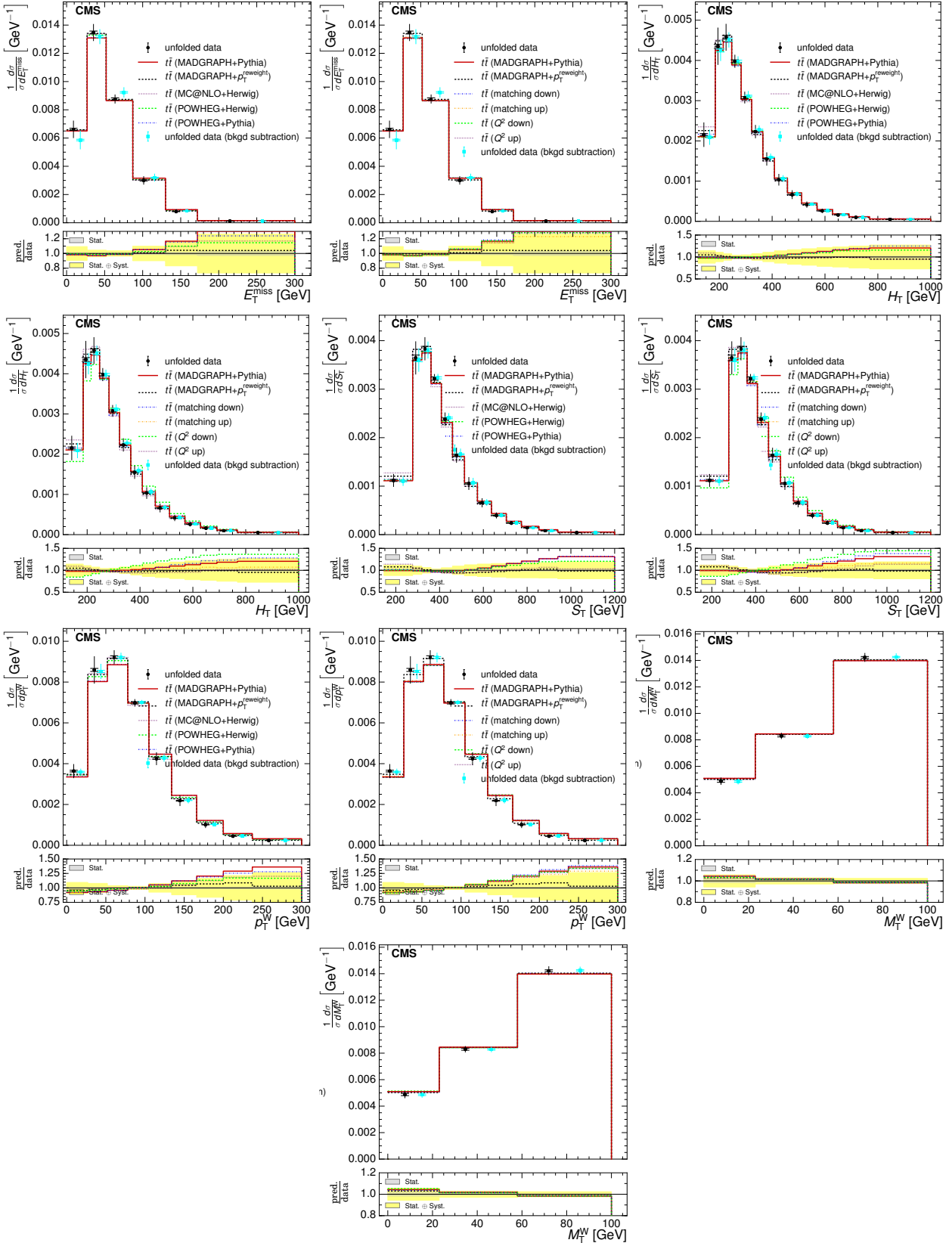


Figure B.18: Comparison of the measured normalised differential cross section, including from the background subtraction method, with respect to  $E_{\text{T}}^{\text{miss}}$ ,  $H_{\text{T}}$ ,  $S_{\text{T}}$ ,  $p_{\text{T}}^{\text{W}}$  and  $M_{\text{T}}^{\text{W}}$  to different Monte Carlo generators: MADGRAPH, POWHEG +HERWIG, POWHEG +PYTHIA and MADGRAPH corrected for top  $p_{\text{T}}$  mismodelling (left) and to different Monte Carlo predictions matching threshold up/down and factorisation scale up/down (right) in the combined electron+jets and muon+jets channel at  $\sqrt{s} = 8$  TeV. The lower plots show the ratio of the predictions to the data.

# C | CMS Binary Chip

Prior to PhD research, the author carried out characterisation studies of the CMS Binary Chip (CBC) for his MSc thesis. The CBC is the proposed 128 channel application specific integrated-circuit (ASIC) readout chip for the silicon strip tracker sub-detector of CMS [67]. These studies were continued during the beginning months of the PhD, as presented in the following sections.

## C.1 Introduction and previous studies

Upgrades to the LHC over the coming years (Phase I) will lead to improvements on the operating parameters of the LHC detailed in Section 2.1. By 2023, the luminosity delivered by the LHC is expected to be  $2 \times 10^{34} \text{cm}^{-2}\text{s}^{-1}$ . After 2023 (Phase 2), Long Shutdown 3 is planned to implement further performance upgrades and will lead to a luminosity of  $5 \times 10^{34} \text{cm}^{-2}\text{s}^{-1}$ . Figure C.1 shows the planned shutdowns and upgrades over the next decade.

The High Luminosity LHC (HL-LHC), as the machine will be known then, will experience higher collision rates, leading to a requirement for an upgraded CMS tracker in order to overcome the problem of radiation damage suffered by the tracker until that point, to ensure it is capable of withstanding the subsequent higher radiation levels, and to allow the tracker to maintain performance with the resulting 100-200 proton-proton interactions per bunch crossing [78].

A description of the CBC is given in [68], and summarised together with a description of the laboratory setup in [67]. In summary, the laboratory setup consisted of the CBC held on a CBC carrier board, connected via an FPGA mezzanine card (FMC) to a field programmable

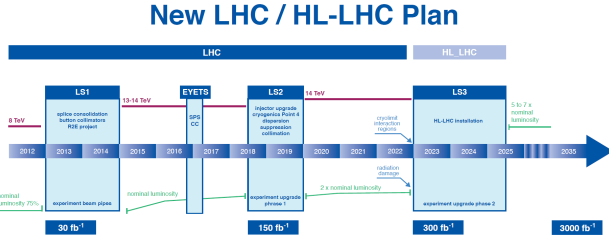


Figure C.1: Schedule of LHC upgrades over the next decade.

gate array (FPGA) which was connected to a controlling computer. In summary, the signal created in a connected silicon sensor would enter the CBC through the analogue front end and a comparator digitises the signal to produce a binary output, a ‘1’ to indicate a ‘hit’ or ‘0’. The CBC includes a setting to read out either ‘electrons’ or ‘holes’, and 24 of the 128 channels were wire bonded out from the chip to allow signal to be injected if desired.

The inclusion of the CBC in the CMS strip tracker will also lead to the provision of tracker data to the L1 trigger, whereas currently the tracker data is only used at HLT level, and L1 trigger decisions are made using muon chambers and calorimeters. The design of the CBC is largely driven by this trigger contribution requirement in order to maintain a practical L1 trigger rate in the high luminosity environment. The upgraded strip tracker will also require a higher granularity in order to maintain low occupancy (a few percent), but simultaneously will need to maintain a low amount of material in order that particle interactions with dead material is minimised so tracks with low  $p_T$  can be measured efficiently. The increased number of channels will require the design power demand of the CBC to be lowered (accomplished in part through the digital readout) from the current 2.7 mW/channel to a targeted 0.5 mW/channel [68, 51, 85].

Tests were carried out on the CBCv1 to verify its operation, to get information about the behaviour of the analogue front-end, to test the response of the CBC to varying sizes of injected charges, to measure the gain at a range of temperatures from -40 °C and 40 °C, and to measure the channel-to-channel variation in pedestal voltage. The basic principle of the tests involved scanning through the values of comparator threshold voltage, creating an s-curve’, and evaluating the point at which the mean output changed from zeros to ones or vice versa.

These already documented tests were carried out only on one chip, however. Continuation of that work, including some studies on a second CBCv1 chip, are outlined below.

## C.2 Measuring signal noise using a capacitor

The noise in the test setup was investigated by attaching a capacitor to the CBC carrier board inputs for one of the channels which was wire bonded to the CBC. At first, short wires were used ( 1 cm in length) to introduce a capacitance to the input signal. However, the capacitance of the board was so low (meaning the capacitance of even very short wires was too high) that no useful measure of the noise in the signal could be obtained from the resulting s-curves. In fact, at no point during the scan of the channel offsets did the comparator return all ‘1’s or all ‘0’s. After modifying the CBC carrier board to allow a capacitor to be plugged directly into an input socket for the bonded channels, the tests were carried out with capacitors ranging from 1 pF to 10 pF. The variation in the widths of these s-curves, a measure of the gaussian distribution of noise in the signal, are shown in Figure C.2. The plots for both electrons and holes are similar and show no trends.

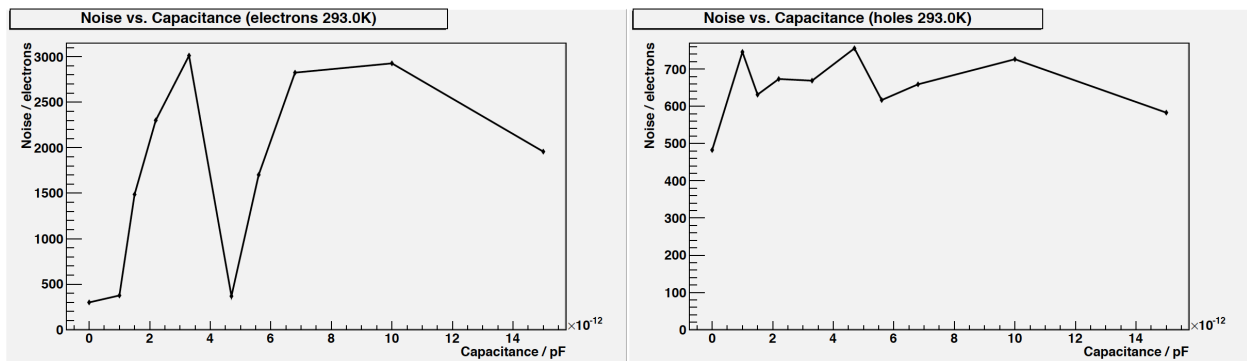


Figure C.2: Noise as a function of added capacitance for channel 65 in ‘electrons’ mode (left) and ‘holes’ mode (right).

The erratic variations over such small changes in capacitance may be explained by the fact that the noise present in the test setup was showing levels of the order of thousands of electrons. The tests to study the variation in noise as a function of added capacitance to an injection channel were therefore of little use, due to the added noise now being so small compared to the noise in the test setup. After establishing that the noise in the system

was associated to the incoming pulse, additional grounding and shielding was introduced in the form of copper tape, insulation between the connecting cables, placing the chip and its carrier board inside an aluminium box and injecting the pulse through a triaxial cable rather than a coaxial cable. Unfortunately the latest results after all these modifications (Figure C.3) show that although the noise on channels which are not connected to the pulse injection cable was reduced to an acceptable level (about 200 electrons), the noise on the connected channel is still extremely high. The apparent limit of 200 electrons at the lower end of the scale is assumed to be due to the granularity of the threshold voltage scans; using finer steps would have resulted in a smaller s-curve width, i.e. lower noise.

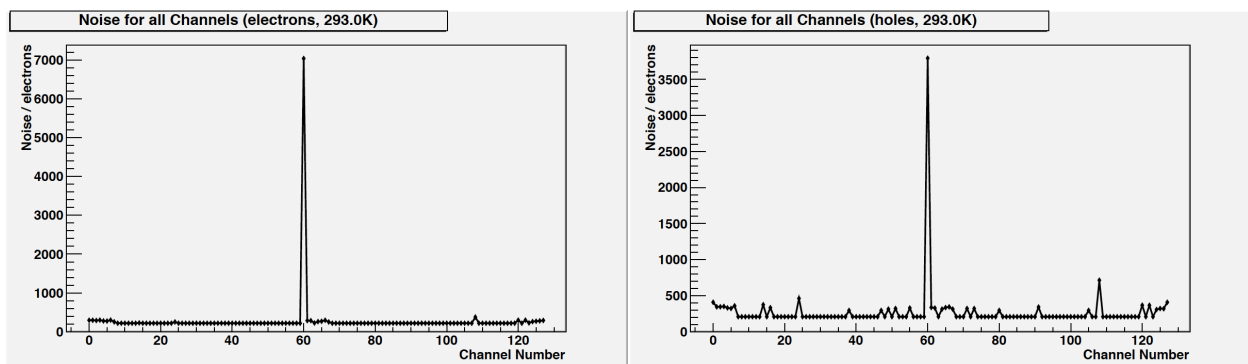


Figure C.3: Noise for all channels with injection cable connected to channel 60 but with no pulse injected, in 'electrons' mode (left) and 'holes' mode (right).

### C.3 Gain

The gain measurement for a second CBC was measured from the data obtained by varying the injected pulse magnitude from the pulse generator to the CBC between 0.3 fC and 4.8 fC. Firstly, by varying the delay between sending a pulse and taking a triggered data sample from the CBC, a picture can be built up of the behaviour of the analogue front-end of the CBC. This will, in fact, give a measure of the voltage in the postamplifier convoluted with any voltage offset in the comparator. Plots of the s-curve mid-point for the range of delays (in steps of 1 ns) is shown for four injected sizes of injected charge in Figure C.4a.

The gain, defined as the mean ratio of the output signal to the input of a system. A plot of the difference between the peak and the pedestal voltages as a function of injected charge can

be produced (Figure C.4b), from which the gradient gives the gain of the CBC at 20 °C in 'holes' mode. This value was calculated as  $31.7 \pm 1.1$  mV/fC

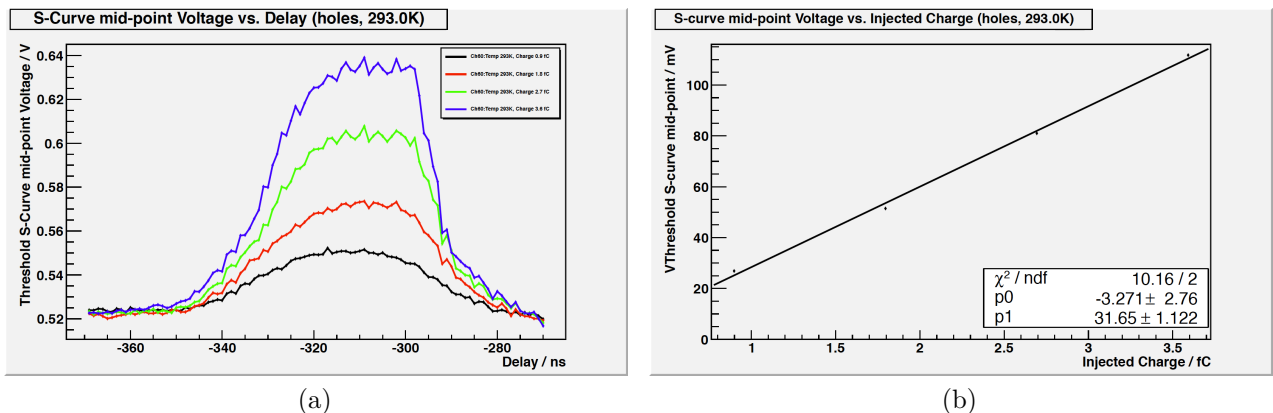


Figure C.4: S-curve mid-point (a) as a function of pulse generator delay and (b) as a function of injected charge in 'holes' mode at 20 °C.

## C.4 Investigating change in Preamp Input Branch Bias Current

The ‘Ipre1’ bias generator register of the CBC governs the current in the input to the preamplifier in the front-end of the chip. Following scans over the Ipre1 range for a range of temperatures from -40 °C to 40 °C (Figure C.5, it was noted that the effect of modifying the current in the preamplifier input seems to flatten out after showing an initial decrease between 10 µA and 100 µA for ‘electrons’ mode, and after an initial increase between values of 10 µA to 50 µA for ‘holes’ mode. NOT REALLY SURE WHAT THIS SHOWS, JUST INVESTIGATED THE EFFECT OF IPRE1. NEED TO PUT A SENTENCE IN HERE ABOUT WHAT THIS TELLS US.

## C.5 Summary

This chapter has presented a short report based on the continuation of work from the author's MSc investigation the CBC. Attempts were made to characterise the noise in the CBC using

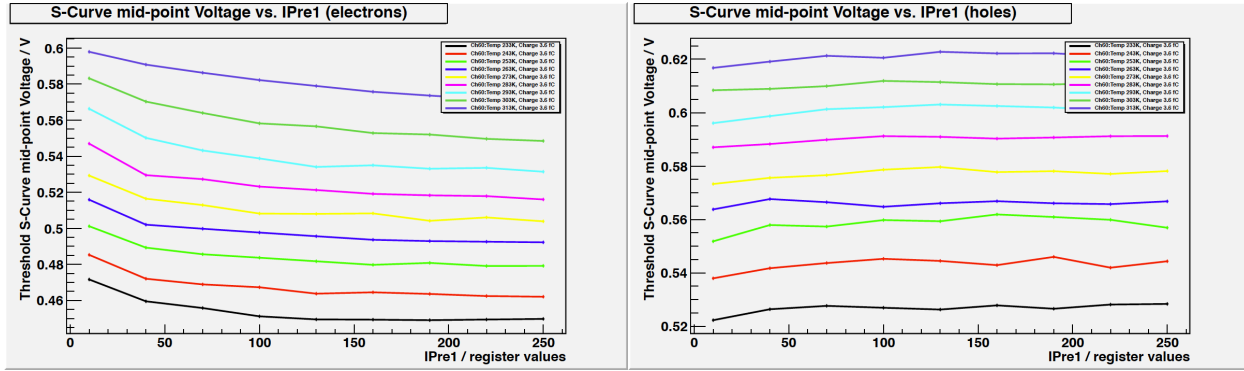


Figure C.5: Variation in s-curve mid-point over range of Ipre1 register values for temperatures from -40 °C to 40 °C.

additional capacitors, but these showed that the noise levels in the test setup were excessively high. Attempts were made to reduce this to below the design target of 1000 electrons. However, the impact of the actions taken were enough only to reduce the noise on CBC channels that are not wire-bonded to approximately 200 electrons, while the noise present in a bonded channel connected to the pulse generator was still several thousand electrons.

The gain of a second CBC was measured in 'holes' mode at 20 °Cas  $31.7 \pm 1.1$  mV/fC, which is in agreement with typical values of readout chips in silicon detectors of between approximately 15 mV/fC and 40 mV/fC [70]. The bias generator regulating the current input to the preamplifier was investigated over its register range at temperatures from -40 °C to 40 °C. It was found that in the region up to 100  $\mu$ A, the comparator voltage decreased in 'electrons' mode, and up to 50  $\mu$ A increased for 'holes' mode.

Following the work in [67] and that presented here, testing has continued on a newer 254-channel version of the chip (CBC2), with triggering capability on-board to contribute to the Level 1 trigger and designed to be bump-bonded as opposed to wire bonded [73, 11]. Prototypes of the modules that will carry the CBCs when installed in the CMS detector have also been produced and tested. The subsequent CBC3 is currently in the design and manufacture stage (TODO:CAN I REFERENCE PRESENTATIONS IN A PHD THESIS?) and is scheduled to be available for testing in approximately May 2016, with an 'insurance' CBC4 scheduled, if necessary, for testing to begin with the final version in 2018.

# References

- [1] Track impact parameter based b-tagging with CMS. Technical Report CMS-AN-2005-041, CERN, 2005. Geneva, Nov 2005.
- [2] Algorithms for b Jet identification in CMS. Technical Report CMS-PAS-BTV-09-001, CERN, 2009. Geneva, Jul 2009.
- [3] Particle-Flow Event Reconstruction in CMS and Performance for Jets, Taus, and MET. Technical Report CMS-PAS-PFT-09-001, CERN, 2009. Geneva, Apr 2009.
- [4] Electron reconstruction and identification at  $\sqrt{s} = 7$  TeV. Technical Report CMS-PAS-EGM-10-004, CERN, Geneva, 2010.
- [5] Performance of b tagging at  $\sqrt{s}=8$  TeV in multijet, ttbar and boosted topology events. Technical Report CMS-PAS-BTV-13-001, CERN, Geneva, 2013.
- [6] Measurement of Z production as a function of pT, Y. Technical Report CMS-PAS-SMP-13-013, CERN, Geneva, 2014.
- [7] Georges Aad et al. Observation of a new particle in the search for the Standard Model Higgs boson with the ATLAS detector at the LHC. *Phys. Lett.*, B716:1--29, 2012.
- [8] Georges Aad et al. Combined Measurement of the Higgs Boson Mass in  $pp$  Collisions at  $\sqrt{s} = 7$  and 8 TeV with the ATLAS and CMS Experiments. *Phys. Rev. Lett.*, 114:191803, 2015.
- [9] Roel Aaij et al. Observation of  $J/\psi p$  resonances consistent with pentaquark states in  $\Lambda_b^0 \rightarrow J/\psi K^- p$  decays. 2015.
- [10] S. Abachi et al. Observation of the top quark. *Phys. Rev. Lett.*, 74:2632--2637, 1995.

- [11] D Abbaneo. Upgrade of the CMS tracker with tracking trigger. *J. Instrum.*, 6:C12065. 10 p, 2011.
- [12] F. Abe et al. Observation of top quark production in  $\bar{p}p$  collisions. *Phys.Rev.Lett.*, 74:2626--2631, 1995.
- [13] Wolfgang Adam, R FrÄijhwirth, Are Strandlie, and T Todor. Reconstruction of Electrons with the Gaussian-Sum Filter in the CMS Tracker at the LHC. Technical Report CMS-NOTE-2005-001, CERN, Geneva, Jan 2005.
- [14] P.A.R. Ade et al. Planck 2013 results. I. Overview of products and scientific results. *Astron.Astrophys.*, 571:A1, 2014.
- [15] Tim Adye. Unfolding algorithms and tests using RooUnfold. pages 313--318, 2011.
- [16] S. Agostinelli et al. GEANT4: A Simulation toolkit. *Nucl. Instrum. Meth.*, A506:250--303, 2003.
- [17] Simone Alioli, Paolo Nason, Carlo Oleari, and Emanuele Re. A general framework for implementing NLO calculations in shower Monte Carlo programs: the POWHEG BOX. *JHEP*, 1006:043, 2010.
- [18] John Allison et al. Geant4 developments and applications. *IEEE Trans. Nucl. Sci.*, 53:270, 2006.
- [19] J. Alwall, R. Frederix, S. Frixione, V. Hirschi, F. Maltoni, et al. The automated computation of tree-level and next-to-leading order differential cross sections, and their matching to parton shower simulations. *JHEP*, 1407:079, 2014.
- [20] G. Antchev, P. Aspell, I. Atanassov, V. Avati, J. Baechler, et al. First measurement of the total proton-proton cross section at the LHC energy of  $\sqrt{s} = 7$  TeV. *Europhys.Lett.*, 96:21002, 2011.

- [21] Roberta Arcidiacono, Angela Brett, Francesca Cavallari, André David, Nicholas Scott Eggert, Giovanni Franzoni, Matteo Marone, Pasquale Musella, Giovanni Organtini, Paolo Rumerio, Alessandro Thea, and Evgueni Vlassov. ECAL Front-End Monitoring in the CMS experiment. Technical Report CMS-CR-2009-181, CERN, Geneva, Jul 2009.
- [22] Nima Arkani-Hamed, Savas Dimopoulos, and G. R. Dvali. The Hierarchy problem and new dimensions at a millimeter. *Phys. Lett.*, B429:263--272, 1998.
- [23] W. A. Bardeen, C. T. Hill, and M. Lindner. Minimal dynamical symmetry breaking of the standard model. *Physical Review D*, 41:1647--1660, March 1990.
- [24] G. Breit and E. Wigner. Capture of slow neutrons. *Phys. Rev.*, 49:519--531, Apr 1936.
- [25] Rene Brun and Fons Rademakers. ROOT -- An object oriented data analysis framework. *Nuclear Instruments and Methods in Physics Research Section A: Accelerators, Spectrometers, Detectors and Associated Equipment*, 389(1-2):81--86, 1997. New Computing Techniques in Physics Research V.
- [26] Erik Manuel Butz. Operation and Performance of the CMS Silicon Tracker. Technical Report CMS-CR-2012-357, CERN, Geneva, Nov 2012.
- [27] Matteo Cacciari, Gavin P. Salam, and Gregory Soyez. The Anti-k(t) jet clustering algorithm. *JHEP*, 0804:063, 2008.
- [28] S. Chatrchyan et al. The CMS experiment at the CERN LHC. *JINST*, 3:S08004, 2008.
- [29] S Chatrchyan et al. Commissioning and Performance of the CMS Silicon Strip Tracker with Cosmic Ray Muons. *JINST*, 5:T03008, 2010.
- [30] Serguei Chatrchyan et al. Determination of Jet Energy Calibration and Transverse Momentum Resolution in CMS. *JINST*, 6:P11002, 2011.
- [31] Serguei Chatrchyan et al. Measurement of the Inclusive  $W$  and  $Z$  Production Cross Sections in  $pp$  Collisions at  $\sqrt{s} = 7$  TeV. *JHEP*, 10:132, 2011.

- [32] Serguei Chatrchyan et al. Measurement of the inclusive production cross sections for forward jets and for dijet events with one forward and one central jet in  $pp$  collisions at  $\sqrt{s} = 7$  TeV. *JHEP*, 1206:036, 2012.
- [33] Serguei Chatrchyan et al. Observation of a new boson at a mass of 125 GeV with the CMS experiment at the LHC. *Phys. Lett.*, B716:30--61, 2012.
- [34] Serguei Chatrchyan et al. Performance of CMS muon reconstruction in  $pp$  collision events at  $\sqrt{s} = 7$  TeV. *JINST*, 7:P10002, 2012.
- [35] Serguei Chatrchyan et al. Energy Calibration and Resolution of the CMS Electromagnetic Calorimeter in  $pp$  Collisions at  $\sqrt{s} = 7$  TeV. *JINST*, 8:P09009, 2013.
- [36] Serguei Chatrchyan et al. Identification of b-quark jets with the CMS experiment. *JINST*, 8:P04013, 2013.
- [37] Serguei Chatrchyan et al. Measurement of differential top-quark pair production cross sections in  $pp$  colisions at  $\sqrt{s} = 7$  TeV. *Eur.Phys.J.*, C73(3):2339, 2013.
- [38] Serguei Chatrchyan et al. Description and performance of track and primary-vertex reconstruction with the CMS tracker. *JINST*, 9(10):P10009, 2014.
- [39] J. H. Christenson, J. W. Cronin, V. L. Fitch, and R. Turlay. Evidence for the 2 pi Decay of the k(2)0 Meson. *Phys. Rev. Lett.*, 13:138--140, 1964.
- [40] Sergio Cittolin, Attila RÃ¡cz, and Paris Sphicas. *CMS The TriDAS Project: Technical Design Report, Volume 2: Data Acquisition and High-Level Trigger. CMS trigger and data-acquisition project*. Technical Design Report CMS. CERN, Geneva, 2002.
- [41] CMS Collaboration. Cmssw framework.
- [42] CMS Collaboration. Technical proposal for the upgrade of the CMS detector through 2020. Technical Report CERN-LHCC-2011-006. LHCC-P-004, CERN, Geneva, Jun 2011.

- [43] CMS Collaboration. Absolute Calibration of the Luminosity Measurement at CMS: Winter 2012 Update. 2012.
- [44] CMS Collaboration. CMS Luminosity Based on Pixel Cluster Counting - Summer 2013 Update. 2013.
- [45] CMS Collaboration. Jet transverse momentum resolution measurement using dijet events. *AN-13-416, work in progress*, 2013.
- [46] DØ Collaboration. B jet identification.
- [47] The ATLAS collaboration. Combination of ATLAS and CMS results on the mass of the top-quark using up to  $4.9 \text{ fb}^{-1}$  of  $\sqrt{s} = 7 \text{ TeV}$  LHC data. 2013.
- [48] E P Corrin. *Development of Digital Readout Electronics for the CMS Tracker*. PhD thesis, Imperial College, London, 2002.
- [49] D. Delikaris, J.P. Dauvergne, G. Passardi, J.C. Lottin, J.P. Lottin, et al. The Cryogenic system for the superconducting solenoid magnet of the CMS experiment. 1998.
- [50] T.Speer et al. Algorithms for b jet identification in CMS. Technical Report CMS-AN-2009-085, CERN, 2009. Geneva, Aug 2009.
- [51] W. Ferguson, D. Braga, J. Fulcher, G. Hall, J. Jacob, L. Jones, M. Pesaresi, M. Prydderch, and M. Raymond. The CBC microstrip readout chip for CMS at the high luminosity LHC. *JINST*, 7:C08006, 2012.
- [52] Cristina Ferro. B-tagging in CMS. *EPJ Web Conf.*, 28:12055, 2012.
- [53] Stefano Frixione, Paolo Nason, and Carlo Oleari. Matching NLO QCD computations with Parton Shower simulations: the POWHEG method. *JHEP*, 0711:070, 2007.
- [54] Stefano Frixione, Paolo Nason, and Carlo Oleari. Matching NLO QCD computations with Parton Shower simulations: the POWHEG method. *JHEP*, 0711:070, 2007.

- [55] Stefano Frixione, Paolo Nason, and Bryan R. Webber. Matching NLO QCD and parton showers in heavy flavor production. *JHEP*, 0308:007, 2003.
- [56] R. Fruhwirth. Application of Kalman filtering to track and vertex fitting. *Nucl.Instrum.Meth.*, A262:444--450, 1987.
- [57] Y. Fukuda et al. Evidence for oscillation of atmospheric neutrinos. *Phys. Rev. Lett.*, 81:1562--1567, 1998.
- [58] J E Gaiser. *Charmonium Spectroscopy from Radiative Decays of the  $J/\psi$  and  $\psi'$* . PhD thesis, Stanford Linear Accelerator Center (SLAC), Stanford, California, U.S.A., August 1982.
- [59] V M Ghete and Cms Collaboration. The cms l1 trigger emulation software. *Journal of Physics: Conference Series*, 219(3):032009, 2010.
- [60] Martyn Gigg and Peter Richardson. Herwig++. 2007.
- [61] D. Griffiths. *Introduction to Elementary Particles*. John Wiley & Sons, New York, USA, 1987.
- [62] TOPLHC Working Group. Toplhc wg summary plots.
- [63] Peter W. Higgs. Broken Symmetries and the Masses of Gauge Bosons. *Phys. Rev. Lett.*, 13:508--509, 1964.
- [64] C. T. Hill. Topcolor: top quark condensation in a gauge extension of the standard model. *Physics Letters B*, 266:419--424, August 1991.
- [65] S. Hoche et al. Matching parton showers and matrix elements. *hep-ph/0602031*, 2006.
- [66] Andreas Hocker and Vakhtang Kartvelishvili. SVD approach to data unfolding. *Nucl.Instrum.Meth.*, A372:469--481, 1996.

- [67] J A Jacob. Investigation of the cms binary chip for strip tracker readout in the cms detector at the hl-lhc. Masters thesis, University of Bristol, Bristol, 2014.
- [68] L. jones. *CMS Binary Chip User Guide 1.0, Science and technology Facilities Council*, January 2012.
- [69] Takaaki Kajita. Atmospheric neutrino results from Super-Kamiokande and Kamiokande: Evidence for neutrino(mu) oscillations. *Nucl. Phys. Proc. Suppl.*, 77:123--132, 1999.
- [70] J. Kaplon et al. Progress in development of the analog read-out chip for silicon strip detector modules for LHC experiments. In *7th Workshop on electronics for LHC experiments, Stockholm, Sweden, 10-14 Sep 2001: Proceedings*, pages 90--94, 2001.
- [71] Vardan Khachatryan et al. Performance of photon reconstruction and identification with the CMS detector in proton-proton collisions at  $\sqrt{s} = 8$  TeV. 2015.
- [72] Min Suk Kim et al. CMS reconstruction improvement for the muon tracking by the RPC chambers. *PoS*, RPC2012:045, 2012.
- [73] Katja Klein. Upgrade of the CMS Tracker. Technical Report CMS-CR-2013-403, CERN, Geneva, Nov 2013.
- [74] Luke Kreczko, Jeson Jacob, Sergey Senkin, and EmyrClement. Analysissoftware: Analysissoftware version for top-12-042 paper, 2015.
- [75] Luke Kreczko, Sergey Senkin, Jeson Jacob, and EmyrClement. Dailypythonscripts: Dailypythonscript version for top-12-042 paper, 2015.
- [76] Luke Kreczko, Sergey Senkin, Jeson Jacob, and EmyrClement. Ntupleproduction: Ntupleproduction version for top-12-042 paper, 2015.
- [77] Christos Leonidopoulos and The CMS Collaboration. Cms tracking performance results from early lhc operation. *The European Physical Journal C - Particles and Fields*, C70:1165--1192, 2010.

- [78] Stefano Mersi. CMS silicon tracker upgrade for HL-LHC. *Proceedings of Science*, RD11:030, 2011.
- [79] Ian G. Moss. Higgs boson cosmology. 2015.
- [80] Paolo Nason. A New method for combining NLO QCD with shower Monte Carlo algorithms. *JHEP*, 0411:040, 2004.
- [81] K.A. Olive et al. Review of Particle Physics. *Chin.Phys.*, C38:090001, 2014.
- [82] M Oreglia. *A Study of the Reactions  $\psi' \rightarrow \gamma\gamma\psi$* . PhD thesis, Stanford Linear Accelerator Center (SLAC), Stanford, California, U.S.A., December 1980.
- [83] F M Palmonari. CMS Silicon Strip Tracker Commissioning and Preliminary Performances. *Nucl. Phys. B, Proc. Suppl.*, 197(1):121--124, 2009.
- [84] Ringaile Placakyte. Parton Distribution Functions. In *Proceedings, 31st International Conference on Physics in collisions (PIC 2011)*, 2011.
- [85] M. Raymond, D. Braga, W. Ferguson, J. Fulcher, G. Hall, J. Jacob, L. Jones, M. Pesaresi, and M. Prydderch. The CMS binary chip for microstrip tracker readout at the SLHC. *JINST*, 7:C01033, 2012.
- [86] Tai Sakuma and Thomas McCauley. Detector and Event Visualization with SketchUp at the CMS Experiment. *J.Phys.Conf.Ser.*, 513:022032, 2014.
- [87] Torbjorn Sjostrand, Stephen Mrenna, and Peter Z. Skands. A Brief Introduction to PYTHIA 8.1. *Comput.Phys.Commun.*, 178:852--867, 2008.
- [88] T Skwarnicki. *A Study of the Radiative Cascade Transitions between the Upsilon-Prime and Upsilon Resonances*. PhD thesis, Deutsches Elektronen-Synchrotron (DESY), Hamburg, Germany, April 1986.

- [89] Thomas Speer, Kirill Prokofiev, R FrÃ¡ijhwirth, Wolfgang Waltenberger, and Pascal Vanlaer. Vertex Fitting in the CMS Tracker. Technical Report CMS-NOTE-2006-032, CERN, Geneva, Feb 2006.
- [90] The CMS Collaboration. *CMS Physics: Technical Design Report Volume 1: Detector Performance and Software*. Technical Design Report CMS. CERN, Geneva, Switzerland, 2006.
- [91] Wolfgang Waltenberger, Rudolf FrâĽŽÂžhwirth, and Pascal Vanlaer. Adaptive vertex fitting. *Journal of Physics G: Nuclear and Particle Physics*, 34(12):N343, 2007.
- [92] Christian Weiser. A Combined Secondary Vertex Based B-Tagging Algorithm in CMS. Technical Report CMS-NOTE-2006-014, CERN, Geneva, Jan 2006.